Microstructural and performance analysis of fuel cell electrodes

by

Mayank Sabharwal

A thesis submitted in partial fulfillment of the requirements for the degree of

Doctor of Philosophy

Department of Mechanical Engineering
University of Alberta

Abstract

Microscopy techniques have emerged as a powerful tool to study the morphology of fuel cell porous media. Mathematical parametrization of the microscopy images is important to characterize the porous media microstructure and compare the differences between various samples. A framework which can process microscopy images to generate a microstructure and perform statistical and functional characterization is necessary to streamline the process of going from images to performance.

This thesis presents an open-source numerical framework for microstructural analysis of fuel cell porous media. The framework can be used to: i) process raw data from microscopy images; ii) statistically characterize the microstructure using two-point correlation function, chord length function and pore size distribution; iii) generate stochastic reconstructions of porous media; iv) generate voxel based meshes; and v) study gas transport, charge transport and electrochemical reactions under dry and wet conditions.

The numerical tools developed in this thesis are used to analyze the effect of catalyst layer microstructure on the transport properties and electrochemical performance by studying the: i) effect of catalyst layer porosity and local saturation on the effective diffusivity; ii) effect of the catalyst layer pore size distribution on the electrochemical performance under dry and wet conditions; and iii) effect of ionomer content and distribution on the effective transport properties and electrochemical performance. Stochastic reconstructions are used to generate catalyst layers (CLs) with different microstructures for these studies.

Numerical simulations are used to study gas transport in CLs with different porosities and local saturations. Partially saturated CL reconstructions were obtained using a novel nucleation based water intrusion algorithm. The effective diffusivities computed for CLs with different porosities and local saturations are used to develop a correlation based on the percolation theory which was only dependent on the effective porosity and average pore radius of the CL.

Electrochemical simulations on CLs with different pore size distributions show negligible variations under dry conditions because mass transport is limited by the interfacial resistance of the ionomer film. Under wet conditions, the electrochemical performance initially remains constant and then decreases rapidly beyond a certain saturation due to pore blockage by liquid water. The results from the current study indicate that a CL with smaller and more hydrophobic pores would be better at delaying the onset of flooding in the CL and therefore, have a higher performance at a given capillary pressure.

CL reconstructions with different ionomer contents and distributions are generated using the ionomer reconstruction algorithm presented in this work. Results show that the ionomer distribution had a significant impact on the effective protonic conductivity and electrochemical performance at low I/C ratios. The effective diffusivity in the CL also decreases when the ionomer distribution is changed from uniform to non-uniform.

Keywords: Microstructure, stochastic reconstructions, catalyst layer, electrochemical reactions, liquid water, diffusion, ionomer films

Preface

Parts of Chapter 2 and 4 of this thesis have been published as M. Sabharwal, L. M. Pant, A. Putz, D. Susac, J. Jankovic and M. Secanell. "Analysis of catalyst layer microstructures: From imaging to performance". *Fuel Cells*, 2016, Volume 16, Issue 2, pp. 734-753. I was responsible for review, development and programming of image processing and numerical tools, analysis, data processing and manuscript writing. L.M. Pant was responsible for development of the statistical analysis functions, technical discussions and manuscript editing. A. Putz was the industrial collaborator who provided technical perspectives and also helped in manuscript revisions. D. Susac and J. Jankovic were the industrial collaborators who were responsible for the imaging of the catalyst layer sample and provided help with manuscript composition and revision. M. Secanell was the supervisory author, and helped shape the manuscript objective, manuscript composition and editing.

Parts of Chapter 2 and 3 have been published as M. Sabharwal, J. T. Gostick and M. Secanell. "Virtual Liquid Water Intrusion in Fuel Cell Gas Diffusion Media". *Journal of The Electrochemical Society*, 2018, Volume 165, Issue 7, pp. F553-F563. I was responsible for review, model development and implementation, data processing and analysis, and manuscript writing and revision. J. T. Gostick was a collaborator who provided the μ-CT images of the gas diffusion media and provided technical perspectives on the manuscript. M. Secanell was the supervisory author and helped with the manuscript concept, writing and review.

Parts of Chapter 2 and 4 have been published as M. Sabharwal, L.M. Pant, N. Patel and M. Secanell. "Computational Analysis of Gas Transport in Fuel Cell Catalyst Layer Under Dry and Partially Saturated Conditions". *Journal of The Electrochemical Society*, 2019, Volume 166, Issue 7, pp. F3065-F3080. I was responsible for review, model development and implementation, data processing and analysis, and manuscript writing and revision. L. M. Pant was responsible for development of the statistical functions, technical discussions and manuscript revision. N. Patel was responsible for development of the stochastic reconstruction algorithm. M. Secanell was the supervisory author and helped with the manuscript

concept, writing and review.

Parts of Chapter 2 have been published as M. Sabharwal and M. Secanell. "Microstructural Analysis of Electrode Performance at Varying Water Contents". *ECS Transactions*, 2018, Volume 86, Issue 13, pp. 51-67. I was responsible for model development and implementation, analysis and manuscript writing. M. Secanell was the supervisory author and helped with the manuscript objective, writing and review.

To my mother

Acknowledgements

First and foremost, I would like to thank my PhD supervisor, Dr. Marc Secanell, for having given me the opportunity to be part of his research group. His profound belief in my abilities, constructive criticism, insightful advice and boundless patience saw me through the highs and lows of my time here as a graduate student. The many (and many) discussions we had on science and life have helped me evolve into the person that I am today. Your guidance and humor will be sorely missed.

During the course of my thesis, I got to meet and interact with some great people who were more than willing to share their knowledge with me. First on this list is Dr. Andreas Putz at MistyWest, Vancouver. His eye for detail and technical insights greatly helped in improving this work. I would like to thank Dr. Jasna Jankovic at University of Connecticut for providing the microscopy images for this work. Special thanks to Dr. Darija Susac at HySA, South Africa for the microscopy images and countless technical discussions which helped me understand the nuances of imaging. I would also like to thank Dr. Jeff Gostick at Chemical Engineering Department, University of Waterloo for providing the micro-CT images for the partially saturated GDL sample. Finally, I would like to thank Dr. Kunal Karan at Department of Chemical and Petroleum Engineering, University of Calgary for the insightful discussions.

None of this work would have been possible without the financial assistance from Natural Sciences and Engineering Research Council of Canada (NSERC), Automotive Fuel Cell Cooperation Corporation (AFCC) and Alberta Innovates Graduate Student Scholarship (AIGSS).

Coming to Edmonton was a big transition and my friends at Energy Systems Design Laboratory (ESDL) made this a smooth one. I would like to thank all the ESDLers for bringing the "life" in graduate student life. The times we spent together were fun and will be cherished. Special thanks to Aslan for all his help during this period and for being the only one working as late as I. I would also like to thank Jie for all the beer sessions we had. And Tim Hortons, for their relentless supply of double-doubles and poppyseed-lemon loaves

that powered me through the writing process on sugar highs.

I read somewhere that true friends are the people who are there for you when they would rather be anywhere else. You know who you are, and I thank you for being there for me through it all. Thank you Tanushree, for the sustenance and the delicious dinners and thank you Abhishek for all the trips to the Rockies and being a patient listener! I often joked that you guys should write me into your will, but I sincerely feel you have become family.

Last but not the least, I would like to acknowledge my family for the emotional support and unconditional love that really made all the difference. Firstly, my parents, who supported my decision to move across continents, knowing full well that they wouldn't see their son more than a few weeks each year. A big thanks to my siblings Aman and Astha, for keeping it all together back home and for giving me all the gossip that I missed out on. My wife Vaishnavi, who has been a constant source of support and steered me back on track everytime I drifted. This thesis would have taken a couple more months if it had not been for her persistent reminders to get "it" done. I am lucky to have such a loving family.

This thesis would not have been made possible without the support and guidance of these people. Thank you!

Table of Contents

List of Tables

List of Figures

Chapter 1

Introduction

1.1 Motivation

The transportation sector accounts for 21% of the primary energy consumption and 23% of the greenhouse gas (GHG) emissions in Canada [14]. GHG emissions are a major contributor to pollution and global climate change. According to the Paris Agreement [15], to tackle the growing threat of climate change Canada pledged to reduce its GHG emissions by 17% and 30% of the 2005 value by 2020 and 2030, respectively. Achieving this target is likely to require the reduction of CO_2 emissions from the transportation sector which currently accounts for 23% of the overall GHG emissions in Canada [14]. To curb the use of fossil fuels in the transportation sector, battery (or electric) and hydrogen fuel cell vehicles are widely seen as a feasible alternative to the traditional gasoline engine vehicles. Hydrogen polymer electrolyte fuel cell vehicles have a distinct advantage over the battery counterparts in terms of refueling time and driving range. This has seen the application of hydrogen fuel cells into passenger cars [16, 17], passenger trains [18], trucks and semi-trucks [17, 19]. In addition to the automotive sector, the use of fuel cells in backup power, forklifts, and portable applications is also being investigated [20].

Cost, efficiency and durability hinder the mass commercialization of polymer electrolyte fuel cells. Eikerling et al. [21] estimate that only 10-20% of the catalyst is utilized in current polymer electrolyte fuel cells. Further, to meet the 2020 U.S. Department of Energy targets of \$30/kW, PEMFCs need to be designed to achieve higher power densities or reduce the use of expensive catalyst (platinum) [22]. Also, improving the design and controlling the operating conditions for PEMFCs is crucial to minimize degradation of the cell and hence improve the lifetime [23]. An understanding of the effect of change in the design parameters, such as composition, type of solvent and fabrication process, on the transport properties and electrochemical performance could aid in the design of polymer electrolyte fuel cell electrodes

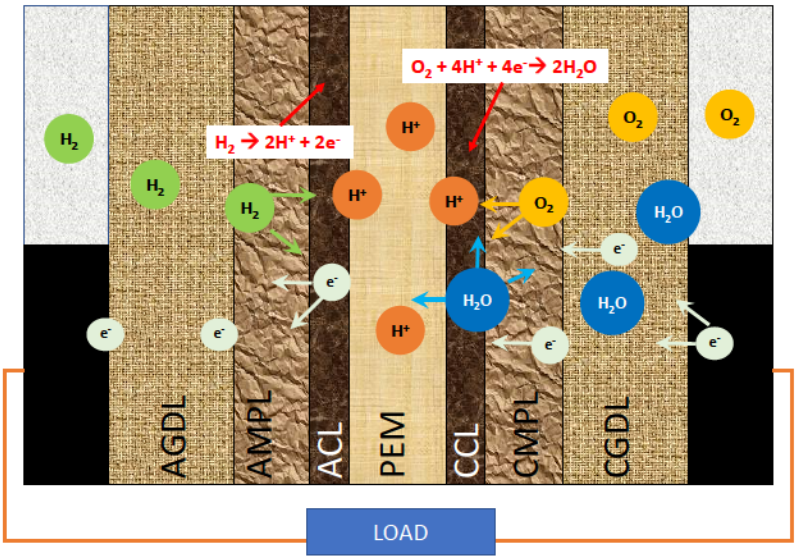

Figure 1.1 – Schematic of a single cell of proton exchange membrane fuel cell showing half channel and half land volume. GDL is the gas diffusion layer, MPL is the micro-porous layer, CL is the catalyst layer, PEM is the proton exchange membrane and 'A' and 'C' signify anode and cathode electrodes, respectively.

which overcome the current challenges.

Figure 1.1 shows the schematic of a proton exchange membrane fuel cell (PEMFC). In a PEMFC, hydrogen enters through the channels on the anode side and reacts to produce protons and electrons. Protons are conducted through the polymer electrolyte membrane (PEM) to the cathode side where they react with the oxygen from the cathode channel and electrons from the cathode land to produce water and heat. The transport of gas, protons and electrons in the PEMFC is achieved by the use of several porous layers which vary in functionality.

The schematic in Figure 1.1 shows a half channel - half land volume of a single cell. The land and channel of the cell on both the anode and cathode side are in contact with a 150-300 μm thick porous layer called the gas diffusion layer (GDL). GDL is made of either carbon paper or carbon cloth and is often treated with PTFE to introduce hydrophobicity [24]. The GDL helps distribute the reactants from the channels and provides an electronic connection from the bipolar plate to the catalyst layer. It is also responsible for the removal of heat and water (both vapor and liquid) produced in the cathode catalyst layer. GDLs often have an additional layer called the micro-porous layer (MPL) embedded onto them. MPLs typically have much smaller pore sizes in the range of 10 nm - 1 μm [25] compared to GDLs which have pore sizes in the range of 1-100 μm [26]. MPLs have been found to improve the perfor-

mance of the fuel cell under wet conditions [27–32] which has been attributed to improved back-diffusion of water from cathode to anode, higher evaporation rates due to increase in temperature in the electrodes and improving water removal from the catalyst layer to the channel.

The heart of the fuel cell is the catalyst layer (CL), a porous composite made of: i) carbon (electron conducting phase); ii) ionomer (proton conducting phase); and iii) a catalyst (usually platinum), which is the center for the electrochemical reaction. The anode and cathode CLs are responsible for the hydrogen oxidation reaction (HOR) and oxygen reduction reaction (ORR) respectively, as shown in Figure 1.1. The anode and cathode CLs are separated by a PEM which conducts protons from the anode to cathode and also allows the diffusion of water to either side while acting as an electronic insulator. Nafion® is commonly used as the polymer electrolyte in both the membrane and CLs in a PEMFC.

To understand the multi-faceted functionality of the porous media in PEMFC, several studies, both experimental and numerical, have investigated the relationship between the composition (and type) of the porous media and their transport properties and performance, e.g., [33–44] to name a few. Several of these studies indicate that even for similar compositions, the transport properties and performance of the porous media vary with the type of material used [39, 45] and method of preparation [35, 36, 38, 44]. Further, Saha et al. [44] also showed, using scanning transmission x-ray microscopy (STXM), that the distribution of the carbon, ionomer and platinum changes with the fabrication method, for example an inkjet printed and decal transferred CL. These observations indicate that the microstructure of the porous media depends on its composition and method of preparation and affects the corresponding transport properties and performance.

Fuel cell porous media microstructure has previously been investigated [4, 25, 26, 46, 47, 47–65], but very few studies [4, 6, 9, 10, 43, 62, 65–67] investigate the effect of composition of porous media on the transport properties and electrochemical performance. The changes in microstructure due to the composition are also seldom investigated especially for CLs. A comprehensive study exploring the relationships between the structure, transport properties and performance of fuel cell electrodes is not available in the current literature and such a study could serve as a design tool to optimize fuel cell electrodes.

The objective of the current thesis is to develop computational tools to study the relationships between the fuel cell porous media microstructure and its effective transport properties and electrochemical performance. Figure 1.2 shows a schematic highlighting the hypothe-

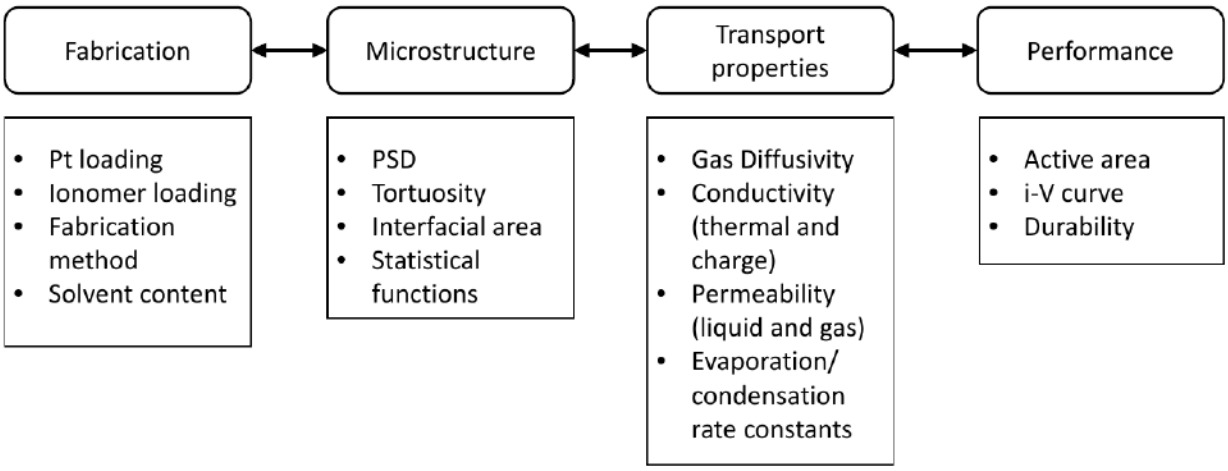

Figure 1.2 – Schematic of the interlinks between the fabrication, structure, transport properties and performance of the porous media.

sized interlinks between the fabrication, microstructure and performance and some of the descriptors for each of the categories. To correlate the fabrication to the microstructure, microscopy images of porous media can be analyzed to extract statistical descriptors such as porosity, tortuosity, pore size distribution (PSD), and two-point correlation function, and correlate the changes in the composition of the porous media to these statistical descriptors. To correlate the microstructure to the properties/performance, mathematical models and numerical simulation tools are required which can be used to study the physical processes in the 3D reconstructions and correlate the changes in effective transport properties such as effective diffusivity, charge and thermal conductivity, liquid and gas permeability, and electrochemical performance to the changes in statistical descriptors for the microstructures generated using image-based [47, 51, 53] or stochastic reconstructions [6, 68, 69]. The latter provides a significant reduction in the time required for sensitivity and parametric analysis but lacks the information about the fabrication and microstructure interlinks. The knowledge of the correlations between fabrication, microstructure, effective transport properties and performance could aid in the design of optimal fuel cell electrodes.

To study the interlinks between the fabrication, structure, transport properties and performance, a numerical framework capable of analyzing microstructures and performing physico-chemical based simulations on 3D image data is required. Such a framework must address the following critical aspects,

1. **Image analysis** - Mathematical parameterization of the microscopy images to extract meaningful information in the form of statistical descriptors such as porosity, tortuosity,

two-point correlation function, chord length function and pore size distribution.

2. **Stochastic reconstructions** - Stochastic reconstructions are required to perform parametric studies that highlight the most relevant statistical descriptors in a porous medium for a given physico-chemical process. Stochastic reconstructions can be generated using simulated annealing method [68] or fabrication based methods involving primary building blocks such as spherical agglomerate growth models [6, 69]. For the simulated annealing method, reconstructed structures are optimized to match reference or some variation of statistical functions extracted from microscopy images. Fabrication based methods such as spherical agglomerate growth models, use random seed points around which the particles grow in a stochastic manner.

3. **Meshing** - In order to perform a numerical calculation on the obtained structure, a computational domain (mesh) needs to be generated from the image data (3D arrays).

4. **Numerical modeling** - The physical and chemical processes occurring in the PEMFC electrodes need to be described by a set of governing equations. These equations must be discretized and solved numerically due to the complex structure of the computational domain.

1.2 Literature Review

Several experimental and numerical studies have investigated fuel cell porous media microstructures. The sections below discuss the state-of-the-art in microstructure generation and numerical modeling of the physical and electrochemical processes occurring in fuel cell porous media. Their advantages and shortcomings are highlighted in this section.

1.2.1 Microstructure generation

1.2.1.1 Direct imaging

Microscopy techniques, such as x-ray computed tomography (X-CT) [26, 47, 52–61, 70], scanning transmission x-ray microscopy (STXM) [44, 71, 72] and focused ion beam-scanning electron microscopy (FIBSEM) [10, 25, 46–51], have been used to visualize the microstructure of fuel cell porous media. The choice of the technique depends on the application and fuel cell layer to be visualized. X-ray computed tomography offers a non-destructive method for imaging the porous media, where 2D x-ray projections of the porous media are captured at several angles and then backprojected to generate the 3D microstructure. X-CT has been

used to reconstruct catalyst layers [52, 53], micro-porous layers [47, 61, 70, 73] and gas diffusion layers [54, 55, 57, 59, 70, 74]. μ-CT or nano-CT technique can achieve voxel resolutions of 1-5 μm or 10-50 nm respectively. nano-CT has also been used to image the ionomer distribution in platinum group free CL using caesium staining [75]. μ-CT has recently been used to obtain 3D reconstructions of partially saturated GDLs [55, 56, 60, 76–79] thereby enabling the study of the changes in the liquid water distributions with compression [60, 80], capillary pressure [55, 56, 76, 79] and temperature gradients [77, 78, 80].

STXM uses an x-ray at different energies to raster a sample and record the intensity of the x-ray transmitted through the material. Different materials would have different absorption edge, i.e., the energy at which the photons cause electrons to jump from an inner shell to an outer shell (excited state), which would depend on the chemical structure of the material. Further, the absorption of photons would depend on the thickness and density of the sample. STXM uses the difference in the absorption just below and above the absorption edge to identify the material present. Then the optical density is computed by using a reference location and using the optical density, the material quantity can be computed. A detailed description of the STXM procedure and tutorial can be found in [81]. STXM has primarily been used to visualize the distributions of carbon, platinum and ionomer in the CL [44, 71, 72, 82]. The same technique has also been recently used to characterize the composition of micro-porous layers [83]. The pixel resolution from STXM is nearly 50 nm in image; however, the sample used has to be ultra-microtomed to a thickness of nearly 100 nm.

FIBSEM is a destructive technique which uses an ion beam (usually Ga^+), to slice the sample and an electron beam to image the exposed sample. Resolutions as high as 2 nm/pixel in the SEM image can be achieved using this technique [51], which make it a favorable option for visualizing the nano pores in catalyst layers [48, 49, 51, 84–87] and microporous layers [25, 46, 47, 50, 88]. However the resolution in the slicing direction is only 10-20 nm thereby leading to significant loss of information in this direction and artificial anisotropy in the structure [51].

Microscopy techniques produce large image data-sets which often require extensive image analysis to remove external noise and provide meaningful information about the underlying structure. Even though different imaging methods often require additional image processing operations, such as backprojections for X-CT [89], depth information for FIBSEM [90, 91] and conversion of intensity maps to optical density maps for the STXM [71], the majority of basic image processing operations such as image alignment or registration, image enhancement and thresholding or segmentation are common to all imaging technique data sets such

that a framework for image analysis can be developed that can be used for a variety of techniques.

Image alignment or registration of the stack of images is typically achieved by fabricating a fiducial marker during sample preparation. Using the fiducial marker, the images can be aligned with a high degree of accuracy using Fourier transform [25, 46, 47], transformations, like rigid body, translation, rotation and affine [49], or minimization of image translation using least squares method [48, 51]. Image thresholding has been conventionally performed by either visual inspection [61, 92] or based on global histograms [26, 46, 48, 52, 73, 74, 93]. The segmented images are then further corrected, using manual segmentation or mathematical operations, to achieve desired porosities and/or improve pore connectivity. These methods rely on manual corrections and cannot take into account local variations in the image intensities, especially in different image slices. More recently, advanced segmentation algorithms such as Sauvola [51, 90, 94] and two-stage backpropagation algorithm [90, 91] have also been used for FIBSEM image segmentation.

Porous media imaging provides an excellent option to study the changes in microstructure with manufacturing methods. However, direct imaging is not an efficient method to perform extensive parametric studies with different microstructures. Since the microstructure is, to this day, difficult to control during fabrication, imaging remains an expensive and time consuming endeavor. Numerically reconstructed geometries are therefore required to study the effect of porous media structure on the transport properties and performance.

1.2.1.2 Stochastic reconstructions

Stochastic reconstructions provide a computationally efficient alternative to direct imaging techniques to generate the microstructure for fuel cell porous media. Microstructures for fuel cell porous media have been generated based on heuristics [6, 69, 95, 96] and geometric abstractions (such as spheres for particles and lines for fibers) [4, 5, 7, 43, 62–65, 97–103]. Heuristic based methods generate random seed points and "grow" the solid phase from these seed points. These methods aim to mimic the particle agglomeration during the fabrication process in a simplistic manner and ignore any colloidal and particle interactions. Microstructures have also been generated using simplified geometric abstractions (such as spheres for particles and lines for fibers) [4, 5, 7, 43, 62–65, 97–103]. These methods often use additional data such as reference statistical functions [99, 104–106] from microscopy images, or experimental measurements, such as mercury intrusion porosimetry (MIP) [65, 97, 107] or BET adsorption isotherms [108] for microstructure generation. This however, is not sufficient to

guarantee statistical equivalence between the stochastic and real microstructure of the porous media. For example, while identical auto (or two-point) correlation function between a generated microstructure and reference microstructure guarantees an identical volume fraction and interfacial area between two structures, it does not enforce any equivalency in pore size and long range connectivity.

Multiple statistical characterization metrics could be used in order to enforce equivalency for a variety of metrics. Recently, stochastic reconstructions utilizing multiple statistical correlation functions have been used for PEMFC CL reconstructions [68, 109, 110]. These reconstructions are performed using a pixel swapping method with a simulated annealing algorithm to optimize the final structure. These reconstructions provide an ideal way to generate statistically equivalent reconstructions of a reference microstructure. However, the computational time for these reconstructions is 2-3 orders of magnitude higher than the heuristic or geometry based reconstructions.

In this work, the approach of random distribution of overlapping particles is used to generate multiple microstructures of CLs to perform parametric studies. Previous works [4, 5, 7, 62–65, 103] which have used this algorithm for CL reconstructions have used a single particle size and only Lange et al. [4, 62, 63] had a parameter to control the amount of overlap of the particles. These limitations will be addressed in the stochastic reconstruction algorithm developed in this work. The parameters of the stochastic reconstruction algorithm are calibrated by comparing the statistical functions of the stochastic reconstructions to those obtained from a real CL microstructure thereby, ensuring statistically representative reconstructions. Simulated annealing based stochastic reconstructions [68, 109, 110] could also be used to generate microstructures which are statistically equivalent to real CLs. However, performing parametric studies with this method would require modifying statistical functions which is not very intuitive while being computationally more expensive. Stochastic reconstructions using overlapping particles, where the particle sizes and degree of overlap can be changed, provide a much more intuitive method for performing parametric studies compared to the heuristic or simulated annealing based methods.

1.2.2 Statistical characterization

Mathematical parameterization of the porous media is essential to quantify their random structure. N-point correlations have been used as statistical descriptors to characterize different morphological features in random heterogeneous porous media for many applica-

tions [109, 111]. However, for fuel cell porous media, a large number of statistical descriptors has rarely been used for statistical characterization. The most commonly used function to characterize the porous media is the pore size distribution [26, 48–51, 54, 65, 101, 112, 113]. The pore size distribution is usually obtained by fitting the largest sphere at a given voxel [26, 48, 50, 51] so that every void voxel is either the center of a sphere or belongs to another sphere with a larger diameter. Pore size distribution influences the gas and liquid transport through the porous media and is used to account for the Knudsen effects in the CL and MPL. However, it does not provide any information about the solid-void interface or the long range connectivity.

Statistical functions such as tortuosity [25, 26, 43, 47, 51, 53, 55, 114], two-point or auto correlation function [95, 98, 109, 115], lineal path function [109, 116] and chord length function [25, 47, 53, 55, 117] have also been used to characterize the fuel cell porous media. Each of these functions provides some information about the porous media morphology. For example, the tortuosity provides information about residence time for diffusing species and is often used in macroscopic models to estimate the effective transport properties from the bulk transport properties for a given phase. The two-point correlation function is defined as the probability of finding two-points at given distance (r) in the same phase. The value of the two-point correlation or autocorrelation function at $r = 0$ corresponds to the volume fraction of the phase and the slope at $r = 0$ provides information about the interfacial area of the porous media. Lineal path function, defined as the probability of finding a line of length r within a phase [118], has seldom been used for fuel cell porous media [109, 116]. The lineal path function contains information about the long range connectivity of the porous media. The chord length function is defined as the probability of finding a chord, i.e., a line connecting two interfaces, of given length within a phase [51, 68]. The chord length function has been used to characterize pore sizes, similar to the pore size distribution function. The mean chord length and mean squared chord length computed as the first and second moment of the chord length function, respectively, have been used to compute the effective Knudsen diffusion coefficient for the porous media using the expression proposed by Derjaguin [53, 63, 119].

The different statistical functions described above provide different morphological information about the porous media. Therefore, the use of multiple correlation functions is crucial to characterize the porous media. They also serve as a tool to analyze the statistical equivalence of stochastic reconstructions, such as those obtained using geometric building blocks [4, 62–64], compared to a microstructure obtained from a deterministic imaging technique. The use of multiple correlation functions to observe differences between different microstructures, especially for fuel cell CLs, has not been performed in literature. Further,

the effect of change in different statistical functions on the transport properties and electrochemical performance of fuel cell electrodes has not been discussed in any of the prior studies in literature.

1.2.3 Functional characterization

The porous layers in PEMFCs are responsible for several physical processes, such as gas, liquid, heat and charge transport, interphase mass transfer and electrochemical reactions. These processes are critical to fuel cell performance and durability. For example, experimental studies [13, 38, 120–123] indicate that the ionomer loading in CLs affects both the proton conductivity and gas diffusivity in the CL. High ionomer loadings result in increased protonic conductivity but lower porosity and pore sizes and thus, lower gas diffusivity and vice-versa for low ionomer loadings. Both protonic conductivity and gas diffusivity affect the electrochemical performance of the fuel cell therefore, an optimal ionomer loading [38, 120–122] is needed to maximize the electrochemical performance. Liquid water accumulation has been shown to severely limit the performance of fuel cell under cold and wet conditions [124–127] especially in ultra-thin electrodes [128]. Further, the low thermal conductivity of MPLs has been hypothesized to alleviate liquid water flooding in the electrodes due to higher evaporation rates [28, 31] and improve the performance of fuel cell electrodes under wet conditions [27, 29]. In-depth understanding of the physical and electrochemical processes occurring in the fuel cell is therefore, critical for improving the performance of fuel cells.

Table 1.1 shows the different transport processes that occur in the different fuel cell layers. Experimental measurements for different effective transport properties, such as gas diffusivity [9, 10, 33, 34, 66, 129–136], protonic conductivity [13, 123], electronic conductivity [10, 61, 137, 138], thermal conductivity [139–145], and electrochemical measurements, such as polarization curves and electrochemical impedance spectroscopy (EIS) have been performed for PEMFC porous layers. Few experimental studies [2, 3, 146] have computed the effective diffusivity in partially saturated GDLs. For CLs, saturation dependent gas diffusivities have not been measured. Saturation dependent transport properties are especially difficult to measure as it is difficult to maintain the liquid water distribution for the duration of the experiment. Although experimental studies can provide accurate estimation of the transport properties and performance they do not provide any information about the microstructure and need to be combined with additional characterization techniques, such as mercury intrusion porosimetry (MIP) [65, 97, 107] or BET adsorption isotherms [108, 147, 148] and imaging techniques, to determine the microstructure of the

porous media. This is often a time and resource intensive process.

Numerical simulation tools provide an ideal way to compute transport properties and electrochemical performance for a given microstructure. Experimental measurements are crucial to validate the predictions of numerical models and essential to build confidence in the models which can then be utilized to perform parametric studies analyzing the effect of different microstructural parameters on the transport properties and performance.

For charge and thermal transport, Ohm's law [4, 61, 64, 69, 113, 149, 150] and Fourier's law [65, 69, 113, 150] have commonly been used to compute the effective charge and thermal conductivities, respectively, for the different layers. This is therefore not discussed any further in the literature review. In this work, Ohm's law is used to model the charge transport in the fuel cell electrodes. For liquid/gas transport and electrochemical reactions, different approaches and models have been used in literature. These are discussed in the following sections.

Table 1.1 – List of the processes in the different fuel cell layers.

Process	CL	MPL	GDL
Gas transport (O_2, H_2O)	✓	✓	✓
Liquid transport (H_2O)	✓	✓	✓
Thermal transport	✓	✓	✓
Electron transport	✓	✓	✓
Evaporation/Condensation	✓	✓	✓
Proton transport	✓	×	×
Electrochemical reaction	✓	×	×

1.2.3.1 Gas transport

Gas transport in fuel cell porous media has been studied using either direct numerical simulation or the Lattice Boltzmann method. The choice of the method usually depends on the pore sizes of the porous media which affects the Knudsen number (Kn), defined as [151],

$$Kn = \frac{\lambda}{d_p} \tag{1.1}$$

where λ is the mean free path of the gas molecules and d_p is the pore diameter. For GDLs, the pore sizes (1-150 μm) are much larger than the mean free path of the oxygen molecules (nearly 69.3 nm at 26 °C and atmospheric pressure [151]) resulting in $Kn = 0.001$, which

indicates that the flow is in the continuum region and thereby, warranting the use of either method with high accuracy [26, 55, 56, 61, 79, 101, 150, 152–156].

For CLs and MPLs, which have smaller pore sizes (2-300 nm) [25, 48, 50, 51], Kn is in the range of 10^{-1}-10^{1} for oxygen gas at 26 °C and atmospheric pressure [151]. This region is the transition region and the use of continuum models to describe this flow is an approximation. Several studies have suggested the use of higher order LBM to account for the Knudsen effects [54, 96, 98]; however a detailed validation with experimental data has not been provided in any of these references. Computational times for LBM simulations are seldom reported ([54–56, 98, 152] do not report computational time). Chen et al. [96] reported computation time of 6 hours on 320 cores for 8 million lattice points without using Knudsen effects. The large computational time associated with the LBM makes it unfeasible for performing optimization studies.

Lange et al. [63] compared the results from the LBM simulations performed by Kim and Pitsch [98] (who used the Knudsen number (Kn) as a tunable parameter) to the continuum approach with a correction to account for Knudsen effects. Lange et al. [63] showed that the results from the continuum approach were similar to the results from LBM simulations for Kn $\sim$ 1. Zheng and Kim [7] computed the effective diffusivities using both approaches, i.e., Fick's second law with Knudsen effects accounted using Bosanquet approximation and LBM. Their results showed that the results from the continuum approach were similar to those obtained from LBM for a range of porosities if a correct local pore radius measure was used to compute the Knudsen diffusivity. Thus, Fick's second law with the Bosanquet approximation for the Knudsen effects [4, 51, 53, 157, 158] is still commonly used to study the gas transport in the CL [4–7, 10, 51, 53, 63, 64, 95, 159] and MPL [46, 47, 50, 61, 69, 159] and it will be used in this thesis.

1.2.3.2 Liquid water transport

Liquid water transport becomes a crucial issue when the fuel cell operates at high current densities and high relative humidity. For fuel cell layers, a typical value for the capillary number (Ca), defined as the ratio of the viscous forces to the surface tension, ranges from 10^{-8}-10^{-6} [160, 161]. Also, for an air-water system, which is the case for the cathode side of a PEMFC, the value of the viscosity ratio (M), defined as the ratio of dynamic viscosity of the non-wetting phase (water) to the wetting phase (air), is of the order of 10^{1}. Based on the results in references [162, 163], the values of Ca and M indicate that liquid water pore filling in the PEMFC porous layers is capillary driven and leads to a regime

called capillary fingering. Macroscopic models, based on Darcy's law [164, 165] or liquid and gas mass and momentum transport with a closure equation [31, 166–169], cannot accurately take into account the local pore morphology which would dictate the filling of the pores with liquid water in the CL, MPL and GDL. Therefore, different approaches, such as pore network models (PNM) [57, 58, 97, 100, 107, 160, 170–176], Lattice Boltzmann method (LBM) [161, 172, 177–182] and full morphology (FM)/morphological image opening (MIO) [50, 100, 102, 113, 172, 176, 178, 183, 184], have been used to simulate liquid water invasion/filling in the PEMFC porous media microstructures.

Pore network models provide a computationally inexpensive method to study the pore filling and liquid water transport in PEMFC porous media and study the effect of local saturation on the transport properties and performance. PNMs idealize the porous media as a network of pores and throats with certain radii. The distribution of pores and throats can be generated either from microscopy images [58, 181, 185] or using random distributions [97, 107, 160, 173, 174, 186, 187] which are calibrated with experimental measurements such as porosity, mercury intrusion porosimetry or saturation-pressure profiles. Pore filling is then controlled by the Young-Laplace equation. Transport properties from PNMs are usually computed by the solving the effective resistor network formed due to the resistances of the pores and throats. The simplicity and computational efficiency of PNMs has led to it being integrated into a full MEA model to predict the local saturation and effective diffusivity of the GDL [188, 189].

Full morphology or morphological image opening models offer a distinct advantage over the PNMs in that they can directly use tomography images without any geometry abstraction [50, 97, 102, 154, 172, 176, 183, 184, 187] and therefore, can be used to, in addition to water transport, to simulate other physical and electrochemical processes. FM use image analysis operations such as erosion with spherical elements followed by image dilation to describe the liquid intrusion into a porous media. The Young-Laplace equation is used to estimate the radius of the largest spherical pore to be intruded with water at a given capillary pressure. A problem with the FM model however, is that the intruding water front is limited to a spherical cap whereas in reality this shape might be ellipsoidal or more complex [97]. Schulz et al. [183] proposed an improvement to the FM model by creating fictitious spheres with diameters increased by the cosine of the contact angle to account for the wettability of the walls. Although this is an improvement over the traditionally used FM model, it would be difficult to model the real porous media surfaces where multiple contact angles might exist along the walls of the same pore and the shape of the liquid water-air interface is still limited to a spherical cap. Therefore, the improvement proposed by Schulz et al. [183] only

improves the capillary pressure-saturation curve.

Full morphology and pore network models assume a quasi-static water front and do not take into account a detailed momentum conservation for the gas and liquid phases and surface tension forces at the liquid interface. Several studies have used LBM [7, 70, 156, 161, 172, 177, 179–181] to describe the liquid water transport in PEMFC porous media which is capable of capturing the intricate dynamics of liquid water and water droplets. Other than LBM, Navier-Stokes equations could also be used to described the liquid water transport using a coupled Eulerian-Lagrangian formulation [190–192] or Volume of Fluid (VOF) method [193–195]. The latter has also been used to simulate liquid water transport in a PEMFC CL [5].

A comparative study of the three approaches to simulate drainage on a borosilicate glass microstructure was performed by Vogel et al. [178]. They noted that PNM provided a good estimate of the capillary pressure-saturation relationship but the accuracy of the water distribution was not discussed in their work because they did not compare the numerical results to tomography images. They also reported that the computational time and cost (in terms of memory) for PNM, FM and LBM was of the order of 1, 1.5 and 10^4-10^5 respectively. A similar comparative study of LBM and FM was also performed by Kim et al. [196]. They performed a qualitative comparison of FM and 2D LBM water distributions to X-ray and neutron images for an air-water system in compacted silica. Their results showed that FM was able to predict similar water distributions as those from the imaging techniques while being computationally more efficient than the 2D LBM model. Both these studies however, did not study fuel cell porous media. Agaesse et al. [176] used PNM and FM to simulate liquid water intrusion in a 3D GDL microstructure obtained using μ-CT technique. They compared the simulated results to μ-CT reconstructions of partially saturated GDL at different capillary pressures and found that both these approaches were able to predict the capillary pressure-saturation curves and liquid water distributions similar to the tomographic reconstructions. The findings from these studies [176, 178, 196] suggests that a FM approach offers a good compromise between the PNM and LBM with sufficient accuracy and practical computational times. It must also be pointed out here that none of these studies [176, 178, 196] simulated gas transport in the partially saturated microstructures to study the importance of predicting accurate liquid water distributions.

In this work, the FM approach is used to study the liquid water distribution in the fuel cell porous media due to the sufficient accuracy and relatively low computational times. Since the focus of this work is to understand the effect of liquid water distribution on the

corresponding transport properties and performance of fuel cell electrodes, a modified implementation of the traditional FM approach is used and the improvement proposed by Schulz et al. [183] is not used.

In addition to liquid and gas transport, water phase change is also critical to fuel cell operation. Understanding the role of the different porous media in the evaporation and condensation of water could help explain the improvement of the fuel cell performance by the addition of a MPL under fully humidified conditions [27–29]. Further, Owejan et al. [28] also reported that the performance improvement was independent of the MPL breakthrough pressure. These observations have lead to several hypotheses regarding the role of the MPL which include (but are not limited to) facilitating higher water removal rate from the cathode due to backdiffusion to anode and higher temperature gradients. Recent studies by Thomas et al. [30] and Zhou et al. [31] attributed the improved performance with an MPL to an increased CL temperature facilitating evaporation of the liquid water. PNM studies of Wu et al. [173, 174] suggest that MPL reduces the local saturation in the GDL by providing a hydrophobic barrier to water entry.

In order to understand the dynamics of interphase mass transfer, better estimates of the evaporation and condensation rates are required. Chapuis et al. [197] used PNM to study the evaporation rates as a function of the GDL wettability. Their results show that the evaporation rate is nearly 25% higher for a hydrophilic (HI) GDL than a hydrophobic (HO) GDL. Further, they also showed that the evaporation pattern in a HI GDL is similar to a capillary fingering pattern whereas for a HO GDL the pattern was flat and similar to an imbibition pattern. Zenyuk et al. [78] measured and simulated evaporation rates in a GDL microstructure with liquid water at different saturations. Their results indicate that the evaporation rate depends on the liquid-gas interfacial area which in turn depends on the saturation. Zenyuk et al. [78] however, did not simulate the evaporation on a GDL microstructure but instead, extracted the water surface and simulated gas diffusion on top of the water surface assuming effective GDL transport properties for the gas diffusion. This approach cannot be applied to discrete liquid water clusters which might be formed in the fuel cell porous media due to local evaporation and condensation. Further effective diffusivity values for partially saturated GDLs vary with average saturation and porosity of the GDL and can decrease by up to 60% in the through-plane direction for a saturation of 12% [55]. Lal et al. [80] measured and simulated evaporation rates on partially saturated GDL tomography reconstructions. Their model simulated vapor transport using Fick's second law assuming that the water vapor mole fraction at the liquid-air interface is the saturation water vapor mole fraction. Their results showed that the evaporation rate depended on the temperature,

flow rate and type of gas in the GDL. Pore network model based simulations of the cathode electrode [198, 199] have been used to show the formation of discrete liquid clusters in the GDL during the operation of the electrode due to condensation under the land and the consequent degradation of performance. Microstructure simulations accounting for the morphology and local water distributions can be used to predict liquid-vapor interfacial area and local saturations which could then be used to predict evaporation/condensation rates in macroscale models such as the one proposed by Zhou et al. [31, 167, 168]. In this work, the liquid water distributions predicted using the FM approach are used to compute the liquid-vapor interfacial area

1.2.3.3 Electrochemical reactions

Electrochemical reactions occur in the CL of the PEMFC. Several studies in the literature [4, 6, 63, 67, 104–106, 149, 200] have used direct numerical simulations to study the electrochemical reactions in the CL microstructure. Recently, Chen et al. [96] used LBM to simulate the electrochemical reactions on a stochastic CL reconstruction. Most of the previous studies use stochastic CL reconstructions [4, 6, 63, 67, 96, 104–106, 149, 200]. Zhang et al. [85, 86] used FIBSEM reconstruction of a CL to study the electrochemical performance of a CL and propose an improvement to the conventional agglomerate model using their micro-scale simulations. A key limitation with most of the prior studies is the use of a Butler-Volmer or Tafel kinetic model to predict the ORR rate. Butler-Volmer and Tafel kinetics are suitable for single electron reactions and cannot account for change in the rate limiting step with overpotential for a multi-step reaction such as the ORR. Therefore, multi-step kinetic models such as the four step double trap model proposed by Wang et al. [201] with fitting parameters from references [202, 203] or the six-step model proposed by Markiewicz et al. [204], would be more suitable to account for the doubling of the Tafel slope for the ORR at high current densities [205].

The impact of ionomer films on the CL performance has gained significant attention in recent years. Experimental studies [11, 22, 206, 207] have provided evidence of a local oxygen transport resistance close to the Pt surface. The work of Shinozaki et al. [208] demonstrated that Nafion covered platinum CL had a lower ORR activity than bare platinum using a rotating disk electrode setup. This has led to the hypothesis of ionomer poisoning the platinum surface. The work of Jinnouchi et al. [209] further demonstrated that the interfacial resistance limiting the ORR is due to densification of the ionomer at the Pt interface. Karan [210] provides a good overview of the experimental studies being performed by several groups to gain further insight of the platinum-ionomer interactions. Macro-scale numerical models [86, 211–216] have used an oxygen dissolution step to account for the interfacial re-

sistance due to the ionomer films and shown that these limit the performance.

For microstructural electrochemical models, two aspects need to be considered, i.e., the reconstruction of the ionomer films in the CL microstructure and the numerical model describing the interfacial oxygen resistance in the ionomer films. Ionomer films in CL reconstructions have primarily been reconstructed by adding a uniform ionomer film [4, 63, 67, 86, 104–106, 149]. Non-uniform ionomer film reconstructions have also been performed in the literature [63, 96, 217, 218]. However, Chen et al. [96] did not analyze the effect of ionomer content and distribution. Ishikawa et al. [218] performed statistical characterization of CLs with different ionomer and platinum loadings but did not analyze the electrochemical performance. Lange et al. [63] analyzed different ionomer distributions and contents but did not analyze the electrochemical performance with the changes in ionomer distributions. Experimental studies [219, 220] have hypothesized that ionomer distribution can affect the performance of the CL. Therefore, understanding the effect of ionomer distribution on CL performance could be valuable for designing improved CLs.

As discussed earlier, the interfacial resistance due to the ionomer films has been shown to limit the performance of the CL. Most of the previous studies [4, 63, 67, 96, 104–106, 149] have ignored the interfacial resistance due to the ionomer film. Only Zhang et al. [86] and this work [51] have used numerical models to account for the interfacial resistance of the ionomer in micro-scale simulations. The implementation by Zhang et al. [86] assumes that the reaction takes place everywhere in the solid region. 3D electron tomography of commonly used carbon supported catalysts [221, 222] shows that majority (70-80%) of the platinum particles reside on the surface of the carbon which can be in contact with the ionomer films. Therefore, it is more probable that the reaction occurs at the solid interface where the platinum and ionomer are likely to be present and the electrochemical reaction in the CL should be modeled as an interfacial reaction rather than a volumetric reaction.

Most of the studies described above considered electrochemical simulations in a dry CL. Only a few studies have simulated gas transport in partially saturated CLs [5, 7, 170] and even fewer [171, 223] have studied electrochemical reactions in partially saturated CLs. Both Aghighi et al. [223] and Hannach et al. [171] used PNMs to simulate electrochemical reactions in CLs. Aghighi et al. [223] simulated the full MEA and heuristically introduced liquid water at the GDL-CL interface at both electrodes. They also allowed for pores in the CL which were in contact with liquid filled pores in GDL to be flooded thereby, assuming a partially hydrophilic CL. Their results showed a decay in performance at high current densities. Hannach et al. [171] studied the electrochemical performance only in the CL and showed

the transient evolution of current density and local saturation in the CL. Their results also showed a decay in the current density with time due to water increase in the local saturation in the CL from the water production by the ORR. PNMs have also been used to simulate the electrochemical reactions in the cathode with phase change [198, 199], however, the emphasis of these studies was the structure of the GDL while the CL structure was treated as a single node thickness network. Therefore, there is a lack of understanding of the effect of local saturation on the electrochemical performance. Further, the effect of CL morphology and wettability on the local saturation and corresponding gas transport and electrochemical performance has not been studied.

To study the electrochemical performance in CLs under dry and wet conditions, the electrochemical model needs to, a) accurately predict the ORR kinetics using a multi-step kinetics; b) account for the interfacial resistance to oxygen transport due to the ionomer films; and c) include effect of local saturation to overcome the shortcomings of previous electrochemical models in literature.

1.2.3.4 Meshing

In order to study the physical and electrochemical phenomena described above, a discretized computational domain is required to solve the partial differential equations (PDEs) describing these phenomena. Therefore, meshing algorithms are necessary to generate a computational domain from the images to perform the numerical simulations. The mesh can be generated from the images in one of the following ways:

1. Direct conversion of the image voxels into cells or lattice points in the mesh [6, 10, 51, 95, 101, 102, 149, 150, 161, 172, 178, 200, 224] so that the mesh resolution is the same as the voxel size.

2. Use of meshing algorithms to extract surfaces and then generate meshes from the images [26, 53, 64].

3. Abstraction of geometry to simplified networks [58, 97, 100, 107, 170–174, 178].

The first approach has been used both in Lattice Boltzmann methods (LBM) [161, 172, 178], where each voxel is treated as a lattice site, and in direct numerical simulations (DNS) [6, 51, 67, 104–106, 149, 154, 200, 225]. The second approach is most commonly used for CFD simulations. The last approach of geometry abstraction is usually employed in pore network models (PNMs) which approximate the geometry as a network. Geometry abstraction results in the loss of morphological features. The direct conversion of voxels into mesh can lead

to overprediction of the interfacial area depending upon the mesh resolution [117]; however, meshing algorithms aiming at smoothing the digitized geometry from the images (microscopy or reconstructed) might not necessarily be accurate because the smallest recoverable feature or interface depends on the voxel size. Also, fuel cell porous media are made up of heterogeneous materials such as high surface area carbon with platinum particles in the CL and carbon fibers in the GDL, which makes it unlikely that the surface of the solid region is smooth. Therefore, the use of voxel based meshes might be deemed as acceptable for modeling the transport processes and performance in the microstructures, given our current level of understanding. It must be noted that the use of voxel based meshes can lead to a rapid increase (n^3) in the mesh cell count as the domain size (n vertices) increases.

Conventional mesh generators contain information about the different phases in the domain as material ids. Apart from the material ids, additional information about the different phases might also be required. For example, the local pore radii in different pores to compute the Knudsen diffusivity or the local ionomer film thickness to compute thickness dependent protonic conductivity. The information about local pore radii has been used in numerical simulations through the creation of external maps and coupling between software [53]. A more efficient option would be to pass such information in the mesh similar to material ids thereby, removing the dependency on external software. A mesh generator capable of handling multiple pieces of information about the geometry is therefore, required to accurately predict the local variability in the transport properties of the microstructure.

1.2.4 Integrated framework for microstructural analysis

Few studies [4, 62, 63, 105] have performed parametric studies using stochastic reconstructions to investigate the effect of morphology on the transport properties and electrochemical performance. These studies however, lack microstructural characterization and did not assess the statistical representativeness of the stochastic reconstructions using microscopy images. Therefore, a comprehensive study which characterizes the change in microstructure and relates it to the transport properties and electrochemical performance is still missing.

Several authors have reported algorithms for image analysis and stochastic reconstructions and numerical models to study the transport properties and electrochemical performance. However, there is no open-source software which has all the components required to study the different aspects of fuel cell porous media microstructures as highlighted in Figure 1.2. GeoDict® [226] is a commercial software capable of generating microstructures

from images and simulating effective transport properties for fuel cell electrodes and other porous materials. It is the most advanced tool available but it does not provide any tools for analysis of the electrochemical performance of the fuel cell. Therefore, to accomplish the objective of this thesis, an open-source numerical framework capable of processing, analyzing and characterizing microscopy images, extracting a voxel based mesh from them and simulating gas, liquid and charge transport to estimate relevant effective quantities as well as simulating electrochemical reactions to determine the performance of the microstructures is required. Such a tool will be helpful in developing the correlation between microstructure, effective transport properties and performance and allow other researchers to build upon the findings of this work.

1.3 Objectives

The objective of this thesis is to study the correlations between microstructure, transport properties and performance. Based on a survey of the current literature in these areas, the following gaps are identified:

1. Lack of a general framework to evaluate statistical functions, transport properties and performance directly from microscopy images;
2. Lack of statistical tools to assess the validity of stochastic reconstructions and characterize the changes across different microstructures;
3. An electrochemical model taking into account multi-step kinetics for ORR and interfacial mass transport resistance due to the ionomer film;
4. A detailed understanding of the effect of local saturation on the transport properties and electrochemical performance;
5. A study of the effect of ionomer film distributions and local ionomer thickness on the effective protonic conductivity and electrochemical performance;

In order to address the aforementioned gaps, the objectives of this thesis are:

1. Development of a unified and open-source numerical framework to:
   (a) analyze microscopy images and statistically characterize porous media;
   (b) generate voxel based meshes and perform numerical simulations to compute effective transport properties, such as diffusivity and electronic and protonic conductivity.

(c) simulate liquid water intrusion in porous media microstructure;

(d) study the performance in dry and partially saturated microstructures of different CL electrodes using an electrochemical model with multi-step kinetics for ORR, interfacial mass transport resistance due to ionomer film and interfacial reaction term.

2. Development of stochastic reconstruction tools to perform PEMFC porous media reconstructions and analyze its feasibility via statistical analysis.

3. Development of a stochastic algorithm to reconstruct ionomer films in CL microstructures to analyze the impact ionomer film distribution and thickness on the effective transport properties and electrochemical performance.

The numerical framework would facilitate the development of correlations to describe the interlinks between fabrication, microstructure, transport properties and performance shown in Figure 1.2. The following studies are performed in this work to highlight the relations between microstructure, transport properties and performance of a CL:

1. Effect of porosity and local saturation on the effective diffusivity of a CL;

2. Effect of pore size distribution on the effective transport properties and electrochemical performance of a CL under dry and wet conditions;

3. Effect of ionomer film distribution on the effective transport properties and electrochemical performance of a CL;

1.4 Structure of the thesis

This thesis is organized into seven chapters. This chapter has provided the motivation and objectives of the work. A detailed literature review was performed to discuss the state-of-the-art for microstructural modeling and gaps in knowledge were identified. Chapter 2 describes the theory and models used for this work. A description of the stochastic reconstruction algorithms, statistical characterization tools, water intrusion algorithm and the numerical models for gas and charge transport and electrochemical reactions as well the solution methodology is provided. Chapter 3 provides validation for the different tools developed in this work. First, the water intrusion algorithm is validated by simulating water intrusion in a dry GDL reconstruction obtained using μ-CT and the results were compared to reconstructions of partially saturated GDL. Next, the statistical and functional characterization tools are applied to a CL reconstruction obtained using FIBSEM and the results such as

pore size distribution, gas diffusivity and polarization curves are compared to experimental results. Chapter 4 uses the stochastic reconstruction algorithm to generate CL reconstructions with different porosities to study gas diffusivity in the CL as a function of porosity and saturation. The results of this analysis are used to develop a correlation to predict effective diffusivity for CLs under dry and partially saturated conditions. Chapter 5 presents the results for a parametric study on the different CL PSDs using stochastic reconstructions to study the effect of PSD on the transport properties and electrochemical performance under dry and wet conditions. Chapter 6 studies the effect of ionomer thickness and content on the effective protonic conductivity and electrochemical performance in the CL. Finally, chapter 7 summarizes the findings of this work and provides an outlook for future directions and applications to other fields.

Chapter 2

Theory[†]

As discussed in Chapter 1, one of the goals of this work is the development of a unified numerical framework capable of performing:

1. microstructure generation using either microscopy images or stochastic reconstructions;
2. statistical analysis of the generated microstructures to mathematically characterize the structure and assess the validity of stochastic reconstructions;
3. physics based simulations to study the physical transport processes and electrochemical reactions in the microstructures.

This chapter describes the theory and algorithms used for image analysis, stochastic reconstruction and statistical functions. The numerical models and solution methodologies used to simulate gas and charge transport, water intrusion and electrochemical reactions are also discussed in detail.

2.1 Microstructure reconstruction

2.1.1 Microscopy image based reconstruction

There are several microscopy techniques which can be used to visualize and reconstruct the microstructure of different fuel cell porous media such as x-ray computed tomography (X-CT) [26, 47, 52–61, 70], scanning transmission x-ray microscopy (STXM) [44, 71, 72] and focused ion beam-scanning electron microscopy (FIBSEM) [10, 25, 46–51]. Since the primary

[†]Parts of this chapter have been published in:
1. M. Sabharwal, L.M. Pant, A. Putz, D. Susac, J. Jankovic, and M. Secanell, *Fuel Cells* 16(6), 2016
2. M. Sabharwal, J. T. Gostick, and M. Secanell, *Journal of The Electrochemical Society* 165 (7), 2018
3. M. Sabharwal, L.M. Pant, N. Patel, and M. Secanell, *Journal of The Electrochemical Society* 166 (7), 2019
4. M. Sabharwal, and M. Secanell, *ECS Transactions* 86 (13), 2018

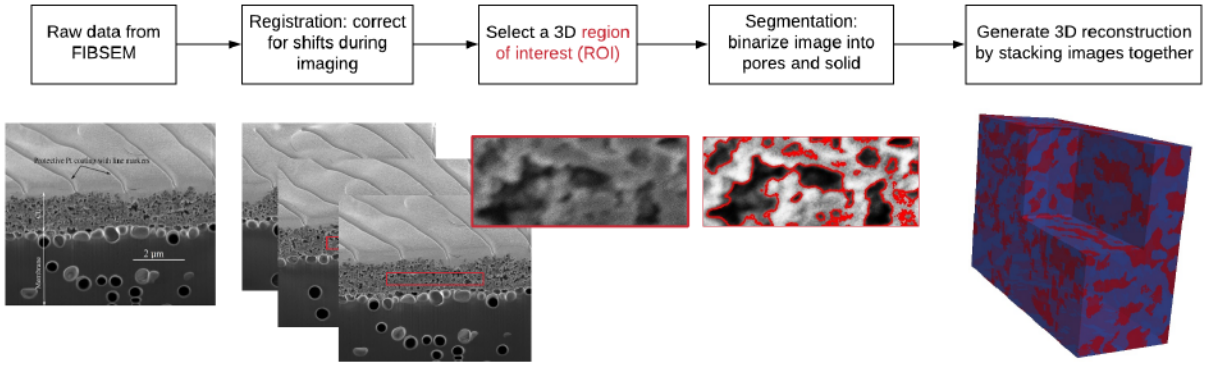

Figure 2.1 – Schematic of the image processing and reconstruction process for FIBSEM data.

focus of this work was the analysis of fuel cell catalyst layers (CLs), only FIBSEM [10, 50, 51] and nano-CT [52, 53] are suitable. In this thesis, FIBSEM was selected as the method of choice. The aim of this work is to develop image processing tools to analyze microscopy images therefore, the FIBSEM imaging was performed by our collaborators at AFCC[1] who can be considered experts in electron microscopy [51].

Figure 2.1 shows the image processing and reconstruction procedure for typical FIBSEM data. As described before, FIBSEM is a destructive technique where an ion beam is used to slice the CL and the exposed CL is then imaged using the scanning electron microscope. The raw data from FIBSEM are a stack of grey-scale images as shown in Figure 2.1. A detailed procedure for FIBSEM can be found in reference [51]. In order to extract the CL morphology from the grey-scale images, several image processing operations need to be performed. The raw data from FIBSEM must be corrected for shifts arising from the lateral movement of the imaging plane due to FIB slicing. Post registration, a 3D section from the stack of images is selected as the region of interest to be segmented. Image enhancement and segmentation is then performed to binarize the images into pore and solid. The segmented images are then stacked together to form a 3D reconstruction of the CL. The different image processing tools required to generate 3D microstructures from raw grey-scale microscopy images are described in the following sections. In this work, image processing tools are developed to analyze microscopy images obtained from FIBSEM. Although much of the discussion is with respect to FIBSEM images, the tools developed can be applied to other microscopy data as well. Details on the procedure for obtaining FIBSEM images for a CL can be found in [51].

[1] Automotive Fuel Cell Cooperation Corporation (`https://en.wikipedia.org/wiki/Automotive_Fuel_Cell_Cooperation`)

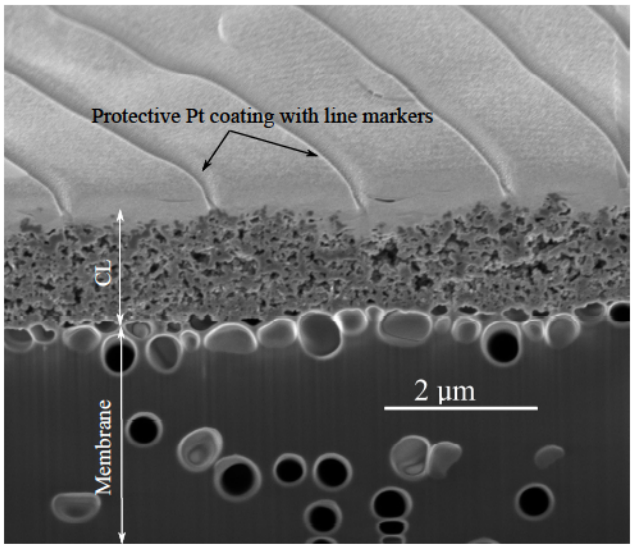

Figure 2.2 – Image of FIBSEM slice of an Inkjet printed CL.

2.1.1.1 Image registration

In FIBSEM, to account for the lateral movement during imaging of consecutive slices, fiducial markers are engraved on the protective platinum layer and used for re-alignment during image processing. Figure 2.2 shows the image of a FIBSEM slice with fiducial markers. To align all the consecutive slices, an in-house python based code is used. A feature detection algorithm is used for identifying the fiducial markers in each slice. The features are identified using a scale invariant feature transform algorithm [227] implemented in the OpenCV library [228]. The algorithm is used to detect the line markers shown in Figure 2.2. The location of these markers in the next image are compared to those in the current image. The next image is then translated in the x-y plane to minimize the least square distance between the feature shifts. The image registration code was developed in python and is available in pyFCST, which is the python image processing and analysis suite in OpenFCST [229]. After alignment of the microscopy images, they can be stacked to form a 3D domain of grey-scale images.

2.1.1.2 Image filtering and binarization

Image segmentation, i.e., differentiation of the image into separate phases, is required to extract the microstructure of the porous media. Microscopy images often have a lot of noise thereby, making image segmentation a challenging process. Therefore, image enhancements operations to improve the contrast and brightness of the image are performed. Contrast limited adaptive histogram equalization [230] followed by Gaussian blurring [231] is used to

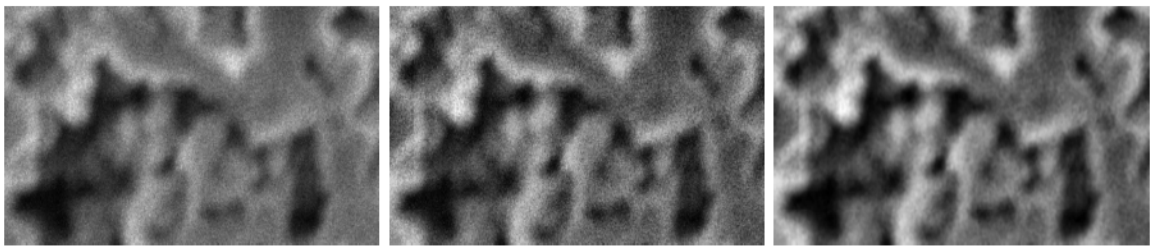

(a) (b) (c)

Figure 2.3 – Illustration of a FIBSEM image at different stages of image pre-processing. a) Raw image after cropping, b) Image after applying contrast limited adaptive histogram equalization, and c) Image after applying contrast limited adaptive histogram equalization and Gaussian blurring

improve the image quality of the raw FIBSEM image. Figure 2.3 shows a raw FIBSEM image at different stages of pre-processing. From the images, it can be seen that the image enhancement filters improve the contrast and sharpness of the image significantly, especially at the solid/pore phase boundaries.

The contrast enhanced and filtered images are segmented using a Sauvola algorithm with a local moving window [51, 94]. A local moving window is used to account for the variation in the image intensity due to fluctuations in the electron beam intensity during image rastering. The threshold value for each pixel, $T(x, y, z)$, which determines if a pixel belongs to the solid or pore phase, is evaluated based on the statistics of a local neighborhood around the pixel, and is given as:

$$T(x, y, z) = m(x, y, z) \left[1 + k \left(\frac{\sigma_i(x, y, z)}{R} - 1\right)\right], \tag{2.1}$$

where $m(x, y, z)$ is the mean pixel intensity of the neighborhood, $\sigma_i(x, y, z)$ is the standard deviation of pixel intensity of the neighborhood, the parameter k can range from $0 - 1$, and R has a value of 128 as suggested by Sauvola and Pietikäinen [94]. The value of R is set as the mid-point pixel intensity for a 8-bit image, and the standard deviation is normalized by this value. The parameters for these algorithms are generally adjusted via trial-and-error based on visual inspection. The neighborhood size and k value can affect the segmentation threshold, and in-turn the structure. For the FIBSEM images, a 3D neighborhood is selected instead of the 2D neighborhood used commonly because the FIBSEM images contains background information of the solid structure visible through the pores. Further, a parallel version of the Sauvola algorithm was also developed to reduce the computational time for the analysis of the large image datasets. The segmented 2D images can then be stacked together to obtain a 3D microstructure.

The image enhancement and binarization routines were developed in python using functionalities from pre-built python libraries such as SciPy [232], mahotas [233] and scikit-image [234]. Additional image segmentation algorithms, such as Otsu's method [235] and Robust Automatic Threshold Selection (RATS) [236], were also implemented. The image enhancement and segmentation algorithms are available in pyFCST [229].

2.1.2 Stochastic reconstructions

Stochastic reconstructions were generated using a random overlapping sphere based algorithm similar to that described in reference [4]. The steps for the overlapping sphere based microstructure reconstructions are as follows:

1. An empty domain (Ω) corresponding to a porosity of 100% is generated as a 3D array with user defined dimensions of $l \times l \times l$. Building blocks for the solid phase, i.e., spheres of a user-defined radius r_d, are generated as local maps using a 3D array (Ω_{map}) with dimensions $2r_d \times 2r_d \times 2r_d$. The radius of the spherical particles can be given as a constant value or a distribution. If a distribution is prescribed, r_d is selected using the specified probability distribution and Ω_{map} is generated at each iteration for the selected r_d value.

2. A random location is chosen in Ω as a center for Ω_{map}.

3. Ω_{map} is inserted into the domain by placing its center at the chosen center in the previous step.

4. As the spheres are continually placed they might start overlapping. The amount of overlap is controlled in this algorithm using an overlap parameter (ψ) which is used to calculate the region of pixels around the solid sphere in Ω which cannot be used as centers. For $0 \leq \psi \leq 1$, all pixels within $(1 - \psi)r_d$ distance from the surface of the sphere are removed, thereby allowing an overlap of ψ. Therefore, $\psi = 1$ would allow free penetration of spheres and $\psi = 0$ would allow no penetration of spheres. Based on ψ value, the feasible center locations are updated by removing all points within the specified neighborhood of existing spheres based on the r_d value (if a distribution is given then the next selected value).

5. Steps 2-4 are continually repeated to place spheres.

6. Once the desired porosity (ε_V) is reached the algorithm ends.

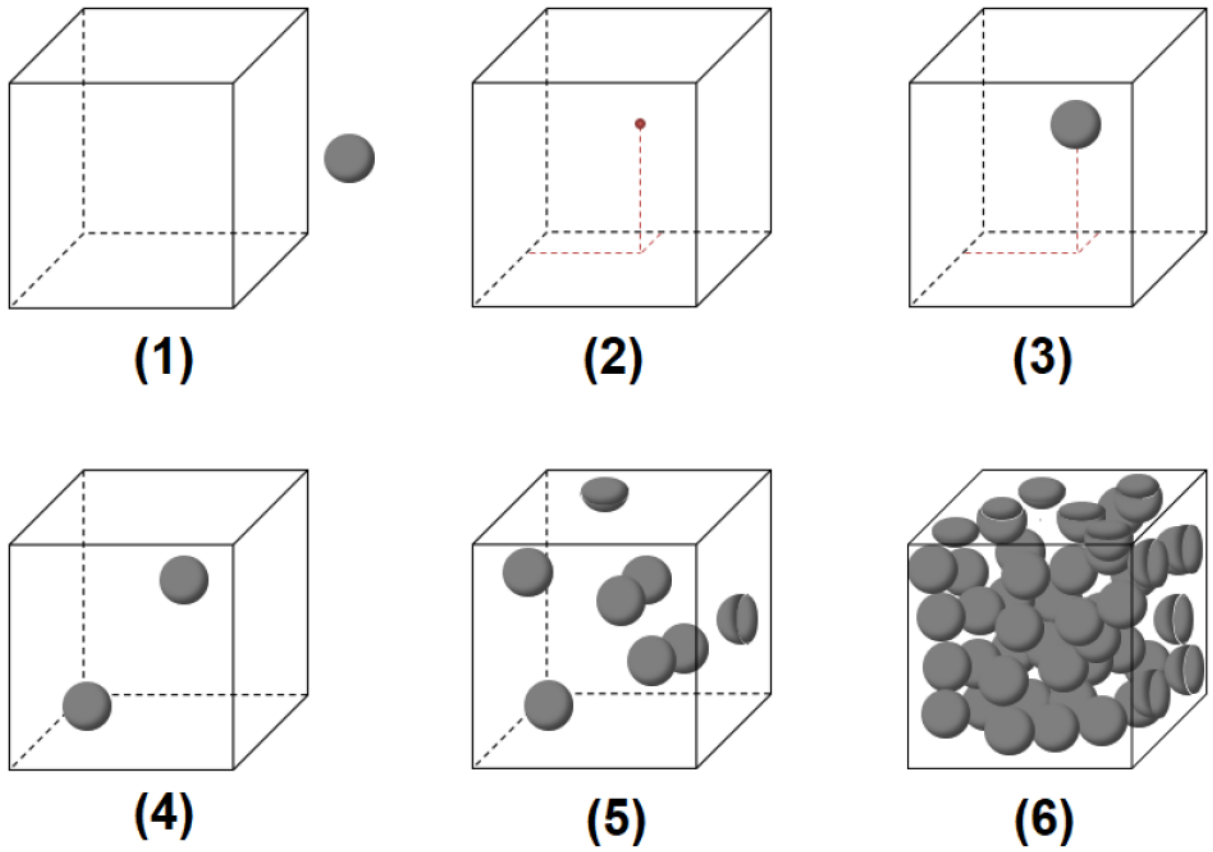

Figure 2.4 – Illustration of the different steps used for generation of a microstructure based on overlapping spheres of a constant radius. The different images represent: (1) Generate the empty domain (Ω) and Ω_{map}; (2) Select a center location from available sites; (3) Place Ω_{map} on the selected site; (4)-(6) Continue the process until the target porosity is achieved.

Figure 2.4 shows a schematic of the different steps described above assuming a constant sphere radius. As described above, the inputs to the algorithm are the domain size (l), sphere radius (r_d) or a particle size distribution, degree of overlap (ψ) and porosity (ε_V) of the microstructure. In addition to spheres any random building blocks can be used by defining an appropriate 3D array map (Ω_{map}).

The algorithm described above has been generalized and improved compared to that reported in references [4, 64] by the addition of functionalities, such as controlled overlapping, multiple building block sizes using particle size distributions and ability to use random building blocks. The stochastic reconstruction algorithm was developed in python and is available in pyFCST [229].

2.2 Statistical functions

Statistical functions provide an ideal way to mathematically characterize the random heterogeneous porous media used in fuel cells. A number of statistical functions have been proposed in literature [68, 111, 237–239] to characterize porous media. Statistical functions provide information about different aspects of the porous media morphology. Two-point correlation function [68, 111, 238, 240] provides an estimate of the phase volume fraction and interfacial area. Lineal path function [68, 118] and two-point cluster function [68, 241] provide information about the long range connectivity of the porous media useful for statistical function based reconstructions [68, 240]. The cluster function is used in this study to extract the primary percolating phase network which is used for numerical simulations. Chord length function [53, 63, 110, 239], which is a subset of the lineal path function, provides an estimate of the pore sizes and is used in this study instead of the lineal path function. Pore size distribution [50, 51, 158] provides an estimate of the characteristic pore sizes which govern the Knudsen diffusivity and capillary based liquid intrusion in the fuel cell porous media. The following sections describe the two-point correlation function, chord length function and pore size distribution which are used to characterize the porous media morphology in this work.

2.2.1 Two-point correlation function

The two-point correlation function, $S_2^{(j)}(r)$, is defined as the probability of finding two random points a distance r apart both belonging to phase j [111]. The two-point correlation functions of different phases are linearly dependent [237]. Therefore, for a binary media, knowledge of two-point correlation function for a single phase is sufficient. The two-point correlation function is related to the specific interphase area (interfacial area per unit volume) as follows [238]:

$$s_j = -\beta \frac{\mathrm{d}}{\mathrm{d}r} S_2^{(j)}(r)\Big|_{r=0}, \tag{2.2}$$

where s_j is the specific interphase area, and β is 4 for 2-D, and 6 for 3-D images, respectively [237]. In the case of a catalyst layer, the slope of the two-point correlation function can be used as an estimate of the pore-solid interface area. For a digitized medium such as a digital image, the two-point correlation function is estimated by translating a line of length r through the image and recording the number of times both ends fall in the same phase. This is then normalized by total number of translations to obtain the probability of finding both ends in same phase. A detailed computational methodology is presented in the literature [110, 238]. The two-point correlation function was implemented by Pant [68] in the Porous

Media Stochastic Reconstruction Toolbox (PMSRT), which is a C++ library, and it was used for this thesis.

2.2.2 Chord length function

The chord length function, $C^{(j)}(r)$, is defined such that $C^{(j)}(r)\mathrm{d}r$ is the probability of finding a chord of length between r and $r + \mathrm{d}r$ in phase j [239]. The chord length function contains information about the separation between phase boundaries. To measure the chord length function, the whole image is scanned in all orthogonal directions for occurrences of chords, and the lengths and occurrences are recorded. The chords are evaluated by scanning the image along a given direction, i.e., x, y or z, until an interfacial pixel is encountered in the phase of interest. This pixel is marked and scanning continues till another interfacial pixel is encountered and the chord is recorded. The occurrences of all chord lengths are normalized by total number of chords [110, 239]. The chord length function implemented by Pant [68] in PMSRT was used for this thesis.

The chord length function can be used to compute the mean chord length (λ) as,

$$\lambda = \int_0^\infty r C^v(r)\mathrm{d}r. \tag{2.3}$$

The chord length function for the pore phase gives an estimate of the pore sizes in the microstructure. The mean chord length for the pore phase has also been used to compute the Knudsen diffusivity in CLs using the Derjaguin approximation [53, 63].

2.2.3 Percolating volume fraction

The percolating volume fraction is the ratio of percolating volume to total void volume. The percolating volume is defined as the void volume which connects any two opposite faces. The percolating volume fraction is a measure of void phase connectivity. The percolating volume is identified using a cluster labeling method. The dual pass algorithm proposed by He et al. [242] is used for cluster labeling in conjunction with Hoshen and Kopelman [243] algorithm.

2.2.4 Pore size distribution

The local pore radius for the porous media is estimated using a sphere fitting algorithm based on the distance transform method described in the literature [50, 158]. An algorithmic description for the sphere fitting algorithm is presented in Figure 2.5. To compute the pore

size distribution for a given microstructure first the Euclidean distance transform (EDT) at every pore voxel is computed. The Euclidean distance transform (EDT) finds the nearest point in the background (different phase) and return the Euclidean distance to it. The mathematical representation in 3D is given by [244],

$$\begin{aligned} \mathrm{EDT}(x,y,z) &= \min\left(i,j,k : 0 \leq i < m \wedge 0 \leq j < n \wedge 0 \leq k < o \wedge b[i,j,k] : d\right) \\ d &= \sqrt{(x-i)^2 + (y-j)^2 + (z-k)^2} \end{aligned} \tag{2.4}$$

where m, n and o are the limits in the x, y and z directions, and $b[i,j,k]$ indicates that the point belongs to the background. The Euclidean distance transform represents the maximum radius of the sphere which can be inscribed within the same phase with the point as the center. After computing the Euclidean distance transform, the algorithm iterates over the radius (r) values and finds all locations where the EDT value is less than or equal to r. Once the feasible locations (D) are identified, a second pass of the distance transform is used to find all locations within r distance of the feasible locations in D and assign them a value of r. Therefore, D contains the centers of the spheres with radius r and the second pass is used to build the rest of the sphere with all pore voxels belonging to a sphere of radius r having a value of r. Thus, every pore voxel is the center of a sphere with radius equal to its distance transform value or part of a larger sphere. The pore size distribution algorithm was implemented in python in the pyFCST library.

2.3 Numerical model

This section describes the numerical models used to simulate the physical and electrochemical processes in fuel cell porous media. The following assumptions are made:

1. Isothermal and isobaric conditions;
2. Gas transport in the CL is diffusion dominated [245];
3. Proton concentration in the ionomer thin films is constant;

2.3.1 Gas transport

Gas transport in the fuel cell porous media is assumed to be governed by Fick's second law,

$$\boldsymbol{\nabla} \cdot (D_i c_{tot} \boldsymbol{\nabla} x_i) = 0, \tag{2.5}$$

where D_i is the gas diffusion coefficient, c_{tot} is the total gas concentration (assumed constant), and x_i is the molar fraction of the gas species.

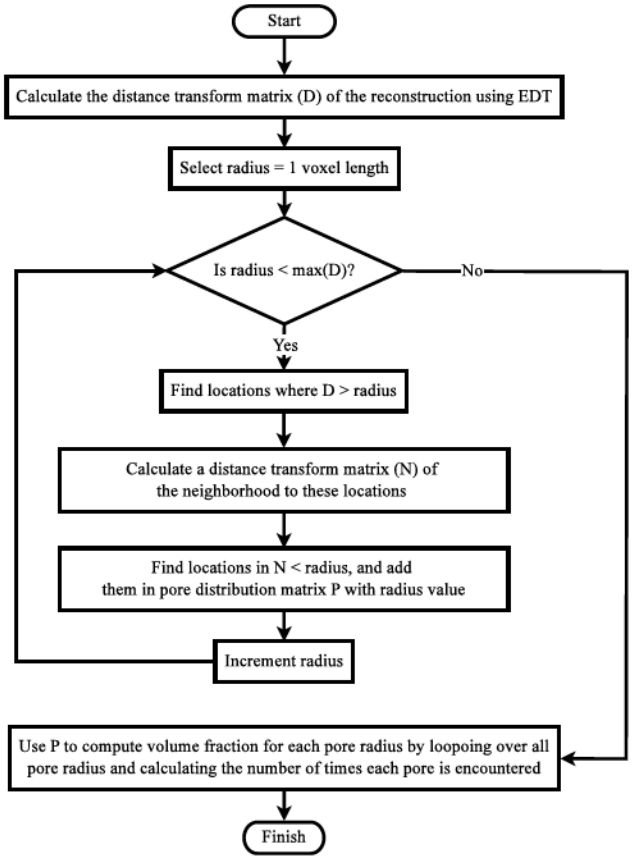

Figure 2.5 – Algorithm for calculating the sphere based pore size distribution. The 3-D matrix P contains radius information at each geometric point with the value denoting the radius of the sphere the point belongs to.

For GDLs, the pore sizes are higher than 1 μm, usually 10-30 μm, which is much higher than the mean free path of gas species (oxygen on the cathode) therefore, D_i for GDLs is equal to the molecular diffusion coefficient (D^m) of the gas species. For CLs and MPLs, which contain nano-pores of the order of 10-50 nm similar to the mean free path of the gas species (60-70 nm for oxygen), Knudsen effects become important. To account for the Knudsen diffusion, the Bosanquet equation [157] is used to compute the gas diffusion coefficient as,

$$\frac{1}{D_i} = \frac{1}{D^m} + \frac{1}{D_i^{Kn}}, \tag{2.6}$$

where D^m is the molecular diffusion coefficient and D_i^{Kn} is the Knudsen diffusion coefficient for the gas species. The latter is calculated using [4, 240, 246]

$$D_i^{Kn} = \frac{2}{3} r_p \sqrt{\frac{8RT}{\pi M_i}}, \tag{2.7}$$

where r_p is the pore radius obtained using the pore size distribution algorithm in Section 2.2.4, R is the universal gas constant, T is the temperature of the gas and M_i is the molecular weight of the gas species. The Knudsen diffusion coefficient is therefore estimated locally at each location in the microstructure using the local pore radius.

To compute the effective diffusivity of a given microstructure, the following boundary conditions are used:

$$\begin{aligned} x_i &= x_i^{in} \text{ on } \Gamma_1, \\ x_i &= x_i^{out} \text{ on } \Gamma_2, \text{ and} \\ (D_i c_{tot} \boldsymbol{\nabla} x_i) \cdot \boldsymbol{n} &= 0 \text{ everywhere else,} \end{aligned} \tag{2.8}$$

where Γ_1 is the inlet plane and Γ_2 is the outlet plane opposite to the inlet plane. The governing equation was simulated using the open-source package OpenFCST [229]. The diffusive gas flow rate at the outlet (N_i^{out}) was calculated from the simulation as,

$$N_i^{out} = \int_{\Gamma_2} (-D_i c_{tot} \boldsymbol{\nabla} x_i) \cdot \boldsymbol{n} dS \tag{2.9}$$

and then used to compute the effective diffusion coefficient (D_i^{eff}) of the porous media using

$$D_i^{eff} = N_i^{out} \frac{L}{A\left(c_i^{in} - c_i^{out}\right)}, \tag{2.10}$$

where L is the shortest distance separating inlet and outlet planes, A is the cross-section area and c_i^{in} and c_i^{out} are the concentrations of gas species i at the inlet and outlet boundary faces, respectively.

2.3.2 Charge transport

Charge transport is assumed to be governed by Ohm's law,

$$\boldsymbol{\nabla} \cdot (\sigma_i \boldsymbol{\nabla} \phi) = 0, \tag{2.11}$$

where σ_i is either the bulk electronic or protonic conductivity of the given phase and ϕ is either the electronic or protonic potential for electron or proton transport respectively.

Similar to gas transport, the boundary conditions used to evaluate the effective conductivity of a given phase are:

$$\begin{aligned} \phi &= \phi^{in} \text{ on } \Gamma_1, \\ \phi &= \phi^{out} \text{ on } \Gamma_2, \text{ and} \\ (\sigma_i \boldsymbol{\nabla} \phi) \cdot \boldsymbol{n} &= 0 \text{ everywhere else,} \end{aligned} \tag{2.12}$$

where Γ_1 is the inlet plane and Γ_2 is the outlet plane opposite to the inlet plane. The governing equation was simulated using the open-source package OpenFCST [229]. The total current at the outlet (I) was calculated from the simulation and used to compute the effective conductivity (σ_i^{eff}) of the porous media using,

$$\sigma_i^{eff} = I \frac{L}{A\left(\phi^{in} - \phi^{out}\right)}, \tag{2.13}$$

where L is the shortest distance separating inlet and outlet planes, A is the cross-section area and, ϕ^{in} and ϕ^{out} are the potentials at the inlet and outlet boundary faces, respectively.

2.3.3 Liquid water intrusion

To study the effect of liquid water accumulation on the gas transport and electrochemical performance of fuel cell porous media microstructures, a quasi-static water intrusion algorithm based on the full morphology model [183] was developed. The algorithm, termed the cluster based full morphology (CFM) method because it relies on image clustering instead of the dilation-erosion approach used in conventional FM [97, 176, 183, 184], used for this work is described in Algorithm 1. Liquid water intrusion can be simulated in a porous media from an external boundary or from within the layer, therefore, two modes of water intrusion are defined as follows:

- **Boundary** - In this mode, the water is injected from an external boundary as shown in Figure 2.6a. This mode of water injection is representative of the liquid water intrusion in a GDL/MPL [57, 58, 107, 185], where the liquid water produced in the CL enters the GDL/MPL from the CL interface. Further, this mode of water injection is also widely used to perform ex-situ characterization of GDLs [1, 56, 59, 97].

Algorithm 1 Cluster based full morphology algorithm for water intrusion [154].[a]

Read original input microstructure Ω^0;
Define the nucleation/intrusion points, contact angle (θ) and number of steps (n);
Compute p_c for every pore pixel in Ω^0 using equation (2.14)
Initialize p^{in} as the minimum liquid pressure to start water intrusion based on the nucleation/intrusion points
Initialize Ω_l = nucleation/intrusion points
(Ω_l has a value of 1 at the locations where water is present.)
Compute $\triangle p = \frac{\max(p_c) - p^{\text{in}}}{n}$
while s<1 **do**
  procedure IDENTIFY LIQUID WATER CLUSTERS
    Obtain the set voxels Φ where $p_c < p^{\text{in}}$
    Cluster connected voxels in Φ and store in Ψ with each cluster denoted by a unique integer j
    Identify cluster indices (j) in Ψ connected to Ω_l and store in array u
  end procedure
  procedure INTRUDE WATER INTO CLUSTERS
    for i = [values in u] **do**
      Find locations x, y, z where $\Psi[x, y, z] == i$
      Set $\Omega_l[x, y, z] = 1$
    end for
    Compute saturation (s) using equation (2.16)
    Record Ω_l for mesh generation
    Increment $p^{\text{in}} = p^{\text{in}} + \triangle p$
  end procedure
end while

[a] All capital Greek symbols denote 3D arrays with dimensions of input microstructure.

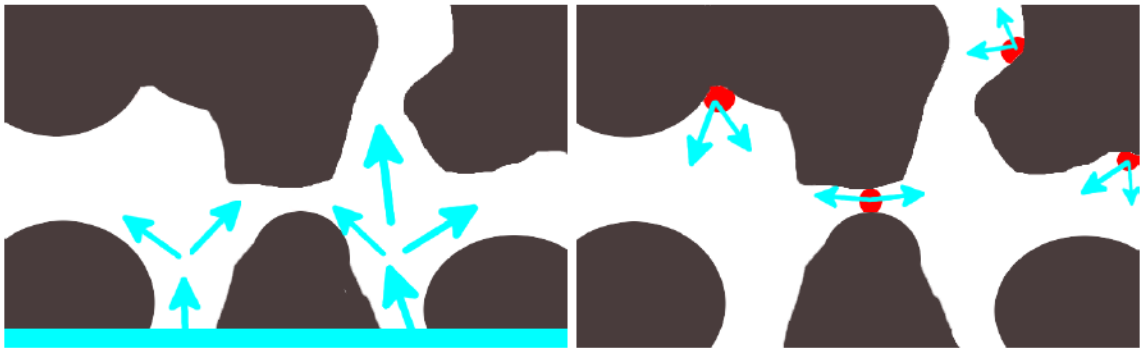

(a) (b)

Figure 2.6 – Illustration of the a) boundary, and b) nucleation based water injection used in this study. Red indicates the nucleation sites and blue arrows indicate liquid water movement

- **Nucleation** - Unlike the GDL where the water was intruded from a single boundary, the liquid water in the CL is intruded using the nucleation mode shown in Figure 2.6b. This is similar to the approach used in the pore network models in references [170, 171] where random agglomerates were activated in the CL to produce water which then intrudes the pores in the CL. In the CL, the ORR takes place on the Pt surface where water molecules would be produced which might form small clusters. Once these clusters exceed the critical diameter given by the Kelvin equation for the local supersaturation they would continue to grow into bulk liquid. It is expected that such a phenomenon might be occurring in the CL where high local supersaturation might exist especially in the small nano-pores. Therefore, this mode of water injection is deemed to be representative of the water intrusion in the CL.

The computational implementation for the CFM algorithm is presented in Algorithm 1. The inputs to the algorithm are:

1. the porous media microstructure as a 3D array or stack of images (Ω^0),
2. the contact angle (θ),
3. the boundary/nucleation points for the liquid water, and
4. the number of discrete steps (n) for incrementing the capillary pressure.

The pores can also be assigned a mixed wettability by specifying a hydrophilic (θ_{HI}) and hydrophobic (θ_{HO}) contact angle instead of assigning a single θ. In this case, the threshold radius (r_{th}), i.e., the radius below which pores are hydrophilic and above which they are

hydrophobic, must also be provided as an input to the algorithm.

With the given inputs, the first step in the algorithm is the calculation of the pore size distribution (PSD) and the capillary pressure (p_c) required to intrude each pore. The capillary pressure was computed using the Young-Laplace equation,

$$p_c = \frac{2\gamma \cos\theta}{r_p} \tag{2.14}$$

where capillary pressure is defined as,

$$p_c = p_l - p_g \tag{2.15}$$

where p_l and p_g are liquid and gas pressures respectively. Therefore, for implementation purposes hydrophilic pores have a negative capillary pressure and hydrophobic pores have a positive capillary pressure. It is assumed that p_g is zero.

The propagation and tracking of the liquid water front is the most crucial step in the algorithm. To improve the efficiency of the algorithm a cluster based approach was formulated as described in Algorithm 1. First, all locations with a capillary pressure lower than the specified liquid pressure at a given step were identified and clustered into groups with unique integer values (j) and stored in a 3D array (Ψ). This step identified all possible locations where the liquid water could be present at the given liquid pressure p^{in}.

The next step was to identify the clusters in Ψ which were connected to the existing water filled pores denoted by Ω_l. This was performed using a logical AND operation between Ψ and Ω_l which returned the unique integers (u) for cluster locations where the water could propagate. To intrude liquid water into the identified clusters, the x, y and z co-ordinates of all points in Ψ corresponding to the integer values in u were found and the corresponding locations were set to 1 in Ω_l.

The saturation (s) at each step is obtained using,

$$s = \frac{V(\Omega_l)}{V_p} \tag{2.16}$$

where $V(\Omega_l)$ denotes the volume of voxels with liquid water and V_p denotes the pore volume of the microstructure. Ω_l is recorded for mesh generation to study the gas transport and electrochemical performance.

The propagation of the liquid water into the microstructure is continued until a saturation of 100% is achieved by increasing the liquid pressure in $\triangle p$ steps. At each liquid pressure step, the meshes for the partially saturated microstructure reconstructions can be obtained by updating liquid water filled pores in Ω_l to the corresponding pore voxels in Ω^0, which can then be used to perform transport and/or electrochemical simulations.

The liquid water intrusion algorithm was developed in python and included in the pyFCST library.

2.3.4 Electrochemical reactions

The electrochemical reaction in the catalyst layer is simulated as a surface reaction at the solid-ionomer interface. The ionomer film was first digitally reconstructed as a uniform film. Different ionomer film distributions were also investigated but these will be discussed later. Figure 2.7a shows a schematic of a single pore with an ionomer thin film and the reaction site. Figure 2.7b shows a CL reconstructed using FIBSEM with a single voxel thick ionomer film at the solid-pore interface in the solid phase.

For the ORR to take place, the following processes are included in the numerical model:

- Diffusion of oxygen in the gas and liquid filled pores and ionomer;
- Proton conduction in the ionomer;
- Interfacial resistance at the ionomer-solid interface to account for ionomer densification near the platinum surface [209] and dissolution of oxygen in the liquid water and ionomer from the gas phase;
- Reaction of oxygen at the ionomer-solid interface using a multi-step ORR mechanism;

Oxygen transport is simulated using Fick's second law given by Equation (2.5). The diffusion coefficient (D_i or D_{O_2} in this case for oxygen) is defined as,

$$\begin{aligned} D_{O_2} &= D_{O_2}^{ionomer} \text{ in ionomer,} \\ D_{O_2} &= D_{O_2}^{water} \text{ in pores filled with liquid water, and} \\ D_{O_2} &= D_{O_2}^{gas} \text{ in pores filled with gas,} \end{aligned} \tag{2.17}$$

where $D_{O_2}^{water}$ and $D_{O_2}^{ionomer}$ are oxygen diffusion coefficients in liquid water and ionomer, respectively. The diffusion coefficient in gas filled pores ($D_{O_2}^{gas}$) is computed using the Bosanquet approximation using Equations (2.6) and (2.7).

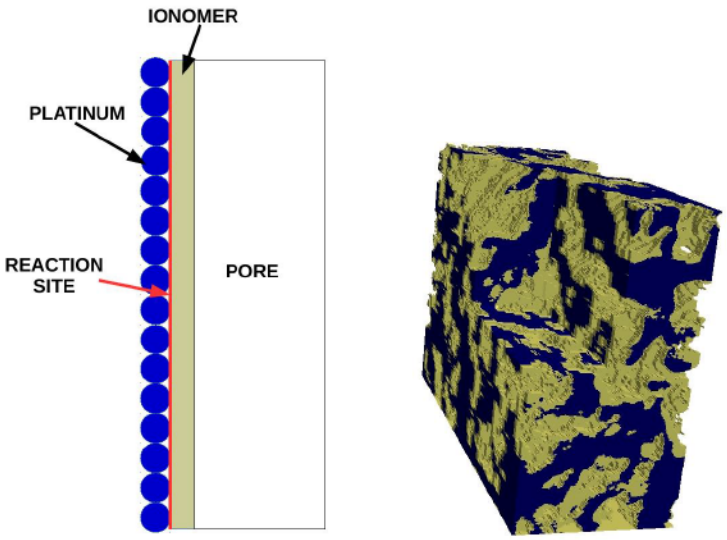

Figure 2.7 – a) Schematic of a single pore with ionomer film for the numerical simulation of electrochemical reactions in the catalyst layer. b) FIBSEM CL reconstruction with digitally reconstructed ionomer film. Blue is the solid phase and yellow is ionomer. Oxygen transport is simulated in the pores and ionomer film. Proton transport is simulated in the ionomer film. Oxygen reduction reaction is simulated at the ionomer-platinum (solid in case of FIBSEM) boundary.

The oxygen diffusion coefficient in the liquid water is computed using the correlation proposed by Wilke and Chang [247]:

$$D_{O_2}^{water} = 7.4 \times 10^{-8} \frac{T(\psi_{H_2O} M_{H_2O})^{0.5}}{\mu V_{\text{gas}}^{0.6}} \tag{2.18}$$

where μ is the viscosity of water in centipoises, T is the absolute temperature, M_{H_2O} is the molecular weight of water, ψ_{H_2O} is an association parameter for solvent water with a value of 2.26 [248] and V_{gas} is the molecular volume of the diffusing gas.

Proton transport in the ionomer films was simulated using Ohm's law, i.e., Equation (2.11). Electron transport in the solid phase was not simulated due to the much higher conductivity of the carbon support [249, 250] compared to the thin ionomer films [12, 251–256]. Therefore, the electronic potential was assumed constant in the domain.

Shinozaki et al. [208] demonstrated the poisoning of the platinum surface by Nafion. Jinnouchi et al. [209] used molecular dynamics simulations to study gas-ionomer and ionomer-platinum interfaces and noted that the local resistance is more likely due to the ionomer-platinum interface. The resistance was attributed to a denser ionomer layer formed around

the platinum particles. To account for the oxygen transport limitation due to ionomer-platinum interactions, an interfacial resistance is introduced into the numerical model at the ionomer-platinum interface. The interfacial resistance is assumed to account for a finite rate of oxygen dissolution in the ionomer and liquid water and the local ionomer-platinum resistance. The current density at the ionomer-platinum interface can thus be computed as,

$$\begin{aligned} \boldsymbol{N}_{O_2} \cdot \boldsymbol{n} &= -k_{O_2} \left(c_{O_2}^{react} - c_{O_{2,s|i}}^{eq} \right), \\ &= \frac{j(c_{O_2}^{react}, \phi_s, \phi_m)}{4F}, \end{aligned} \tag{2.19}$$

where $\boldsymbol{N}_{O_2}$ is the molar flux of oxygen at the ionomer-solid interface, k_{O_2} is an effective interfacial resistance, $c_{O_{2,s|i}}^{eq}$ is the equilibrium oxygen concentration obtained using Henry's law corresponding to the oxygen concentration in the ionomer domain, and $c_{O_2}^{react}$ is the oxygen concentration at the ionomer-catalyst interface used for calculating the current density j. ϕ_s is the electronic potential of the solid phase. The first equation in Equation (2.19) accounts for the solubility resistance and interfacial resistance due to the ionomer film to the oxygen transport. The functional form of this resistance is unknown therefore, the functional form used in this work is based on that used in references [211, 216]. Since this resistance has a linear form, it was shifted to the reaction site without loss of any accuracy in the model. This also helped to improve computational efficiency as the solution variable for oxygen concentration was the same throughout the domain and internal fluxes within the domain did not have to be accounted for.

The current density at the surface of the catalyst particle, j, is calculated using the double trap kinetics model [201] with the free energies obtained by Moore et al. [202]. Since the double trap model combined with Equation (2.19) is non-linear, the surface reaction model is solved at each quadrature point, in each cell at the interface, using a Newton-Raphson non-linear equation solver to obtain the current density at the solid-gas interface. This value is then used as a boundary condition at the solid-gas interface in the micro-scale model.

The kinetic model is used to compute the current density per unit area of platinum. It is necessary to change this value to per unit solid-gas interface area because the boundary condition is applied to the solid-gas interface of the reconstruction. If the location of the platinum particles is known, the active area can be distributed only to those specific locations. In this case however, the exact location is not known and therefore, the active area of platinum is distributed over the total solid-ionomer interface. To estimate the active area of platinum per unit solid-ionomer interface area, $A_{Pt,s|i}$, the total active area of platinum in the catalyst layer, A_{Pt}, defined as active area of platinum per unit mass of platinum, is

obtained from the experimentally obtained electrochemically active surface area (ECSA), using

$$A_{Pt} = \text{ECSA} \times (V_{rec}) \times \frac{m_{Pt}}{\delta_{CL}}, \tag{2.20}$$

where V_{rec} is the volume of the reconstructed CL, m_{Pt} is platinum loading and δ_{CL} is the thickness of the CL.

The total solid-gas interface area of the reconstruction is calculated using

$$A_{s|i} = \int_{\Gamma_{s|i}} dS, \tag{2.21}$$

where $\Gamma_{s|i}$ is the solid-ionomer interface boundary. Using the total active area of platinum in the catalyst layer, A_{Pt}, and solid-ionomer interface area, $A_{s|i}$, the active area of platinum per unit area of the solid-ionomer interface can be found out as,

$$A_{Pt,s|i} = \frac{A_{Pt}}{A_{s|i}}. \tag{2.22}$$

The active area of platinum per unit area of the solid-ionomer interface is used to convert the current density from per unit area of platinum to per unit area of the solid-ionomer interface.

Since the reaction was assumed to take place at the ionomer-solid interface, the reaction terms for both oxygen and protonic potential appear as Neumann boundary conditions. The boundary conditions to simulate electrochemical reactions are,

$$\begin{aligned} c_{O_2} &= c_{O_2}^{in} \quad \text{at all external walls,} \\ (-D_{O_2}\boldsymbol{\nabla} c_{O_2}) \cdot \boldsymbol{n} &= \frac{j}{4F} A_{Pt,s|i} \quad \text{at } \Gamma_{s|i}, \\ \phi_M &= \phi_M^{in} \quad \text{at all external walls,} \\ -\sigma_M \boldsymbol{\nabla}\phi_M \cdot \boldsymbol{n} &= j A_{Pt,s|i} \quad \text{at } \Gamma_{s|i}. \end{aligned} \tag{2.23}$$

where σ_M is the protonic conductivity, $c_{O_2}^{in}$ is the oxygen concentration in the gas phase at the boundary and ϕ_M^{in} is the protonic potential at the boundary. The boundary conditions in Equation (2.23) can be used for representative elementary volume (REV) of a CL. This assumes that the domain is small enough that the change in oxygen concentration and protonic potential across the domain is negligible, as in the case of agglomerate models [40].

To study the performance of CLs, another set of boundary conditions to simulate the entire CL thickness were used. The boundary conditions to simulate the entire through-plane

thickness of the CL are,

$$\begin{aligned} c_{O_2} &= c_{O_2}^{in} \quad \text{at } \Gamma_{CL|GDM}, \\ (-D_{O_2}\boldsymbol{\nabla} c_{O_2})\cdot \boldsymbol{n} &= \frac{j}{4F} A_{Pt,s|i} \quad \text{at } \Gamma_{s|i}, \\ (-D_{O_2}\boldsymbol{\nabla} c_{O_2})\cdot \boldsymbol{n} &= 0 \quad \text{at } \Gamma - (\Gamma_{s|i} \cup \Gamma_{CL|GDM}), \\ \phi_M &= \phi_M^{in} \quad \text{at } \Gamma_{CL|Membrane}, \\ -\sigma_M \boldsymbol{\nabla}\phi_M \cdot \boldsymbol{n} &= j A_{Pt,s|i} \quad \text{at } \Gamma_{s|i}, \\ -\sigma_M \boldsymbol{\nabla}\phi_M \cdot \boldsymbol{n} &= 0 \quad \text{at } \Gamma - (\Gamma_{s|i} \cup \Gamma_{CL|Membrane}). \end{aligned} \tag{2.24}$$

These boundary conditions are representative of oxygen diffusion from the CL-GDM (gas diffusion media) interface ($\Gamma_{CL|GDM}$) to the CL-Membrane interface ($\Gamma_{CL|Membrane}$). The membrane and all external boundaries are assumed to have a no-flux condition while the reaction is simulated on ionomer-solid interface. Oxygen crossover into the membrane is assumed to be zero as the focus of the current is to study the analyze the performance of the CL and not the entire MEA. For the proton conduction, a proton potential is specified at the CL-Membrane interface and all external walls are assumed to have a no-flux condition. These conditions represent a CL with symmetry conditions in the in-plane direction and no oxygen cross-over into the membrane.

2.3.5 Solution methodology

To compute effective transport properties, such as diffusivity and conductivity, the governing equations in Sections 2.3.1 and 2.3.2 were solved with the boundary conditions given by Equations (2.8) and (2.12), respectively. In this thesis, the governing equations are discretized using the Bubnov-Galerkin finite element method. To obtain the weak form of the governing equations given by Equations (2.5) and (2.11), the governing equations are multiplied by scalar test function (v) and then integrated over the the domain (Ω),

$$\int_\Omega v\left[\boldsymbol{\nabla}\cdot(A\boldsymbol{\nabla}u)\right] d\Omega = 0 \tag{2.25}$$

where A is a transport coefficient (e.g., diffusivity for the gas diffusion and conductivity for the charge transport) and u is the solution function. Using tensor algebra, the integral on the LHS of Equation (2.25) can be written as:

$$-\int_\Omega \boldsymbol{\nabla} v\cdot(A\boldsymbol{\nabla}u)d\Omega + \int_\Omega \boldsymbol{\nabla}\cdot(v\ A\boldsymbol{\nabla}u)d\Omega = 0, \tag{2.26}$$

and using the divergence theorem the second term on the LHS can be simplified to,

$$-\int_\Omega \boldsymbol{\nabla} v\cdot(A\boldsymbol{\nabla}u)d\Omega + \int_\Gamma (v\ A\boldsymbol{\nabla}u)\cdot\boldsymbol{n}d\Gamma = 0, \tag{2.27}$$

where Γ denotes the boundaries for the domain Ω and $\boldsymbol{n}$ is the outward normal to boundary. Lagrange linear elements were used to approximate the test (v) and solution (u) functions in the weak form of the governing equation. Since, the stiffness matrix ($\boldsymbol{K}$) for the linear system of equations obtained from Equation (2.27) is symmetric and positive definite, the Conjugate Gradient (CG) method is used to solve the system of equations. The use of CG also results in an order of magnitude lower computational time compared to direct solvers, such as UMFPACK, in 3D.

For simulations including electrochemical reactions, the boundary conditions given by Equations (2.23) and (2.24), are non-linear as they depend on the solution variables. In this case, a Picard solver with adaptive under-relaxation was used [257]. A Picard solver was chosen instead of a Newton method so that the non-linear boundary condition in the second term in Equation (2.27) which would appear on the Jacobian matrix if using a Newton method can be moved to RHS of the weak-form formulation, as it is evaluated based on the solution at the previous Picard iteration. The advantage of using the Picard solver is that the stiffness matrix remains symmetric therefore, CG method can be used to solve Equation (2.28). Further, the stiffness matrix does not need to be re-evaluated at every Picard iteration. For micro-scale simulations with several million degrees of freedom, these two advantages significantly improve the computational efficiency of the simulations.

For the Picard solver, the solution at each non-linear iteration, $\boldsymbol{u}^{N+1}$, is computed using

$$\boldsymbol{u}^{N+1} = (\boldsymbol{K})^{-1}\, \boldsymbol{f}(\boldsymbol{u}^{N}), \tag{2.28}$$

where $\boldsymbol{K}$ is the stiffness matrix, and $\boldsymbol{f}(\boldsymbol{u}^{N})$ is the non-linear right hand side vector computed using the solution at the previous iteration $\boldsymbol{u}^{N}$.

The solution to be used for the next step $\widetilde{\boldsymbol{u}}^{N+1}$ is then updated using

$$\widetilde{\boldsymbol{u}}^{N+1} = \boldsymbol{u}^{N} + \gamma\left(\boldsymbol{u}^{N+1} - \boldsymbol{u}^{N}\right) \tag{2.29}$$

where γ is an under-relaxation factor that depends on the difference between the solutions at the current and previous iterations. It is computed using

$$\gamma = \begin{cases} \gamma_{min} + (1-\gamma_{min})\exp[-\alpha(\delta-\epsilon)] & for\ \delta > \epsilon, \\ 1 & for\ \delta < \epsilon, \end{cases} \tag{2.30}$$

where ϵ is the error tolerance, and δ is the L_∞ norm of the change in the solution given as

$$\delta = \max_i \mid \boldsymbol{u}_i^{N+1} - \boldsymbol{u}_i^{N} \mid \tag{2.31}$$

As $\boldsymbol{u}^{N+1} \rightarrow \boldsymbol{u}^{N}$, the value of $\gamma \rightarrow 1$. Two convergence criteria are used for the Picard solver,

$$\begin{aligned} \frac{\parallel u^{N+1} - u^{N} \parallel_2}{\text{DOFs}} &< \epsilon^{abs} \\ \frac{\parallel u^{N+1} - u^{N} \parallel_2}{\text{DOFs} \parallel u^{N+1} \parallel_2} &< \epsilon^{rel} \end{aligned} \tag{2.32}$$

where $\parallel u^{N+1} \parallel_2$ and $\parallel u^{N+1} - u^{N} \parallel_2$ represents the L_2 norm of the current solution and the difference between the solution at the current and previous iteration, respectively, DOFs indicates the total number of degrees of freedom, ϵ^{abs} is the absolute tolerance which was set to 10^{-7} and ϵ^{rel} is the relative tolerance of the solution which was set to 10^{-5} for the simulations. The simulations were deemed to have converged when both the criteria in Equation (2.32) were met. The residual for both the governing equations (Equations (2.5) and (2.11)) was also computed and analyzed during the Picard iterations to ensure that the solution satisfied the governing equations.

The governing equations for gas and charge transport and electrochemical reactions were implemented in the open-source simulation toolbox OpenFCST [229]. The Picard solver with under-relaxation was also developed as a part of the OpenFCST package [229]. The code developed was parallelized to further reduce the computational cost when simulating tens of millions of DOFs especially, for the non-linear electrochemical simulations.

2.3.6 Meshing

Meshing is performed by direct conversion of the image voxels to a 3D unstructured VTK mesh. The VTK mesh is generated using a python class developed in pyFCST which uses the TVTK library [258]. The VTK mesh can be used to pass a micro-scale mesh with multiple material IDs at the same resolution as the input image, i.e., the cell size of the mesh is the same as the voxel size. The advantage of the VTK mesh implementation in pyFCST is the ability to pass additional information in the form of "field data". Field data can be used to pass additional information about every cell in the mesh including the boundaries. This feature has been used in this work, for example, to pass the pore size of every pore voxel (as KnudsenRadius field) computed using the PSD algorithm in Section 2.2.4 and the local thickness of the ionomer thin films to the ionomer voxels (as IonomerThickness field; discussed later). The implementation of the VTK writer class in pyFCST and the reader class in OpenFCST allows the mesh to contain as many fields of information as required, therefore allowing for local information to be embedded in the mesh. This eliminates the need to use external maps to pass information which is required for conventional meshing

tools [53].

In order to reduce the size and complexity of the computational domain, cluster identification is used to extract the percolating network of the different phases and use only these to generate the meshes. All clusters in the image are first identified and labeled using the dual pass algorithm proposed by He et al. [242] for cluster labeling in conjunction with Hoshen and Kopelman [243] algorithm. The percolating clusters for the different phases to be used in the simulation are then extracted and a VTK mesh is generated using each voxel in the images as a cell in the finite element mesh. For example, for a gas diffusion simulation the percolating pore network is extracted whereas for an electrochemical simulation the percolating networks for gas and liquid filled pores and ionomer are extracted to generate the meshes. The percolating network extraction algorithm used in this work was developed by Pant [68].

The meshing tool developed in this work generates meshes directly from a stack of images thereby enabling easy manipulation of the images to change the mesh sizes. As will be discussed in the later chapters, nearest neighbor interpolation was used to coarsen (reduce voxel resolution) the 3D images to reduce the mesh size and computational cost. This allowed me to study the effect of the mesh resolution which will be discussed later.

Chapter 3

Analysis of liquid water transport in GDLs[†]

The numerical tools described in Chapter 2 are used here to study liquid water intrusion in GDLs and to study the corresponding effect on gas transport. The objective of this study is to validate the cluster based full morphology algorithm described in Section 2.3.3 as a tool to predict liquid water intrusion in fuel cell porous media. For this study, a μ-CT reconstruction of a dry GDL sample is used to simulate the liquid water intrusion. The partially saturated GDL microstructures obtained from simulations are compared to experimental μ-CT images of a partially saturated GDL.

Section 3.1 provides a brief description of the GDL microstructure and the inputs used to simulate liquid water intrusion. To assess the accuracy of the simulated liquid water profiles simulated and μ-CT images are compared based on three metrics namely: i) capillary pressure-saturation curve (discussed in Section 3.2), ii) voxel based comparison (discussed in Section 3.3) and, iii) gas transport in partially saturated GDLs (discussed in Section 3.4). Section 3.5 provides a summary of the results for this study.

3.1 Simulation setup

μ-CT image reconstructions of dry and wet Toray TGP-H-120 GDL with 10% PTFE content previously published in [55, 56] were used in this study. Water intrusion was simulated on a binarized dry GDL structure having a domain size of 1995 μm $\times$ 1995 μm $\times$ 281.96 μm with a pixel resolution of 1.33 μm in each direction and a porosity of 65.8%. The partially

[†]Parts of this chapter have been published in: M. Sabharwal, J. T. Gostick, and M. Secanell, *Journal of The Electrochemical Society* 165 (7), 2018

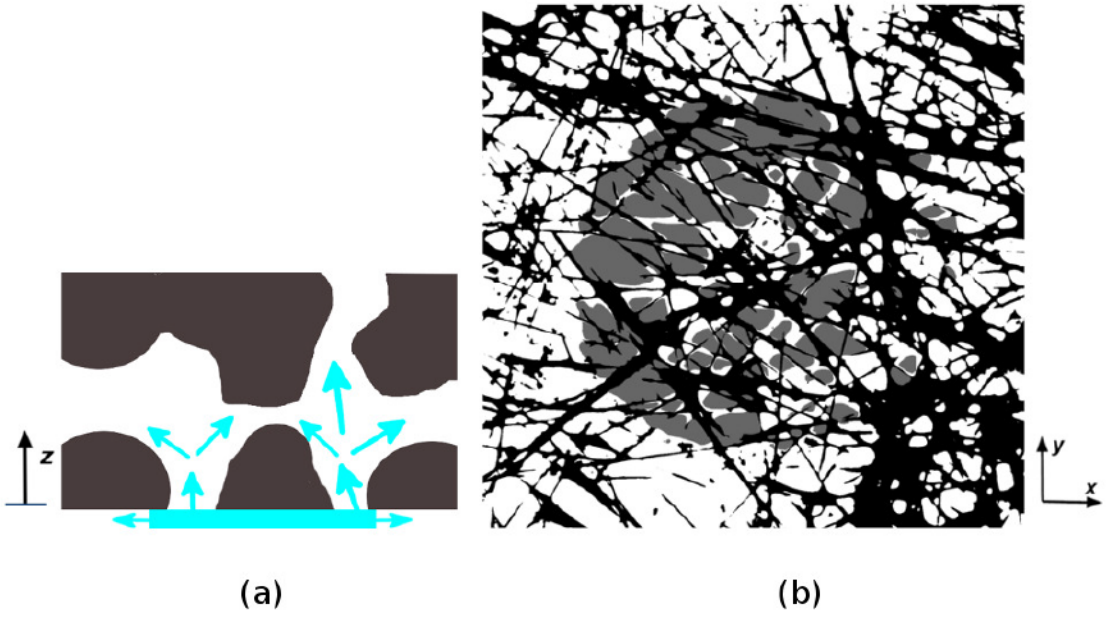

Figure 3.1 – a) Schematic of the boundary based mode for water intrusion into the GDL. b) GDL slice at the inlet (z=0) showing the initial liquid water intrusion points. (Black indicates the GDL fibers, white indicates the empty pores and grey indicates liquid water.)

saturated GDL microscopy reconstructions were obtained for a capillary pressure range of 1 to 8 kPa with 1 kPa increments. Details about the experimental setup, μ-CT technique and image thresholding can be found in references [55, 56].

The cluster based full morphology algorithm described in Section 2.3.3 is used to simulate liquid water intrusion in the dry GDL reconstruction obtained from μ-CT images. Water intrusion was simulated numerically using a boundary based method. Figure 3.1a shows a schematic of the boundary based method where water from a circular reservoir region, shown in Figure 3.1b, representative of the pipe in the experimental setup, is intruded into the sample. The liquid pressure in the reservoir was increased to intrude the water into the GDL both in the through-plane (z direction) and in-plane (x and y directions), as shown by the arrows in Figure 3.1a. The propagation of the liquid water front into the GDL was tracked using Algorithm 1 on page 31. The circular region shown in Figure 3.1b on the z=0 plane was provided as an input to the algorithm as the initial water intrusion points (Ω_l). For this study, the GDL was assumed to be hydrophobic with a contact angle of 110°.

Figure 3.2 shows the liquid water profiles obtained by simulation in the GDL at capillary

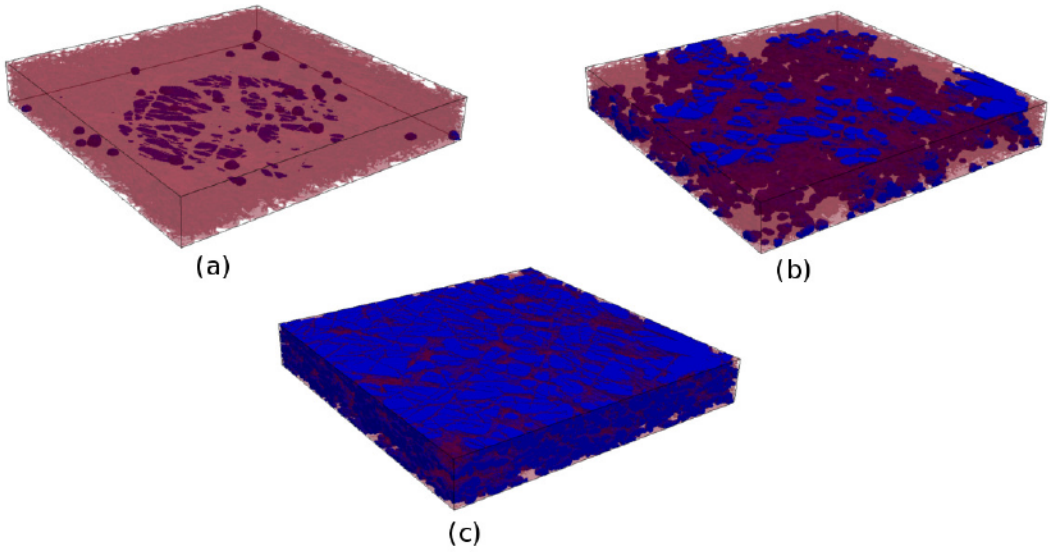

Figure 3.2 – 3D liquid water profiles in the GDL obtained using CFM model at a capillary pressure of: a) 1 kPa, b) 4 kPa and, c) 8 kPa.

pressure of 1, 4 and 8 kPa. Due to the cluster based approach used, water intrusions steps are relatively fast for a GDL domain size with 477 million DOFs. To perform a single water intrusion step at a given capillary pressure the algorithm took an average of 6 minutes on a single core of Intel(R) Xeon(R) CPU E5-2690 v2 with a clock speed of 3.00 GHz. Computation times for water intrusion simulations are seldom reported in literature. Vogel et al. [178] reported that both the computational time and cost (in terms of RAM requirement) for PNM, FM and LBM were of the order of 1, 1.5 and 10^4-10^5 respectively. Based on the values reported by Vogel et al. [178] the computational time for PNM would be lower than the CFM model used in this study but the computational time for LBM would be on the order of 4-40 weeks on a single core processor. Below three properties are compared between the numerical liquid water intrusion algorithm and μ-CT imaging results, namely: i) capillary pressure-saturation curve, ii) 3D liquid water profiles, iii) gas diffusivity in partially saturated GDLs.

3.2 Capillary pressure-saturation relationship

Capillary pressure-saturation curves are commonly used to characterize liquid water transport in porous media [1, 97, 102, 183, 259]. Figure 3.3 shows the saturation as a function of capillary pressure for the simulated water intrusion using the CFM model, the experimental tomographic reconstructions and the ex-situ experimental data in reference [1] for the same material. For the CFM simulations, a constant contact angle was assigned to all the pore surfaces. Since the local contact angles for the GDL reconstruction were not known

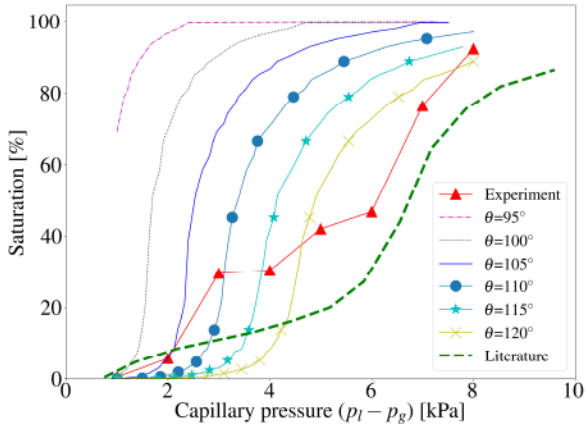

Figure 3.3 – Saturation as a function of the capillary pressure for water intrusion into a 10% PTFE Toray TGP-H-120 GDL from tomographic reconstructions (experimental), simulated using the CFM model with contact angle varied between 95°-120° and literature data [1].

a parametric study was performed by varying the contact angle between 95°-120° in the Young-Laplace equation. An increase in the contact angle for the simulations resulted in an increase in the capillary pressure required to obtain a given saturation without any change in the shape or slope of the capillary pressure-saturation curve.

Comparison of the simulated capillary pressure-saturation curves obtained using the proposed CFM model to those obtained from μ-CT images and previously reported experimental data by Gostick et al. [1] for the same material in Figure 3.3, shows that the CFM model predicted higher saturations for capillary pressures of 4-8 kPa compared to the saturation values from μ-CT images and previously reported in reference [1] for all contact angles used. However it must be noted that the sigmoid shape of the simulated capillary pressure-saturation curve resembles the experimental data by Gostick et al. [1]. The difference in the saturation values at a given capillary pressure between the simulation and experiments is likely due to the use of a 180° contact angle for estimating the pore sizes. The different contact angles used in Figure 3.3 for the CFM simulations are merely a fitting parameter using the Young-Laplace equation. Although the CFM predicted capillary pressure-saturation curve for the sample used in this study is quite different from the μ-CT and literature curves, a FM model has been shown to be able to predict the capillary pressure-saturation curve for SGL^{TM}24BA [176]. Therefore, analysis of different samples might be to improve the limitations of the CFM model. Schulz et al. [183] proposed an improvement to the FM model by creating fictitious spheres with diameters increased by the cosine of the contact angle to account for the wettability of the walls. Although this is an improvement over the traditionally used FM model, it would be difficult to model the real GDL surfaces where multiple

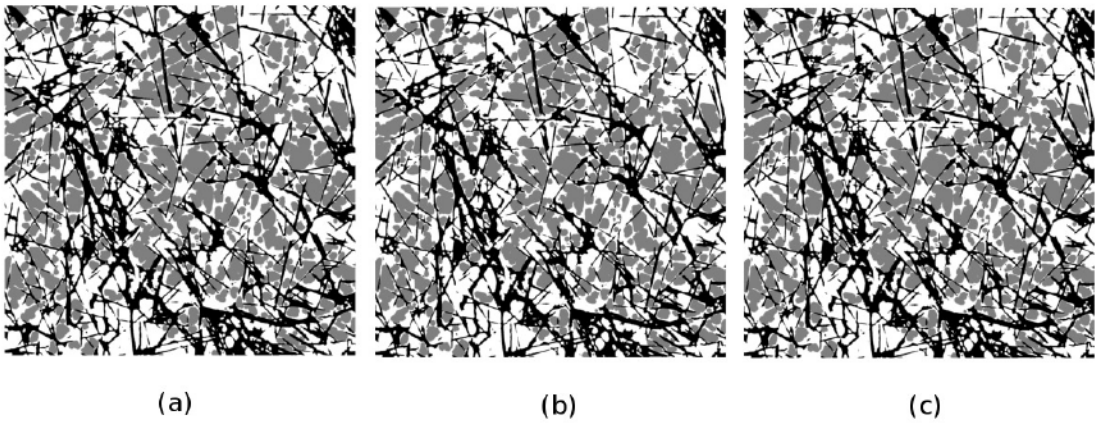

Figure 3.4 – Images showing the simulated water distribution for contact angle of a) 100°, b) 110° and, c) 120° at a saturation of 39% at 50% through-plane depth of the GDL. (Black indicates the GDL fibers, white indicates the empty pores and grey indicates liquid water.)

contact angles might exist along the walls of the same pore. The method used in this study to fit the capillary pressure with a contact angle using the Young-Laplace equation is an approximation and a future study would investigate the implementation of a more accurate representation of the local contact angle in the GDL.

Figure 3.4 shows the liquid water distribution at a saturation of 39% at half through-plane depth of the GDL reconstruction using contact angles of 100°, 110° and 120°. It can be seen that for the same saturation (of 39%) the liquid water distribution for the different contact angles is identical in the GDL due to the reasons explained earlier. It must also be noted that for the CFM simulations the effect of the contact angle on the saturation and water distribution can be neglected as long as the wettability (i.e., hydrophobicity of the pores) is maintained and therefore, the contact angle can be used as a fitting parameter. This warrants the comparison of the water distribution between the μ-CT images and CFM simulations of the partially saturated GDLs at similar saturations rather than capillary pressure which will be discussed in Section 3.3.

3.3 Liquid water distributions

Capillary pressure-saturation curves provide averaged information about the liquid water transport through the whole porous media. However to validate the profile and distribution of liquid water in the porous media, a one-to-one comparison must be made between the

numerically simulated and microscopy reconstructed 3D liquid water distributions. To validate the liquid water intrusion algorithm developed in this study, the 3D water distributions from the simulations were compared to the 3D water distributions from μ-CT images. In order to compare liquid water distributions with the same volume fraction of water, simulations and experiments were compared at similar saturation values. It must be noted that since the simulation uses a discrete pore size distribution of the GDL obtaining identical saturation values as the experiments is difficult. To achieve similar saturation values to the experiments, the number of steps n in Algorithm 1 was increased to 100.

Figures 3.5 and 3.6 show a comparison of the experimental and simulated liquid water distributions in the x-y plane at 25%, 50% and 75% through-plane (z) depth of the GDL from the inlet at a saturation of nearly 30% and 46% respectively. Comparing the liquid water distribution between the simulations and experiments in Figure 3.5, it can be seen that the simulated water clusters in Figures 3.5b, 3.5d and 3.5f appear in similar regions as those seen in the μ-CT images in Figures 3.5a, 3.5c and 3.5e. However the simulated water clusters appear more discrete compared to the liquid water clusters from the μ-CT images. The discrete nature of the simulated liquid water clusters also exists at the higher saturation of nearly 46% as shown in Figures 3.6b, 3.6d and 3.6f. Additionally, for both the saturations, i.e., 30% and 46%, the simulation predicts excessive liquid water clusters, especially near the outlet, compared to the experimental reconstructions as shown by the comparison of Figures 3.5e and 3.5f and Figures 3.6e and 3.6f.

Based on the comparison of the liquid water distributions, two issues exist between the simulated and experimental water distributions. The first one is the presence of discrete capillary fingers of liquid water in the simulations compared to the larger clusters in the μ-CT images. The discrete liquid water clusters seen in the simulated liquid water distributions in Figures 3.5 and 3.6 can be attributed to the algorithm used for estimating the pore sizes for the GDL. Figure 3.7 shows the pore size distribution and liquid water distribution at $s = 32.01\%$ for a GDL slice at 50% through-plane depth. As discussed in Section 2.3.3, the PSD algorithm assigns spherical radii to the pores. Therefore, pore voxels which are closer to the fibers or in between two large pores are assigned a smaller pore radius as shown in Figure 3.7a. Consequently, the liquid water does not intrude these pores as shown in Figure 3.7b where the capillary pressure is 3.12 kPa corresponding to all pores with radius bigger than 15.9 μm that are connected to the water network being flooded. Note that this algorithm is similar to that used in previous FM results for fuel cell porous media, e.g., references [102, 113, 176, 184], therefore it is likely that the previous work experienced similar problems. The FM liquid water distributions shown by Agaesse et al. [176] also showed

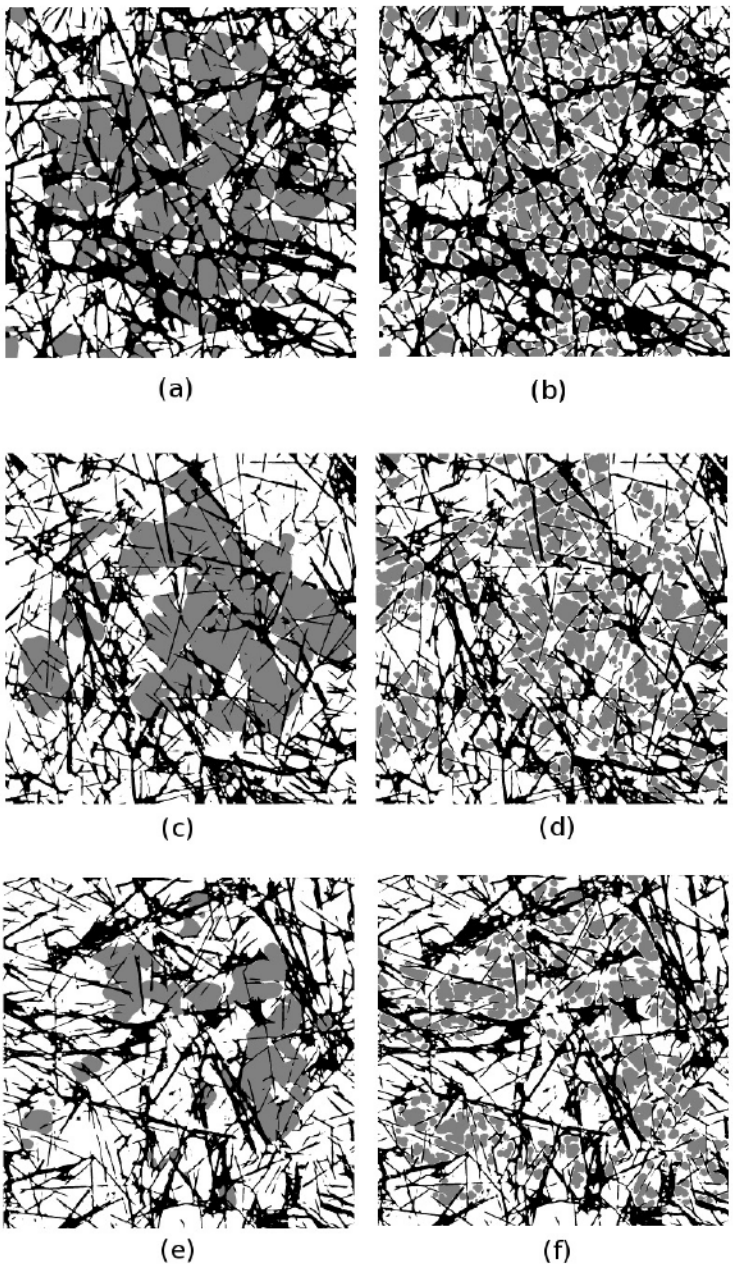

Figure 3.5 – Images showing the liquid water distribution from a) experimental reconstruction and b) CFM simulation at 25% through-plane depth from the inlet, c) experimental reconstruction and d) CFM simulation at 50% through-plane depth from the inlet, e) experimental reconstruction and f) CFM simulation at 75% through-plane depth from the inlet. The experimental reconstruction had a saturation of 30.43% at a capillary pressure of 4 kPa. The CFM simulation had a saturation of 32.01% at a capillary pressure of 3.12 kPa. (Black indicates the GDL fibers, white indicates the empty pores and grey indicates liquid water.)

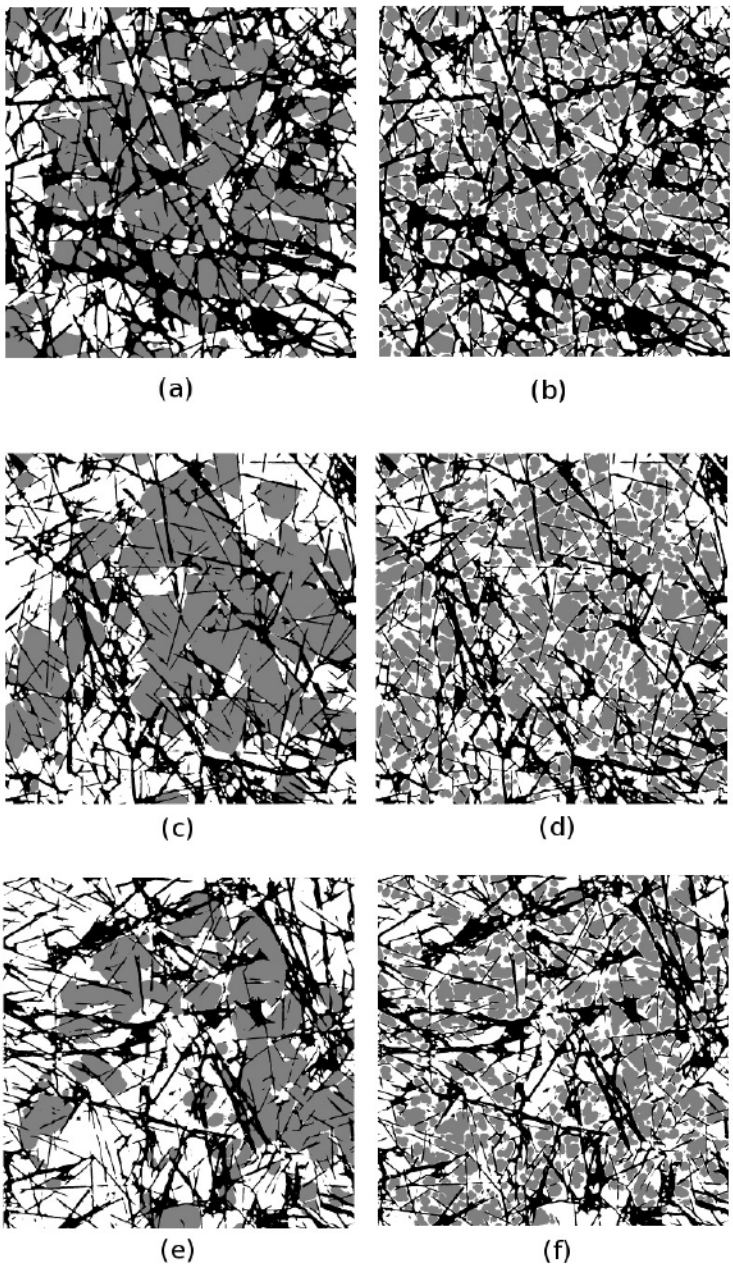

Figure 3.6 – Images showing the liquid water distribution from a) experimental reconstruction and b) CFM simulation at 25% through-plane depth from the inlet, c) experimental reconstruction and d) CFM simulation at 50% through-plane depth from the inlet, e) experimental reconstruction and f) CFM simulation at 75% through-plane depth from the inlet. The experimental reconstruction had a saturation of 46.79% at a capillary pressure of 6 kPa. The CFM simulation had a saturation of 45.19% at a capillary pressure of 3.26 kPa. (Black indicates the GDL fibers, white indicates the empty pores and grey indicates liquid water.)

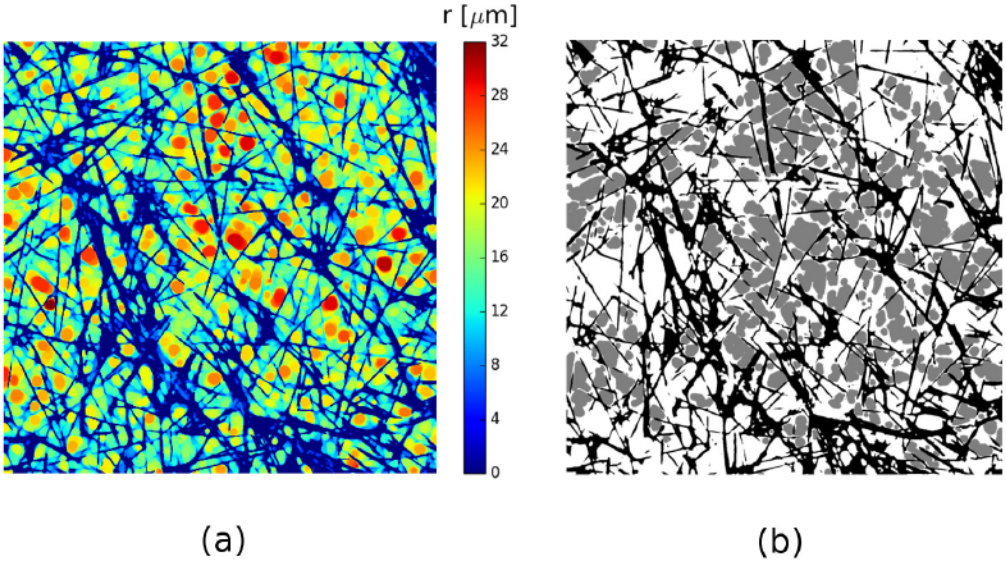

Figure 3.7 – Images showing a) the pore sizes, and b) simulated liquid water distribution at $s = 32.01\%$ for a GDL slice at 50% through-plane depth from the inlet. The pore sizes are indicated by the corresponding colorbar. For the liquid water distribution, black indicates the GDL fibers, white indicates empty pores and grey indicates liquid water.

a larger number of clusters compared to the experimental distributions. Since, Agaesse et al. [176] did not show 2D profiles of the liquid water distributions in the GDL slices it was difficult to observe the granularity in the simulated liquid water distribution. Similar discrete capillary fingers can also be seen in the FM simulation results on compacted silica sand by Kim et al. [196]. Image processing operations to better discretize the void space into pores using advanced methods analogous to those developed for pore network extraction [176, 260] could help improve the granularity of the liquid water distribution. Another improvement to the current model could be the use of Purcell toroid model [261] instead of the Young-Laplace equation to account for the liquid water intrusion. These improvements to the existing CFM model will be investigated in a later study.

The second issue is the prediction of excessive liquid water clusters in the simulations as seen in Figures 3.5d, 3.5f, 3.6d and 3.6f. This is likely due to the variation of the local contact angle in the GDL pores which has not been accounted for in the simulations.

Although the primary source of error between the simulated and reconstructed liquid water profiles is attributed to the formulation of the numerical model, the uncertainties associated with the experimental setup and μ-CT images must also be pointed out. It must be noted that the μ-CT images were obtained using manual segmentation of grey-

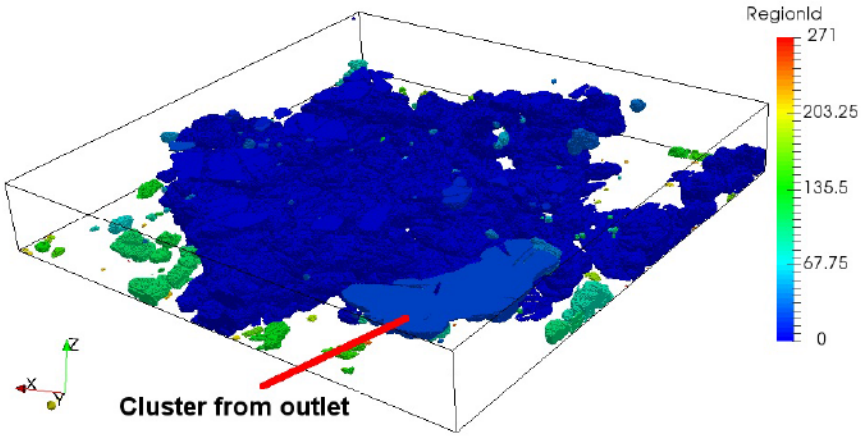

Figure 3.8 – Liquid water distributions from μ-CT images at a capillary pressure of 3 kPa. The profile is colored based on the connectivity with the colorbar showing the disconnected regions identified in the 3D water profile.)

scale images [56] which might have resulted in an overprediction of the connectivity of the liquid clusters. Details of the experimental methods and image processing procedures can be found in [56]. Inconsistencies in the reconstructions can be seen in Figure 3.8 where a liquid water cluster (near top edge) is originating from the outlet which is supposed to be in contact with a hydrophobic membrane. This would affect the boundary condition for the CFM simulations where the outlet face in contact with the hydrophobic membrane is assumed to be non-penetrable by the liquid water. Further, the liquid water behavior in the hydrophilic membrane might also influence the boundary condition for the liquid water intrusion at the inlet face. This indicates the need for well controlled experiments together with development of optimal reconstruction algorithms to reduce uncertainties due to image analysis, leaks in the system and evaporation. These would also facilitate the development of more representative numerical models.

Figure 3.9 shows the local average saturation profiles in the through-plane direction for the cases discussed above. Local average saturation profiles are obtained as the ratio of the number of pixels assigned to the water phase to the sum of pixels in the void and water phase in a 2D cross-section (XY plane) at a given distance from the bottom (inlet plane) of the GDL. The experimental reconstructions exhibit a steeper gradient in the local saturation across 25-75% of through-plane depth. Saturation gradients of 22.17% and 17.97% are observed at s=30.43% and 46.79% in the μ-CT images, respectively, compared to 11.15% and 6.1% variation in the corresponding simulations. The local saturation profiles from tomography and simulated water distributions exhibit less than 8% discrepancy in saturation between 25%-75% of through-plane depth for both the saturation cases. The tomographic water distributions show a larger variation in the local saturation from inlet to outlet com-

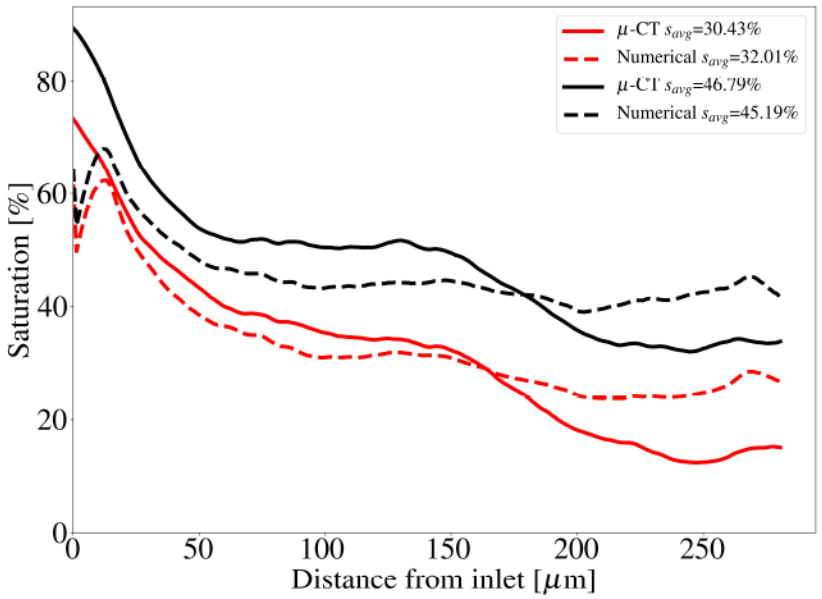

Figure 3.9 – Local saturation profiles in the through-plane direction for the tomographic and simulated liquid water distributions for the cases described in Figures 3.5 and 3.6.

pared to the CFM water distributions. Further, it can be seen that the numerical simulations are affected by the boundaries which result in an extrema near the inlet and outlet. This is likely due to the pore size computation algorithm where the distance transform near the edges is computed by looking for the closest solid voxel within the domain. This leads to the creation of larger but incomplete spherical pores near the domain boundaries which result in the local peaks in saturation near the inlet and outlet.

In order to quantify the agreement between experimental and numerical results the number of liquid water voxels which are identical in both images as a fraction of the total liquid water voxels is shown in Figure 3.10. The random distribution line indicates the average agreement that would be obtained if water was assigned randomly to the void space for a given saturation. Since higher saturation means more pores will have water, the probability that a pixel would be assigned to the water phase increases proportionally with saturation. Comparing the agreement of the simulations to the average random line, it can also be seen that the proposed model provides significantly higher accuracy (15-40%) compared to a random water distribution. Figure 3.10 shows that for saturations between 29-50% the CFM model is able to predict 56-60% of the liquid water voxels observed in the μ-CT images. The quantitative one-to-one comparison of the liquid water distributions from the experimental μ-CT images and numerical simulation using FM model shows that the developed

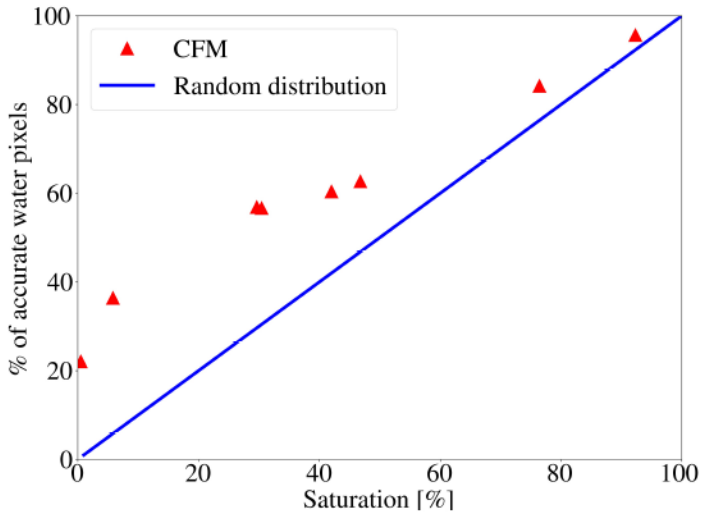

Figure 3.10 – Percentage of identical water voxels from the experimental and simulated water distributions as a function of the saturation.

CFM model is able to predict the liquid water intrusion in the GDL for saturations in the range 29-100% with a accuracy of 56% and higher. In the 6-29% saturation region, which is of particular interest for fuel cell simulations, μ-CT data was not available. Therefore, the accuracy of the CFM algorithm cannot be estimated in this region, however it is likely to be between 40 and 60% based on the results at higher saturations as well as the results from Agaesse et al. [176] where similar agreement is observed using a FM approach.

Although the accuracy of the CFM model for a saturation of 6% is only 22%, this is much higher than a random distribution of liquid water which would have an accuracy of less than 6% (with the value approaching 6% for a large number of realizations). This suggests that the numerical model is able to capture some of the characteristics of the water intrusion even at these low saturations. As discussed earlier, there are several uncertainties associated with the μ-CT images, primarily the boundary conditions that should be used at the inlet and outlet of the GDL, and simulations parameters such as local wettability and contact angle in the GDL pores. Therefore, the current level of agreement between the simulated and experimental water distributions was deemed acceptable. This figure also provides a quantifiable benchmark to compare future models to study liquid water intrusion.

3.4 Gas transport in partially saturated GDLs

Liquid water distribution predictions were required in order to predict transport in the GDL at varying saturation levels. In order to analyze if the current level of accuracy on water distribution was appropriate to estimate transport properties, the proposed CFM model was used to generate the pore space available to gas transport for partially saturated media and the results of mass transport simulations were compared to the effective diffusivity predictions obtained from simulations on the wet μ-CT images. This comparison would determine whether the current level of accuracy in the water distribution is appropriate to predict gas transport in the partially saturated GDL.

3.4.1 Dry and wet diffusivity of GDL

As described in Section 2.3.6, gas transport was simulated on the partially saturated GDL reconstructions by direct conversion of the image voxels to mesh cells. To improve computational efficiency, the cell resolution was coarsened to 2.66 μm in all directions from the original 1.33 μm. Gas transport was simulated using Fick's second law as described in Section 2.3.1. The average simulation time for the dry GDL sample with nearly 46 million DOFs (domain size of 1.995 mm $\times$ 1.995 mm $\times$ 0.282 mm) was 3.6 hours on a single core of Intel(R) Xeon(R) CPU E5-2690 v2 with a clock speed of 3.00GHz.

Figure 3.11 shows the formation factor in the Cartesian directions as a function of the saturation for the partially saturated GDL reconstructions from μ-CT data and numerical simulations using CFM model. Formation factor is defined as the ratio of the effective diffusivity to the bulk diffusivity. At zero saturation, the formation factor in the x, y and z direction is 0.418, 0.404 and 0.224 respectively. The average in-plane (x and y) formation factor is 0.411 for the dry GDL reconstruction which agrees with experimental in-plane formation factor values in the range of 0.31-0.54 [66] for the Toray TGP-H-120 sample with 10% PTFE loading and porosity in the range of 0.61-0.73. The through-plane (z) formation factor for the dry GDL reconstruction is 0.224 which is also in agreement with previously reported experimental values in the range of 0.14-0.33 for Toray 120 samples [2, 129, 130].

The formation factor in all directions decreases with an increase in saturation. At a given saturation, the formation factor for the liquid water distributions from CFM model (solid line) is higher than those obtained from the μ-CT images (dashed line) in the x and y direction. However the difference in the formation factor values for the x and y direction between the μ-CT and numerical reconstructions of the partially saturated GDLs is less than 20% for saturations below 40%. For higher saturations, the difference in the formation factor

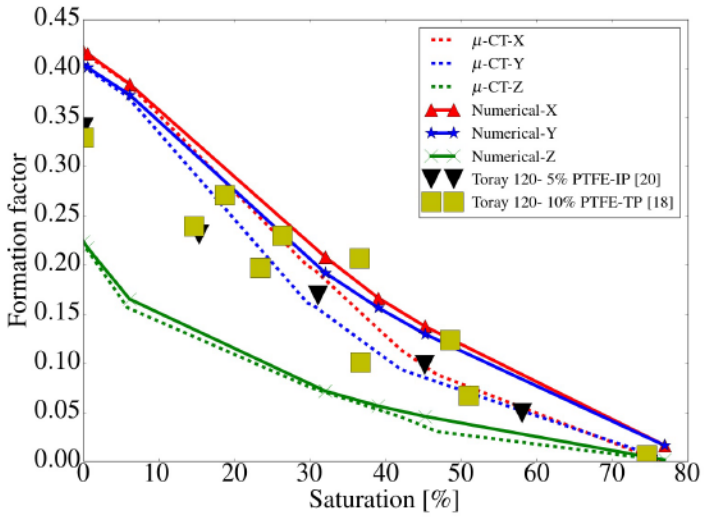

Figure 3.11 – Variation of the formation factor in the x, y and z directions with saturation of the GDL from μ-CT and numerical reconstructions compared to previously reported literature data for partially saturated Toray TGP-H-120 GDLs [2, 3]. For the numerical and μ-CT images, x and y are in-plane directions and z is through-plane direction. Tranter et al. [3] measured the in-plane (IP) diffusivity of partially saturated Toray TGP-H-120 GDL with 5% PTFE. Hwang and Weber [2] measured the through-plane (TP) diffusivity of partially saturated Toray TGP-H-120 GDLs with 10% PTFE loadings.

values increases to nearly 67% for s=42%. The formation factor in the z direction is nearly identical for both the CFM and μ-CT images at different saturations.

The higher deviation observed in the in-plane formation factors for saturations above 40% might appear as a surprise because the accuracy of the liquid water distribution for these cases is above 60% whereas for saturations below 40% the accuracy of the liquid water distribution is lower. To analyze the reason for the larger discrepancy in the predicted effective diffusion coefficients at high saturation levels, saturation profiles for GDL slices in the x and y direction are shown in Figure 3.12 at low and high saturation levels. Saturation profiles for GDL slices in the z direction are given in Figure 3.9 for the same saturation levels. Figure 3.12 shows that the μ-CT images exhibit a much larger variation in the local saturation compared to the CFM simulations at high saturation with local saturation in certain regions as high as 70%. The high saturation local areas lead to a significant drop in the effective porosity in these regions and consequently a sharp decrease in the effective diffusivity. These peaks are not seen in the CFM simulations where the local saturation increases nearly uniformly through the whole domain. This explanation is further strengthened by the loss of a percolating pore path in the x direction in the μ-CT images at a saturation of 76% which is also not observed in the CFM simulation predictions. Figure 3.9 shows that large variation in saturation are not observed in the z even at high saturation, and in this direction there is a much higher accuracy for the through-plane (z) formation factor. The peaks in μ-CT reconstruction could be due to a higher water affinity towards these regions due to a lower contact angle, or to issues with reconstructed images as shown in Figure 3.8. Assuming the former, the difference in the growth of the local saturation peaks between the μ-CT reconstruction and numerical simulations is likely due to changes in local contact angles. Experimental knowledge of local contact angles and improvements to the CFM model might help to better capture the gradients in the local saturation profiles.

Figure 3.11 also shows a comparison of the formation factors for partially saturated GDLs from μ-CT and CFM simulations to previously reported literature data for Toray TGP-H-120 GDLs [2, 3]. Tranter et al. [3] measured the in-plane diffusivity for partially saturated Toray TGP-H-120 GDL with 5% PTFE. The simulated formation in-plane (x and y) factors for the μ-CT and CFM simulations have a maximum formation factor difference of $\pm$ 0.05 compared to the experimental values in reference [3].

Hwang and Weber [2] measured the through-plane diffusivities for Toray TGP-H-120 GDL with different PTFE loadings. Hwang and Weber [2] data for 10% PTFE had a higher porosity than the μ-CT reconstruction used in this study, 0.73 vs 0.66. The wet TP forma-

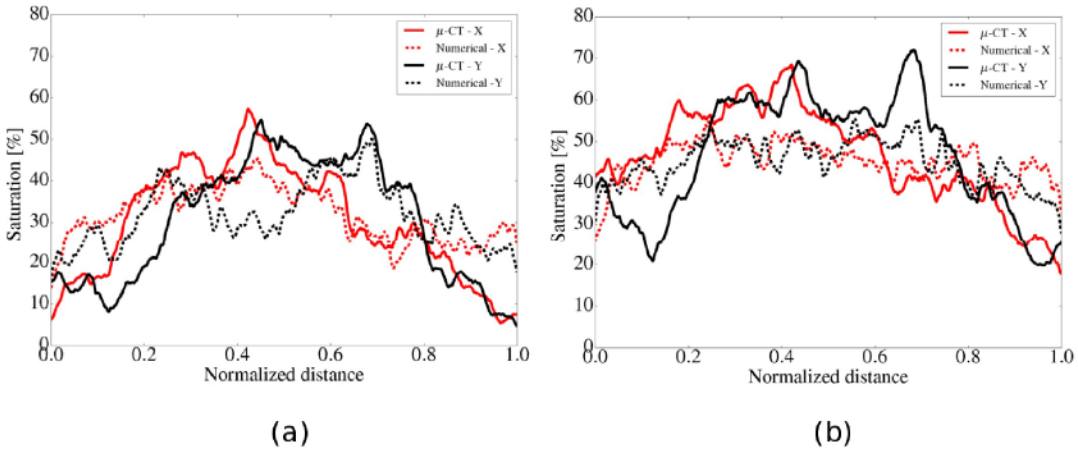

Figure 3.12 – In-plane (x and y) local saturation profiles from the CFM simulations and μ-CT images for an average saturation of a) 30.43% in μ-CT images and 32.01% in numerical simulations and b) 46.79% in μ-CT images and 45.19% in numerical simulations. The profiles are for the same liquid water distributions shown in Figures 3.5 and 3.6, respectively.

tion factors reported by Hwang and Weber [2] are nearly twice the TP (z) formation factors for the μ-CT and CFM simulated partially saturated GDLs. This difference could be due to variability of the material however, it is difficult to explain the discrepancies based on the current study.

The present analysis shows that the difference in the IP and TP formation factors between the μ-CT and CFM simulated structures was less than 20% for saturations below 40%. Other algorithms, such as LBM, VOF or Lagrangian-Eulerian formulation, might be able to predict more realistic water distributions but given the good agreement between μ-CT and CFM effective diffusivity predictions this improvement might not justify the increased computational expense.

3.4.2 Effect of voxel size

The GDL reconstruction used in the current study was extremely large (470 million voxels) and required large computational resources (RAM and CPU time) to perform the numerical simulations. To circumvent this problem coarsening the image resolution to decrease the voxel count (and hence the computational requirement) was explored. Three sections were extracted from the dry GDL reconstruction and coarsened by factors of 2 and 4, corresponding to voxel resolution of 2.66 μm and 5.32 μm in each direction, respectively, to quantify the relative difference in the formation factor for diffusion with respect to the voxel resolution.

The three stacks labeled as Stack 1, Stack 2 and Stack 3 had dimensions of 931 μm $\times$ 931 μm $\times$ 281.96 μm (700 $\times$ 700 $\times$ 212 voxels), 532 μm $\times$ 532 μm $\times$ 281.96 μm (400 $\times$ 400 $\times$ 212 voxels) and 532 μm $\times$ 532 μm $\times$ 281.96 μm (400 $\times$ 400 $\times$ 212 voxels), respectively, and were taken from different parts of the dry GDL reconstruction. For the partially saturated conditions, Stacks 1, 2 and 3 were selected from the same location (as the dry GDL reconstruction) from the μ-CT GDL reconstruction at an average saturation of 46.79% and capillary pressure of 6 kPa.

Table 3.1 shows the formation factors in the in-plane (x and y) and through-plane (z) direction for Stack 1 at different voxel resolutions under dry and partially saturated (s_{global}=46.79%, p_c=6 kPa) conditions. Similar comparisons for Stacks 2 and 3 can be found in Tables 3.2 and 3.3. It was ensured that coarsening of the voxel resolution did not affect the porosity and percolating pore volume and the change in the porosity, percolating pore volume and saturation was less than 1% of the original value. The error (ϵ) defined as,

$$\epsilon = \frac{F_{\text{coarse}} - F_{\text{original}}}{F_{\text{original}}} \times 100. \tag{3.1}$$

The formation factors under dry and partially saturated conditions increase with a decrease in the voxel resolution for all the stacks. Under dry conditions, it was found that applying a coarsening factor of two and four results in an overestimation of the formation factors of at most 4.35% and 22% respectively, for all three cases. Every level of coarsening reduces the computation time by a factor of approximately 10 from the original image computation time of about 25,000 seconds.

For the partially saturated GDL, the local saturation in the three stacks was different from the average saturation of the entire GDL due to the stacks being extracted from different locations of the full GDL microstructure. Stack 1 had the highest local saturation of 62.52% which led to a significant decrease in the formation factor. For the partially saturated Stack 1, the 2X and 4X coarsening led to an average of error of 9% and 33% respectively, in the in-plane formation factor. The through-plane (z) formation factor for Stack 1 was extremely low (order of 10^{-4}) thereby the coarsening led to extremely high errors of 80-360%. For Stack 2 and Stack 3 the local saturations were 17.46% and 44.88% respectively. The coarsening for Stack 2 and Stack 3 showed a similar trend to the dry formation factors. Therefore, the coarsening factor of 2X, used in Section 3.4.1, was deemed to be acceptable as it resulted in less than 7% error in the formation factor except for near saturation threshold value. The relatively low error in the effective diffusivity due to coarsening also indicates that the μ-CT images for the GDL could be imaged with a higher pixel dimension without loss of accuracy for transport studies.

Table 3.1 – Formation factors (F) and relative errors for Stack 1 at different coarsening factors under dry and partially saturated (s_{global}=46.79%) conditions. ε^{eff} is the effective porosity.

Coarsening factor	Voxel resolution [μm]	s=0%							s_{global}=46.79%, s_{local}=62.52%						
		ε^{eff}	F			Error [%]			ε^{eff}	F [$\times 10^{-2}$]			Error [%]		
			x	y	z	x	y	z		x	y	z	x	y	z
None	1.33	0.659	0.43	0.45	0.24				0.247	5.44	3.73	0.04			
2X	2.66	0.659	0.44	0.45	0.25	2.23	1.67	4.35	0.247	5.88	4.10	0.08	8.08	9.93	80.42
4X	5.32	0.659	0.47	0.48	0.28	9.40	7.62	19.22	0.247	7.05	5.09	0.20	29.59	36.54	361.2

Table 3.2 – Formation factors (F) and relative errors for Stack 2 at different coarsening factors under dry and partially saturated (s_{global}=46.79%) conditions. ε^{eff} is the effective porosity.

Coarsening factor	Voxel resolution [μm]	s=0%							s_{global}=46.79%, s_{local}=17.46%						
		ε^{eff}	F			Error [%]			ε^{eff}	F [$\times 10^{-2}$]			Error [%]		
			x	y	z	x	y	z		x	y	z	x	y	z
None	1.33	0.670	0.43	0.45	0.24				0.553	0.28	0.25	0.11			
2X	2.66	0.670	0.44	0.45	0.25	2.23	1.67	4.35	0.553	0.29	0.27	0.12	3.48	6.63	4.96
4X	5.32	0.670	0.47	0.48	0.28	9.40	7.62	19.22	0.553	0.32	0.30	0.14	12.94	21.24	25.82

Table 3.3 – Formation factors (F) and relative errors for Stack 3 at different coarsening factors under dry and partially saturated (s_{global}=46.79%) conditions. ε^{eff} is the effective porosity.

Coarsening factor	Voxel resolution [μm]	s=0%							s_{global}=46.79%, s_{local}=44.88%						
		ε^{eff}	F			Error [%]			ε^{eff}	F [$\times 10^{-2}$]			Error [%]		
			x	y	z	x	y	z		x	y	z	x	y	z
None	1.33	0.644	0.39	0.39	0.18				0.355	1.54	0.45	0.37			
2X	2.66	0.644	0.40	0.39	0.18	2.55	1.46	4.29	0.355	1.58	0.47	0.39	2.82	3.47	4.59
4X	5.32	0.644	0.43	0.42	0.22	9.37	8.27	22.62	0.355	1.76	0.56	0.50	14.23	24.95	34.62

3.5 Summary

The cluster based full morphology algorithm developed by the author was used to simulate water intrusion in μ-CT reconstruction of a Toray TGP-H-120 GDL with 10% PTFE content. The simulated water distributions were compared to μ-CT images of the GDL at different saturations using three metrics, namely, capillary pressure-saturation curve, liquid water distributions and effective diffusivity. Comparison of the capillary pressure-saturation curves between the μ-CT images and CFM simulations showed that the shape of the capillary pressure-saturation curve was similar to the previously reported literature data for the same sample. A parametric study for the contact angle showed that an increase in the contact angle shifted the curve forward on the capillary pressure axis while the water distributions at the same saturation were unaffected. Any disagreement in the capillary pressure-saturation curve might be attributed to either the limitations of the FM approach, which relies on spherical pores, or issues with the experimental setup. A very good agreement between the capillary pressure-saturation curves from FM and μ-CT images was shown by Agaesse et al. [176] using a similar approach. Therefore, numerical study on multiple datasets is required to identify the reasons for this deviation and improve the CFM model.

A one-to-one comparison of the water distributions at similar saturations between the μ-CT images and CFM simulations showed good agreement, with more than 56% of the liquid water voxels at identical locations for saturations between 29-100%. At lower saturation the agreement was lower. Agreement at lower saturations is also needed as saturations of 8-25% are expected in GDL materials during fuel cell operation [167, 168, 262]. A major difference between the CFM and μ-CT water distributions, was the appearance of small, discrete liquid water clusters in the CFM simulations compared to the larger water clusters in the μ-CT images. This was partly due to the sphere fitting algorithm used for the study which fitted smaller spheres near the GDL fibers. Further improvement of the numerically predicted water distributions would require knowledge of the wettability and contact angles for the local pore walls as well as development of better algorithms to characterize the pore sizes. Although this information is difficult to obtain for the commonly used GDL materials, it might be available for radiation grafted GDLs [263] where controlled HI and HO regions can be engineered within GDLs.

Gas transport was studied on the dry and partially saturated GDLs using Fick's second law. The effective diffusivity values computed for the dry GDL sample were found to be in good agreement with previously reported experimental data in literature. For the wet effective diffusivity values, the CFM predicted liquid water distributions were sufficient to

predict the in-plane effective diffusivity values with less than 20% error for saturations below 40%. The significant drop in the in-plane effective diffusivity values for the μ-CT images at saturations greater than 40% was attributed to the high local saturation variations observed in the in-plane direction, which create bottlenecks in the percolating gas network and eventually lead to the loss of a percolating gas network. The reason for high local saturations observed in the μ-CT images is likely a lower contact angle in some regions which was not accounted for in the CFM simulations where the contact angle was considered uniform. The through-plane effective diffusivities were similar for both the CFM and μ-CT simulations which was likely due to a better agreement in the local saturation profiles in the through-plane direction. The predicted in-plane diffusivities also agreed well with literature data while the predicted through-plane diffusivities were underestimated by a factor of 2 compared to the experimental data. This discrepancy was attributed to the differences in the predicted saturation distributions and material variability which was difficult to analyze in the current study due to only one 3D reconstruction available for the GDL.

Chapter 4

Analysis of gas transport in CLs[†]

In this chapter, the statistical analysis tools and numerical models are used to study the effect of porosity and liquid water saturation on the gas transport in CLs is discussed. Section 4.1 discusses the CL reconstructions using focused ion beam-scanning electron microscopy (FIBSEM) and stochastic reconstructions. Stochastic reconstructions with varying porosities were generated using the reconstruction algorithm described in Section 2.1.2. Section 4.2 discusses the comparison of the statistical functions of the stochastic reconstructions to the corresponding functions from a CL reconstruction obtained using FIBSEM. This analysis was used to determine the parameters for the reconstruction algorithm. The effect of porosity on effective gas diffusivity of the CL is presented in Section 4.3. Section 4.4 shows the variation of the effective diffusivity as a function of local saturation in the CL for a range of porosities. The parametric study is used to develop a correlation to predict the effective diffusivity of the CL as a function of the porosity and saturation.

4.1 Catalyst layer reconstruction

A thin, low-loading inkjet printed CL with a Pt loading of 0.025 mg/cm^2 and ionomer loading of 30% by weight was imaged using FIBSEM. The fabrication method has been described in detail by Shukla et al. [38]. The detailed procedure for the FIBSEM has been described by Sabharwal et al. [51]. The raw FIBSEM images were aligned using the registration algorithm described in Section 2.1.1.1. The aligned images were enhanced using applying contrast limited adaptive histogram equalization [230] followed by Gaussian blurring [231]. The improved images were then segmented using the Sauvola algorithm [94] with a 3D neigh-

[†]Parts of this chapter have been published in:
1. M. Sabharwal, L.M. Pant, A. Putz, D. Susac, J. Jankovic, and M. Secanell, *Fuel Cells* 16(6), 2016
2. M. Sabharwal, L.M. Pant, N. Patel, and M. Secanell, *Journal of The Electrochemical Society* 166 (7), 2019

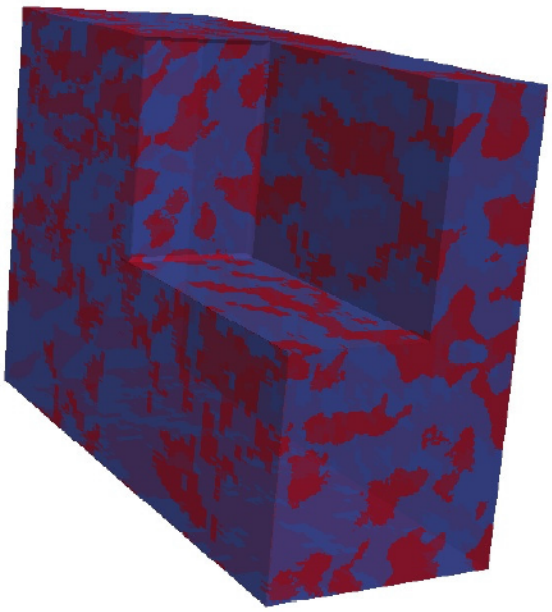

Figure 4.1 – 3-D reconstruction of the solid-pore network from the FIBSEM imaging of the Inkjet CL (the pore and solid networks are shown in red and blue, respectively).

borhood described in Section 2.1.1.2. The FIBSEM reconstructed CL had dimensions of 848 nm × 447 nm × 1220 nm (424 × 176 × 61 pixels) and a porosity of 39.7%. Figure 4.1 shows the 3D microstructure of the FIBSEM reconstructed CL with the pores being red and solid in blue.

The overlapping sphere based algorithm described in Section 2.1.2 was used to generate multiple stochastic reconstructions to study the gas diffusivity as a function of porosity and saturation. However, it is important to determine the statistical equivalence of the stochastic reconstructions compared to the structure of a real CL. Statistical correlation functions such as pore size distribution, two-point correlation function in the void phase ($S_2^v(r)$) and chord length function in the void phase ($C^v(r)$) were used as parameters to quantify the representativeness of the stochastic reconstructions compared to the real CL microstructure obtained from FIBSEM.

For the comparison, stochastic reconstructions with a porosity of 40% similar to the porosity of 39.7% from the FIBSEM microstructure were used. A domain size of 600 nm × 600 nm × 600 nm with a voxel resolution of 2 nm in every direction was used. The domain size was calculated based on the findings by Sabharwal et al. [51] where a domain size of nearly 500 nm in every direction was found to provide a representative elementary volume for gas transport. Since the particle radius for the spherical particles used to generate the

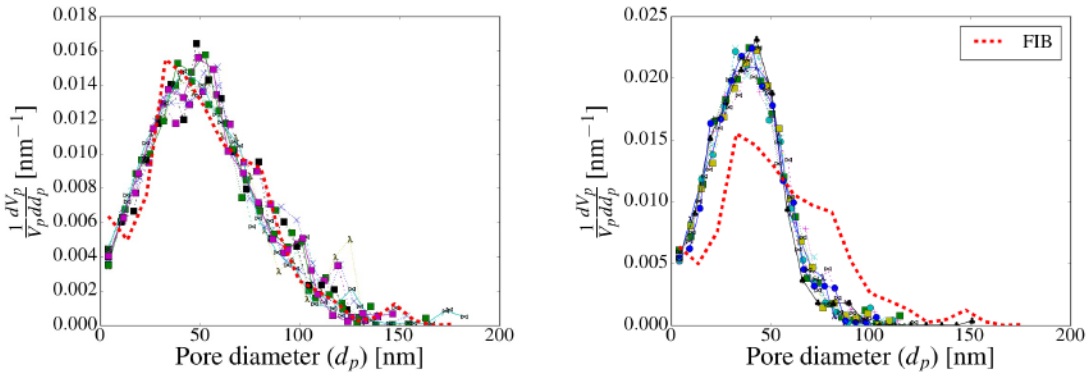

(a) (b)

Figure 4.2 – Pore size distribution for 10 reconstructions with $r_d = 40$ nm and a) $\psi = 1$, and b) $\psi = 0.3$.

stochastic reconstructions was not known, a parametric study was performed on the spherical particle radius to determine the value that would better represent the real CL structure. The spherical particle radius was varied between 20-50 nm (10-25 voxels), based on the reported size of a primary carbon particle [264] and 10 reconstructions were generated for each set of parameters to ensure statistical significance of the results. In the current study, the particle size for each reconstruction was considered constant even though in reality the carbon particles would have a particle size distribution [264]. The effect of multiple particle sizes will be evaluated in a future study. For this study, the penetration parameter (ψ) was set to 1 allowing free penetration of the spheres so that only the particle radius was the unknown parameter. Figure 4.2 shows the effect of ψ for the 10 reconstructions with $r_d = 40$ nm. Limiting the degree of penetration, i.e., reducing the amount of overlap permitted between spheres, results in a decrease in the pore sizes as shown by the narrowing of the PSD curve. Further, the mean pore radius decreases from 26.6 nm to 19.3 nm when ψ is changed from 1 to 0.3. A detailed study on the effect of ψ on the microstructure of the CL will be performed in a future study.

Stochastic reconstructions with r_d of 20 nm, 30 nm, 40 nm and 50 nm and $\psi = 1$ were generated with porosity of 0.4. For each case, 10 stochastic reconstructions were performed to gauge the statistical significance of the results. Statistical functions were computed for each of the reconstructions with different r_d values and compared to those obtained from the FIBSEM dataset.

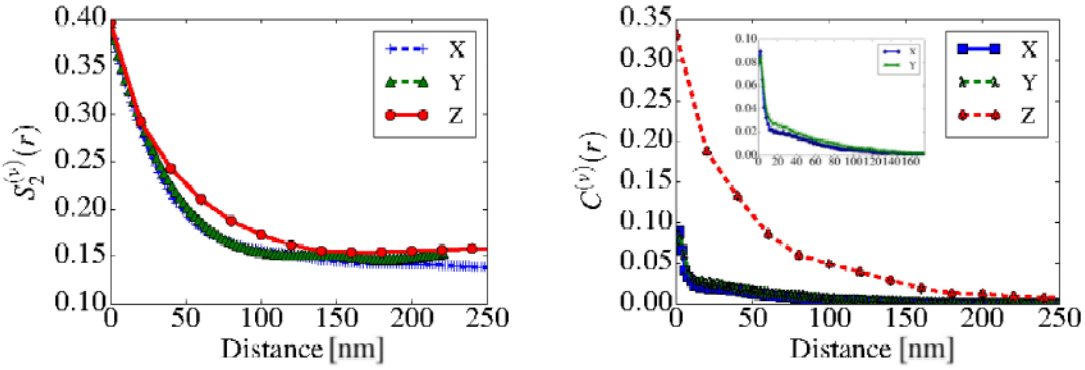

(a) (b)

Figure 4.3 – a) Two-point correlation function, and b) chord length function for the pore phase in the x, y and z direction for the FIBSEM CL reconstruction.

4.2 Statistical analysis of CLs

Figure 4.3a shows the two-point correlation function in the x, y and z directions for the pore space in the FIBSEM CL reconstruction. The two-point correlation functions are equal to the porosity of the sample at a distance of zero and stabilize to a value of ϵ_V^2 at very large distances. The correlation function has nearly identical values in the x and y direction but significantly different values in the z direction. The specific interface area (area per unit volume) can be estimated by the slope of the two-point correlation function. Table 4.1 shows the specific interface area for FIBSEM CL reconstruction. The specific areas are computed for each plane separately, and then summed together to obtain the total interface area. The specific surface area in the xz and yz planes are much higher than that in the xy plane.

Figure 4.3b shows the chord length functions in the x, y and z directions for the pore phase in the FIBSEM CL reconstruction. The chord length function provides an indication of pore size, even though the chord length sizes are higher than the pore sizes because the chords in this case are only traced along coordinate lines instead of in all directions. Figure 4.3b (inset) shows that the chord length function is different in the x and y direction. The function has higher values in the y direction for chord lengths in the range of 0-100 nm, indicating anisotropy between the in-plane (x) direction and through-plane (y) direction. As with the two-point correlation function the chord length function in the z direction is different than in the x and y direction. The chord length function in the z direction has a significant probability of finding chords upto 220 nm whereas the value becomes almost zero for chords of length 160 nm in the x and y direction. Table 4.1 shows the mean chord length

for the FIBSEM reconstruction estimated using Equation (2.3).

The statistical analysis of the binarized FIBSEM reconstruction shows significant anisotropy in the z direction for all computed statistical functions as well as some anisotropy between the x and y direction for the chord length function. The anisotropy in the x and y direction indicates possible changes in the pore morphology due to the evaporation process and the layer-by-layer deposition method. This will be further evident when analyzing the effective diffusivities. The anisotropy between x and z directions could be either due to the morphology of the pores or due to the reduced resolution in the z direction, i.e., FIB slicing direction. Since x and z directions are both in the plane of the catalyst layer, it seems unlikely that the CL morphology would be significantly different in these two directions. The discrepancy in the statistical functions is therefore most likely due to the lower resolution, i.e., 20 nm, in the z direction as compared to the resolution of approximately 2 nm in the x and y directions. The reduced resolution results in a loss of information about the sample that is milled away by the FIB, and better imaging or reconstruction methods are needed to correct for this lack of resolution. Given the artificial anisotropy in the z direction due to the imaging technique only the x and y directions statistical functions are used as reference for comparison with the statistical functions from the stochastic reconstructions.

Figure 4.4a-d shows a stochastic reconstruction with 40% porosity using particles with a radius of 20 nm, 30 nm, 40 nm and 50 nm respectively as well as the local pore size. The local pore radius is computed using the pore size distribution algorithm described in Section 2.2.4 and is used to account for Knudsen effects in the gas diffusion simulations. Figure 4.5 shows the pore size distribution (PSD) for the stochastic reconstructions. Since Figure 4.5 shows the pore size distribution as a probability distribution function, the area under the curve for the four figures is 1. For all the cases, the smallest pore size is determined by the voxel resolution, i.e., 2 nm. The largest pore radius increases with an increase in the particle size. For the reconstructions shown in Figure 4.4, the largest pore radius increases from 38 nm to 55, 67 and 90 nm as the particle radius is increased from 20 nm to 50 nm. The increase in pore size becomes more evident when analyzing the pore size distribution for the 10 different reconstructions for each of the particle sizes. Further, the probability of finding pores larger than 100 nm in diameter is 0 for particle radius of 20 nm but increases to 1%, 7% and 20% for increasing particle radius.

The red dashed line in Figure 4.5 shows the pore size distribution of the reference CL reconstruction obtained using FIBSEM. It can be seen from Figure 4.5 that the stochastic reconstructions with particle sizes of 20 nm and 30 nm overpredict the fraction of small pore

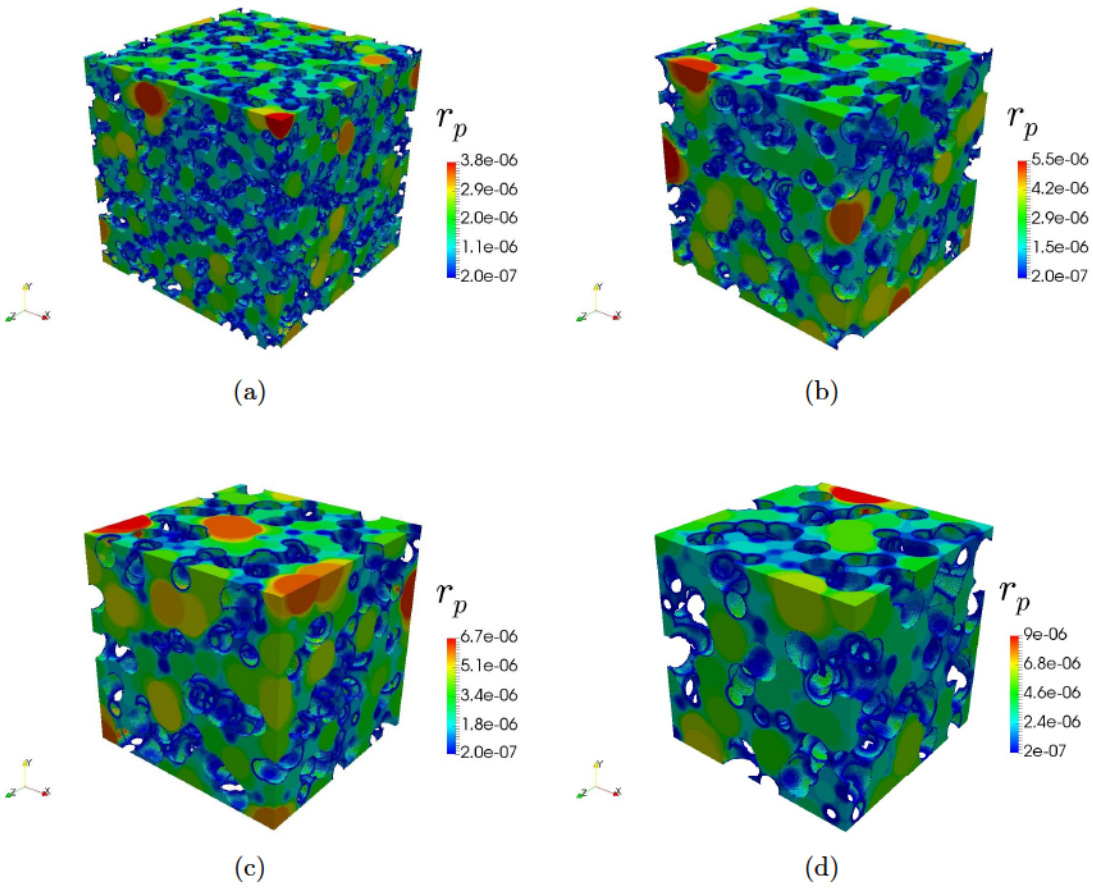

Figure 4.4 – Pore phase of one of the CL reconstructions with a porosity of 40% with spherical particle radius of a) 20 nm, b) 30 nm, c) 40 nm and d) 50 nm. The pores are colored according to their radius in cm.

sizes compared to the FIBSEM reconstruction. Stochastic reconstructions with particle size 40 nm show similar pore size distributions to that of the FIBSEM reconstructions. They even show some of the extremely large pores with diameter greater than 150 nm. With a further increase in the particle radius to 50 nm, the pore sizes become much larger than those observed in the FIBSEM reconstructions with some pores becoming as large as 230 nm in diameter.

Figure 4.6 shows the two-point correlation function in the void phase ($S_2^v(r)$) in the x and y directions for stochastic reconstructions with spherical particle radius of 20 nm to 50 nm. The red dashed line in Figures 4.6a-h shows the two-point correlation the FIBSEM microstructure. The two-point correlations in the x and y directions for reconstructions with particle size of 40 nm are similar to those obtained from the FIBSEM microstructure in the x and y direction. For reconstructions with particle radius of 20 nm and 30 nm, the

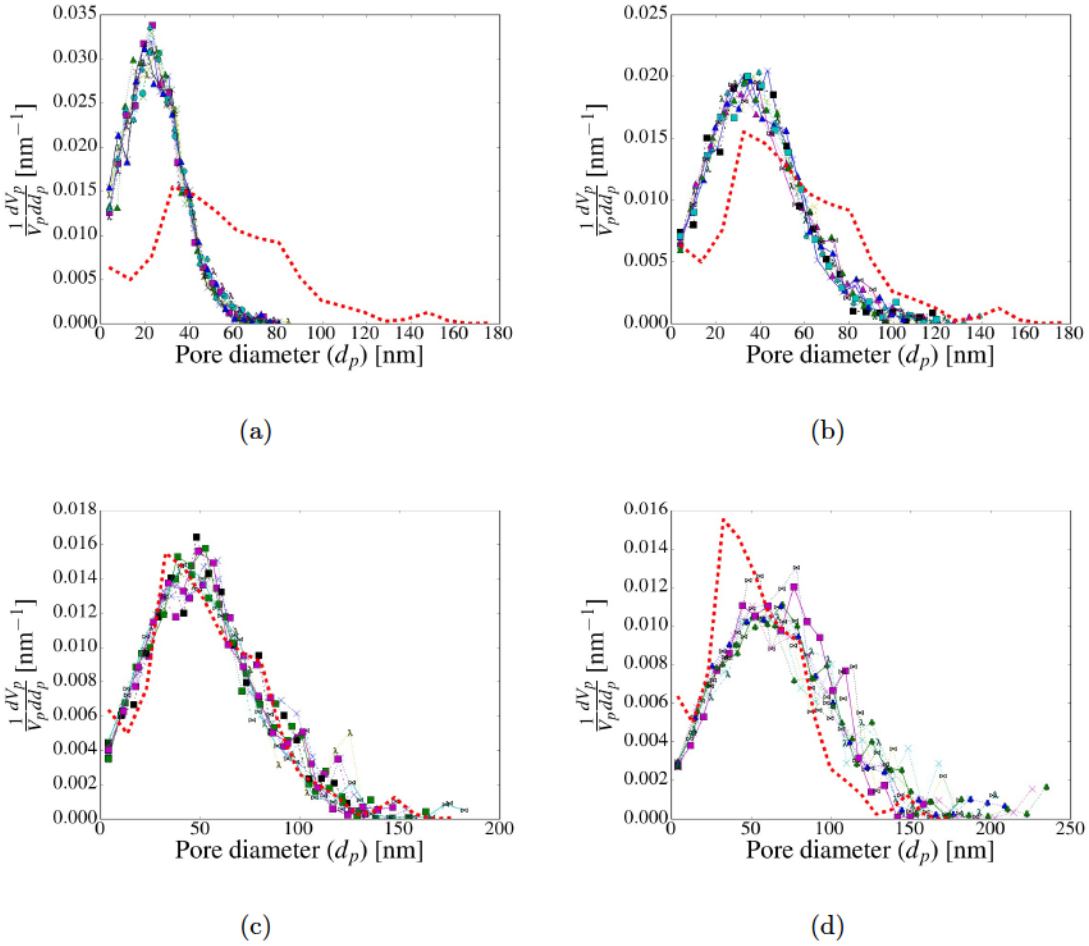

Figure 4.5 – Pore size distribution for stochastic reconstructions with spherical particle radius of a) 20 nm, b) 30 nm, c) 40 nm and d) 50 nm. V_p is the pore volume and d_p is the pore diameter. The red dashed line is the pore size distribution obtained from the reference FIBSEM CL reconstruction.

two-point correlation function is underpredicted for $r < 100$ nm. For reconstructions with particle radius of 50 nm, the two-point correlation shows slightly higher values in the x direction but similar values in the y direction. It must be noted that the two-point correlation function in the z direction is not used for comparison because of the artificial anisotropy of the FIBSEM microstructure in the FIB slicing direction. Due to a lower resolution of nearly 20 nm in the FIB slicing direction (z) there is loss of information in the z direction of the CL microstructure which results in the artificial anisotropy. This has been discussed in detail by Sabharwal et al. [51].

As discussed in Section 2.2.1, the slope of the two-point correlation function at $r = 0$ is proportional to the interfacial area between the solid and pores. From Figures 4.6a-d, it can be seen that the slopes of the stochastic reconstructions with particle radius of 20 nm and 30 nm are steeper than the FIBSEM reconstruction. This indicates that the specific interfacial area between the solid and void phase for these reconstructions would be higher than that observed in the FIBSEM reconstruction. However, the slope of the two-point correlation function for reconstructions with particle radius of 40 nm are very similar to those from the FIBSEM reconstructions as seen from Figures 4.6e and 4.6f. The slope of the two-point correlation function for reconstructions with particle radius of 50 nm appears lower than the slope of the FIBSEM. The average specific interfacial area for the 10 reconstructions for each particle radius are shown in Table 4.1. The stochastic reconstructions with particle radius of 20 nm and 30 nm overestimate the total specific interfacial area by 88% and 24% respectively. This can be explained by the higher fraction of smaller pores in these reconstructions compared to the FIBSEM reconstruction. The average total specific interfacial area for stochastic reconstructions with particle radius of 40 nm is much closer to the FIBSEM reconstruction with a difference of only 7%. With a further increase in the particle radius to 50 nm, the average total specific interfacial area decreases further due to increase in the pore sizes as shown in Figure 4.5.

Figure 4.7 shows the chord length function in the void phase ($C^v(r)$) for stochastic reconstructions with particle radius of 20 to 50 nm. The chord length function for stochastic reconstructions with particle radius of 40 and 50 nm closely resembles the functions from the FIBSEM data. For stochastic reconstructions with particle radius of 20 and 30 nm, the chord length function has a higher value for smaller r compared to the FIBSEM data. Table 4.1 shows the average mean chord length (λ) for the reconstructions calculated using Equation (2.3). The mean chord length for the reconstructions with particle radius of 40 nm are nearly identical to those from the FIBSEM whereas the mean chord lengths for the reconstructions with r_d of 20 and 30 nm are significantly smaller. Although the chord

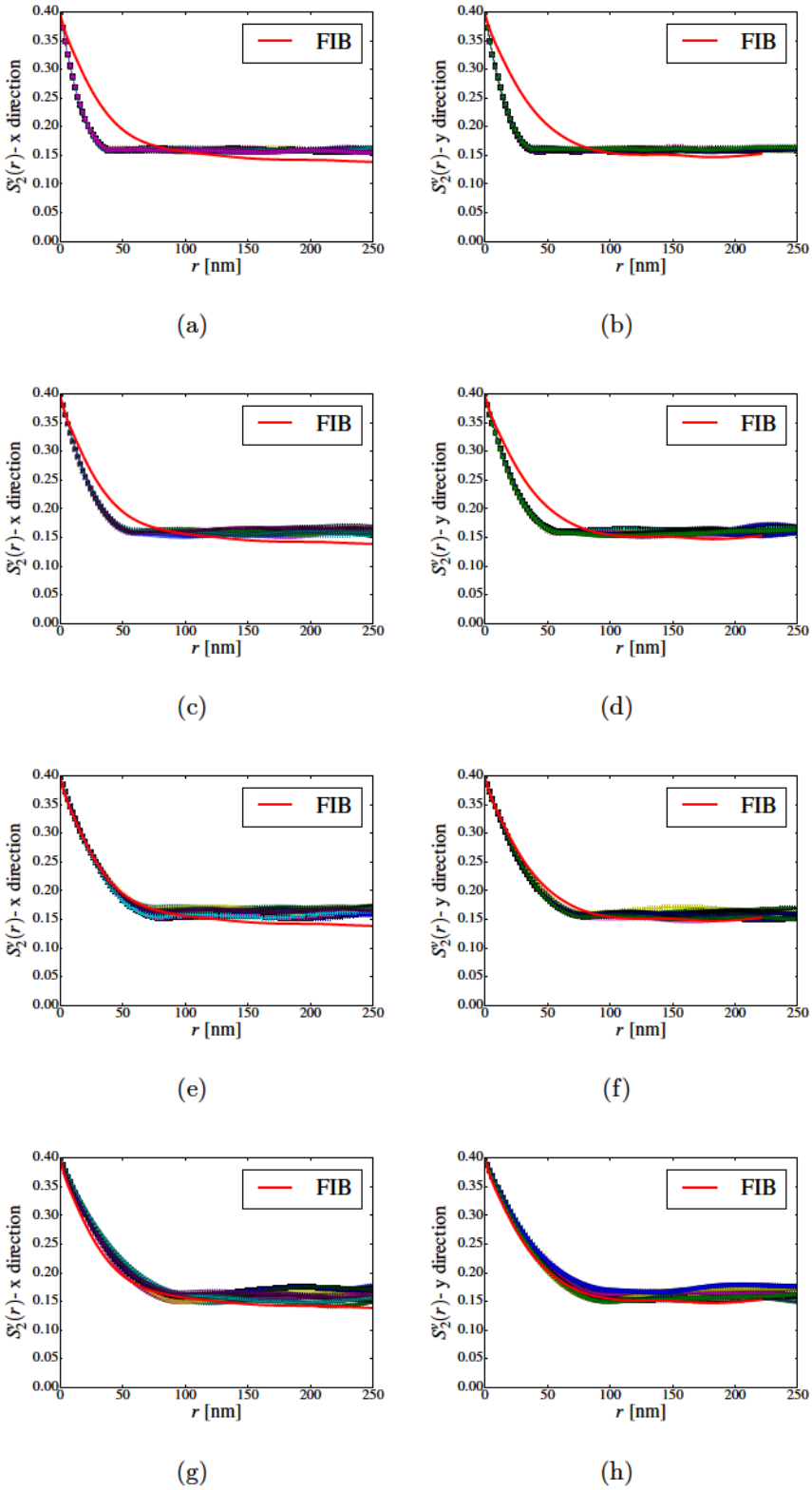

Figure 4.6 – Two-point correlation in the void phase in: a) x and b) y direction for stochastic reconstructions with particle radius of 20 nm; c) x and d) y direction for stochastic reconstructions with particle radius of 30 nm; e) x and f) y direction for stochastic reconstructions with particle radius of 40 nm; g) x and h) y direction for stochastic reconstructions with particle radius of 50 nm

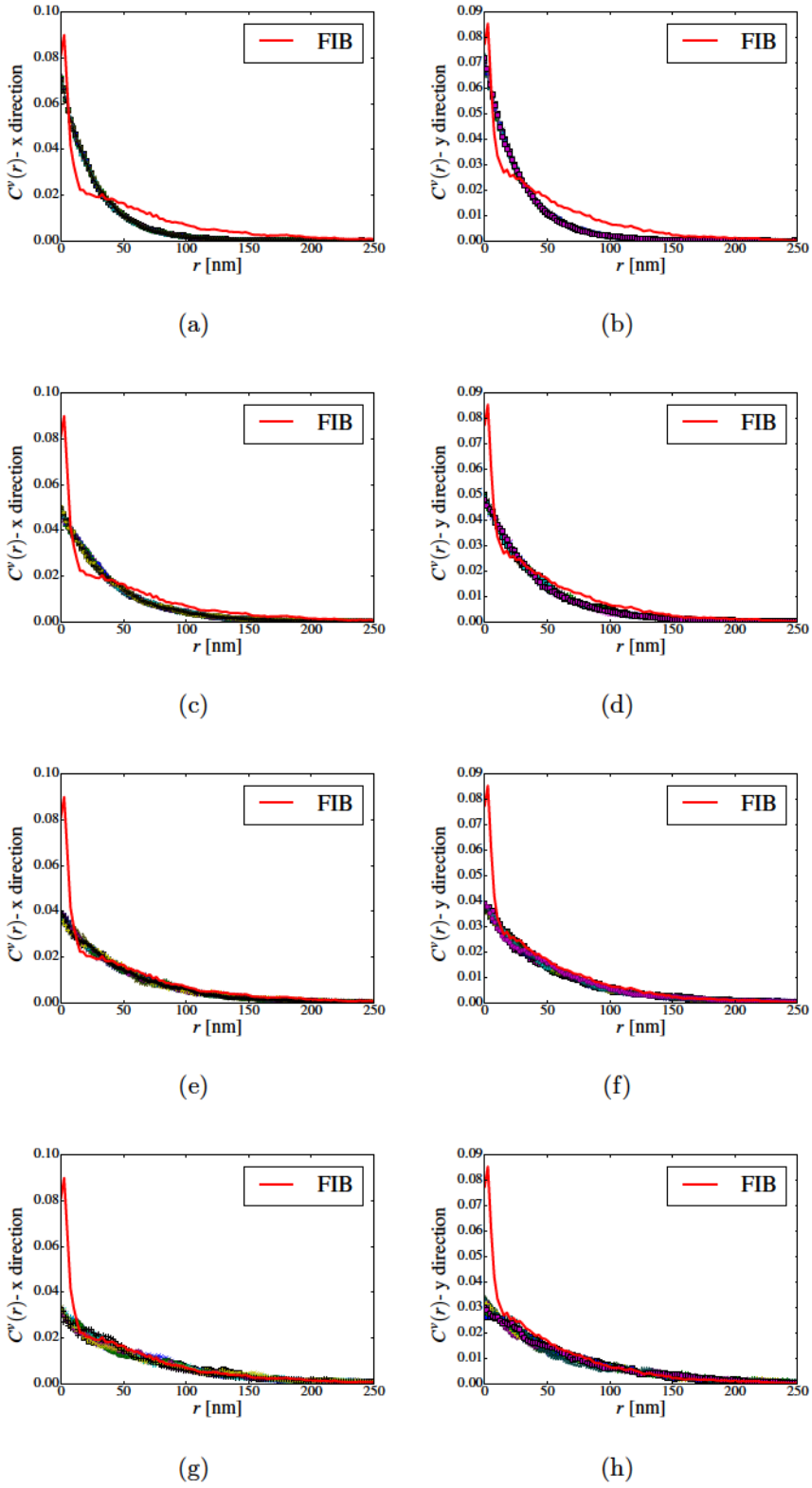

Figure 4.7 – Chord length function in the void phase in: a) x and b) y direction for stochastic reconstructions with particle radius of 20 nm; c) x and d) y direction for stochastic reconstructions with particle radius of 30 nm; e) x and f) y direction for stochastic reconstructions with particle radius of 40 nm; g) x and h) y direction for stochastic reconstructions with particle radius of 50 nm

Table 4.1 – Average specific solid-void interface area and the mean chord length for the stochastic reconstructions with different particle radius (r_d) and FIBSEM reconstruction.

Case	Specific interface area ($m^2/m^3 \times 10^{-6}$)				Mean chord length (nm)
	xy	yz	zx	Total	
FIBSEM	10.30	16.91	14.64	41.85	54.0
$r_d = 20$ nm	26.26	26.26	26.25	78.76	28.3
$r_d = 30$ nm	17.29	17.33	17.28	51.90	41.3
$r_d = 40$ nm	12.96	12.94	12.98	38.88	53.2
$r_d = 50$ nm	10.18	10.13	10.16	30.47	65.6

length function appears to be similar between the reconstructions with particle radius of 50 nm and the FIBSEM reconstruction, the mean chord length for this case is 65.6 nm which is nearly 20% higher than the mean chord length of the FIBSEM data. This is likely due to a higher probability of the longer chords due to the larger pore sizes as seen in Figure 4.5d.

The correlation functions and pore size distributions for the different stochastic reconstructions with the same particle radius are also similar thereby, indicating that the reconstructions can be considered as REVs. Comparison of the statistical functions of the stochastic reconstructions to those obtained from the FIBSEM reconstructions shows that: a) selecting the appropriate particle size in reconstructions is critical to achieve a statistically equivalent structure to a real CL; and b) in this case, the stochastic reconstructions with particle radius of 40 nm are statistically equivalent to the FIBSEM microstructure of the CL used in this study. Therefore, reconstructions with a particle size of 40 nm are used for analysis of diffusion as a function of porosity and local saturation in the CL.

4.3 CLs gas diffusivity under dry conditions

Gas transport model described in Section 2.3.1 was used to simulate oxygen transport in the CL reconstructions. The primary percolating pore network, i.e., the largest connected pore network which has connectivity to the boundaries, was extracted from these reconstructions and used to generate the meshes. The diffusion of an oxygen-nitrogen mixture is simulated in the pore network of the reconstructions using Equation (2.5) and boundary conditions described in Equation (2.8). The values of $x_{O_2}^{in}$ and $x_{O_2}^{out}$ are chosen as 0.4 and 0.01 for these simulations which are then used to compute the effective diffusion coefficient in the

microstructures. The overall formation factor, F, defined as,

$$F = \frac{D^{eff}}{D^{molecular}}, \tag{4.1}$$

for the FIBSEM reconstruction is 0.021, 0.029 and 0.037 in the x, y and z directions respectively. The effective diffusivity in the z direction is 43% and 22% higher than the values in the x and y direction respectively. The difference in the formation factor values in the in-plane directions (x and z) is likely an artifact due to the lower resolution in the z direction, the slicing direction with a resolution of 20 nm, compared to the 2 and 2.54 nm resolution in x and y directions. Diffusion is a three dimensional process with the structure in all directions influencing the diffusion value, therefore, the true in-plane diffusivity is likely to be between the two values for x and z with the value in the x direction being likely to be more representative based on the higher resolution in this direction, i.e., 2 nm. This result highlights one of the main issues with FIBSEM tomography: a lower resolution in the in-slice direction might lead to artificial anisotropy.

4.3.1 Effect of porosity

To determine a correlation for the effective diffusivity of CLs, the effect of porosity on the effective diffusivity is analyzed. The overlapping sphere based algorithm described in Section 2.1.2 was used to generate multiple reconstructions with varying porosities and r_d = 40 nm. The domain size for each reconstruction was 600 nm × 600 nm × 600 nm with a voxel resolution of 2 nm in every direction. The porosity of the reconstructions was varied between 1-10% in increments of 1% and from 10-100% in increments of 10%. 10 reconstructions were generated for each porosity value to provide statistically significant results. To simulate gas diffusion in the generated stochastic reconstructions the percolating pore network is extracted.

Reconstructions with porosities below 6% did not contain a percolating pore network in at least one or more Cartesian directions. Therefore, a porosity of 5% is chosen as the percolation threshold (ε_{th}), which is the porosity above which a percolating pore network exists. Similarly, it must be noted that the stochastic reconstructions with porosity higher than 70% were found to have no percolating solid network thereby, indicating that such a structure might be infeasible. Therefore, the effective diffusivity was only computed for stochastic reconstructions with porosities upto 70%.

Figure 4.8 shows the pore phase for one of the CL reconstructions with porosity of 7%, 50% and 70%. An increase in porosity leads to an increase in the pore sizes, with the largest

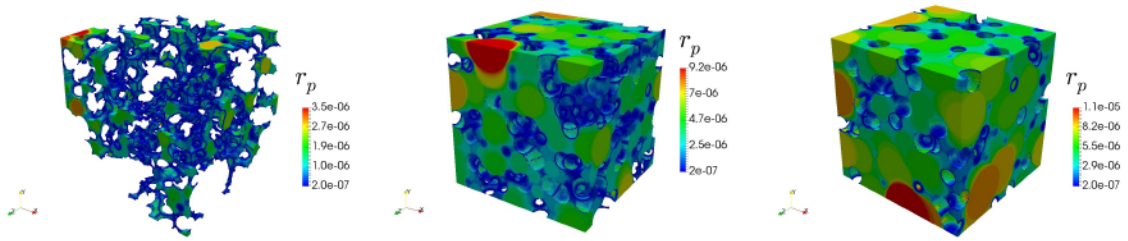

(a) (b) (c)

Figure 4.8 – Pore phase of one of the CL reconstructions with a porosity of a) 7%, b) 50% and c) 70% using a particle radius of 40 nm. The pores are colored according to their radius in cm.

pore radius increasing from 35 nm at a porosity of 7% to 92 nm at a porosity of 50% and 108 nm at a porosity of 70%. Figure 4.9 shows the effective diffusivity in the x, y and z directions as a function of porosity for the different stochastic reconstructions. The effective diffusivities are computed at a temperature of 80°C using molecular oxygen diffusivity of 0.273 cm^2/s. As expected, the effective diffusivity in the Cartesian directions increases with an increase in porosity.

It can be seen from Figure 4.9 that for a given porosity the values of the effective diffusivities in the three directions are nearly identical indicating an isotropic structure. This is expected because the overlapping sphere algorithm is not biased in any direction and the building blocks are spheres which are also isotropic. Further, it can also be seen that the effective diffusivities for the 10 reconstructions with the same porosity show similar effective diffusivities with a standard deviation of less than 3.5% about the mean value. This also ensures that the average diffusivities computed for each porosity using 10 reconstructions is statistically representative.

The results from Figure 4.9 can be used to develop a functional dependence of the effective diffusivity of the CL to its porosity. Macro-scale MEA models [41, 42, 166, 167, 169] rely on such semi-empirical relations to compute the effective diffusivity in the fuel cell porous media. Recently, Zheng and Kim [7] and Shin et al. [8] have proposed a tortuosity model given by Equation (4.2) to estimate the effective diffusivities for the CLs,

$$D^{eff} = \frac{\varepsilon_V}{\tau} D \tag{4.2}$$

where the tortuosity factor (τ) in Equation (4.2) is related to the porosity using a Bruggeman type correlation,

$$\tau = \varepsilon_V^{-\alpha} \tag{4.3}$$

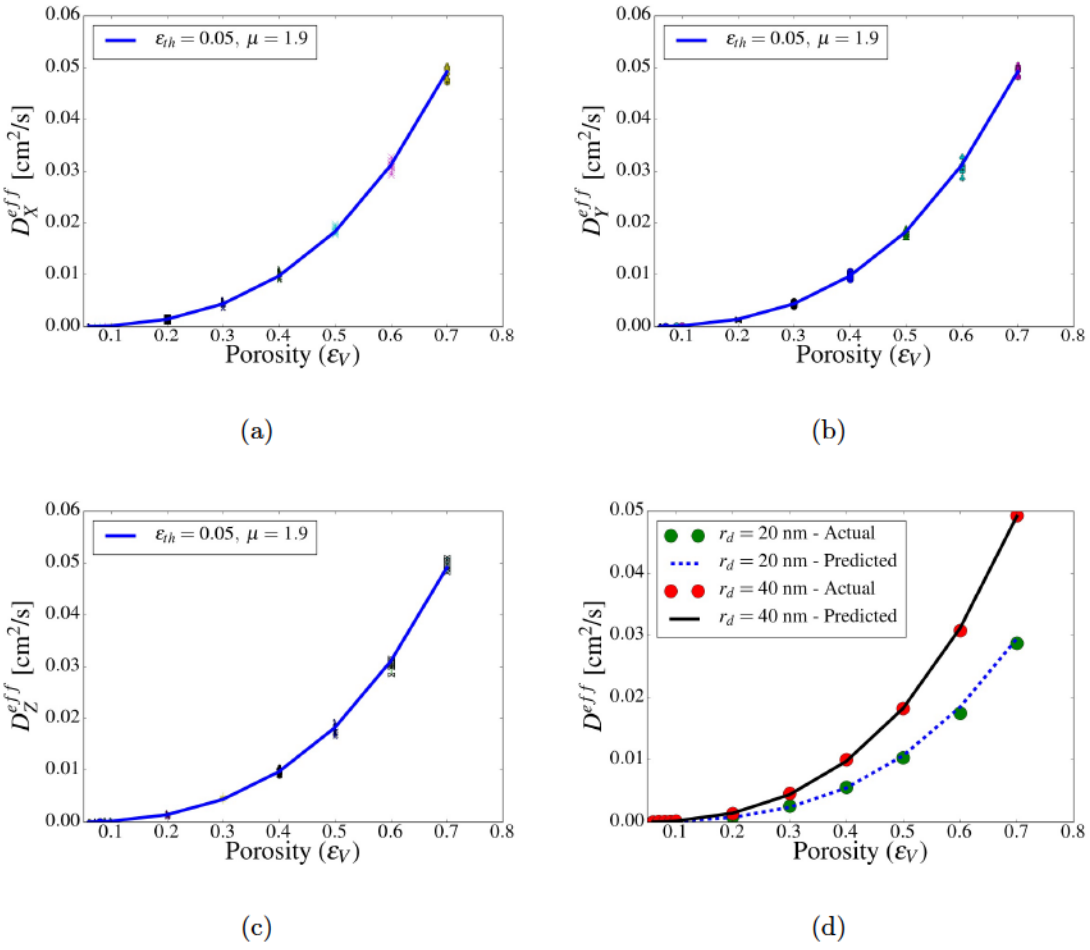

Figure 4.9 – Effective diffusivity in the a) x, b) y and c) z direction as a function of the porosity. d) Average effective diffusivity for r_d = 20 nm and r_d = 40 nm as a function of porosity. The best fit line is estimated based on Equation (4.4) with ε_{th} = 0.05 and μ = 1.90, which is the fitting parameter estimated using least square fit, for the results for reconstructions with r_d = 40 nm.

where α is a fitting parameter which has a value of 0.5 for the Bruggeman correlation. Zheng and Kim [7] computed a value of 0.75 for α and used $D = 1.07D^{molecular}$ to fit the effective diffusivity values. Shin et al. [8] computed the value of α to be 0.746 using the shape of streaklines and used $D = D^{Kn}_{avg}$. However, a common problem with the correlation of the form proposed in Equation (4.2) is the lack of information about the connectivity of the pores, as the porous media will continue to have a non-zero diffusivity even at extremely low porosities. A consequence of this can be found in the optimization study by Secanell et al. [41] where the optimal CL porosity was computed as 2.5%, whereas in reality such low porosities are likely to lead to a loss of percolating pore network.

An alternate correlation to determine the effective diffusivity for the CLs is based on percolation theory [167, 265–267] and given by,

$$D^{eff} = D^{pore}\left(\frac{\varepsilon_V - \varepsilon_{th}}{1 - \varepsilon_{th}}\right)^{\mu}\mathcal{H}(\varepsilon_V - \varepsilon_{th}) \tag{4.4}$$

where ε_{th} is the percolation threshold value and μ is a fitting parameter. The Heaviside step function ($\mathcal{H}(\varepsilon_V - \varepsilon_{th})$) in Equation (4.4) is added to enforce that, for porosities below the percolation threshold, the effective diffusivity is zero because a percolating gas diffusion network would not exist. This is a major distinguishing factor from the Bruggeman correlation and previous correlation functions based on Equation (4.2) such as the work of Zheng and Kim [7] and Shin et al. [8] which could predict non-zero effective diffusivities below the percolation threshold.

The bulk diffusivity (D^{pore}) of the CL in Equation (4.4) is obtained using the Bosanquet approximation given by Equation (2.6) where the average Knudsen diffusion coefficient (D^{Kn}_{avg}) can be computed using Equation (2.7) and the local pore radius (r_p) must be replaced by a mean pore radius (r_{avg}). Equations (4.4) and (2.6) are fitted to the effective diffusivities of the stochastic CL reconstructions shown in Figure 4.9 to estimate exponent (μ).

The statistical reconstruction simulation results can also be used to estimate the fitting parameters in Equation (4.4) and the most appropriate Knudsen mean pore radius. In this case, ε_{th} is estimated by direct analysis of the percolating pore network for the stochastic reconstructions. As mentioned earlier, for porosities below 6% there was loss of percolating pore network in at least one or more Cartesian directions for the reconstructions. Therefore, ε_{th} is chosen to be 0.05 which is the value above which a percolating pore network exists.

To compute the average Knudsen diffusion coefficient (D^{Kn}_{avg}), an average pore radius (r_{avg}) must be computed. The average pore radius is computed as the arithmetic mean of

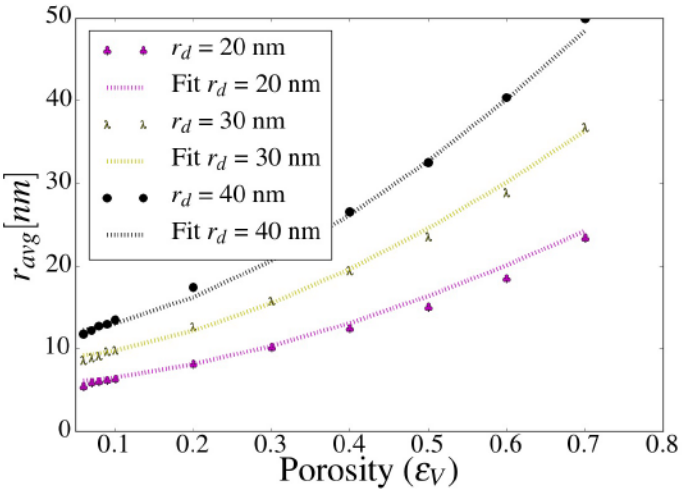

Figure 4.10 – Average Knudsen radius as a function of porosity for stochastic reconstructions with particle radius of 20-40 nm. The dashed lines are the best fit lines for average Knudsen radius as a function of r_d and ε_V.

the pore radii for every pore [4, 7, 8],

$$r_{avg} = \left[\int_i r_i \frac{dX_i}{dr} dr\right] \tag{4.5}$$

where dX_i is the volume fraction of pores having radius r_i. Since the pore radius is directly proportional to the Knudsen diffusivity, this method assumes that the average Knudsen radius is such that it results in an average Knudsen diffusivity equivalent to the effective Knudsen diffusivity obtained when transport through all pores occurs in parallel. Figure 4.10 shows the average Knudsen radius computed using the PSD of the stochastic reconstructions with r_d = 20, 30 and 40 nm and Equation (4.5). As discussed earlier, for porosities below 6% and higher than 70% there is a loss of percolating pore and solid network respectively. Therefore, r_{avg} for these porosities are not shown in Figure 4.10 and not taken into account to determine the best fit curve. The best fit curves in Figure 4.10 were estimated by minimizing the least-square of the difference between r_{avg}.

$$r_{avg} = r_d \left(1.66\varepsilon_V^{1.65} + 0.289\right) \tag{4.6}$$

For the coefficients given in Equation (4.6), the R^2 value for the fit is 0.996.

Once ε_{th} and r_{avg} have been obtained, the value of μ is obtained by minimizing the least-square difference between the results in Figure 4.9 and Equation (4.4) with $\varepsilon_{th} = 0.05$. The optimal value of μ obtained for all the cases is 1.90. The R^2 values for the fit is 0.994 indicating a good fit between the data and Equation (4.4) with $\varepsilon_{th} = 0.05$ and $\mu = 1.90$. In summary,

Equation (4.4) with $\varepsilon_{th} = 0.05$, $\mu = 1.90$ and D^{pore} obtained using Equations (2.6), (2.7) and (4.6) provides an excellent prediction of gas diffusivity for a statistically representative CL structure. Figures 4.9a-c show the best fit for effective diffusivity in the x, y and z directions as a function of porosity. Figure 4.9d shows the best fit line for the average effective diffusivity (D^{eff}) of the reconstructions with $r_d = 40$ nm as a function of porosity.

10 reconstructions with $r_d = 20$ nm and porosities ranging from 0.06-0.7 were generated. The effective diffusivity for these reconstructions was computed as shown in Figure 4.9d. The effective diffusivity for reconstructions with $r_d = 20$ nm are smaller than the reconstructions with $r_d = 40$ nm due to the smaller pore sizes for the former case. This was also shown earlier in Figure 3.7 for reconstructions with a porosity of 0.4. To further assess the validity of the Equations (2.6), (2.7) and (4.6), they were used to predict the effective diffusivity for reconstructions with $r_d = 20$. From Figure 4.9d it is clear that the correlation proposed by Equations (2.6), (2.7) and (4.6) with $\mu = 1.90$ and $\varepsilon_{th} = 0.05$ can accurately predict the dry effective diffusivity even for reconstructions with a different microstructure from those used to develop the correlations.

4.3.2 Comparison to literature

In order to assess the validity of the diffusivities calculated using the stochastic reconstructions and used to derive the correlation function above, the predicted diffusivities in this study are compared to previously reported literature values. To aid in this comparison the formation factor (F) defined in Equation (4.1) is used. The average formation factor value at a given porosity is determined by averaging the effective diffusivities in the three Cartesian directions over the 10 reconstructions. The average formation factor for the stochastic reconstructions at a porosity of 40% (similar to the porosity of 39.7% for the FIBSEM CL) is 0.037 which is similar to the average formation factor of 0.025 ± 0.010 (x and y average and standard deviation) for the reference FIBSEM CL. The standard deviation in the formation factor for the reference FIBSEM CL is computed from the domain size study performed in reference [51]. The z direction values for the FIBSEM reconstruction are not considered due to the artificial anisotropy in the z direction [51].

Figure 4.11 provides a comparison of the obtained average overall formation factors obtained from the stochastic reconstructions to those previously reported in literature [4, 6–10, 51]. Yu et al. [9] measured the effective diffusivities for CLs with platinum supported on amorphous carbon and platinum supported on graphitized carbon with different ionomer

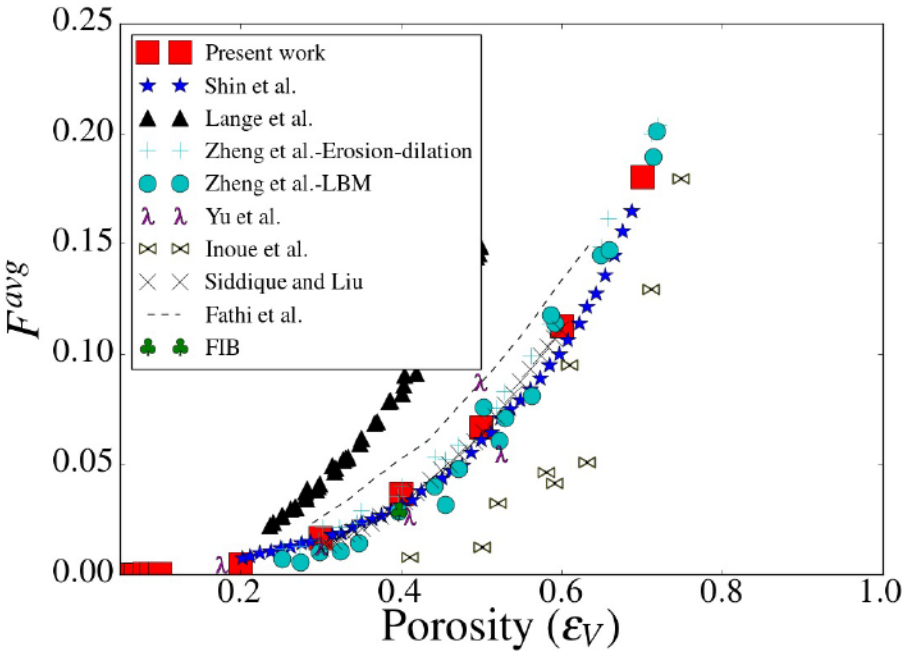

Figure 4.11 – Comparison of average formation factor (F^{avg}) for the stochastic reconstructions based on overlapping spheres with previously published studies in literature. Lange et al. [4], Fathi et al. [5], Siddique and Liu [6], Zheng and Kim [7] and Shin et al. [8] computed the effective diffusivities numerically using stochastic reconstructions for CLs. Yu et al. [9] and Inoue et al. [10] experimentally measured the effective diffusivity of CLs with different ionomer loadings.

to carbon ratios (I/C) ranging from 0.5-1.5. The porosity and pore size distribution was measured using mercury intrusion porosimetry (MIP). The formation factors obtained from the stochastic reconstructions show good agreement with the predicted effective diffusivities with an error of less than 25%. Figures 4.12a-c show the pore size distributions of the stochastic reconstructions with porosities of 0.3-0.5 compared to those measured by Yu et al. [9] for similar porosities. For all porosities, the PSDs from Yu et al. [9] are shifted towards higher pore sizes compared to the stochastic reconstructions. Further, the PSDs from Yu et al. [9] did not consider pore sizes less than 25 nm due to limitations of the equipment. This resulted in the higher probability values for the larger pores compared to the PSDs from the stochastic reconstructions. The discrepancy in the formation factor values is likely due to the different microstructures for the CLs from the two studies as evident from the PSDs.

Inoue et al. [10] measured the effective diffusivity of CL samples with ionomer to carbon ratios of 0.8-1.4. The formation factor values reported by Inoue et al. [10] are 3-4 times smaller than predicted effective diffusivity values from the stochastic reconstructions with porosities in the range of 0.4-0.6. For porosities higher than 0.6, the error reduces to less than 40%. To identify the reason for discrepancy in the formation factor values, the pore size distributions reported by Inoue et al. [10] using N_2 adsorption are analyzed for ionomer to carbon ratio of 1 and 1.3 corresponding to a porosity of 0.5 and 0.6 respectively. Figure 4.12c and 4.12d show the comparison of the PSDs from Inoue et al. [10] to the stochastic reconstructions. For $\varepsilon_V = 0.5$, the PSD from Inoue et al. [10] are similar to the stochastic reconstructions with pore sizes as high as 213 nm. For $\varepsilon_V = 0.6$, the PSD from Inoue et al. [10] shows a higher probability for pore sizes less than 100 nm compared to the stochastic reconstructions, which might lead to a lower effective diffusivity observed by Inoue et al. [10]. Analysis of the two PSDs however, does not provide any conclusive information to explain the high discrepancy between the predicted formation factors in this study and those obtained by Inoue et al. [10]. Further, the formation factor calculations on FIBSEM reconstructions of the CLs performed by Inoue et al. [10] also overpredicted the formation factors by 2 times. Since Inoue et al. [10] did not report any of the statistical functions for their reconstructions it is difficult to ascertain the reason for the overprediction of the diffusivity values by the simulations.

Lange et al. [4] numerically studied the effective diffusivity in stochastic reconstructions generated using overlapping spheres similar to this work. The formation factor values from Lange et al. [4] are much higher than those obtained in this work. This is surprising because the particle diameter used by Lange et al. [4] is 20 nm which is smaller than the one used in this study and the effective diffusivity increases with an increase in particle diameter [4].

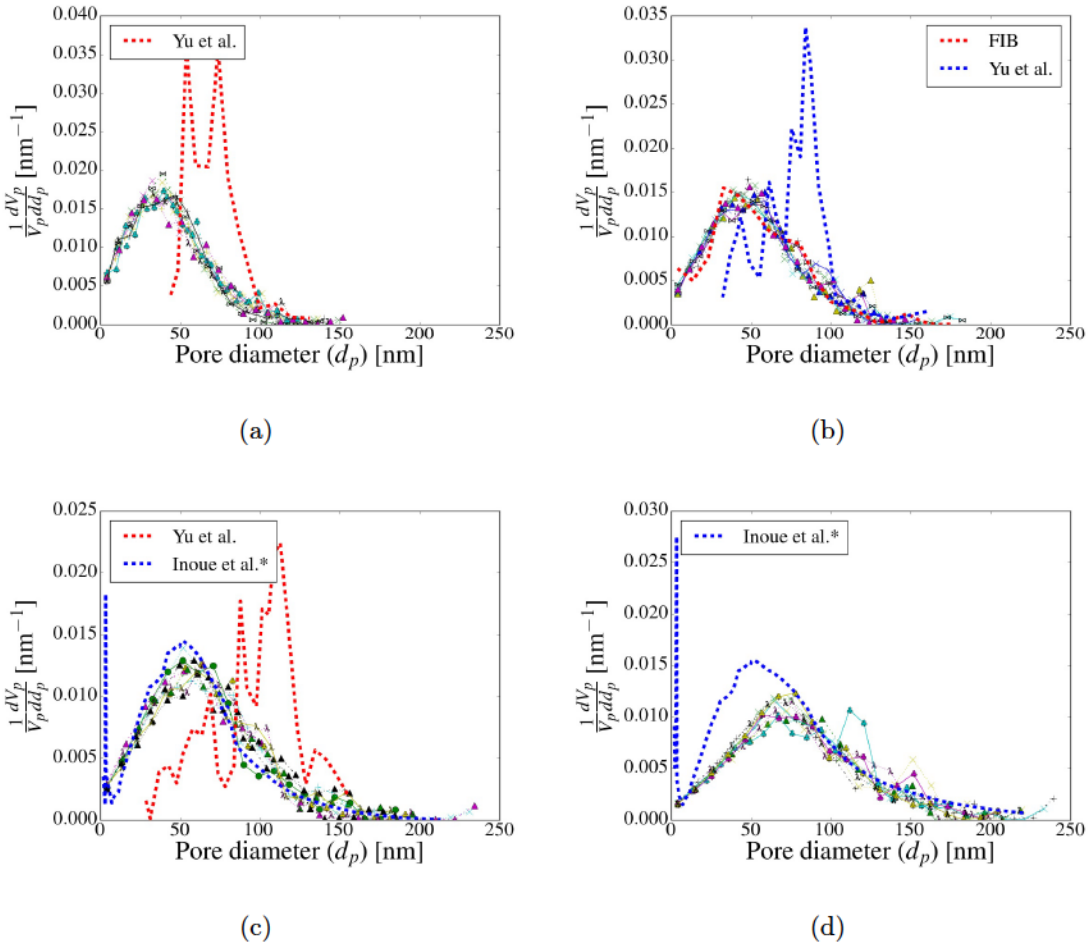

Figure 4.12 – Comparison of PSD of stochastic reconstructions with $r_d = 40$ nm and porosity of a) 0.3, b) 0.4, c) 0.5 and d) 0.6, to experimentally measured PSDs for CLs with different ionomer to carbon ratio [9, 10]. (* Porosity was estimated based on the reported I/C ratio of the samples used for nitrogen adsorption and the reported porosity values for the CLs with the same I/C ratio.)

Further, Lange et al. [4] also accounted for local Knudsen effects similar to this work. The difference between the effective diffusivity values could be attributed to the method used to compute the local Knudsen effects. Lange et al. [4] used an average length in the directions around a pore. This approach underestimates the Knudsen resistance as shown by the Zheng and Kim [7] who compared the approach proposed by Lange et al. [4] to results from erosion-dilation based pore radius (similar to this study) and LBM.

Fathi et al. [5] used an overlapping sphere based stochastic reconstruction, similar to Lange et al. [4] and this study, to study the effective diffusivity as a function of porosity. As seen in Figure 4.11, the diffusivity values obtained by Fathi et al. [5] are higher than those obtained in the present study. This is again due to the underprediction of Knudsen effects due to the use of an average length around the pore similar to Lange et al. [4].

Siddique and Liu [6] used a heuristic pixel based reconstruction method to generate CL reconstructions with different porosities and then performed numerical simulations on the reconstructions to obtain the effective diffusivities. The results from this study are in good agreement with those from Siddique and Liu [6] as shown in Figure 4.11 with a discrepancy of less than 10% for porosities in the range of 0.4-0.6.

Zheng and Kim [7] numerically computed the effective diffusivity for CL microstructures with different porosities generated using a sphere based simulated annealing method. The effective diffusivities by Zheng and Kim [7] were computed using continuum simulations using a local Knudsen resistance with the pore radius computed using morphological image opening, similar to the spherical pore radius used in this study. However, for the continuum simulations they used a mean pore radius to estimate the Knudsen diffusivity and did not account for the local Knudsen resistances. They also used LBM to compute the effective diffusivities of the microstructures. The average formation factor values from the stochastic reconstructions at different porosities in this study are in good agreement with the formation factor results from Zheng and Kim [7] using LBM and erosion-dilation approach with a maximum error less than 10% except for the formation factor computed at a porosity of 30% using the erosion-dilation method where the error is 22%. This comparison also shows the accuracy of continuum models that account for local Knudsen effects is similar to that of LBM while being computationally efficient.

Shin et al. [8] computed the effective diffusion coefficient for randomly generated CL microstructures. Although the formation factor values from Shin et al. [8] are in good agreement with the results from Zheng and Kim [7] and this work, the numerical method

used by Shin et al. [8] is questionable. Firstly, the voxel resolution was set to 20 nm which would ignore the smaller pores in the CL which are seen in the FIBSEM reconstruction [51] as well as experimental PSDs [9, 134, 148]. Coarsening the voxel resolution also leads to an increase in the effective diffusivity value as shown in our previous work [51]. Secondly, the effective diffusivity is computed using,

$$D^{eff} = \frac{\varepsilon_V}{\tau} D^{Kn}_{avg} \tag{4.7}$$

where ϵ_V is the porosity, τ is the tortuosity factor computed from an effective relation between the effective molecular diffusivity to the bulk molecular diffusivity [8] and D^{Kn}_{avg} is the average Knudsen diffusivity computed from a mean pore size. This correlation ignores any effect of the molecular diffusivity which is typically accounted for using the Bosanquet equation [4, 7, 51]. Further, local Knudsen effects are ignored when using a mean pore diameter which would lead to higher diffusivities [4, 7]. This is partially compensated by multiplying the average Knudsen diffusivity by the ratio of $\frac{\varepsilon_V}{\tau}$.

Comparison of the average formation factors from the stochastic reconstructions used in this work to previously reported numerical and experimental data shows that the values are in good agreement. Additionally, the previous numerical studies did not compare the statistical equivalence of the generated microstructures to an actual CL morphology which was done for the stochastic reconstructions used in this study. This provides good confidence in the predicted diffusivity values to develop an effective diffusivity correlation for the CL.

4.4 CLs gas diffusivity under wet conditions

To study the effect of local saturation on the effective diffusivity, liquid water was intruded into the reconstructions using the nucleation based water intrusion method described in Section 2.3.3. The smallest pores, i.e., pores having a radius of 2 nm, were treated as nucleation sites and assumed to be initially filled. The reason for treating these pores as nucleation sites has been explained earlier in Section 2.3.3. Water intrusion was then carried out using the CFM algorithm described in Algorithm 1 with $n = 100$ and a hydrophobic contact angle (θ) of 93° was assumed based on the environment scanning electron microscopy measurements reported in reference [268]. Although a contact angle of 93° was assumed for this study, it was shown in our previous work [154] that the liquid water distribution using the CFM algorithm does not change with contact angle as long as the pore wettability (i.e., hydrophilicity or hydrophobicity) remains the same. The contact angle only changes the value of the capillary pressure required to intrude the pores. The liquid distributions, and hence

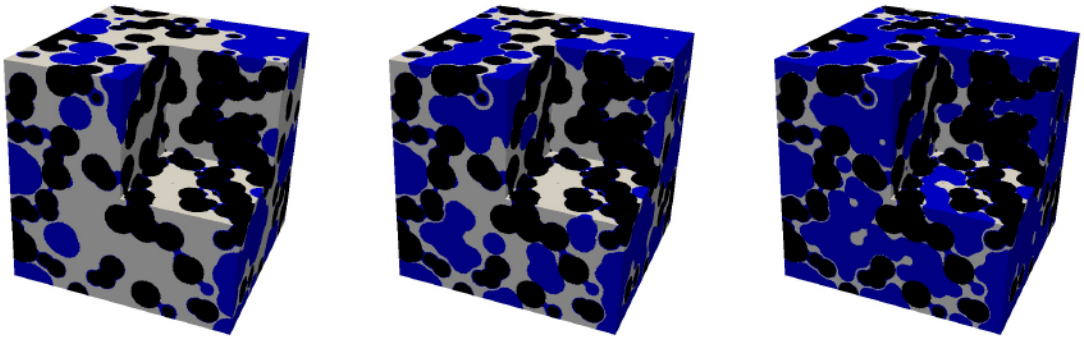

(a) (b) (c)

Figure 4.13 – Liquid water distribution in a partially saturated CL reconstruction with a dry porosity of 50% at a saturation of a) 29.7%, b) 55%, and c) 79.3%. Black is solid phase, white is pore phase and blue is liquid water.

the effective diffusivity at a given saturation, does not change with contact angle. Partially saturated CL reconstructions were recorded at intervals of at least 5% saturation difference. The partially saturated CL reconstructions were then converted to voxel based meshes by direct conversion of voxels to mesh cells. The pores filled with liquid water were assumed to be impervious to gas transport and therefore, considered part of the solid region. The local pore radii were recomputed to account for the change in the Knudsen effects due to liquid water intrusion. The effective pore networks, i.e., pores not flooded with liquid water, were extracted and used for gas transport simulations.

4.4.1 Effect of local saturation

To study the effect of local saturation on the effective diffusivity, stochastic reconstructions with $r_d = 40$ nm and porosities in the range of 0.3-0.6, typical for fuel cell CLs [9, 11], were used. Figure 4.13 shows the liquid water distribution in one of the CL reconstructions with a dry porosity of 0.5 at various saturations.

Figure 4.14 shows the ratio of average wet effective diffusivity to the average dry effective diffusivity for stochastic reconstructions with porosities in the range of 0.3-0.6. As shown earlier for the dry case, the effective diffusivities in the three Cartesian directions were similar therefore, only the average effective diffusivity is shown for the wet case. The wet diffusivity of the CLs decreases with an increase in the saturation as seen in Figures 4.14. Further it can be seen that for a given saturation the ratio of the wet effective diffusivity to the dry effective diffusivity is almost identical for all the stochastic reconstructions irrespective of

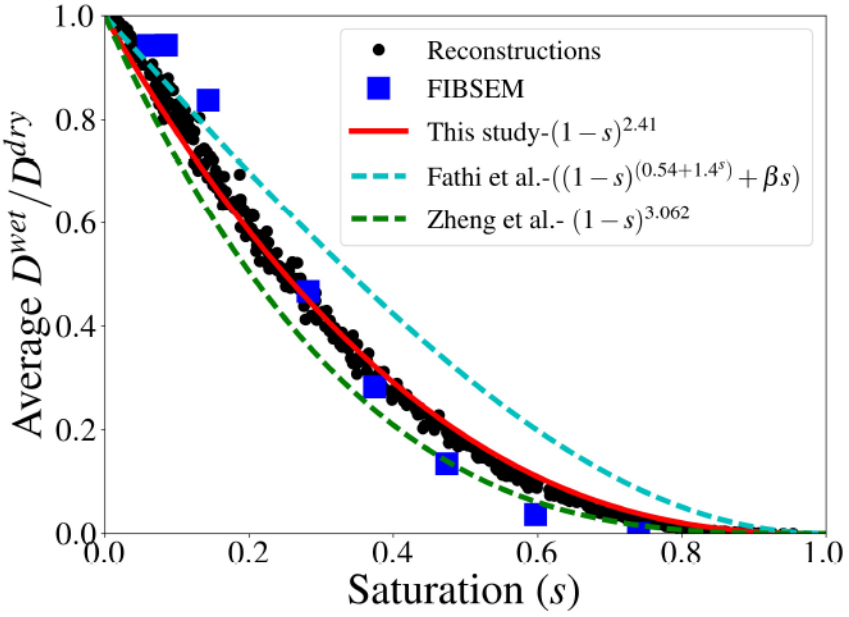

Figure 4.14 – Ratio of the average wet effective diffusivity to the average dry effective diffusivity as a function of saturation. The best fit line is estimated based on Equation (4.8) with a value of exponent γ shown in the graph, which is the fitting parameter estimated using least square fit. Fathi et al. [5] and Zheng and Kim [7] numerically computed the effective diffusivity for partially saturated stochastic CL reconstructions.

their porosity. This indicates that the ratio of the wet effective diffusivity to the dry effective diffusivity is independent of the dry porosity. The predicted effective diffusivities of the partially saturated stochastic CL reconstructions are in good agreement with the average (of x and y) wet diffusivities obtained from the FIBSEM CL reconstruction with a maximum error of 18% for saturations below 45%.

Similar to the dry case, the results in Figure 4.14 can be used to estimate a correlation for the effective diffusivity of partially saturated CLs. A power law is commonly used to describe the ratio of wet effective diffusivity to dry effective diffusivity of fuel cell porous media [2, 5, 7, 55]. Equation (4.8) shows the correlation used to estimate the best fit curve in Figure 4.14, where D_{dry}^{eff} is given by Equation (4.4), s is the saturation and γ is an empirical coefficient estimated by minimizing the least square difference between the results in Figure 4.14 and Equation (4.8),

$$D_{wet}^{eff} = D_{dry}^{eff}\,(1-s)^{\gamma}\,\mathcal{H}(\varepsilon_V(1-s)-\varepsilon_{th}). \tag{4.8}$$

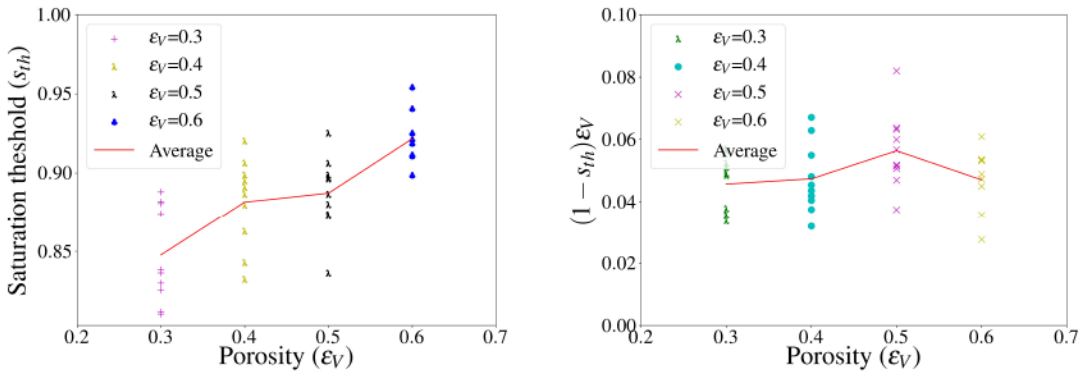

(a) (b)

Figure 4.15 – Variation of a) threshold saturation and b) effective porosity at threshold saturation with porosity for the different stochastic reconstructions.

The optimal value of γ estimated using a non-linear solver is 2.41 which gives a R^2 value of 0.995 for the curve fit. To estimate the functional form of the Heaviside step function in Equation (4.8), the saturation threshold (s_{th}), i.e., the saturation above which a percolating gas network does not exist, is shown in Figure 4.15a. The saturation threshold increases from 0.84 to 0.92 when the porosity increases from 0.3-0.6. Thus, a Heaviside step function of the form $\mathcal{H}(s - s_{th})$ cannot be used as s_{th} depends on the porosity of the CL. However, a plot of the effective porosity at the saturation threshold shown in Figure 4.15b, is nearly constant at 0.047 except for the reconstructions with $\varepsilon_V = 0.5$, which is slightly higher at 0.056 due to outliers. Therefore, the functional form of the Heaviside step function shown in Equation (4.8) is appropriate as it accounts for the loss of the percolating gas network with an increase in saturation with the percolation threshold (ε_{th}) still having a value of nearly 0.05.

Figure 4.14 also shows a comparison of the predicted wet effective diffusivities from the present study to previous numerical studies [5, 7]. Fathi et al. [5] intruded water into the stochastic CL reconstructions using a nucleation approach similar to this study. However, they used a physics based volume of fluid (VOF) method to track the liquid intrusion as opposed to the image based CFM approach used in this study. Fathi et al. [5] proposed a correlation for the ratio of wet effective diffusivity to dry effective diffusivity of the form shown in Figure 4.14. The wet effective diffusivities obtained by Fathi et al. [5] are higher than those predicted from the current study. The higher values obtained by Fathi et al. [5] are likely due to the underprediction of the Knudsen effect as shown earlier for their dry effective diffusivities. Further, Fathi et al. [5] did not account for the change in Knudsen ra-

dius with saturation which results in an overprediction of the effective diffusivities as shown by Zheng and Kim [7].

Zheng and Kim [7] used LBM to intrude liquid water into a stochastic CL reconstruction. They claimed to have simulated liquid water generation due to the ORR in the CL however, this is difficult to assess as the numerical details for the liquid water intrusion model were not provided. The wet effective diffusivities computed using LBM by Zheng and Kim [7] and fitted to a power law, similar to this study, are shown in Figure 4.14. The value of γ computed by Zheng and Kim [7] was 3.062 for a pressure of 1 atm and changed to 2.982 at a pressure of 1.5 atm. Zheng and Kim [7] also reported that when using pore scale simulations without accounting for local Knudsen effects the γ value reduced to 1.815. The value of γ obtained in the current study is smaller than that predicted from the LBM simulations in reference [7].

The discrepancy between the γ value from Zheng and Kim [7] and the current study might be due to two reasons. Firstly, the higher order LBM method is able to account for Knudsen effects more accurately for water-air interfaces than the assumption of impermeable water interface used in this study. The second reason could be the difference in the microstructure of stochastic reconstructions. The mean pore diameter for the reconstructions by Zheng and Kim [7] ranges from 71-154 nm for porosity range of 0.3-0.7 while for the present study the mean pore diameter ranges from 25-65 nm for the same porosity range. Statistical correlation functions were not provided by Zheng and Kim [7] for their structures therefore, the differences in the morphology of the reconstructions cannot be analyzed. Further, Zheng and Kim [7] used only a single base structure to compute the wet effective diffusivities so they did not account for any statistical variability in the structures or effect of porosity. In the present study, the correlation is derived based on nearly 450 data points from 40 reconstructions with porosities in the range of 0.3-0.6. The value of γ computed from the present results can range between 2.24-2.51 depending on the data set used. Therefore, it is reasonable to assume that the wet effective diffusivities predicted in the current study are within the bounds of microstructure variation.

Thus far, this study has shown that using an effective porosity for the wet samples defined as $\varepsilon_{eff} = \varepsilon_V(1-s)$, resulted in a constant saturation threshold. It is reasonable to ask if, instead of using Equation (4.8), which adds a new term and coefficient to Equation (4.4), the latter could be used by simply replacing ε_V by ε_{eff} in Equations (4.4) and (4.6). Thus, the following correlation,

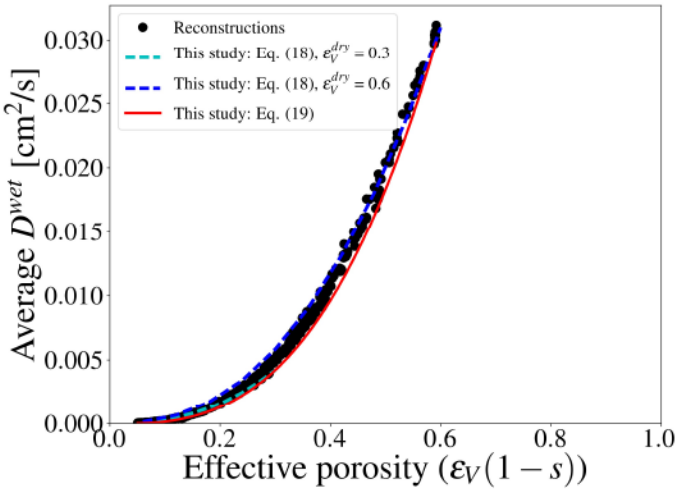

Figure 4.16 – Comparison of wet effective diffusivity as a function of effective porosity (ε_{eff}) using the two correlations (Equations (4.8) and (4.9)) proposed in this study.

$$D^{eff} = D^{pore}\left(\frac{\varepsilon_V(1-s)-\varepsilon_{th}}{1-\varepsilon_{th}}\right)^{\mu}\mathcal{H}(\varepsilon_V(1-s)-\varepsilon_{th}) \tag{4.9}$$

is used with $\mu = 1.90$ and $\varepsilon_{th} = 0.05$ to predict wet diffusivity. Figure 4.16 shows a comparison of the two correlations given by Equations (4.8) and (4.9) as a function of the effective porosity. For Equation (4.8), the wet effective diffusivity depends on the dry effective diffusivity and hence, the dry porosity therefore, the two extreme cases with porosities of 0.3 and 0.6 are shown in Figure 4.16. The expression given by Equation (4.9) provides a R^2 value of 0.986 compared to 0.995 when using Equation (4.8). Therefore, Equation (4.9), although does not provide as good of a fit as Equation (4.8), provides an excellent approximation while removing the need for an extra parameter.

The correlation for the effective diffusivity proposed in this study was developed by validating the statistical functions of the stochastic reconstructions against an inkjet printed CL. Further, the predictions of the dry diffusivity of the CLs with different porosities were found to be consistent with experimental data which were for different CLs than the one used in this study. Also, based on comparison of the predictions for the reconstructions with a different r_d (than the one used to develop the correlation), as shown in Figure 4.9d, the correlation should be valid for CLs with different particle sizes (r_d). In summary, Equation (4.9) combined with Equations (2.6), (2.7) and (4.6), with only two fitting parameters, provides an accurate prediction of dry and wet diffusivities in CL and is suitable for use in volume-average single cell models.

4.4.2 Liquid-vapor interfacial area in the CL

The liquid-vapor interfacial area variation with saturation is an important parameter used to model the liquid water evaporation in the macro-homogeneous models [31, 167, 168]. Zhou et al. [31, 168] showed that under wet conditions evaporation of the liquid water in the CL becomes crucial to transport liquid water out of the CL and MPL and prevent complete flooding. Therefore, knowledge of the liquid-vapor interfacial area variation with saturation from the micro-scale models can be used in the macro-homogeneous models to accurately describe the evaporation process.

As described earlier in Section 4.4.1, stochastic reconstructions with $r_d = 40$ nm and porosities ranging from 0.3 to 0.6 at different saturations were used. Figure 4.17 shows the specific liquid-vapor interfacial area as a function for the saturation. The specific interfacial area is defined as the liquid-vapor interfacial area per unit volume of the CL. Since the total CL volume for all the reconstructions irrespective of their porosity is the same, the specific interfacial area is directly proportional to liquid-vapor interfacial area. The interfacial area increases with saturation to a maximum at a saturation of nearly 75% and decreases to zero at 100% saturation. An increase in porosity leads to an increase in the specific interfacial area at a given saturation. The increase in the specific interfacial area becomes more prominent around the maxima where the difference between the interfacial area for reconstructions with porosity of 0.6 is nearly 30% larger than the interfacial area for the reconstructions with porosity of 0.3.

It must be noted that the liquid-vapor interfacial area would depend on the wettability of the pores and the pore sizes. Therefore, this property would strongly depend on the type of CL used and the data should be treated with care when trying to extrapolate to different CLs.

4.5 Conclusions

Numerical simulations were used to study the gas transport in CL reconstructions obtained from FIBSEM and stochastic reconstructions under dry and wet conditions. The stochastic reconstructions were generated using an overlapping sphere algorithm with different particle sizes. Analysis of the statistical correlation functions and effective diffusivity for the FIBSEM CL reconstruction showed that the loss of resolution in the FIB slicing direction

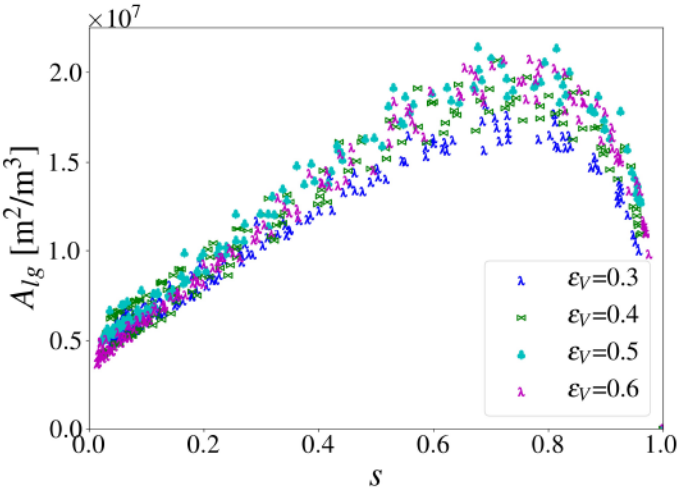

Figure 4.17 – Specific liquid-vapor interfacial area as a function of saturation (s) for the stochastic reconstructions with $r_d = 40$ nm and porosities ranging from 0.3 to 0.6.

resulted in artificial anisotropy in the CL microstructure. Statistical correlation function analysis is presented as a tool to determine the representativeness of CL microstructure from the stochastic reconstructions. Statistical correlation functions for the stochastic reconstructions were compared to those obtained from the FIBSEM reconstruction. It was found that stochastic reconstructions with $r_d = 40$ nm had two-point correlation function, chord length function, pore size distribution, specific interfacial area and mean chord length similar to those from the FIBSEM reconstruction thereby, warranting the use of these reconstructions to study the gas diffusivity in the CL. The detailed comparison of the statistical functions also provides a method to determine the representativeness of the stochastic reconstructions for fuel cell porous media, which has largely been ignored in prior numerical studies.

Then, gas diffusion was studied in the stochastic CL reconstructions with varying porosities under dry conditions. Analysis of the percolating pore network at different porosities showed that for porosities below 6% there was a loss of percolating gas network in the CL reconstructions. Effective diffusivity was isotropic for the stochastic reconstructions and increased with an increase in the porosity. A correlation for the effective diffusivity of the CL and its porosity was developed based on percolation theory. An empirical correlation was developed for the Knudsen radius based on the analysis of the pore size distributions for the stochastic reconstructions and used to compute the bulk diffusion coefficient in the pores which was used in the correlation. The percolation threshold was computed from the

analysis of the percolating pore network and found to be 0.05 while the exponent for the correlation was computed to be 1.90. The effective diffusivity predictions for the stochastic reconstructions under dry conditions were also compared to experimental and numerical values from literature and found to be in good agreement.

To study the impact of local saturation on the gas transport in the CL, a novel nucleation based water intrusion algorithm is presented. A cluster based full morphology algorithm is used to track the liquid water interface. The liquid-vapor interfacial area which is critical to estimate the evaporation rates in macro-homogeneous models was calculated as a function of saturation for the different CL reconstructions. The liquid-vapor interfacial area increased to a maximum up to a saturation of nearly 75% and then decreased to zero at 100% saturation. Gas diffusion simulations were carried out on the partially saturated CL reconstructions with dry porosities in the range of 0.3-0.6. To account for the change in the pore morphology and Knudsen effects, pore sizes were recalculated assuming liquid water to be impervious to gas. The predicted effective diffusivity decreases with an increase in saturation for all the reconstructions. At a given saturation, the ratio of wet effective diffusivity to dry effective diffusivity were similar for all reconstructions irrespective of their porosity. The predicted wet effective diffusivities were used to develop a correlation valid for both dry and wet effective diffusivity in the CLs.

Chapter 5

On the effect of catalyst layer pore size distribution

Porosity and pore size distribution (PSD) are the most commonly used metrics to characterize fuel cell porous media microstructure [26, 48–51, 54, 65, 101, 112, 113]. Advanced macroscale models have used the pore size distribution function as a closure equation to account for microscale effects on the local saturation in porous media [31, 166–169]. Experimental studies [269–271] have used pore formers to modify the porosity and PSD of CLs. Fischer et al. [269] and Gamburzev and Appleby [270] showed that the use of pore formers resulted in an improvement in the performance due to larger pore sizes which reduced mass transport losses. Yoon et al. [271] however, showed a decrease in the performance with an increase in pore former. Reasons for their observation were, unfortunately, not provided. Given the controversies, understanding the role of the CL PSD on the electrochemical performance is important for the design of CLs. In this chapter, the effect of catalyst layer pore size distribution on the electrochemical performance under dry and partially saturated conditions is investigated.

The effect of pore size distribution on the effective diffusivity was briefly discussed in Figure 4.9, where it was shown that the smaller pore sizes obtained for reconstructions with $r_d = 20$ nm resulted in lower effective diffusivities compared to the reconstructions with $r_d = 40$ nm which had much larger pore sizes (shown in Figure 4.5 for a porosity of 40%). Effective diffusivity is therefore, not discussed in this chapter. Section 5.1 describes the microstructure generation and the statistical characterization of the generated microstructures. Sections 5.2 and 5.3 discuss the electrochemical performance results for the CL under dry and partially saturated conditions. Section 5.4 discusses the effect of voxel resolution on the electrochemical performance.

5.1 Microstructure generation and statistical analysis

The overlapping sphere based reconstruction algorithm described in Section 2.1.2 was used to generate CL microstructures with different pore size distributions. To change the pore size distribution the particle radius used to generate the CL reconstructions was changed to 30, 40 and 50 nm. Two different porosities of 0.3 and 0.5 were used for each particle radius. The generated microstructures had dimensions of 400 nm × 400 nm × 1500 nm with a voxel resolution of 5 nm in each direction. A voxel resolution of 5 nm was used instead of either 2 or 2.5 nm because the focus of this study was on the electrochemical performance. The effect of the voxel size on the electrochemical performance prediction is discussed later. The domain size in the in-plane direction is selected as 400 nm because this size was shown to be sufficient to describe a representative elementary volume (REV) by Sabharwal et al. [51]. The domain size in the through-plane direction is 1500 nm instead of 400 nm because it was shown by Sabharwal and Secanell [272] that the effect of local saturation on the electrochemical performance of the CL cannot be captured on a REV domain and a microstructure representative of the thickness of the CL is required. Even though a through-plane length of 1500 nm is not the full thickness of a coventional CL, it is of a similar magnitude to the low loading electrodes discussed in Shukla et al. [38] and representative of low loading inkjet printed electrodes.

Figure 5.1 shows the pore phase and Knudsen radius distribution for reconstructions with a particle radius of 30 and 50 nm and porosity of 0.3 and 0.5. The pore sizes increase with an increase in the particle radius and porosity. Figure 5.2 shows the pore size distribution for the reconstructions with particle radii of 30, 40 and 50 nm and porosity of 0.3 and 0.5. When the porosity is 0.3, the average pore radius increases from 16.2 to 21.2 nm to 29.9 nm as the particle radius increases from 30 to 50 nm. An increase in porosity also results in an increase in the pore sizes as well as the fraction of pores greater than 100 nm. Increasing the porosity from 0.3 to 0.5 results in an increase in the average pore size from 16.2 nm to 24.1 nm and 29.9 nm to 44.4 nm for reconstructions with particle radius of 30 and 50 nm respectively. The probability of finding pores larger than 100 nm also increases from less than 1% to 5.5% and from 19.1% to 48.8% for the reconstructions with a particle radius of 30 and 50 nm respectively.

Figure 5.3 shows the void phase two-point correlation function in the x direction for the CL reconstructions. The statistical functions were identical in the x, y and z direction, thereby showing that the reconstruction is isotropic, so only the x direction is shown here. The slope of the two-point correlation function at $r = 0$ decreases with an increase

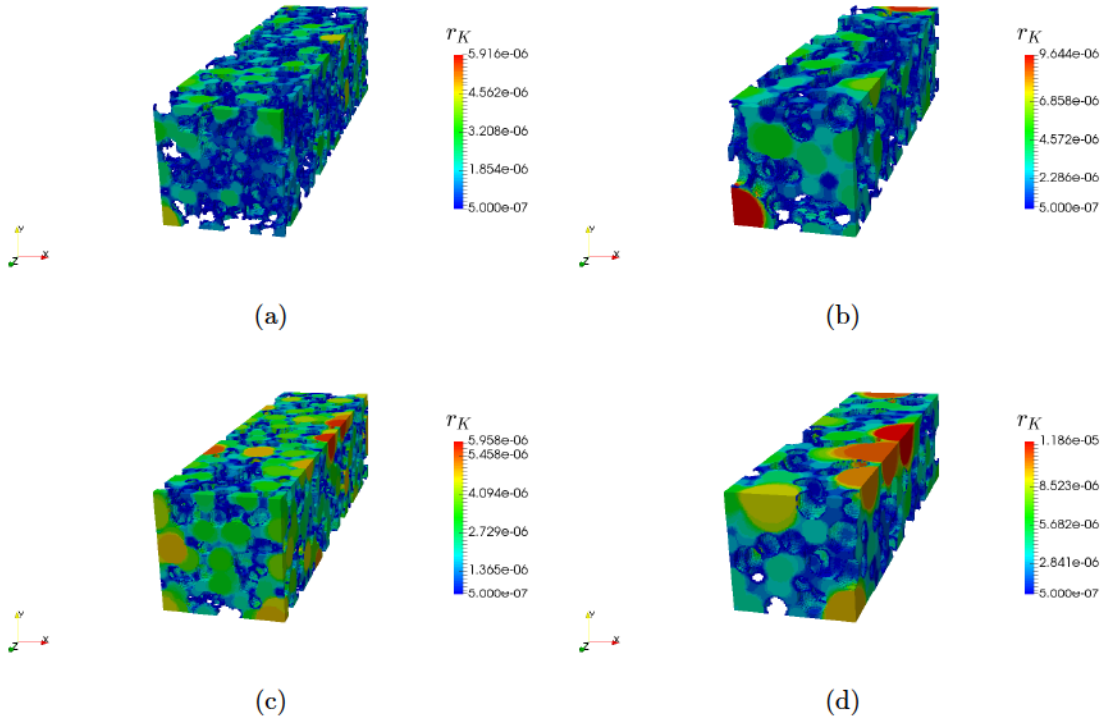

Figure 5.1 – Pore phase of the CL reconstructions with: porosity of 0.3 and particle radius of a) 30 nm and b) 50 nm; porosity of 0.5 and particle radius of c) 30 nm and d) 50 nm. The pores are colored according to their pore radius.

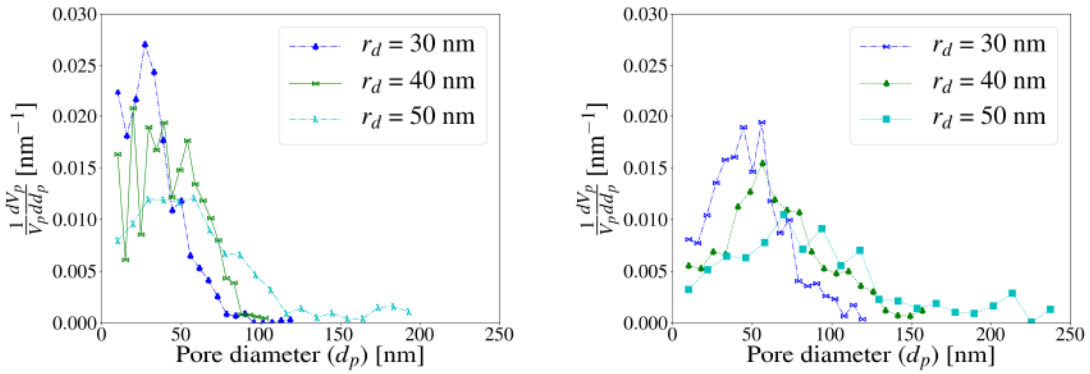

Figure 5.2 – Pore size distributions for the CL reconstructions with different particle sizes (r_d) and porosity of a) 0.3 and b) 0.5.

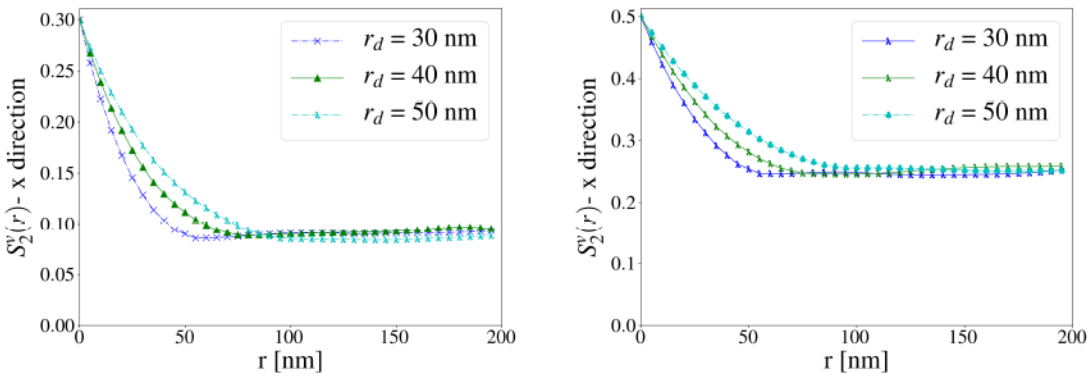

Figure 5.3 – Two-point correlation function in the x direction for the void phase ($S_2^v(r)$) for the CL reconstructions with different particle sizes (r_d) and porosity of a) 0.3 and b) 0.5.

in the particle radius highlighting a decrease in the interfacial area between the void and non-void phase. For a porosity of 0.3, the specific interfacial area, defined as the ratio of interfacial area per unit volume of the CL, decreases from 4.71×10^5 cm^2/cm^3 to 3.62×10^5 cm^2/cm^3 to 2.88×10^5 cm^2/cm^3 for reconstructions with particle radius of 30, 40 and 50 nm respectively. For reconstructions with the same particle radius, the slope of the two-point correlation function at $r = 0$ and consequently, the specific interfacial area changes less than 2.5%.

Figure 5.4 shows the chord length function for the void phase for the CL reconstructions. An increase in the porosity and particle radius results in a higher probability of finding larger chords which indicates larger pore sizes. Both chord length function and pore size distribution are related to the pore sizes and therefore, a change in the pore sizes between different CLs can be captured with both these functions. Table 5.1 shows the mean chord lengths computed using the chord length function and Equation (2.3) for the CL reconstructions. The mean chord length increases with an increase in the particle size and porosity. The mean chord length has been used to model the Knudsen diffusivity of CLs using the Derjaguin approximation [53, 63]. Therefore, an increase in the mean chord length indicates a decrease in the Knudsen resistance to mass transport in the CL.

Electrochemical reactions were simulated in the CL reconstructions with particle radii of 30, 40 and 50 nm and porosity of 0.3 and 0.5. To simulate the electrochemical performance of the CL reconstructions, ionomer was reconstructed as uniform films at the solid-pore in-

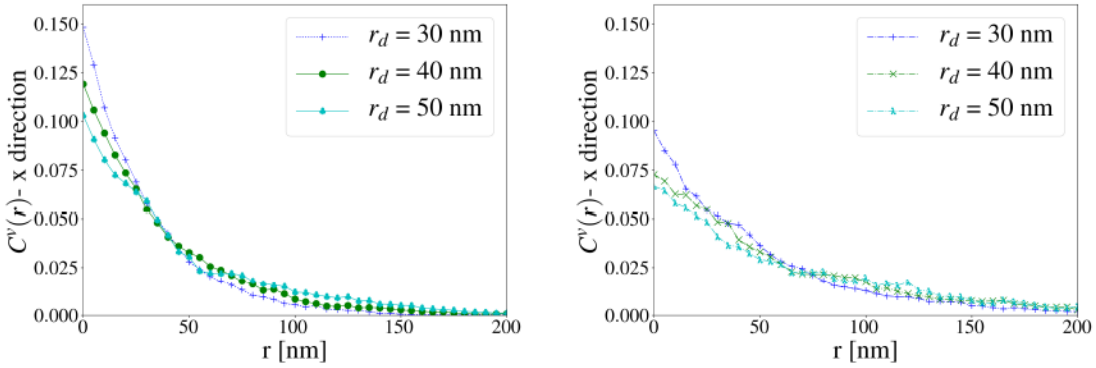

Figure 5.4 – Chord length function in the x direction for the void phase ($C^v(r)$) for the CL reconstructions with different particle sizes (r_d) and porosity of a) 0.3 and b) 0.5.

Table 5.1 – Mean chord length (in nm) for the reconstructions with different porosities (ε_V) and particle sizes (r_d).

Reconstruction	$\varepsilon_V = 0.3$	$\varepsilon_V = 0.5$
$r_d = 30$ nm	34.28	55.48
$r_d = 40$ nm	43.11	69.71
$r_d = 50$ nm	52.40	83.11

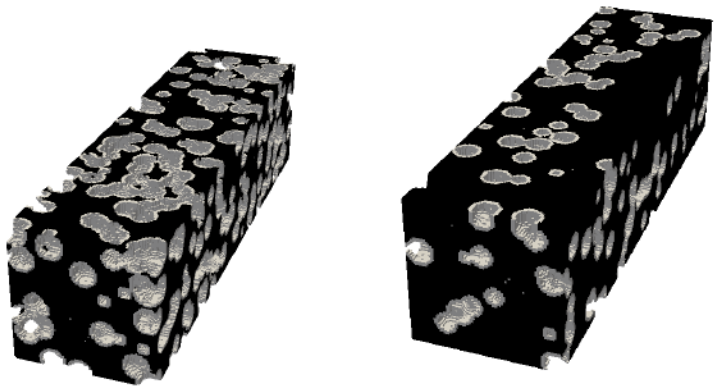

(a) (b)

Figure 5.5 – Mesh for the CL reconstructions with particle radius of 40 nm and porosity of a) 0.3 and b) 0.5. White is the ionomer film and black is the pore space.

terface. Since the objective of this study was to study the effect of pore size distribution, the ionomer films were assumed to be part of the solid phase, thereby keeping the pore phase unchanged. The ionomer volume fraction was maintained constant at 0.184 for all the reconstructions. Electrochemically active surface area (ECSA) of 65.4 m^2/g Pt based on the value reported by Shukla et al. [38] for an inkjet printed CL with 0.026 mg Pt/cm^2 was used for this study. The total active area (A_{Pt}) calculated using Equation (2.20) was kept constant for all the reconstructions. The total active area was distributed uniformly at the solid-ionomer interface for every reconstruction. This resulted in different local active surface area values for the different reconstructions because the solid-ionomer interfacial area varied between reconstructions.

5.2 Effect of pore size distribution on CL performance under dry conditions

Figure 5.5 shows the computational domain for the CL reconstructions with $r_d = 40$ nm and porosity of 0.3 and 0.5. The percolating pore network and percolating ionomer network was extracted for the CL reconstructions and used to generate the mesh. In addition to the material ids, the mesh also contained information about the local pore radii which was used to compute the local Knudsen diffusivity in every pore cell.

The operating conditions for the electrochemical simulations are an absolute pressure of 1 atm, temperature of 80°C and relative humidity of 50%. At these conditions, the oxygen

molar fraction in the channel is 0.161. The boundary conditions given by Equation (2.24), i.e., a Dirichlet boundary condition on one side and no-flux on the other side for both the proton conduction and oxygen transport, are used for these simulations. Assuming negligible mass transport losses in the diffusion media, an oxygen molar fraction of 0.161 was applied as the boundary condition in Equation (2.24). A protonic potential of 0 V was applied on the opposite side which assumes negligible kinetic and ohmic losses in the anode and membrane. A constant electronic potential corresponding to the cell voltage was applied in the domain. The protonic conductivity of the ionomer film was assumed to be that of a Nafion membrane at the given operating conditions. The non-linear system of equations was linearized using Picard's method and the linear problem was solved using a parallel CG solver. The total current was computed at the ionomer-solid interface using the kinetic model with the final oxygen and protonic potential profiles and then normalized by the in-plane cross-sectional area of the reconstruction to obtain the current density (A/cm^2) in the CL.

Figure 5.6 shows the polarization curves for the CL reconstructions with $r_d = 30$, 40 and 50 nm and porosity of 0.3 and 0.5. There is a negligible difference between the performance of the CL reconstructions with different PSDs with a maximum difference of 0.09 A/cm^2 at a cell voltage of 0.3 V for the different reconstructions. Figure 5.6b also shows the iR free polarization curve for a CL with a Pt loading of 0.026 mg/cm^2 and Nafion loading of 30% by weight which had a similar ionomer volume fraction (0.16) and porosity (0.5). The current density predictions for the CL reconstructions are similar to those from Shukla et al. [11] in the kinetic region. Since, the current study ignores mass transport losses in the diffusion media, the simulations predict much higher current densities at lower cell voltages. To investigate the reason for the negligible difference between the performance of CLs with significantly different pore sizes, the oxygen molar fraction and protonic potential profiles in the CL reconstructions were analyzed.

Figure 5.7 shows the oxygen molar fraction in the pore phase of the CL reconstructions with $r_d = 40$ nm and porosity of 0.3 and 0.5 at a cell voltage of 0.4 V. The change in the oxygen molar fraction across the domain is 8% for the reconstruction with a porosity of 0.3 and only 3.7% when the porosity is 0.5. The low drop in oxygen concentration across the CL is due to the ionomer film interfacial resistance which has been accounted in this study and shown to be the limiting mass transport resistance [51, 209, 211, 216]. Numerical models accounting for the interfacial ionomer resistance have shown a drop in oxygen molar fraction of less than 20% for a 5 μm CL [168] and nearly 10% for low-loading electrodes [211] in the through-plane direction. Significant mass transport losses were however, observed under the land [31, 168, 211] but these would require a very large computational domain. An

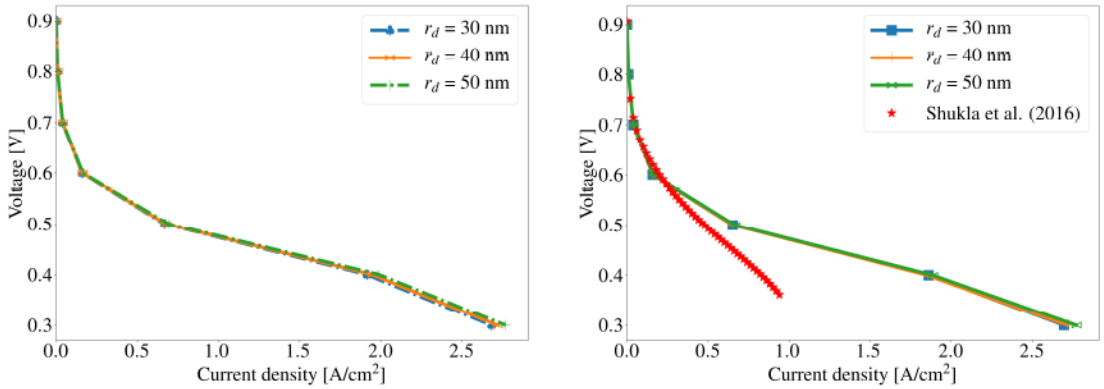

(a) (b)

Figure 5.6 – Polarization curve for CLs with different particle sizes (r_d) and porosity of a) 0.3 and b) 0.5 at 80°C, 1 atm and 50% RH with zero local saturation. iR free polarization curve from Shukla et al. [11] is shown for a CL with Pt loading of 0.026 mg/cm^2 and 30% Nafion loading by weight.

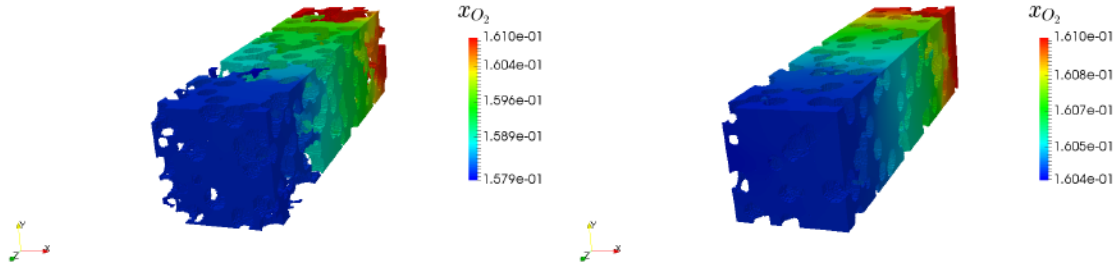

(a) (b)

Figure 5.7 – Oxygen molar fraction profile at 0.4 V in the pore phase of the CL reconstruction with r_d = 40 nm and porosity of a) 0.3 and b) 0.5.

increase in the solid-ionomer interfacial area with a decrease in the pore sizes would result in lower local fluxes and lower interfacial resistance at the solid-ionomer interface. However, the negligible change in performance with PSD indicates that the magnitude of change of the interfacial area and hence, the local resistance is not enough to affect the performance.

Figure 5.8 shows the protonic potential in the ionomer phase of the CL reconstructions at a cell voltage of 0.4 V. Since the ionomer volume fraction was the same for all the reconstructions, the protonic potential drop across the CL was similar for all the reconstructions. For the CL reconstructions shown in Figure 5.8, the protonic potential drop across the CL is 16 mV and 25 mV for a porosity of 0.3 and 0.5 respectively. The relatively similar protonic

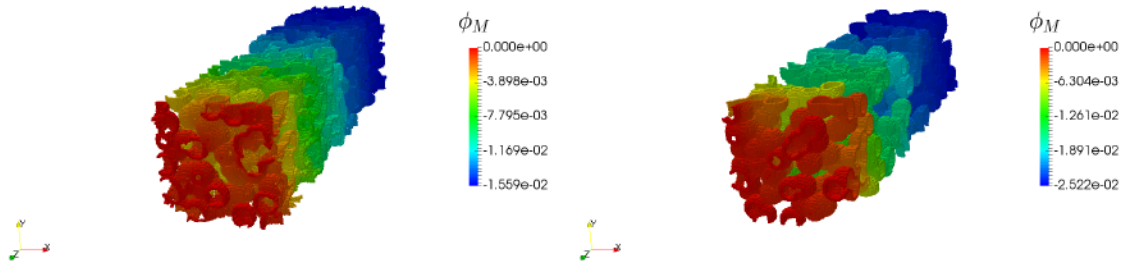

(a) (b)

Figure 5.8 – Protonic potential profiles (in V) at 0.4 V in the ionomer phase of the CL reconstruction with $r_d = 40$ nm and porosity of a) 0.3 and b) 0.5.

potentials in the domain would result in similar overpotentials (η), defined as,

$$\eta = \phi_S - \phi_M - E^{\text{ref}}, \tag{5.1}$$

where ϕ_S is the electronic potential which was kept constant in the domain and E^{ref} is the open cell voltage calculated at the reference state. Since both the overpotential and oxygen molar fraction were found to be similar throughout the domain for all the reconstructions, the total currents and hence, the current densities are similar for the reconstructions with varying pore size distributions.

Results from the current study show that there are no changes in the performance of the CL under dry conditions with pore size distribution. This is contrary to the experimental studies [269, 270] who observed an improvement in the performance for all cell voltages with the use of pore formers and attributed it to an increase in the pore sizes. Fischer et al. [269] obtained the electrochemical performance at a cell temperature of 75°C and 100% RH on the cathode side while Gamburzev and Appleby [270] operated the cell at 50°C and did not report the RH. Therefore, it is likely that at high current densities the CL was flooded and it would be better to compare the results at high current densities to those for the wet performance of the CL in the following section. Both these studies also observed an improvement in the performance in the kinetic region, likely due to an increase in the ECSA, which has not been taken into account in this study. These studies [269, 270] however, did not report the change in porosity and pore size distribution therefore, it is difficult to ascertain the change in pore sizes due to the use of pore formers. Thus, an experimental study is required, which characterizes the change in pore size distribution and consequent effect on the electrochemical performance of electrodes fabricated with and without pore formers. Such a study would be useful to prove/disprove the results from the current study and provide guidance

for future numerical simulations.

5.3 Effect of pore size distribution on CL performance under partially saturated conditions

To study the effect of local saturation on the electrochemical performance of CLs with different PSDs, liquid water was intruded into the reconstructions using the nucleation based water intrusion method described in Section 2.3.3. To simulate the liquid water intrusion, the smallest pores, i.e., pores having a radius of 5 nm, were treated as nucleation sites and assumed to be initially filled. The reason for treating the smallest pores as the nucleation sites has been discussed earlier in Section 2.3.3. These nucleation sites account for about 7.7-7.9% and 3.9-4.6% of the total porosity for reconstructions with a porosity of 0.3 and 0.5 respectively. However, for the CL reconstruction with $\varepsilon_V = 0.3$ and $r_d = 30$ nm, the HI fraction was 12.8%. The remaining pores in the CLs were treated as hydrophobic (HO) with a contact angle of 93° based on the environment scanning electron microscopy measurements reported by Yu et al. [268]. As discussed in the previous chapters when using the CFM model, the contact angle only changes the value of the capillary pressure required to intrude the pore and not the actual saturation profile. However, changing the wettability of the pores, i.e., increasing the hydrophilic fraction, would result in a change in the saturation profiles.

Liquid water intrusion was simulated using the CFM model and the parameters described above for the different CL reconstructions. Figure 5.9 shows the capillary pressure-saturation curves for CL reconstructions with $r_d = 30$, 40 and 50 nm and porosity of 0.3 and 0.5. The y intercept on Figure 5.9 indicates the hydrophilic fraction for the different reconstructions. At a given capillary pressure, an increase in the pore sizes results in an increase in saturation. At a capillary pressure of 263 kPa, the saturation in the CL reconstructions varied from 20% to 78% with an increase in the pore sizes. The capillary pressure values in Figure 5.9 are much higher than the experimental data reported by Kusoglu et al. [259]. However, Kusoglu et al. [259] reported a maximum capillary pressure of nearly 30 kPa, which would mean that minimum radius for the hydrophobic pores in the CL is 253 nm. This is likely due to their samples having large cracks and a high hydrophilic pore fraction. Further, Kusoglu et al. [259] simulated liquid water intrusion from the CL boundary in contact with a liquid water reservoir whereas this study simulates a nucleation based approach where water intrusion occurs from within the CL. Since, the wettability of the pores in the CL is unknown, more experimental data analyzing liquid water intrusion in the CL and microscopy reconstructions

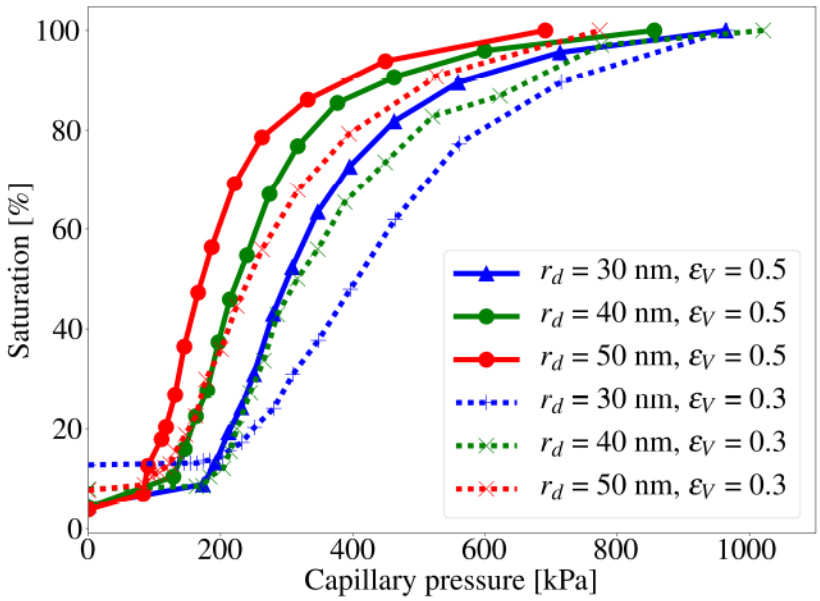

Figure 5.9 – Capillary pressure-saturation curves for CL reconstructions with different r_d and porosities.

at various saturations, similar to those for GDLs [55, 56, 60, 76–79], could be valuable to gain insight into the local wettability and saturation profiles in the CL.

Table 5.2 shows the threshold saturation (s_{th}), defined as the saturation beyond which a percolating gas network does not exist, for the different reconstructions used in this study. For the reconstructions with a porosity of 0.3, the threshold saturation ranges from 73-80%. The threshold saturation increases with an increase in porosity. The capillary pressure required to achieve the threshold saturation decreases with an increase in the particle radius for a porosity of 0.3. This is expected because an increase in particle radius results in an increase in the pore radii leading to higher saturations at lower capillary pressures. For a porosity of 0.5, the capillary pressure at s_{th}, decreases when r_d increases from 30 to 40 nm but then increases for $r_d = 50$ nm.

To study the electrochemical performance, the local saturation was computed using the CFM simulation at a given capillary pressure. The percolating pore network, i.e., gas and liquid filled pores, and the percolating ionomer network were extracted. The local saturation is therefore, not coupled to the electrochemical reaction. Oxygen transport was simulated in the gas (diffusivity obtained using Equation (2.6)) and liquid filled pores (diffusivity obtained using Equation (2.18)) and ionomer films (diffusivity is 9.726e-6 cm^2/s [273]) and proton

Table 5.2 – Threshold saturation (s_{th}) for the different reconstruction used in this study.

Porosity	Particle radius (nm)	Threshold saturation (s_{th})	Capillary pressure at s_{th} (kPa)
0.3	30	0.774	560.6
	40	0.735	449.2
	50	0.792	394.4
0.5	30	0.818	462.7
	40	0.855	376.7
	50	0.938	449.2

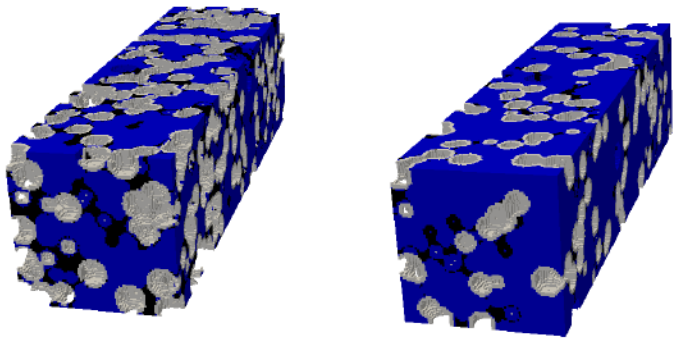

(a) (b)

Figure 5.10 – Mesh for the CL reconstructions with particle radius of 40 nm and a) porosity of 0.3 at a capillary pressure of 449 kPa and saturation of 73.5% and b) porosity of 0.5 at a capillary pressure of 462 kPa and saturation of 90.6%. White is the ionomer film, black is the gas filled pore space and blue is the liquid water filled pore space.

transport was simulated in the ionomer films. The Knudsen radii for the gas filled pores was recomputed assuming the liquid water surface to be impermeable to the gas molecules. The electrochemical reaction was simulated at the ionomer-solid interface. Figure 5.10 shows the partially saturated CL computational domain for two cases with $r_d = 40$ nm and different porosities.

Figure 5.11a shows the current density as a function of the local saturation at a cell voltage of 0.4 V for the CL reconstructions. The same operating conditions as those used to simulate the dry electrochemical performance in Section 5.2 were used. The current density initially remains nearly constant with an increase in saturation and then decreases rapidly with a further increase in saturation. The current density is initially constant because at low saturations the gas transport mainly takes place through the gas filled pores (by-passing any liquid filled pores), thereby the oxygen concentration in the domain remains nearly constant. A further increase in saturation (beyond 50% for $\varepsilon_V = 0.3$ and 70% for $\varepsilon_V = 0.5$) leads to

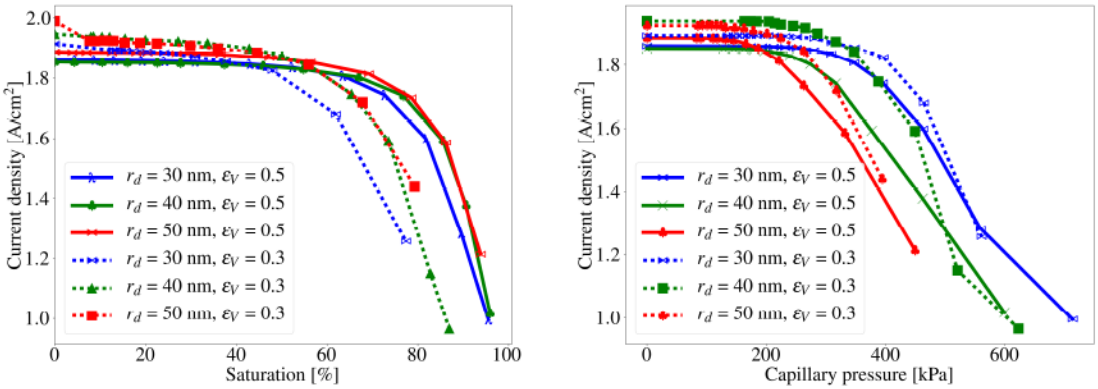

(a) (b)

Figure 5.11 – a) Current density for CLs with different particle sizes (r_d) and porosities at a cell voltage of 0.4 V as a function of the average saturation in the CL. b) Current density for CLs with different particle sizes (r_d) and porosities at a cell voltage of 0.4 V as a function of the capillary pressure. The operating conditions were 80°C, 1 atm absolute pressure and an oxygen molar fraction of 0.161 at the CL-diffusion media interface.

a decrease in the performance. Finally at saturation higher than the threshold saturation, there is a rapid decrease in current density due to mass transport losses as a result of the liquid filled pores forming bottlenecks for oxygen transport. The current density at a given saturation increases with an increase in pore sizes because of the higher Knudsen diffusivity (and hence overall gas phase diffusivity) and lower mass transport losses for CLs with larger pore sizes.

Although Figure 5.11a compares the electrochemical performance of the different CLs as a function of the local saturation, it must be noted that the local saturation in the CL is governed by the capillary pressure which in turn depends on the adjacent layers such as MPL or GDL. Figure 5.11b shows the current density as a function of the capillary pressure for the different CLs. The current density initially remains nearly constant with capillary pressure and then decreases rapidly with an increase in capillary pressure. A decrease in the CL pore size results in a higher current density at a given capillary pressure. This is because of the higher liquid pressure needed to intrude the smaller pore sizes in the CL.

Figure 5.12 shows the oxygen molar fraction in the pore phase of the CL reconstruction with $r_d = 40$ nm and porosity of 0.3 and 0.5 at a capillary pressure of 449 kPa (saturation of 73.5%) and 462 kPa (saturation of 90.6%) respectively. Unlike the dry case, much higher mass transport losses are observed at the pore scale with a maximum concentration drop of

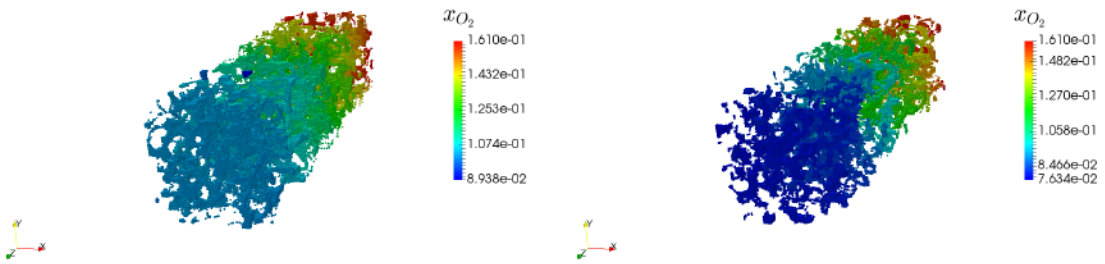

(a) (b)

Figure 5.12 – Oxygen molar fraction profile at 0.4 V in the pore phase of the CL reconstruction with r_d = 40 nm and a) porosity of 0.3 at a capillary pressure of 449 kPa and saturation of 73.5% and b) porosity of 0.5 at a capillary pressure of 462 kPa and saturation of 90.6%.

44.5% and 52.6% for the reconstructions with porosity of 0.3 and 0.5 and a capillary pressure of 449 and 462 kPa respectively and cell voltage of 0.4 V. The significantly higher mass transport losses observed in Figure 5.12, compared to Figure 5.7 for the dry case at the same cell voltage, are due to the liquid water filled pores which have a 3 to 4 orders of magnitude lower oxygen diffusivity than the molecular oxygen diffusivity in air. The liquid water filled pores form bottlenecks in the pore space, thereby resulting in significant mass transport losses. Therefore, the current density for the CL reconstruction shown in Figure 5.12a is 21.7% higher than the reconstruction in Figure 5.12b.

Figure 5.13 shows the protonic potential in the ionomer films for the same CL reconstructions as Figure 5.12. The protonic potential gradient across the CL is 14 mV and 21 mV for the CL reconstructions shown in Figures 5.13a and 5.13b respectively. The relatively low change in the protonic potentials indicates that the ionomer films have negligible impact on the current density for this study. This is consistent with the motivation of this study to isolate and study the effect of the CL pore size distribution on the electrochemical performance.

The results from the current study suggest that significant capillary pressures (greater than 300 kPa) are required for the PSD to have an effect on the performance of the CL. Experimental studies [274–277] have reported breakthrough capillary pressures of 4-8 kPa for commercial GDLs with MPL. At these capillary pressures, the local saturation in the CLs used in this study is between 3-12%. At these low saturations, there is negligible change in the electrochemical performance of the CL thereby, indicating that the CL PSD has no impact on the electrochemical performance.

However, the experimental studies have the entire MPL/GDL surface in contact with

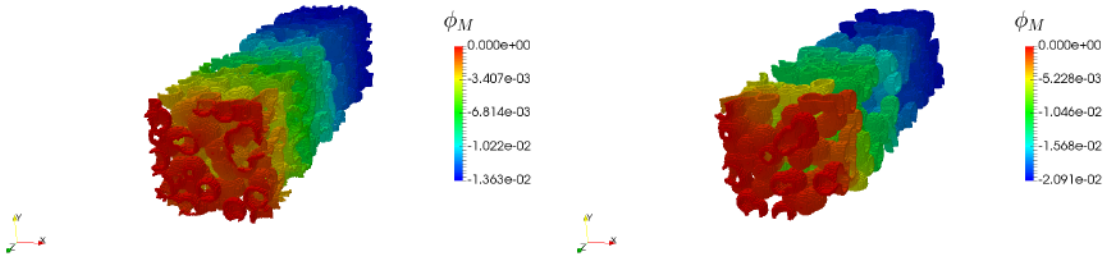

(a) (b)

Figure 5.13 – Protonic potential profiles (in V) at 0.4 V in the ionomer phase of the CL reconstruction with r_d = 40 nm and a) porosity of 0.3 at a capillary pressure of 449 kPa and saturation of 73.5% and b) porosity of 0.5 at a capillary pressure of 462 kPa and saturation of 90.6%.

liquid water which might not be the case for liquid water transport at the CL-MPL interface. Figure 5.14 shows the probability of finding liquid water at the CL-MPL interface for the different reconstructions used in this study. The probability (F(Liquid,MPL))was calculated as,

$$F(\text{Liquid,MPL}) = \frac{A_w}{A_{\text{pores}}}\varepsilon_V \tag{5.2}$$

where A_w is the area of liquid water on the CL-MPL interface and A_{pores} is the total area of pores at the CL-MPL interface. It can be seen that for a saturation of 40% the probability of finding liquid water at CL-MPL interface is less than 0.2 for reconstructions with $\varepsilon_V = 0.3$ and less than 0.3 for reconstructions with $\varepsilon_V = 0.5$. Therefore, the breakthrough capillary pressure for liquid water from CL-MPL would depend on the probability of having liquid water at the CL-MPL interface and a crack in the MPL at the same location, which would be even lower than the probability reported in Figure 5.14. It must also be noted that the capillary pressure reported in this study would also be affected by the hydrophilic pore fraction as an increase in the hydrophilic pore volume would result in higher saturations at lower capillary pressures.

5.4 Effect of voxel size on the electrochemical performance of CL

To study the effect of voxel size on the electrochemical performance of the CL, electrochemical simulations were carried out on a stochastic CL reconstruction with a porosity of 0.4, a uniform ionomer film of thickness 7.5 nm (3 voxels), i.e., an ionomer volume fraction of 0.16, and dimensions of 400 nm × 400 nm × 1500 nm (160 × 160 × 600 voxels). Voxel resolution

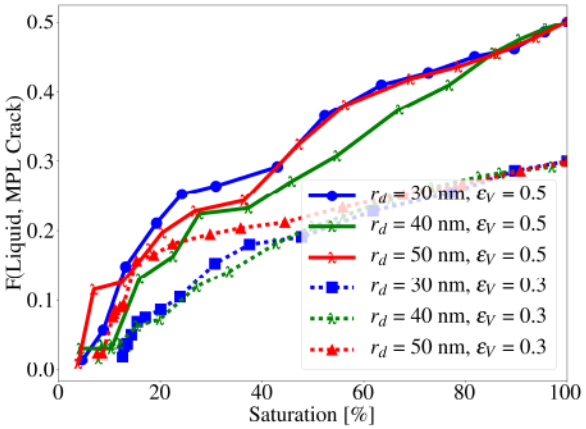

Figure 5.14 – Probability of finding liquid water at the CL-MPL interface as a function of saturation in the CL for reconstructions with r_d = 30, 40 and 50 nm and porosity of 0.3 and 0.5.

was either 2.5 nm in each direction or 5 nm, where for the latter case the voxel resolution was decreased by a factor of 2 using a nearest neighbor interpolation [68]. A uniform ionomer film of thickness 7.5 nm (3 voxels) was generated to get an ionomer volume fraction of 0.16. Liquid water was intruded in the CL microstructure using the nucleation based water injection algorithm described earlier. For water intrusion, the smallest pores having a radius of 2.5 nm were assumed to be the hydrophilic nucleation sites and were initially flooded. This resulted in a hydrophilic percentage of 3.8% in the CL. All other pores were treated as hydrophobic with a contact angle of 93° [268]. Electrochemical simulations were carried out on the CL at saturation of 0% (dry case), 25% and 59%.

Table 5.3 shows the change in porosity, percolating pore volume fraction, ionomer volume fraction and percolating ionomer volume fraction due to coarsening of the voxel resolution. There is negligible change in the pore and ionomer networks when the voxel resolution is changed from 2.5 to 5 nm. Further coarsening of the voxel resolution to 10 nm lead to a drastic decrease in the percolating ionomer volume fraction to 0.02. The latter was expected because the ionomer thickness was assumed to be uniform at 7.5 nm which is below the 10 nm voxel resolution.

To simulate the electrochemical reactions, the local active surface area was set to 0.2 cm^2 CL/ cm^2 ionomer-solid interface [51]. The operating conditions were 80°C, 1 atm absolute pressure and 50% RH. Similar to the simulations above, an oxygen molar fraction of 0.161 and protonic potential of 0 V were used as Dirichlet boundary conditions in Equation (2.24). The electronic potential was maintained constant in the domain at the cell voltage of 0.4 V.

Table 5.3 – Effect of voxel resolution on the porosity and ionomer volume fraction of the stochastic reconstruction.

Coarsening factor	Voxel resolution [nm]	ε_V	Percolating pore network [%]	ε_N	Percolating ionomer network [%]
None	2.5	0.4	99.8	0.159	98.6
2X	5	0.4	99.9	0.157	99.9

Table 5.4 – Variation in current density at a cell voltage of 0.4 V at different saturations with change in voxel resolution.

Coarsening factor	Voxel resolution [nm]	s=0% i [A/cm^2]	s=25% i [A/cm^2]	s=59% i [A/cm^2]
None	2.5	1.49	1.48	1.44
2X	5	1.46 (-1.75%)	1.46 (-1.75%)	1.42 (-1.6%)

Table 5.4 shows the current density at the given conditions for different saturations at the two voxel resolutions. It can be seen that coarsening the voxel resolution leads to a decrease in the current density of less than 2%, however it results in a reduction in the number of degrees of freedom from 9.4 million to 1.28 million, thereby decreasing the computational time from 4.7 hours to 1.1 hour as well as reducing RAM requirements. The relatively small change in the current density and decrease in resource requirements justifies the use of 5 nm voxel resolution to analyze the electrochemical performance at different saturations for CLs.

5.5 Conclusions

Stochastic reconstructions with different particle sizes and porosities were used to generate CL reconstructions with different pore size distributions. An increase in the particle radius and porosity resulted in an increase in the average pore size, the mean void chord length and the volume fraction of pores greater than 100 nm in diameter and a decrease in the specific interfacial area.

Numerical simulations were performed on the stochastic reconstructions to study the effect of pore size distribution on the electrochemical performance at dry conditions. Polarization curves for CLs with different pore size distributions under dry conditions showed negligible differences. This was due to a less than 10% drop in the oxygen molar fraction across the CL at a cell voltage of 0.4 V which indicated that the interfacial resistance due to

the ionomer film was the dominant mass transport resistance. This was consistent with the through-plane oxygen profiles observed in other studies which had accounted for this resistance. The results were contradictory to experimental studies which showed an improvement in performance with the use of pore formers. However, these studies lacked any microstructure characterization. Therefore, experimental studies which combine electrochemical and microstructure characterization, using imaging techniques and mercury intrusion porosimetry, are required to guide the numerical simulations.

Liquid water intrusion into the CL reconstructions was simulated using a nucleation based water intrusion algorithm to study the effect of local saturation on the electrochemical performance of CL reconstructions with different PSDs. The partially saturated CLs were used to simulate the electrochemical performance which accounted for oxygen transport in the gas and liquid water filled pores and ionomer films and proton transport in the ionomer films. The electrochemical performance of all CLs initially remained constant with an increase in capillary pressure and then decreased rapidly with a further increase. The significant drop in current density was due to blockage of the gas filled pore network, resulting in much larger mass transport losses due to lower oxygen diffusivity in liquid water. It was found that CLs with smaller pore sizes resulted in lower saturations at a given capillary pressure and hence, it is speculated that they would result in lower losses in the electrochemical performance since the breakthrough pressure into the MPL would control liquid pressure in the CL. At the same saturations, CLs with the larger pore sizes had better performance due to higher Knudsen diffusivity in the pores. Experimental studies are required to determine: a) liquid water intrusion curves for CLs; and b) the breakthrough capillary pressures for a CL and MPL assembly. Such studies should be complemented with microstructural characterization using imaging techniques and numerical modeling to improve the understanding of these phenomena.

Chapter 6

On the effect of ionomer distribution

Ionomer is the proton conducting phase in the catalyst layer. Increasing the ionomer content provides more proton conducting network in the catalyst layer however, an increase in the ionomer content leads to a decrease in the porosity which impedes gas and liquid transport. Experimental studies [38, 39, 120–122, 278–280] have proposed the existence of optimal ionomer loadings for PEMFC catalyst layers. Several studies [219, 220, 281, 282] have hypothesized that modification of the ionomer distribution could also lead to an increase in the performance. Microstructural modeling studies [4, 63, 67, 86, 104–106, 149] have reconstructed ionomer films to simulate proton transport in the CL to study electrochemical simulations. Recent studies on ionomer thin films [12, 251–256] show that the conductivity of ionomer thin films is different from those of the bulk membrane previously used in numerical studies [4, 63, 67, 104–106, 149] and depend on the film thickness, temperature, relative humidity, heat treatment and substrate on which the ionomer films were studied.

In this chapter, the effect of ionomer distribution and content on the effective transport properties and the electrochemical performance of the CL is discussed. The thin film dependent conductivity reported in recent experimental studies is used to model the proton transport in the reconstructed ionomer thin films. Section 6.1 describes the reconstruction algorithm used to generate the ionomer films. Section 6.2 shows the statistical functions for the reconstructions with varying ionomer distributions and content. Sections 6.3 and 6.4 discuss the results of the numerical simulations used to compute the effective transport properties and electrochemical performance for the different ionomer contents and distributions.

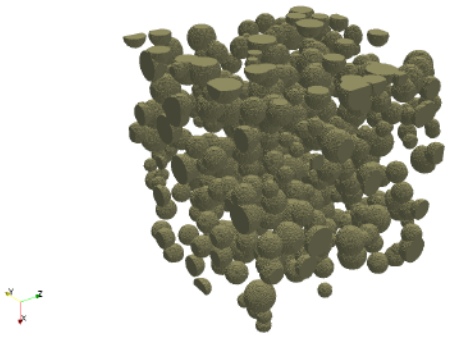

Figure 6.1 – Solid phase (carbon and platinum) of the base microstructure used to study different ionomer distributions. The dimensions of the reconstruction are 600 nm × 600 nm × 600 nm with a voxel resolution of 2 nm in each direction and a solid volume fraction of 0.25.

6.1 Microstructure generation

For this study, the base microstructure was generated using the overlapping sphere algorithm described in Section 2.1.2 with multiple particle sizes and free overlap ($\psi = 1$). The microstructure was generated using particles with radii of 20, 30 and 40 nm having a probability of 0.25, 0.5 and 0.25 respectively. The solid volume fraction, i.e., carbon and platinum, was fixed at 0.25. Figure 6.1 shows the solid phase of the generated base structure with dimensions of 600 nm × 600 nm × 600 nm with a voxel resolution of 2 nm in each direction. A voxel resolution of 2 nm is chosen for this study because the objective of this chapter is to study the effect of the ionomer film distribution and therefore, using a higher voxel size would provide less flexibility in varying the ionomer film distributions which have been reported to have a thickness of 4-16 nm [283]. Even though a minimum thickness of 4 nm was found in the tomographic reconstruction [283], a resolution of 2 nm is chosen to provide better control over the film thickness while ensuring that the minimum thickness was 2 voxels or 4 nm. The domain size of 600 nm in the x, y and z directions was shown to be a representative elementary volume (REV) to study the statistical functions and effective diffusivity [51, 284] and therefore, it is assumed to be sufficient to predict the effective protonic conductivity. The same solid structure is used to study different ionomer distributions by generating the ionomer films on the solid structure. This was done to eliminate any effect of the underlying solid structure on the statistical and functional characterization and limit all changes to the effect of ionomer film distributions. The ionomer film reconstruction algorithm is described in the following section.

6.1.1 Ionomer reconstruction algorithm

Ionomer thin films were digitally reconstructed using a stochastic algorithm based on an input probability of the ionomer film distribution. Figure 6.2 shows a schematic of the ionomer reconstruction algorithm. The ionomer is generated in the void phase. This was used to generate the uniform ionomer film in the previous chapters to ensure that the pore network was unaffected by the generation of the ionomer films. The steps of the algorithm are described below,

1. A 3D binary structure (Figure 6.2a) with solid and void phase is provided as an input to the algorithm. The ionomer films are generated either in the void phase (i.e., coated on the solid phase) of the input microstructure.

2. The distance transform is measured on the phase in which the ionomer is to be deposited. The distance transform discretizes the phase of interest into layers based on the distance from the solid-void interface. Thus, each unique value of the distance transform indicates a layer. An example of this is shown in Figure 6.2b where the distance transform is computed in the void phase and the value increases from black to white with black being a value of zero.

3. The input probability ($p(x)$) of the ionomer distance from the solid-void interface is read. This gives the probability of finding an ionomer voxel at a distance x from the solid-void interface. $p(x)$ is converted into an equivalent number of cells to be deposited into each layer of the distance transform discretized phase based on the desired ionomer volume fraction and the total volume of the microstructure. The input distribution controls the nature of the generated ionomer films. For example, a uniform input distribution would result in uniform ionomer films whereas non-uniform or random distributions would result in patchy ionomer networks.

4. The next step in the algorithm is the layer-by-layer deposition of the required number of cells to each layer of the discretized phase (given distance from the solid-void interface) starting with the layer closest to the solid-void interface, i.e., distance of zero from the solid-void interface. To generate the ionomer cells in the layer at a distance x from the solid-void interface, a probability array is created to store the probability of all viable locations which are a distance x from the solid-void interface. A viable location is defined as any location which is a non-ionomer voxel in the discretized phase. In order to ensure connectivity of the ionomer films, the probability of a viable location is scaled by a smoothing factor if it is adjacent to an existing ionomer cell in the current (distance x) or previous (distance $x-1$) layer. Figure 6.2c shows the probability

distribution at one of the iterations. White colored cells have the highest probability in Figure 6.2c.

5. The probability array is then used to pick random locations where ionomer cells can be placed. In order to improve efficiency of the code, groups (more than one cell at a time) of ionomer cells are placed randomly within the structure simultaneously according to the existing probability array. Figure 6.2d shows the multiple ionomer cells placed during a single iteration.

6. Steps 3-5 are repeated until the appropriate number of cells have been placed in each layer to satisfy the input distribution and achieve the desired volume fraction. Figures 6.2e and 6.2f show the evolution of the ionomer film generation at different distances from the solid-void interface.

The algorithm for ionomer generation was implemented in python as a part of the open-source package pyFCST.

The inputs to the ionomer reconstruction algorithm described above are: a) initial microstructure, b) probability of the ionomer distribution and c) smoothing factor. The microstructure shown in Figure 6.1 is provided as the initial microstructure. The ionomer films are grown on the solid surface, therefore ionomer distribution affects the porosity and pore sizes. The smoothing factor is set to 100, thereby making it 100 times more probable that new ionomer cells are placed adjacent to existing ionomer cells.

To generate different ionomer distributions, the probabilities for the ionomer distributions were obtained from a normal distribution with a mean of zero and different standard deviations. The input distributions were obtained by modifying the standard deviation (σ) for the normal distributions and obtaining the probabilities using,

$$f(x) = F(x+1) - F(x), \tag{6.1}$$

where $f(x)$ is the probability of finding an ionomer voxel at a distance x from the solid-void interface, $F(x)$ is the cumulative distribution function for a normal distribution defined as,

$$F(x) = \frac{1}{2}\left[1 + \text{erf}\left(\frac{x-\mu}{\sigma\sqrt{2}}\right)\right], \tag{6.2}$$

where μ is zero and erf is the error function. It must be noted that only the positive half of the normal distribution function is used to generate the input probability for the ionomer film reconstructions. $f(x)$ was computed for all integer distances upto 3σ from the solid-void

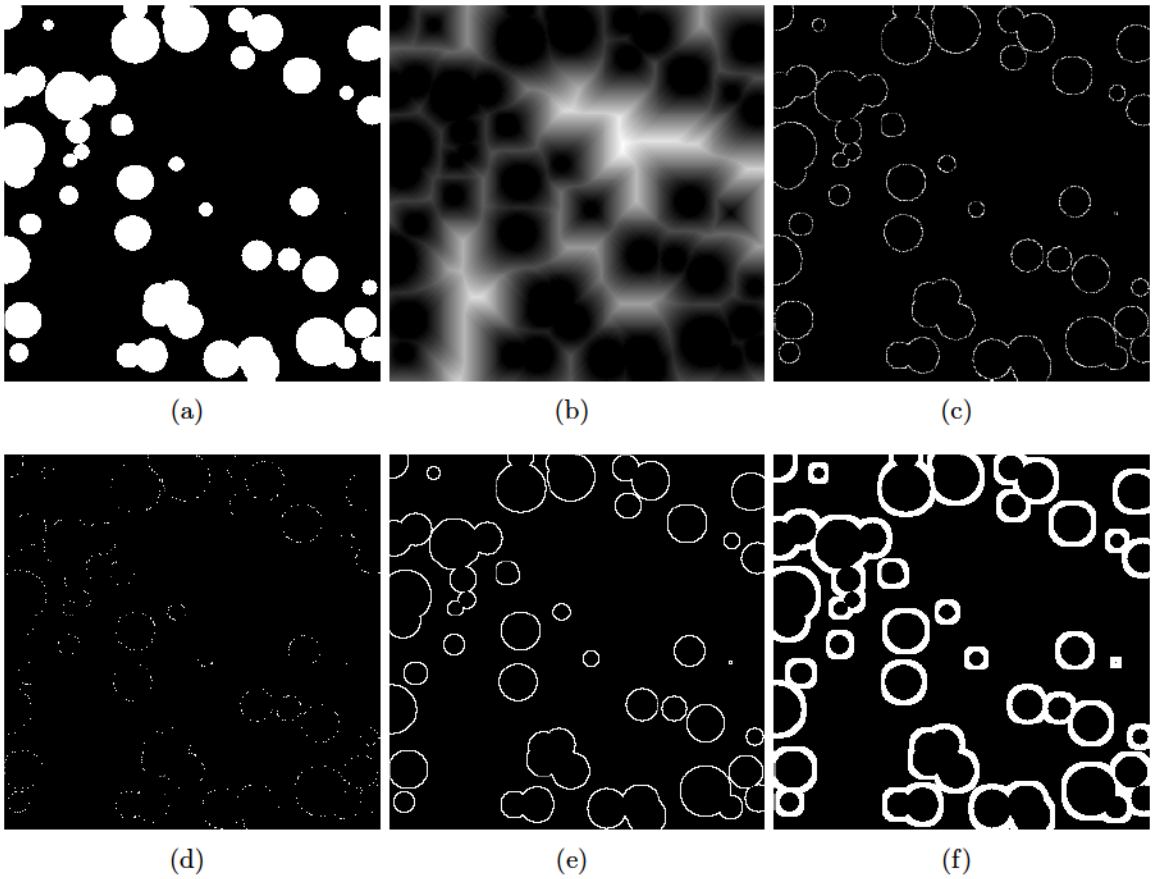

Figure 6.2 – Schematic of the ionomer reconstruction algorithm applied to generating ionomer films in the solid phase of the microstructure. a) 3D input microstructure with solid in white and pore in black; b) Distance transform in the void phase (distance increases from black to white); c) Probability of cells to be selected for ionomer placement; d) Multiple ionomer cells placed from randomly selected cells; and, e) and f) Growing the ionomer film one layer at a time from the solid-void interface.

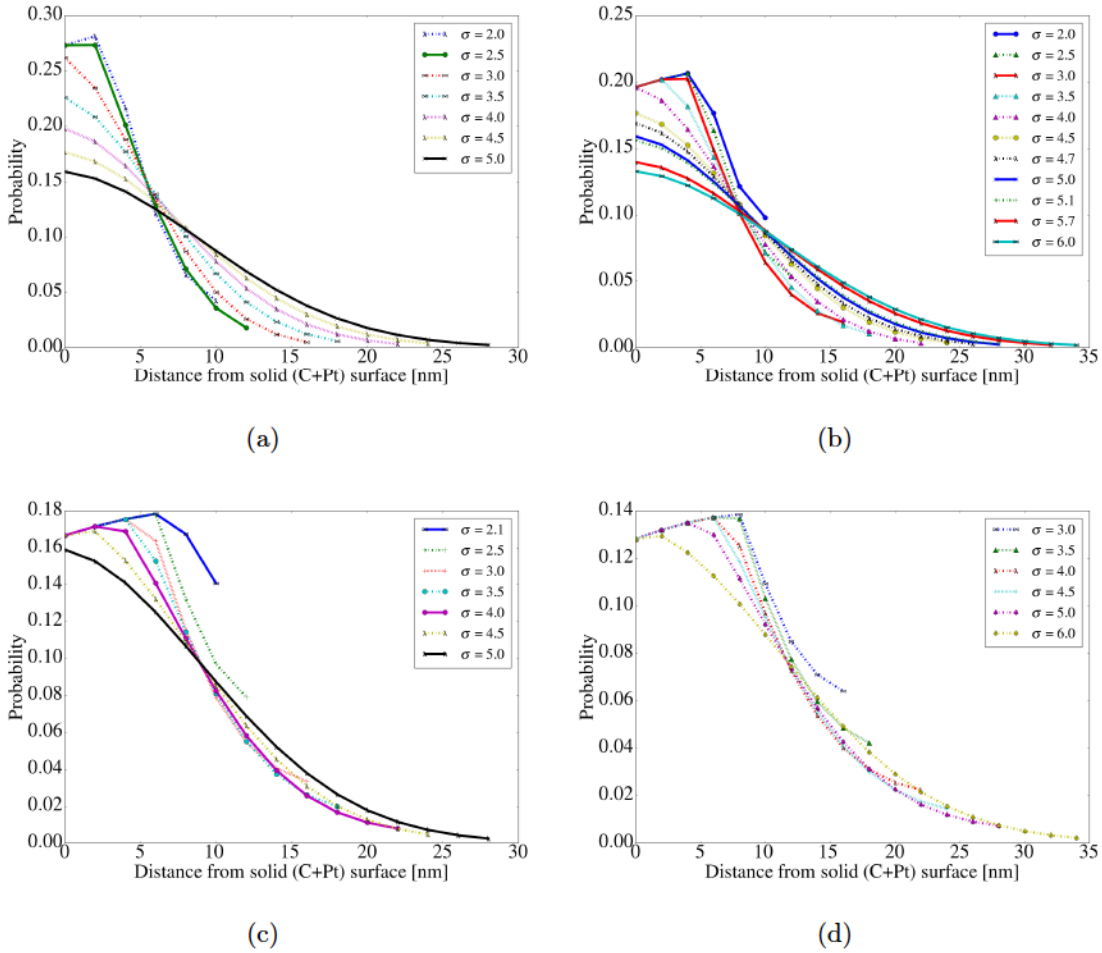

Figure 6.3 – Probability functions for the ionomer distributions for reconstructions with ionomer volume fraction of a) 0.122, b) 0.17, c) 0.20 and, d) 0.26.

interface and then normalized so that the sum of probabilities was 1 (compared to 0.4985 since half the normal distribution upto 3σ was used). Additionally, to ensure that the required ionomer volume fraction is met especially for lower σ values, the probabilities were re-adjusted to farther distances because the layers close to solid surface were 100% filled and could not satisfy the high probability value obtained from the normal distribution.

Figure 6.3 shows the input probability to generate different ionomer distributions for an ionomer volume fraction of 0.122, 0.17, 0.2 and 0.26 corresponding to an I/C ratio of 0.53, 0.74, 0.87 and 1.13 respectively based on the solid volume fraction for a doctor blade CL reported by Zhou et al. [168]. An increase in σ of the normal distribution function leads to higher probabilities of finding ionomer cells farther from the solid-void interface. As mentioned earlier, for low σ values the probabilities were re-adjusted to ensure that the desired

volume fraction was achieved. This re-adjustment can be observed for $\sigma = 2$ for all cases where the probability of finding a film on the surface is lower than finding it 2-5 nm away which is uncharacteristic of a normal distribution with zero mean but in line with an increase of available optionsdue to the larger radius.

6.2 Statistical characterization

The probability functions shown in Figure 6.3 were used to generate ionomer distributions with different volume fractions. For every σ value, one reconstruction was generated because the domain size of 600 nm in each direction was shown to be statistically representative. This was demonstrated by the negligible variation in statistical functions and effective diffusivities from the results in Chapter 4 and a previous study [51]. Figure 6.4 shows the ionomer distribution at the same location for reconstructions with an ionomer volume fraction of 0.17 and σ values ranging from 2 to 6. With an increase in σ, the ionomer distribution becomes more irregular with larger differences in local ionomer thickness. Further, with an increase in σ, the coverage, defined as the fraction of the solid surface covered by ionomer, also decreases which can be seen clearly in Figures 6.4d and 6.4e.

Figures 6.5a-c show 2D slices of the ionomer distribution at 25%, 50% and 75% of the depth in the z direction for an ionomer volume fraction of 0.122 and $\sigma = 2$. At a low σ value, the ionomer distribution is uniform and an increase in the ionomer volume fraction results in a uniform increase in the ionomer film thickness. This is shown in Figures 6.6a-c, 6.7a-c and 6.8a-c for I/C ratios of 0.74, 0.87 and 1.13 with uniform distribution for σ values between 2 to 3. Figures 6.5d-f, 6.6d-f, 6.7d-f and 6.8d-f show 2D slices of the ionomer distribution at 25%, 50% and 75% of the depth in the z direction for different ionomer volume fractions (ε_I) with a non-uniform ionomer distribution ($\sigma = 5$ for I/C = 0.53, $\sigma = 6$ for I/C = 0.74, $\sigma = 5$ for I/C = 0.87 and $\sigma = 6$ for I/C = 1.13). An increase in σ leads to more non-uniform ionomer distributions and a loss of coverage especially at lower ionomer contents (I/C = 0.53 and 0.74). The effect of σ is less pronounced for higher ionomer contents ($\varepsilon_I = 0.2$ and 0.26) where the ionomer films close to the solid surface remain uniform due to the high ionomer volume fraction.

Figure 6.9 shows the two-point correlation function in the x direction for the ionomer phase ($S_2^i(r)$) for different ionomer distributions and I/C ratios. For the statistical functions, only the functions in one direction, x in this case, are shown because the functions had identical values in the x, y and z directions indicating an isotropic structure. An increase in σ

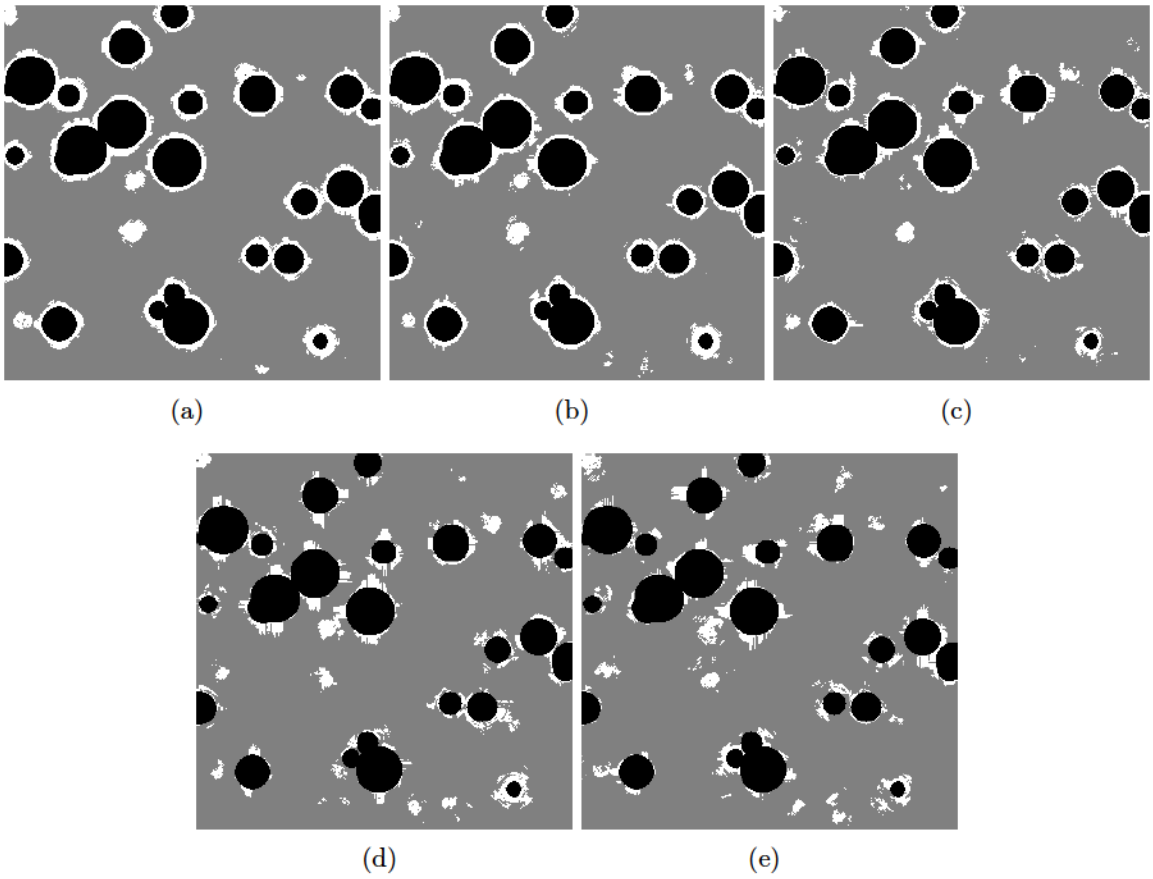

Figure 6.4 – Ionomer distribution at the same location for a ionomer volume fraction of 0.17 with σ of a) 2, b) 3, c) 4, d) 5 and e) 6. Ionomer is shown in white, pores are grey and solid is black.

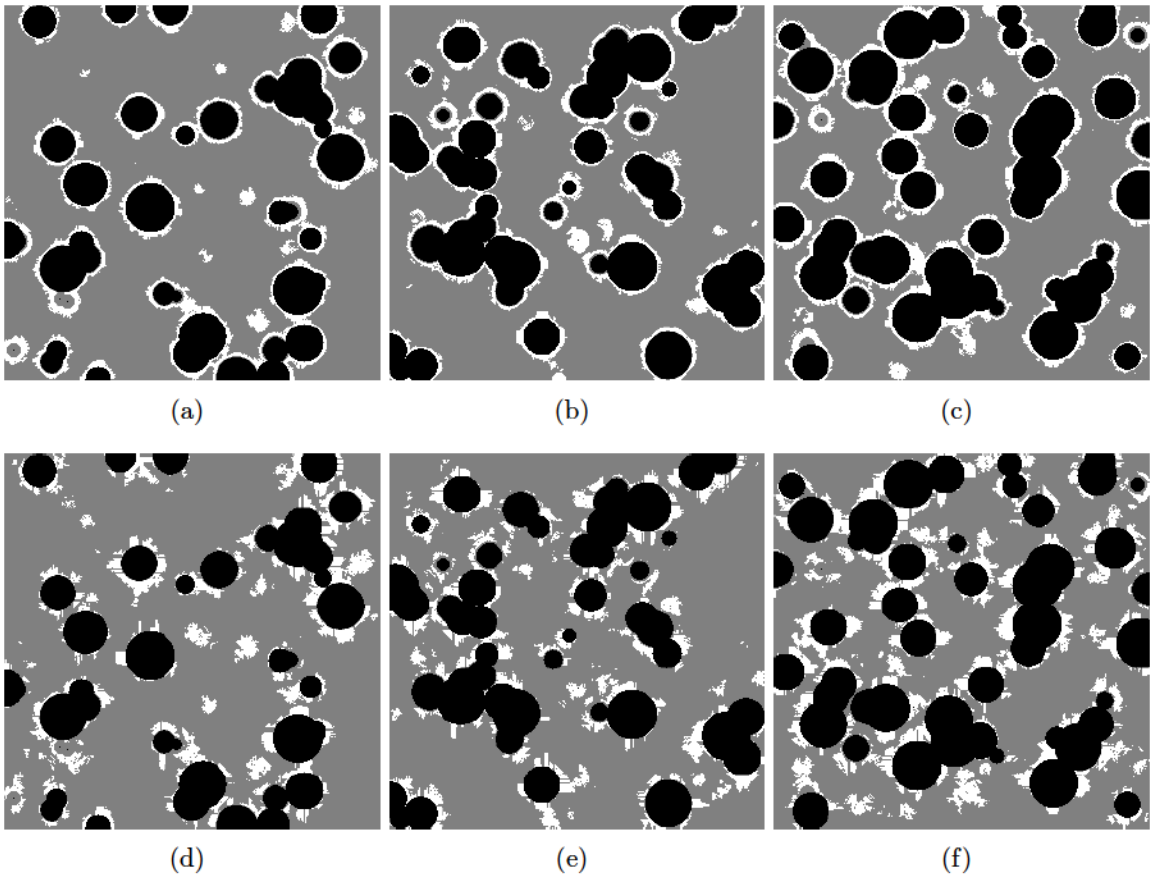

Figure 6.5 – Ionomer distribution at: a) 25%, b) 50% and c) 75% z depth for I/C = 0.53 with $\sigma = 2$ and d) 25%, e) 50% and f) 75% z depth for I/C = 0.53 with $\sigma = 5$. Ionomer is shown in white, pores are grey and solid is black.

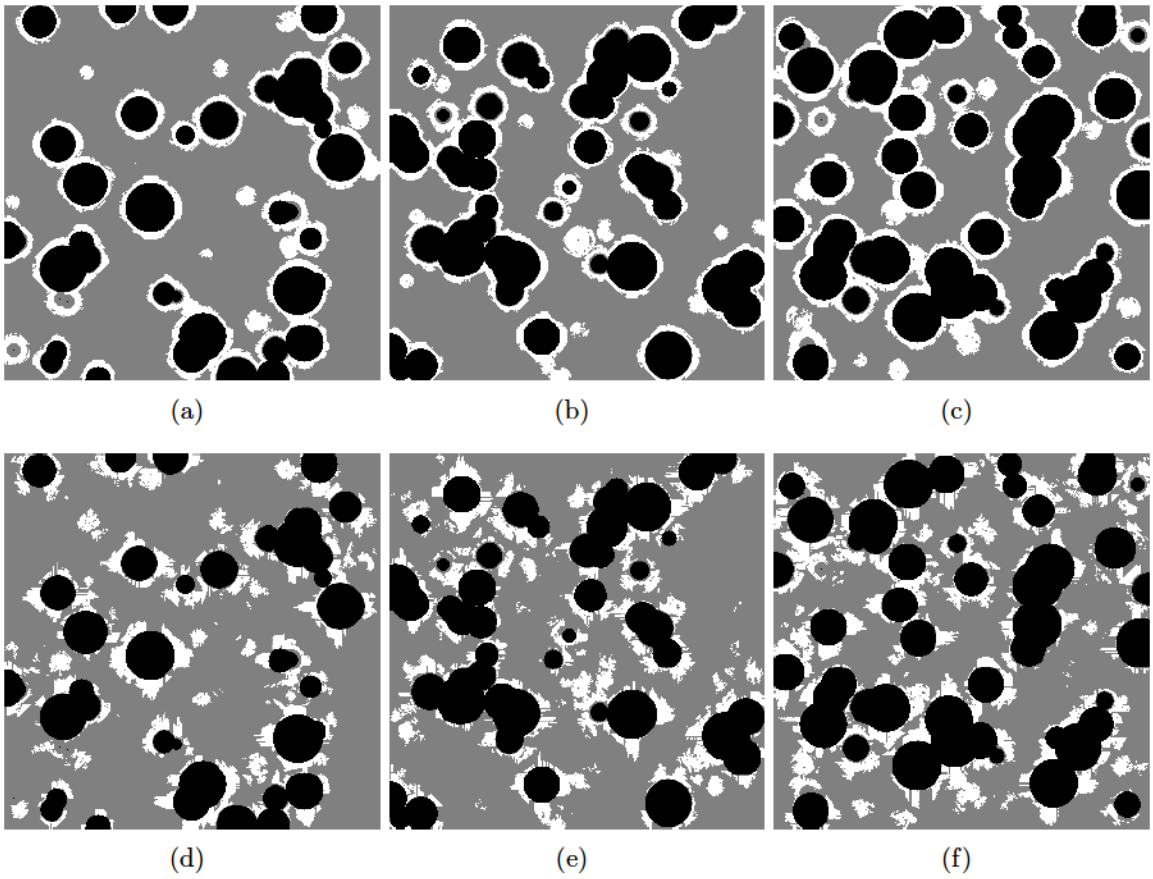

Figure 6.6 – Ionomer distribution at: a) 25%, b) 50% and c) 75% z depth for I/C = 0.74 with $\sigma = 2$ and d) 25%, e) 50% and f) 75% z depth for I/C = 0.74 with $\sigma = 6$. Ionomer is shown in white, pores are grey and solid is black.

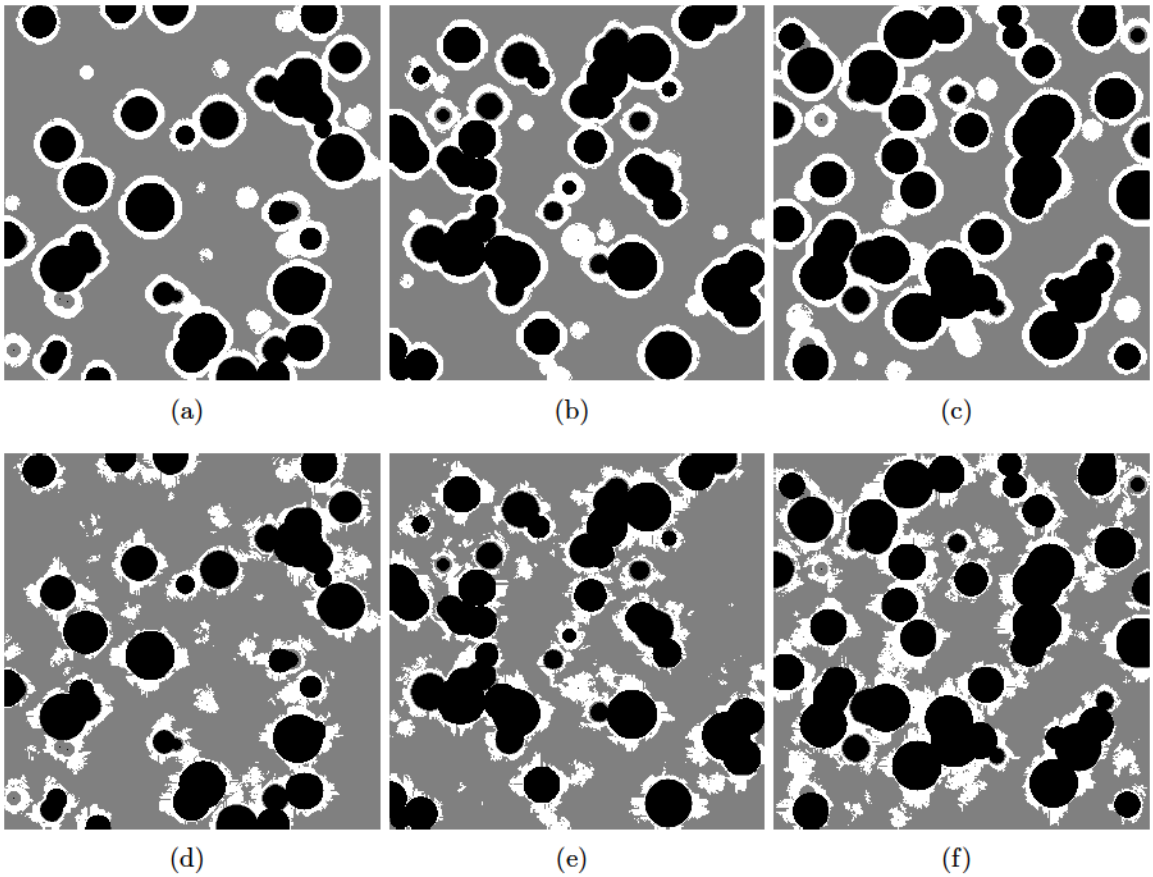

Figure 6.7 – Ionomer distribution at: a) 25%, b) 50% and c) 75% z depth for I/C = 0.87 with $\sigma = 2.1$ and d) 25%, e) 50% and f) 75% z depth for I/C = 0.87 with $\sigma = 5$. Ionomer is shown in white, pores are grey and solid is black.

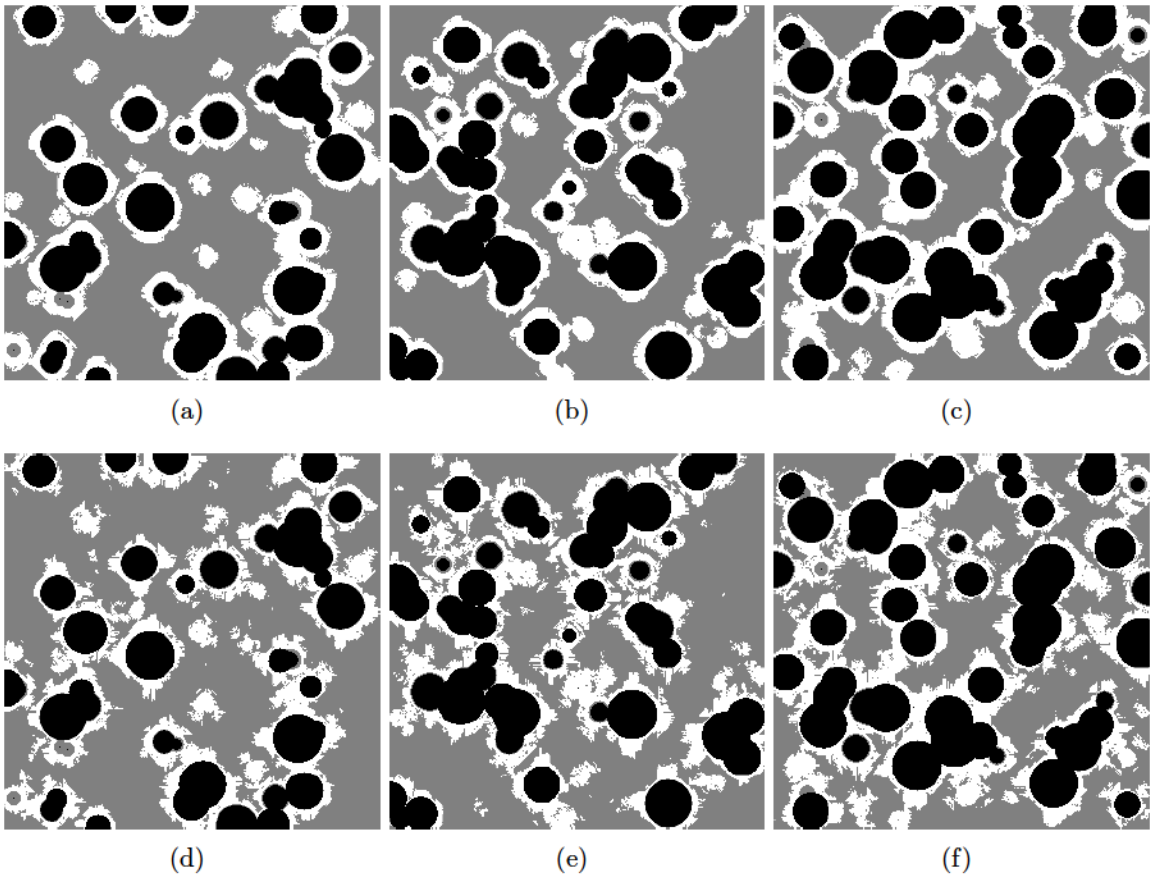

Figure 6.8 – Ionomer distribution at: a) 25%, b) 50% and c) 75% z depth for I/C = 1.13 with $\sigma = 3$ and d) 25%, e) 50% and f) 75% z depth for I/C = 1.13 with $\sigma = 6$. Ionomer is shown in white, pores are grey and solid is black.

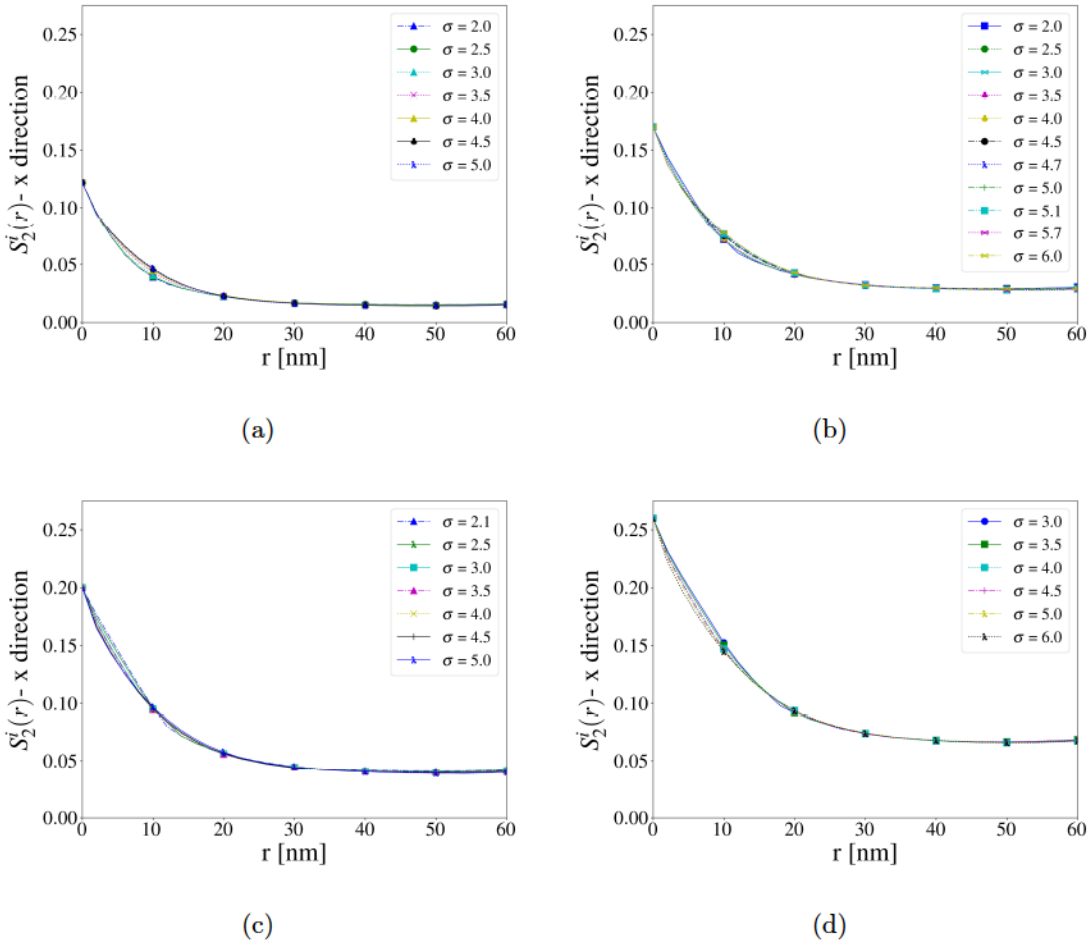

Figure 6.9 – Two-point correlation function in the x direction for the ionomer phase for different ionomer distributions with an I/C ratio of: a) 0.53, b) 0.74, c) 0.87 and d) 1.13.

leads to an increase in the slope of the two-point correlation function at $r = 0$. This can be clearly seen for I/C ratios of 0.87 and 1.13. An increase in the slope of the two-point correlation function indicates an increase in the interfacial area between the ionomer and the pores (assuming full ionomer coverage). This is expected as an increase in σ leads to non-uniform ionomer distributions and hence, more of the ionomer surfaces are exposed to pore and solid.

Figure 6.10 shows the chord length function for the ionomer phase ($C^i(r)$) for different ionomer distributions and I/C ratios. At low σ values (2-3 for I/C ratios of 0.53, 0.74 and 0.87 and 3-4 for I/C ratio of 1.13), the chord length function shows distinct maxima indicating that there is a maximum probability of finding chords of that length. This is expected for a uniform ionomer distribution. For higher σ values, the chord length function monotonically decreases with an increase in the chord length, therefore indicating a more

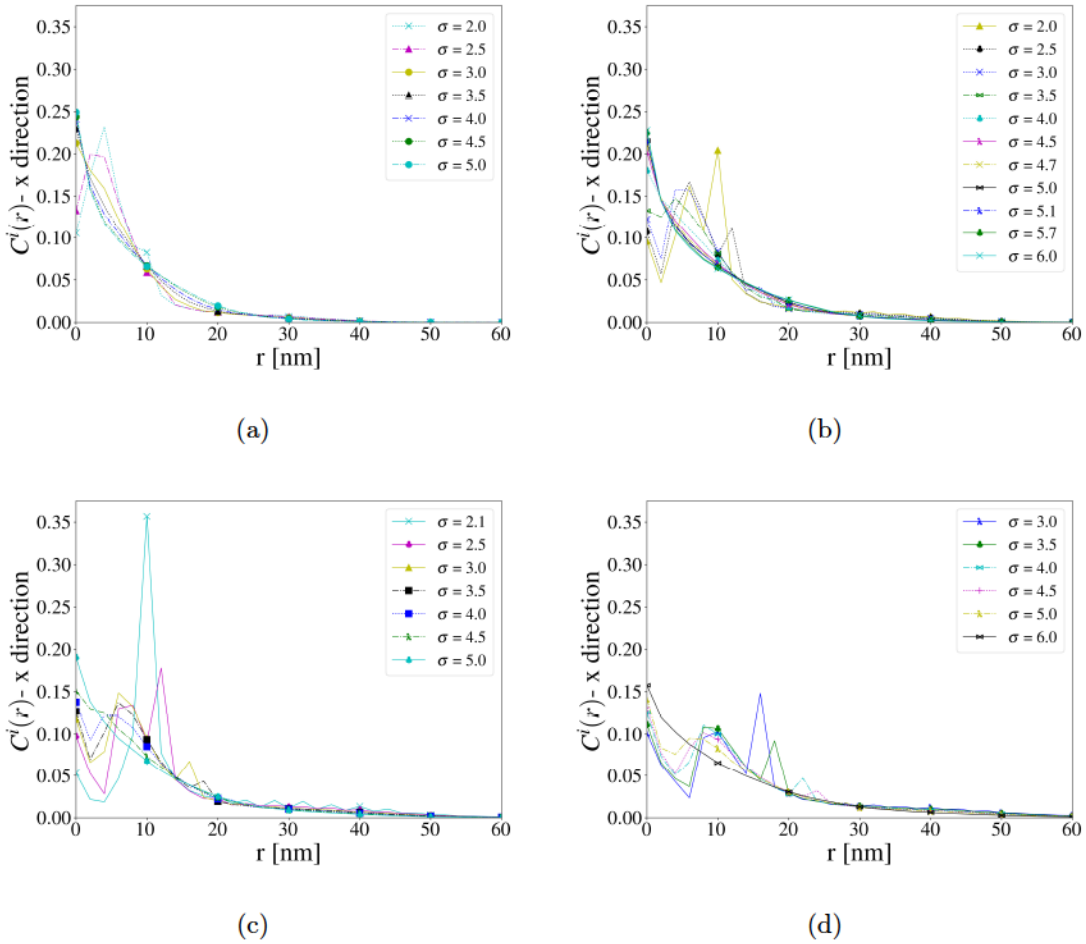

Figure 6.10 – Chord length function in the x direction for the ionomer phase for different ionomer distributions with an I/C ratio of: a) 0.53, b) 0.74, c) 0.87 and d) 1.13.

random ionomer distribution. Also, an increase in the I/C ratio leads to an increase in the probability of finding longer chords due to an increase in the film thickness.

Figure 6.11 shows the 3D reconstructions of the ionomer films with different σ values for I/C ratios of 0.53 and 1.13 with the ionomer films colored by local thickness. The local thickness of the ionomer films is computed using the minimum chord lengths. For every ionomer voxel at the solid-ionomer interface, the minimum length of a line within the ionomer phase connecting the ionomer-solid interface to another ionomer interface, in any of the Cartesian directions is used as the thickness of the ionomer film. The minimum chord length in the Cartesian directions is chosen to characterize the film thickness because it represents the constrictions in the proton conducting network for the numerical simulations to evaluate effective protonic conductivity and electrochemical reactions. The average thickness is then

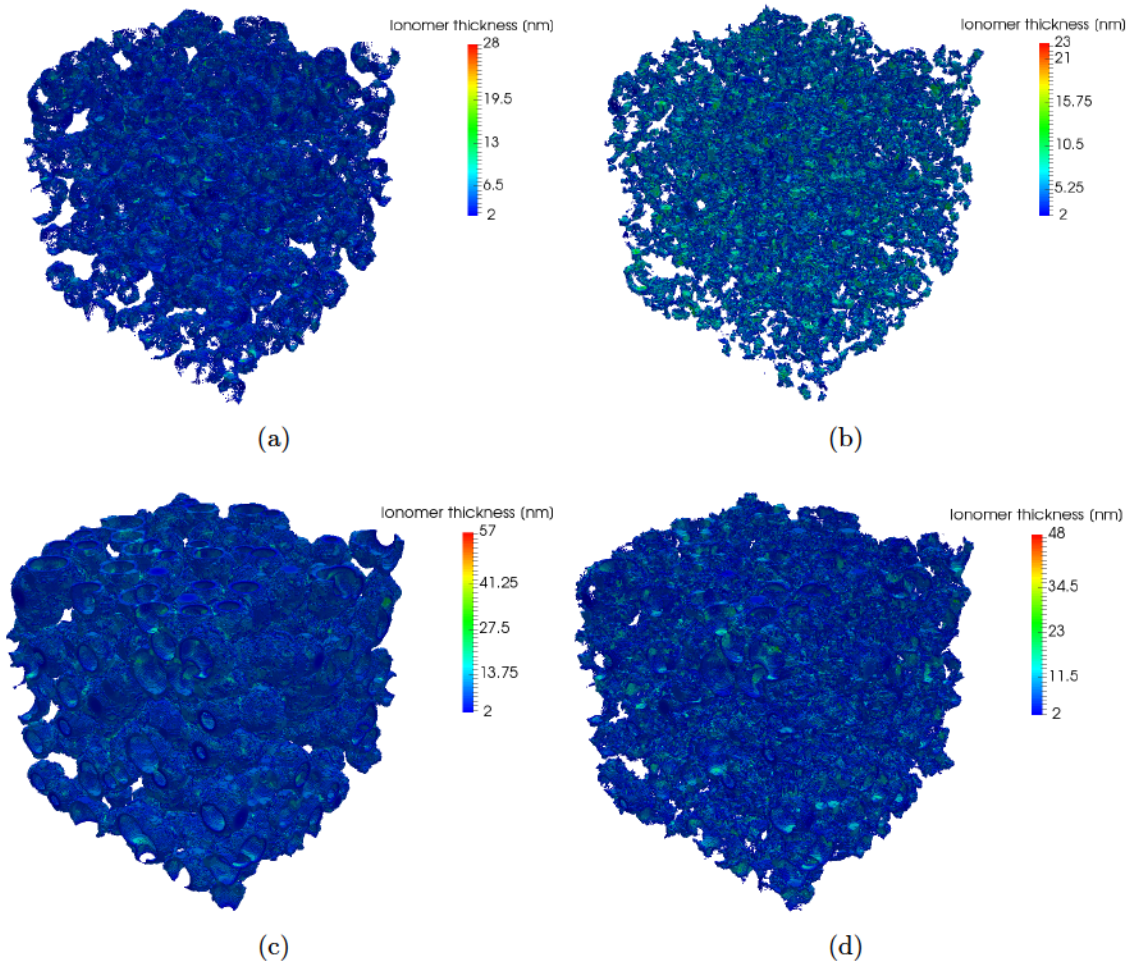

Figure 6.11 – 3D ionomer reconstructions with local thickness of the ionomer films for: I/C ratio of 0.53 with a) $\sigma = 2$ and b) $\sigma = 5$; I/C ratio of 1.13 with c) $\sigma = 3$ and d) $\sigma = 6$.

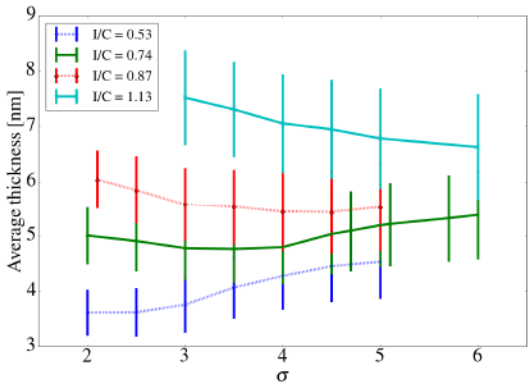

Figure 6.12 – Average thickness of the ionomer films reconstructed using distributions with different σ values and different I/C ratios. The error bars on the thickness value indicate $\pm$ 0.25 $\times$ standard deviation in the local film thickness.

computed as the average of the thickness value for all ionomer voxels at the solid-ionomer interface.

Figure 6.12 shows the average thickness of the ionomer films reconstructed using distributions with different σ values for different I/C ratios. An increase in the I/C ratio from 0.53 to 1.13 leads to an increase in the average thickness from a 3.5 - 4.5 nm range to a 6.6 - 7.6 nm range. The effect of the distribution parameter σ on the average thickness depends on the ionomer content. At low ionomer contents, an increase in σ results in an increase in the average thickness because an increase in σ results in a stacking up of the ionomer voxels to form thicker films while reducing the ionomer coverage as shown in Figures 6.5 and 6.6. At higher ionomer contents, an increase in σ results in a decrease in the average thickness because the minimum chord length is reduced due to more finger like geometries forming with an increase in the non-uniformity as shown in Figures 6.11c-d even though the coverage remains constant.

Figure 6.12 also shows the standard deviation in the local thickness of the ionomer films as the error bars for every σ value. The standard deviation of the local thickness of ionomer films is strongly dependent on the distribution parameter σ. An increase in σ results in an increase in the standard deviation of the local thickness and the increase is more pronounced at lower ionomer contents.

Figure 6.13 shows the ionomer film coverage on the solid surface for different ionomer distributions and ionomer contents. At low I/C ratios, an increase in σ leads to a decrease in the ionomer coverage. For higher I/C ratios however, the coverage remains close to 100%

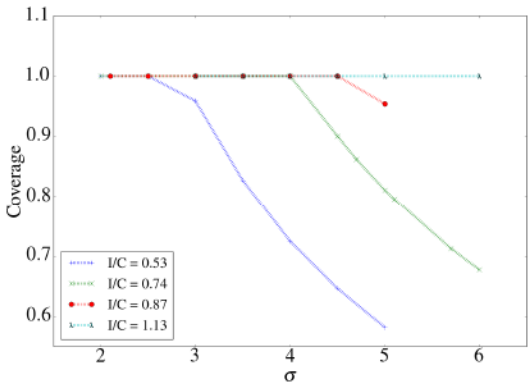

Figure 6.13 – Ionomer film coverage on the solid surface as a function of σ value for different reconstructions.

even for relatively high σ values. This is likely due to the method used in this study to distribute the ionomer which based on imaging studies [283] assumes ionomer forms thin films. The ionomer structure would depend on the type of solvent, ionomer content and preparation method [281, 282, 285] and might form aggregates which have not been accounted for in the reconstruction algorithm.

Figure 6.14 shows the void phase two-point correlation function ($S_2^v(r)$) in the x direction for different ionomer distributions and I/C ratios. The y intercept on Figures 6.14a-d shows the porosity of the reconstructions. An increase in the I/C ratio from 0.53 to 1.13 leads to a decrease in the porosity from 0.63 to 0.49. Similar to the two-point correlation for the ionomer phase, the slope of the two-point correlation for the void phase increases with an increase in σ indicating a higher interfacial area between the void and non-void (ionomer and solid) phase. Figure 6.15 shows the void phase chord length function ($C^v(r)$) for different ionomer distributions and I/C ratios. Unlike the chord length function for the ionomer phase, no maxima are observed in the void phase chord length function. An increase in the ionomer distribution parameter σ leads to an increase in the chord length function for $r < 10$ nm indicating a decrease in the pore size. The decrease in the pore size with an increase in σ is further evident when analyzing the pore size distribution in Figure 6.16.

Figure 6.16 shows the changes in pore size distribution with the ionomer distribution parameter σ and I/C ratio. An increase in σ leads to a decrease in the pore sizes for all I/C ratios. The mean pore radius, defined as the weighted arithmetic mean of the local pore radii (Equation (4.5)), decreases from 35.2 nm to 26.8 nm and from 30.2 nm to 22.6 nm for the two extreme σ values for an I/C ratio of 0.53 and 1.13 respectively. Therefore,

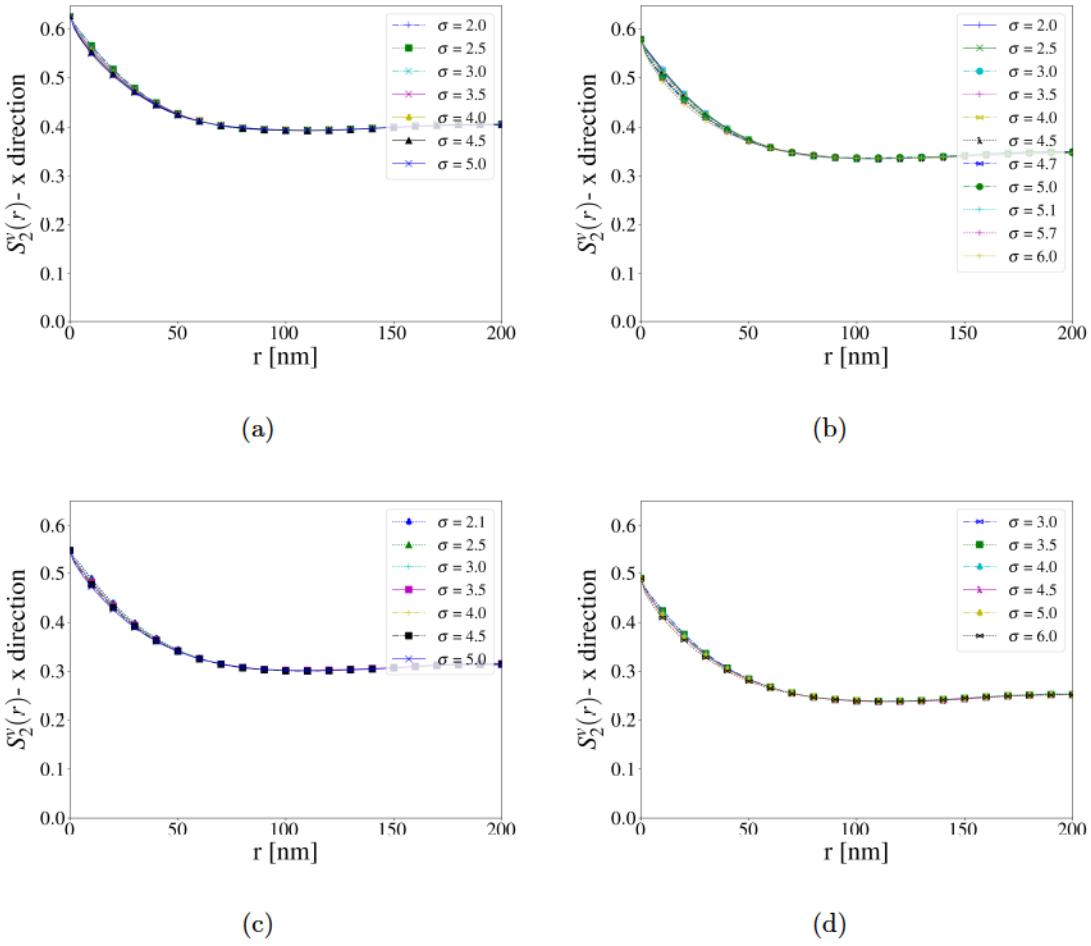

Figure 6.14 – Two-point correlation function in the x direction for the void phase for different ionomer distributions with an I/C ratio of: a) 0.53, b) 0.74, c) 0.87 and d) 1.13.

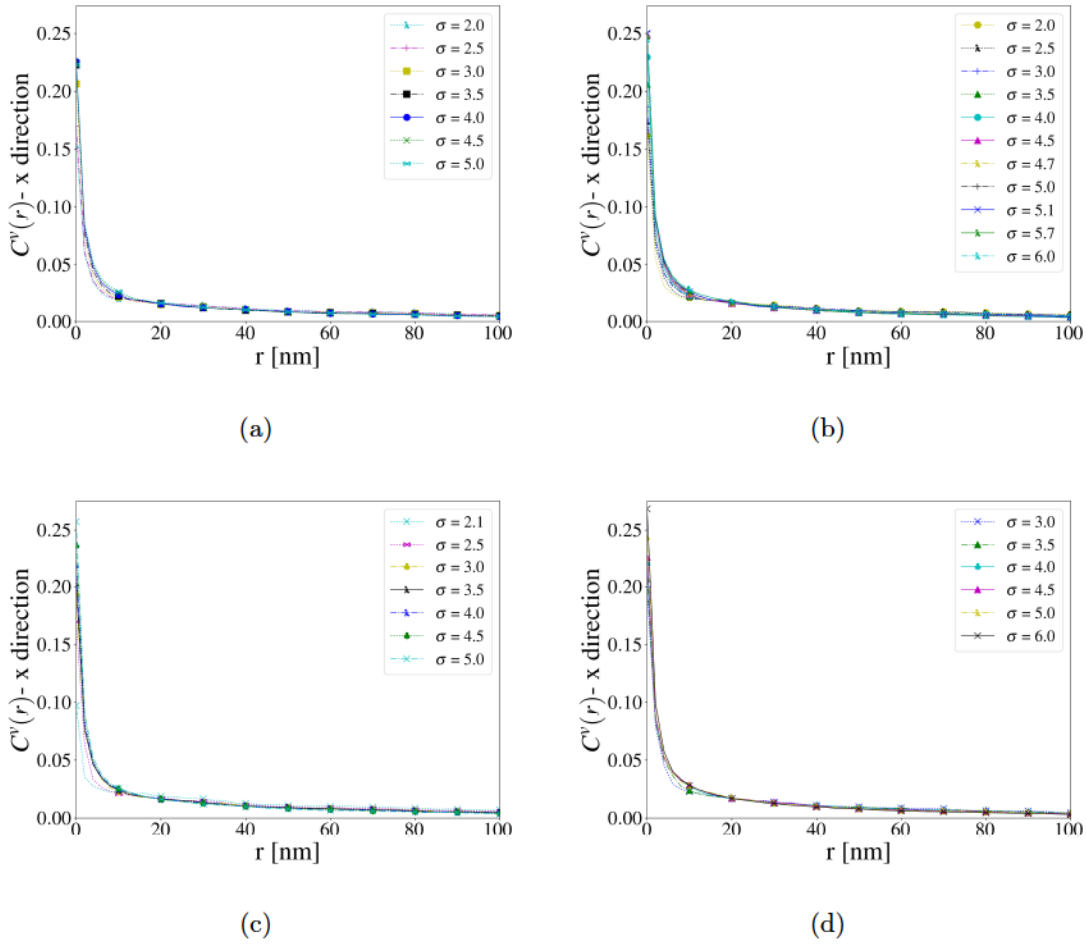

Figure 6.15 – Chord length function in the x direction for the void phase for different ionomer distributions with an I/C ratio of: a) 0.53, b) 0.74, c) 0.87 and d) 1.13.

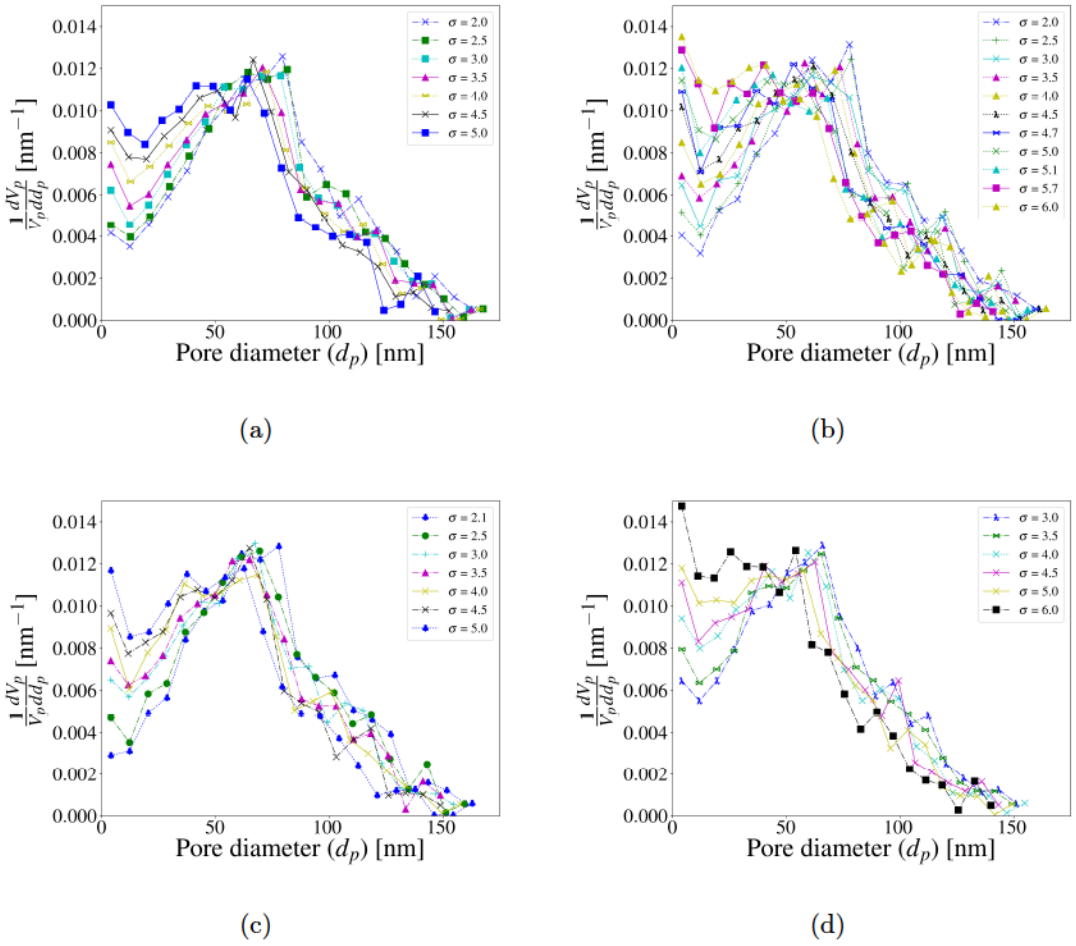

Figure 6.16 – Pore size distribution for the reconstructions with different ionomer distributions with an I/C ratio of: a) 0.53, b) 0.74, c) 0.87 and d) 1.13.

the ionomer distribution can have a significant impact on the pore structure even for same ionomer loadings. Further, an increase in the I/C ratio also leads to a decrease in the average pore size due to a decrease in the porosity.

6.3 Effect of ionomer content and distribution on transport properties

Reconstructions with different ionomer content and distribution were used to simulate proton conduction in the ionomer phase and oxygen diffusion in the pore phase and to compute the effective protonic conductivity and effective diffusivity for the reconstructions. As discussed earlier, the conductivity of thin films depends on the thickness, temperature and relative

Table 6.1 – Value of fitting parameters used to predict the bulk protonic conductivity of Nafion thin films as a function of thickness.

Parameter	60°C and 80% RH	30°C and 20% RH
a	1.12×10^{-3}	5.99×10^{-3}
b	-1.84	-6.78

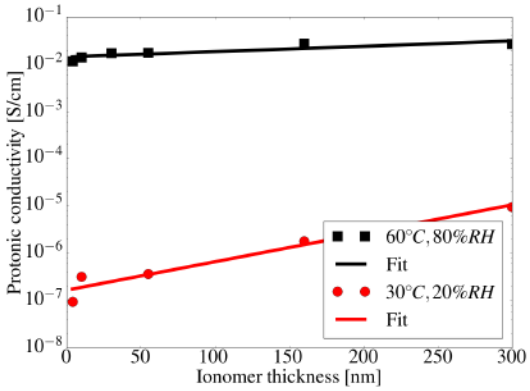

Figure 6.17 – Ionomer film conductivity as a function of film thickness from experimental data reported by Paul et al. [12]. The numerical fit is given by Equation (6.3).

humidity [12, 251–256]. Paul et al. [12] have shown that the conductivity of ionomer thin films is strongly affected by confinement effects and thus, thickness (as shown in Figure 6.17). Therefore, a local ionomer thickness dependent bulk protonic conductivity (σ^{bulk}) was used. The numerical fit in Figure 6.17 is estimated using an exponential relationship between the film conductivity (σ^{bulk}) and thickness (t) which can be expressed as:

$$\log_{10}(\sigma^{\text{bulk}}) = at + b, \tag{6.3}$$

where a and b are fitting parameters which depend on the temperature and RH. Table 6.1 shows the values of the fitting parameters a and b for the two conditions used in this study. To generate the meshes to study the proton conduction in the reconstructed ionomer films, first the percolating ionomer network was extracted and then the local thickness of the ionomer films was computed. The local thickness was passed as field data for every voxel in the VTK mesh.

Figure 6.18a shows the effective protonic conductivity as a function of I/C ratio for the uniform ionomer distributions using the thickness dependent local conductivity. An increase in the ionomer volume fraction leads to an increase in the protonic conductivity. Figures 6.18b shows the ratio of the effective protonic conductivity (σ_M^{eff}) for non-uniform ionomer reconstructions to the effective protonic conductivity of a uniform ionomer recon-

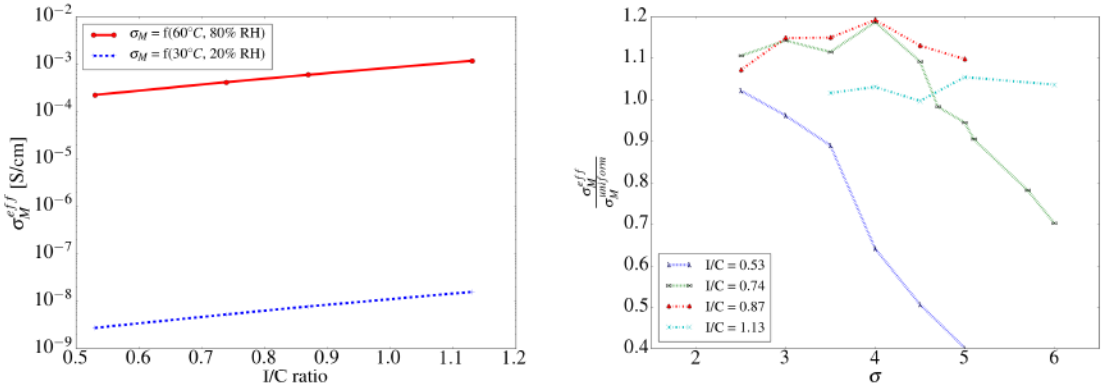

(a) (b)

Figure 6.18 – a) Effective protonic conductivity as a function of the I/C ratio for reconstructions with uniform ionomer distribution ($\sigma = 2$ for I/C = 0.53 and 0.74, $\sigma = 2.1$ for I/C = 0.87 and $\sigma = 3$ for I/C = 1.13). b) Ratio of effective protonic conductivity to the effective protonic conductivity for a uniform ionomer distribution using conductivity as a function of film thickness at 60°C and 80% RH.

struction ($(\sigma_M^{uniform})$ with the same volume fraction at 60°C and 80% RH. The variation of $\frac{\sigma_M^{eff}}{\sigma_M^{uniform}}$ with σ was identical at 30°C and 20% RH so it is not shown here. At low I/C ratios, an increase in the σ results in a decrease in the effective protonic conductivity. At high I/C ratios, the change in ionomer distribution has negligible effect on the effective protonic conductivity of the CL. The reason for the change in the effective protonic conductivity at low I/C ratios could be due to: a) variation in local ionomer thickness; and b) change in tortuosity of the ionomer network.

To study the effect of the local ionomer thickness, a new simulation with constant film conductivity was performed. Figure 6.19 shows the $\frac{\widehat{\sigma_M^{eff}}}{\widehat{\sigma_M^{uniform}}}$ for these simulations. As can be observed, Figure 6.18b and 6.19 have identical values demonstrating local conductivity changes do not have an impact on the overall protonic conductivity. At low I/C ratios, a decrease in the ratio of $\frac{\widehat{\sigma_M^{eff}}}{\widehat{\sigma_M^{uniform}}}$ also indicates an increase in the tortuosity of the ionomer network for the non-uniform ionomer distributions because the bulk conductivity and ionomer volume fraction were constant.

Figure 6.20 shows a comparison of the experimentally determined effective protonic conductivities for pseudo-catalyst layers (without platinum) to those obtained in this study. The average effective conductivity at 60°C and 80% RH was computed using an Arrhenius equation with E_a reported by Paul et al. [12]. The simulated effective conductivities are roughly

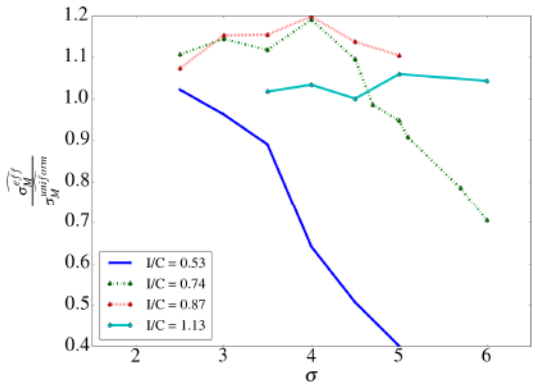

Figure 6.19 – Ratio of effective protonic conductivity to the effective protonic conductivity for a uniform ionomer distribution using a constant bulk conductivity.

an order of magnitude lower than the values reported by Iden et al. [13]. This discrepancy might be attributed to the interactions between the ionomer films and substrate. The protonic conductivity of thin films used for this study was based on thin films self-assembled on SiO_2 whereas the Iden et al. [13] used a layer with carbon. Shim et al. [253] showed that the water uptake in ionomer thin films was dependent on the substrate. Additional experimental data is therefore required to accurately describe the ionomer thin film network in the CL.

Reconstructions with different ionomer distributions and I/C ratios were also used to study the effective diffusivity of the CL. To compute the effective diffusivity the percolating pore network is extracted for mesh generation and used for simulation. The diffusion in ionomer phase is ignored for this case due to the relatively low solubility of oxygen in ionomer (Henry's constant of $3.1664\times\ 10^{10}$ Pa cm^3/ mol for Nafion membrane) and much lower bulk diffusion coefficient (3 to 4 orders of magnitude smaller for Nafion membrane) which would have negligible effect on the total oxygen flux when a constant concentration gradient is applied.

Figure 6.21a shows the gas phase formation factor, defined as the ratio of effective diffusivity to bulk diffusivity, as a function of the ionomer distribution parameter σ for different I/C ratios. The effective oxygen diffusivity decreases with an increase in the I/C ratio due to a decrease in porosity and pore sizes. The effective diffusivity also decreases with an increase in σ due to a decrease in the pore sizes as shown in Figure 6.16.

Figure 6.21b shows a comparison of the average effective diffusivity values from this study to those measured by Yu et al. [9]. Yu et al. [9] measured the effective diffusivity

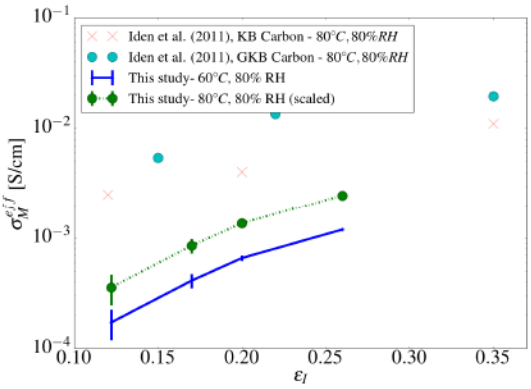

Figure 6.20 – Comparison of experimentally measured CL effective protonic conductivity (σ_M^{eff}) by Iden et al. [13] at different ionomer volume fractions (ε_I) to the average effective conductivity (error bars denote the standard deviation) predicted in this study. The experimental data by Iden et al. [13] was measured at 80°C and 80% RH for Ketjen Black (KB) and Graphitized Ketjen Black (GKB) pseudo catalyst layers. Arrhenius equation with the activation energy (E_a) reported by Paul et al. [12] was used to compute the effective conductivities at 80°C and 80% RH from the values at 60°C and 80% RH.

for CLs with different I/C ratios for two different catalysts, i.e., platinum on amorphous carbon (Pt/V_A) and platinum on graphitized carbon (Pt/V_G). Similar trends are observed, however the average formation factors predicted in this study are higher because of the higher porosity of the CL reconstructions in this study. For example, the porosity of the CL with I/C of 0.53 in this study was 0.628 where as the porosity of the CLs (measured using MIP) with I/C of 0.5 from Yu et al. [9] was 0.498 and 0.524 for Pt/V_A and Pt/V_G respectively. The average formation factor of 0.050 for the reconstructions with an I/C ratio of 1.13 and a porosity of 0.49 is similar to the value of 0.055 from Yu et al. [9] for a porosity of 0.498.

6.4 Effect of ionomer content and distribution on electrochemical performance

Electrochemical reactions were simulated using the model described in Section 2.3.4 to study the effect of the ionomer distribution and content on the electrochemical performance of the CL. For the electrochemical study, reconstructions with dimensions 400 nm × 400 nm × 1200 nm with a voxel resolution of 2 nm in each direction were used. The through-plane thickness of the CL was increased to 1200 nm to account for oxygen and protonic potential gradients across a CL and the boundary conditions given by Equation (2.24) were used. The in-plane thickness was fixed at 400 nm which was found to be a sufficient cross-sectional

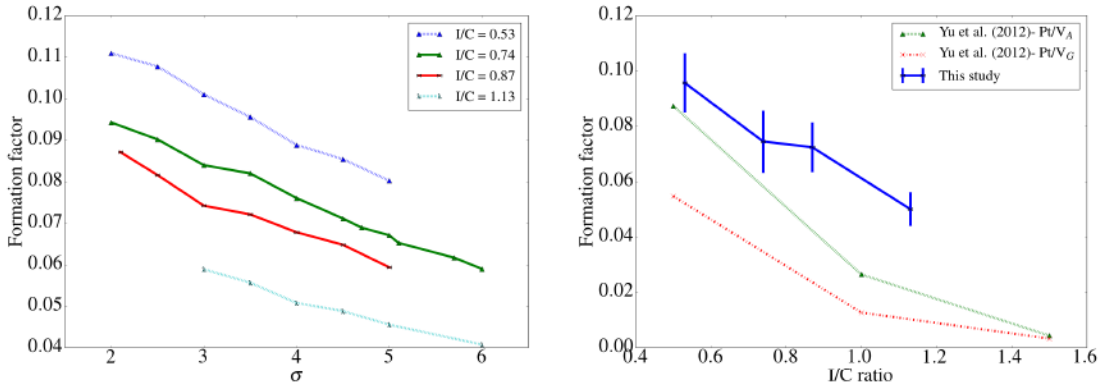

Figure 6.21 – a) Gas phase formation factor as a function of ionomer distributions for different I/C ratios. b) Comparison of the average formation factor values from this study to experimental effective diffusivity measurements by Yu et al. [9].

area for statistical representativeness by Sabharwal et al. [51]. The base reconstruction was generated using the same parameters as earlier, i.e., solid (carbon and platinum) volume fraction of 0.25, spherical particles with radii 20, 30 and 40 nm with a probability of 0.25, 0.5 and 0.25 respectively and free overlap. The ionomer was coated on the microstructure with a volume fraction of 0.122, 0.17, 0.20, 0.26 and 0.30 corresponding to I/C ratio of 0.53, 0.74, 0.87, 1.13 and 1.30 respectively. For each ionomer volume fraction, a uniform ionomer distribution (low σ value of 2 or 3) and a non-uniform ionomer distribution (high σ value of 5 or 6) were used.

The electrochemical simulations were carried out assuming 10% oxygen in nitrogen mixture at 80°C, 1 atm pressure and 50% RH. At these conditions, the oxygen molar fraction in the channel is 0.0768. This was directly applied as a boundary condition in Equation (2.24), thereby ignoring any mass transport losses in the channel and diffusion media. The current density was computed at a cell voltage of 0.3 V which was applied as a constant electronic potential in the CL. The protonic potential at the CL-Membrane interface was assumed to be 0 V, thereby ignoring any ohmic losses from the anode CL and membrane. The electrochemically active surface area (ECSA) was distributed uniformly on the solid surface of the reconstruction. However, only the solid surface in contact with the ionomer was considered active, thereby accounting for the effect of ionomer coverage on the solid surface. The protonic conductivity in the ionomer film was kept constant at 0.08 S/cm (maximum conductivity of 10 nm films reported by Paul et al. [12]) due to the negligible change in effective protonic conductivity with local ionomer thickness.

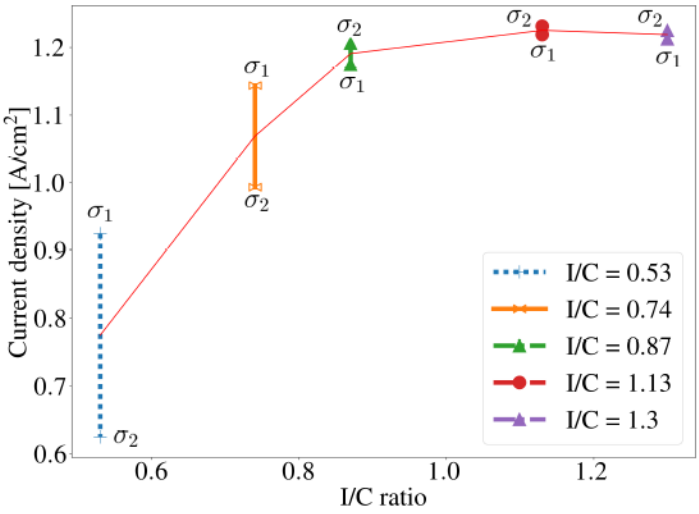

Figure 6.22 – Current density at 0.3 V for different I/C ratios in 10% oxygen in air at 80°C and 1 atm absolute pressure. For a given I/C ratio, a uniform (σ_1) and non-uniform (σ_2) ionomer distribution was used and $\sigma_2 > \sigma_1$.

Figure 6.22 shows the current density at 0.3 V for CL reconstructions with different I/C ratios and ionomer distributions. The average current density increases with an increase in the I/C ratio upto 1.13. Further increase in the I/C ratio results in a slight decrease of 10 mA/cm^2. At low I/C ratios, the current density decreases with an increase in the ionomer distribution parameter σ. The drop in current density with an increase in σ is due to: i) a decrease in the coverage thereby, resulting in a decrease in the active area; ii) a decrease in the effective protonic conductivity and diffusivity; iii) increased local fluxes resulting in higher interfacial resistance; and iv) an increase in percolating ionomer volume fraction. For higher I/C ratios, there is less than 2.5% change in the current density with σ. To better understand the reason for the variation in current density with I/C ratio and ionomer distribution(and lack there of at high I/C ratios), the protonic potential and oxygen molar fraction profiles are analyzed.

Figure 6.23 shows the oxygen molar fraction in the CL reconstructions with I/C ratio of 0.53, 1.13 and 1.30 with different ionomer distributions. There are no mass transport losses observed in the CL even at the highest I/C ratio of 1.30 where the drop in oxygen molar fraction across the domain is less than 1.5%. The reason for the lack of mass transport losses in the CL under dry conditions were discussed in Section 5.2. There are no mass transport losses observed in the current study for an I/C ratio of 1.30 which corresponds to a Nafion loading of 41%. This is consistent with the results from Shukla et al. [38] for

thin low loading electrodes, who observed a plateau in the performance for Nafion loadings from 20-40%. Shukla et al. [38] reported a drop in performance with a further increase in the Nafion loading to 50% by weight which resulted in a porosity of less than 0.3. For the CL reconstructions, the porosities are much higher with a value of 0.45 at an I/C ratio of 1.3.

Figure 6.24 shows the protonic potential profile in the CLs. An increase in the Nafion loading results in a decrease in the protonic potential drop across the CL. CL reconstructions with an I/C ratio of 0.53, which had the lowest effective protonic conductivity, show the largest drop in protonic potential across the CL. As a result, CL reconstructions with I/C ratio of 0.53 had the lowest current density due to lower overpotentials (Equation (5.1)) in the domain, given that the oxygen molar fraction profiles for all the cases were nearly identical. Comparison of the protonic potential profiles in Figures 6.23a and 6.24b also indicates an increase in the local fluxes at the solid-ionomer interface due to an increase in the overpotential with a decrease in coverage. At higher I/C ratios, the effective protonic conductivity increases, thereby resulting in lower ohmic losses and hence, an increase in the current density.

Several experimental studies [38, 39, 120–122, 278–280] have shown an optimal Nafion loading of 30-40% by weight for conventional and low loading electrodes, the former being more representative of these simulations due to the lower layer thickness. For the current study, the optimal Nafion loading was found to be 38% by weight, i.e., an I/C ratio of 1.13. However, experimental studies show a significant drop in the electrochemical performance for higher I/C ratios which is not seen in the results from the current study.

6.5 Conclusions

Stochastic reconstructions were used to study the effect of ionomer loading and ionomer distribution on the CL morphology, transport properties and electrochemical performance. The solid phase of the reconstructions was generated using the overlapping sphere algorithm with different particle sizes. Ionomer films were reconstructed on the solid phase using a film based reconstruction algorithm which allowed control over the ionomer distribution using an input probability function.

Statistical functions were used to characterize the change in ionomer films and pores in the CL reconstructions with a change in ionomer distribution and volume fraction. Changing the ionomer distribution from uniform to non-uniform resulted in an increase in the

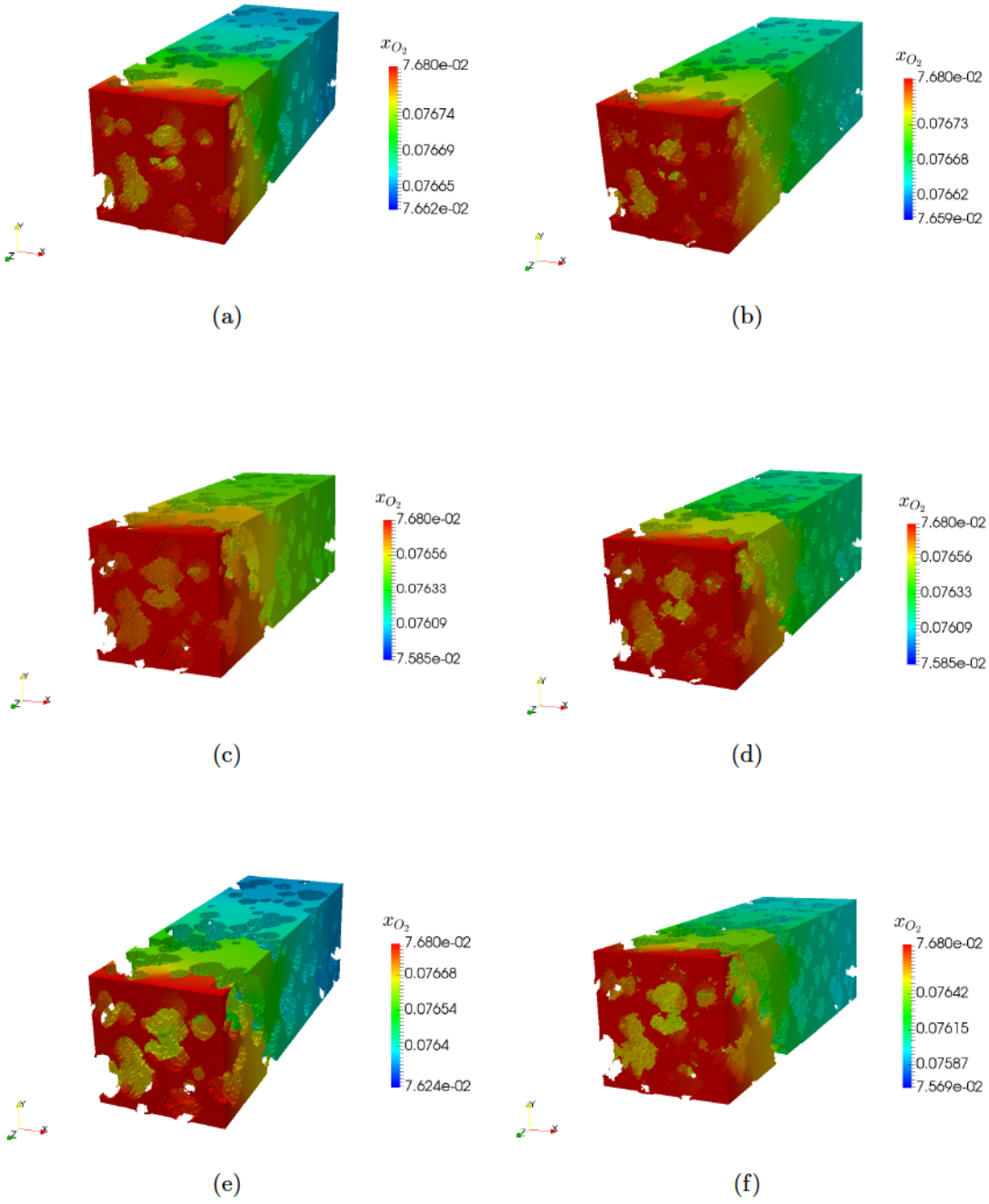

Figure 6.23 – Oxygen molar fraction profiles at 0.3 V in the pore phase of the CL reconstruction with: I/C ratio of 0.53 and a) $\sigma = 2$ and b) $\sigma = 5$; I/C ratio of 1.13 and c) $\sigma = 3$ and d) $\sigma = 5$; I/C ratio of 1.30 and e) $\sigma = 3$ and f) $\sigma = 6$.

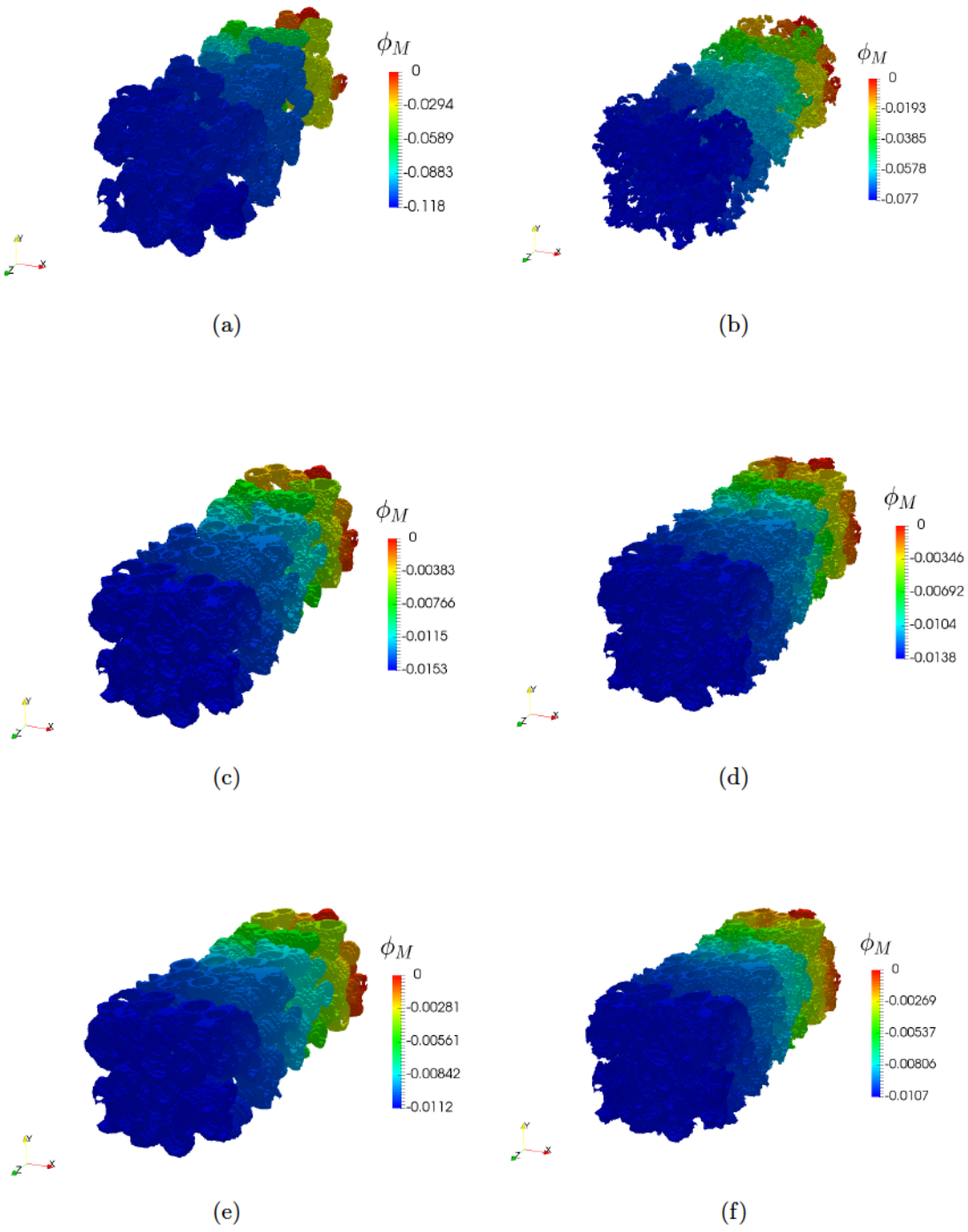

Figure 6.24 – Protonic potential profiles (in V) at 0.3 V in the ionomer phase of the CL reconstruction with: I/C ratio of 0.53 and a) $\sigma = 2$ and b) $\sigma = 5$; I/C ratio of 1.13 and c) $\sigma = 3$ and d) $\sigma = 5$; I/C ratio of 1.30 and e) $\sigma = 3$ and f) $\sigma = 6$.

specific interfacial area, larger chords in the ionomer phase and decrease in coverage. Uniform ionomer films showed distinct peaks in the chord length function for the ionomer phase while for non-uniform ionomer distributions, the chord length function decreased monotonically with an increase in chord lengths. Varying the ionomer distribution and content also resulted in a modification of the pore morphology in the CL reconstructions. Increase in ionomer content and non-uniform ionomer distributions resulted in smaller pore sizes which also resulted in smaller chords in the pore phase.

Numerical simulations were used to compute the effective protonic conductivity and effective diffusivity of the CLs with different ionomer content and distribution. An ionomer thickness dependent local bulk protonic conductivity was used to compute the effective protonic conductivity of the CLs. The effective protonic conductivity increased with an increase in the ionomer volume fraction. At low I/C ratios, the effective protonic conductivity decreased for non-uniform ionomer films due to an increase in the geometric tortuosity factor of the ionomer network and a change in the local ionomer thickness had negligible effect. For higher I/C ratios, the effective protonic conductivity showed negligible change with the ionomer distribution. The effective diffusivity decreased with an increase in the ionomer volume fraction and non-uniformity of the ionomer distribution because of a decrease in the pore sizes.

Electrochemical simulations were performed on the CLs with different I/C ratios and ionomer distributions. An increase in the I/C ratio resulted in an increase in the current density at 0.3 V upto an I/C ratio of 1.13, beyond which the current density remained nearly constant. The increase in current density was due to an increase in the protonic conductivity and coverage in the CL. At low I/C ratios, a change in the ionomer distribution from uniform to non-uniform resulted in a decrease in the current density due to a decrease in the coverage and higher ionomer film interfacial resistance. For high I/C ratios, ionomer distribution had negligible effect on the current density. The results from the current study show that the ionomer distribution has a significant impact on the effective transport properties and electrochemical performance at low I/C ratios.

Chapter 7

Conclusions and future work

Advancements in microscopy techniques are enabling the visualization and reconstruction of fuel cell porous media microstructures. Microscopy techniques provide large data sets describing the actual morphology of the porous media; however, extraction of meaningful information from these data sets using image analysis remains a challenge. The aim of this work was to develop a numerical framework to analyze microscopy images and study physical and electrochemical processes in the obtained microstructures. Such a numerical framework combined with imaging techniques is critical to analyze the effect of the porous media fabrication on its morphology and functionality. A better understanding of the correlations between fabrication, microstructure and functionality (transport properties and electrochemical performance) could aid in the design of optimal porous media for fuel cell applications.

This thesis presents a unified open-source numerical framework to go from microscopy images to transport properties and performance. Image processing routines to perform image registration, enhancement and segmentation were developed to binarize microscopy images. Statistical functions, such as two-point correlation function, chord length function and pore size distribution, were used to characterize the porous media microstructure. A voxel based meshing algorithm with the ability to input local information about the structure was developed to convert 3D images of microstructures to computational domains for numerical simulations. Numerical models were developed to simulate liquid water intrusion, gas and charge transport, and electrochemical reactions in the microstructures. To overcome the shortcomings of the previously reported models in literature, the electrochemical model was improved to account for the effect of ionomer thin films on the gas transport, multi-step ORR kinetics, interfacial reaction in the CL and gas transport in liquid water. The numerical framework was developed as part of the open-source package OpenFCST [229].

To simulate the liquid water intrusion in the fuel cell porous media, a cluster based full morphology (CFM) algorithm was developed. The CFM algorithm was validated against μ-CT images of a partially saturated GDL sample [154] by comparing: a) capillary pressure-saturation curves; b) liquid water distributions; and c) effective diffusivity in partially saturated GDLs obtained from the CFM algorithm and μ-CT images. It was found that the capillary pressure-saturation curves from μ-CT images and CFM simulations were similar at low capillary pressures but differed at higher capillary pressures. The liquid water distributions from μ-CT images were compared to those from CFM simulations at similar saturations and shown to have good agreement. The partially saturated GDL reconstructions from μ-CT images and CFM simulations were used to compute the effective diffusivity as a function of saturation. Comparison of the effective diffusivitivies in the partially saturated GDL reconstructions from μ-CT images and CFM simulations showed good agreement. The disagreement between the liquid distributions from the μ-CT images and CFM simulations was attributed to: a) the limitations of the CFM approach, which uses spherical pores, b) lack of knowledge of local contact angles in the GDL, and c) errors associated with the experiment. This comparison showed that the CFM algorithm had sufficient accuracy to describe the liquid water intrusion in the fuel cell porous media.

The developed numerical framework was used to analyze FIBSEM images of a CL [51]. Statistical analysis of the binarized FIBSEM images showed that the loss of resolution in the FIB slicing direction resulted in artificial anisotropy in the CL microstructure. Numerical simulations were performed on the CL reconstruction to study the gas transport and electrochemical performance of the CL under dry conditions. The effective diffusivity computed for the CL reconstruction was dominated by Knudsen effects and found to be similar to previously reported literature data. The artificial anisotropy in the FIB slicing direction resulted in a much higher effective diffusivity in that direction due to a lower tortuosity due to lack of morphological information. Additionally, it was found that for a domain size below 400 nm there was high variability in the local effective diffusivity. A parametric study was performed to analyze the effect interfacial resistance of the ionomer film to mass transport. Results of the electrochemical simulations showed that the interfacial resistance due to the ionomer film was the limiting mass transport resistance for the ORR. A novel nucleation based water intrusion algorithm was used to simulate water intrusion in the FIBSEM CL reconstruction and study the electrochemical performance as a function of local saturation [272]. It was found that there were negligible electrochemical losses with saturation when considering a CL representative elementary volume (REV) of dimensions of 400 nm. However, mass transport losses were observed in CL reconstructions with the entire through-plane thickness at different saturations. Thus, it was concluded that a large through-plane thickness of the CL

must be used to study the electrochemical performance of partially saturated CLs.

The objective of developing the numerical framework for microstructural analysis and modeling of fuel cell porous media was to understand the correlations between the microstructure, transport properties and electrochemical performance for fuel cell CLs, especially under partially saturated conditions which was missing in literature. Therefore, several parametric studies were performed to elucidate the relationship between the microstructure, transport properties and electrochemical performance of CLs.

Stochastic reconstructions were used to study the effective diffusivity of CLs as a function of porosity and local saturation [284]. An overlapping sphere based reconstruction algorithm was used to generate the CL reconstructions with different porosities. Comparison of statistical functions between the stochastic reconstructions with different particle radii and a CL reconstruction obtained using FIBSEM was used to determine the parameters to generate statistically representative CL reconstructions. Gas transport was simulated in CL reconstructions with different porosities under dry conditions to obtain a correlation for effective diffusivity based on percolation theory. The effective diffusivities for the CLs with different porosities were found to be in agreement with literature data. A nucleation based water intrusion algorithm was used to obtain partially saturated CL reconstructions with different dry porosities. Effective diffusivities were computed for these reconstructions to obtain the functional dependence of the effective diffusivity on the local saturation in the CL. It was found that a percolation theory based correlation function which was dependent on the effective porosity of the CL was sufficient to predict the dry and wet effective diffusivity of the CLs.

The overlapping sphere based reconstruction algorithm was also used to study the effect of CL pore size distribution (PSD) on the electrochemical performance of the CL under dry and wet conditions. The PSD of CLs was changed by modifying the particle radius used to generate the reconstructions and porosity of the CL. A reduction in the pore sizes resulted in an increase in the slope of the two-point correlation thereby indicating an increase in the interfacial area. The chord length function also showed a higher probability of finding larger chord lengths with an increase in the pore sizes. Electrochemical simulations were performed on the CL reconstructions with different PSDs and porosities under dry conditions. It was found that the change in PSD had negligible effect on the dry performance of the CL. This was due to the lack of mass transport losses in the CL with the interfacial resistance due to the ionomer film being the limiting mass transport resistance. Further, it was noted that the mass transport losses in the diffusion media and land-channel effects were ignored in

the current simulations which might contribute to performance of the CL. The nucleation based water intrusion algorithm was used to simulate liquid water intrusion in the CL reconstructions. Electrochemical performance initially remained constant and then decreased rapidly with an increase in capillary pressure due to the mass transport losses from oxygen transport in liquid filled pores. A decrease in the pore sizes resulted in better performance due to lower saturations at a given capillary pressure.

The effect of ionomer content and distribution on the transport properties and electrochemical performance of the CL was also analyzed. The ionomer films were reconstructed on the solid surface using a stochastic algorithm which generated the ionomer films layer-by-layer. The ionomer film distribution was controlled using an input probability function which was used to vary the ionomer distributions from uniform to non-uniform. Statistical functions were computed on the ionomer and void phase to characterize the microstructure. Changing the ionomer distribution from uniform to non-uniform resulted in an increase in the specific interfacial area for both the ionomer and void phase and a decrease in the pore sizes. For the uniform ionomer distributions, peaks were observed in the chord length distribution indicating a maximum probability of obtaining chords of a certain length. Effective protonic conductivity was calculated for the reconstructions using a film conductivity which was dependent on the film thickness, temperature and RH. The effective protonic conductivity was found to be dependent on the ionomer film tortuosity and showed negligible changes with the change in local ionomer film thickness. The effective diffusivity in the pores was found to decrease with an increase in the volume fraction and non-uniformity of the ionomer films. Electrochemical simulations were performed on the CL reconstructions with different ionomer volume fractions and distributions. An optimal I/C ratio of 1.13 was found from the electrochemical simulations which was consistent with experimental data from literature. At low I/C ratios, electrochemical performance of the CL decreased for non-uniform ionomer films due to a loss in coverage and higher ionomer film interfacial resistance. The results of the current study showed that the ionomer distribution is an important parameter which affects the transport properties and electrochemical performance especially when the ionomer content is low.

Based on the results of the electrochemical simulations for thin, low loading electrodes, the ideal electrode should have an I/C ratio of 1.13 and should have small pore sizes to delay flooding of the CL.

The open-source numerical framework developed in this study can also be used to analyze microstructures for other applications such as transport in soil [196, 286, 287] and rocks [288],

lithium ion batteries [289–292], solid oxide fuel cells [293], electrolyzers [294] and porous media for drug delivery [295]. The framework also provides a baseline for future studies in the area of microstructural modeling which can build upon it. The following sections highlight the contributions of this thesis and provide an outlook for future work.

7.1 Contributions

In terms of novel numerical methods in literature, the contributions of this work are:

1. developing a stochastic method to reconstruct PEMFC porous media and ionomer films for CLs;
2. developing an image processing framework to seamlessly obtain a computational mesh and a list of statistical correlation functions from either microscopy or reconstructed images;
3. developing numerical tools to perform liquid water intrusion in porous media;
4. developing numerical tools to study gas and charge transport, and electrochemical performance in microstructures under dry and wet conditions;

The tools developed in this study are part of an open-source framework called OpenFCST [229] and were validated with experimental data. These tools therefore, provide a benchmark for future studies on fuel cell microstructure based modeling.

In the area of advancing the knowledge of the field, the key contributions of this work are:

1. proposing a novel correlation to predict the effective diffusivity of CLs under dry and wet conditions;
2. demonstrating the effect of CL pore size distribution on the transport properties and electrochemical performance under dry and wet conditions;
3. demonstrating the effect of local ionomer distribution and content on the electrochemical performance of CLs;

This study is the first attempt at a systematic approach to analyzing the microstructure of a CL using statistical functions and correlating the changes to transport properties and electrochemical performance, especially under wet conditions. In addition to the studies

discussed in this thesis, the developed numerical framework was also used to analyze the morphology of different CLs using FIBSEM [51, 225, 296] and study transport [51, 225] and electrochemical reactions in these reconstructions under dry [51] and wet conditions [272].

7.2 Future work

As discussed before, the numerical tools developed in this study provide a framework for morphological analysis and study of physical and electrochemical processes for fuel cell porous media microstructure. Future studies should try to build upon the strengths of this framework and improve the models by accounting for additional physics. In this regard, accounting for the following physical processes could be useful:

1. Evaporation in the porous media [78, 80];
2. Contact resistance for electronic transport [61];

Thomas et al. [30] and Zhou et al. [31] attributed the improvement of performance in a fuel cell with MPL under wet conditions to higher evaporation caused by the MPL due to its low thermal conductivity. Therefore, analysis of evaporation in the fuel cell porous media is important in understanding the role of the MPL and GDL under wet conditions. Few studies in literature [78, 80] have modeled evaporation using Fick's law with saturation pressure boundary condition at the gas-liquid interface. These studies are good to represent the ex-situ experiments for liquid water evaporation in a GDL but to understand the in-situ evaporation in MPLs and GDLs, the thermal transport equation must be coupled with vapor transport. Such an evaporation model would be useful to better understand the role of the MPL in PEMFCs under wet conditions.

Most studies in literature, including this one, ignore the effect contact resistance on electronic transport. Kotaka et al. [61] showed that for MPLs the experimentally measured electronic conductivity was 39 times lower than the simulated effective electronic conductivity when contact resistance was ignored. Microstructural simulations combined with the image processing tools developed in this study could be used to develop a model for the contact resistance within the fuel cell porous media. This could also provide insight into the low thermal conductivity of MPLs because both electronic and thermal transport occur in the solid phase of the MPL.

Electrochemical simulation results in Chapters 5 and 6 showed that there were no mass transport losses in the CL under dry conditions. This was attributed to the mass transport

losses in the diffusion media and land-channel effects that were ignored in the current study. To account for these effects the microstructure simulations need to be coupled to macroscale models [31, 40, 167, 188, 189] which can be used to simulate the physical and electrochemical processes at the MEA level. Such a coupling between the two scales could be important to translate information from the microscale simulations to experimentally measurable quantities at the PEMFC scale and also, to optimize the overall fuel cell performance from a microstructure perspective.

References

[1] J. T. Gostick, M. A. Ioannidis, M. W. Fowler, M. D. Pritzker, Wettability and capillary behavior of fibrous gas diffusion media for polymer electrolyte membrane fuel cells, Journal of Power Sources 194 (1) (2009) 433–444.

[2] G. Hwang, A. Weber, Effective-diffusivity measurement of partially-saturated fuel-cell gas-diffusion layers, Journal of The Electrochemical Society 159 (11) (2012) F683–F692. doi:10.1149/2.024211jes.

[3] T. Tranter, P. Stogornyuk, J. Gostick, A. Burns, W. Gale, A method for measuring relative in-plane diffusivity of thin and partially saturated porous media: An application to fuel cell gas diffusion layers, International Journal of Heat and Mass Transfer 110 (2017) 132–141.

[4] K. J. Lange, P.-C. Sui, N. Djilali, Pore scale simulation of transport and electrochemical reactions in reconstructed pemfc catalyst layers, Journal of The Electrochemical Society 157 (10) (2010) B1434–B1442. doi:10.1149/1.3478207.

[5] H. Fathi, A. Raoof, S. Mansouri, M. T. van Genuchten, Effects of porosity and water saturation on the effective diffusivity of a cathode catalyst layer, Journal of The Electrochemical Society 164 (4) (2017) F298–F305. doi:10.1149/2.0871704jes.

[6] N. Siddique, F. Liu, Process based reconstruction and simulation of a three-dimensional fuel cell catalyst layer, Electrochimica Acta 55 (19) (2010) 5357–5366. doi:10.1016/j.electacta.2010.04.059.

[7] W. Zheng, S. H. Kim, The effects of catalyst layer microstructure and water saturation on the effective diffusivity in pemfc, Journal of The Electrochemical Society 165 (7) (2018) F468–F478. doi:10.1149/2.0711807jes.

[8] S. Shin, A.-R. Kim, S. Um, Computational prediction of nanoscale transport characteristics and catalyst utilization in fuel cell catalyst layers by the lattice boltzmann method, Electrochimica Acta 275 (2018) 87–99. doi:10.1016/j.electacta.2018.04.138.

[9] Z. Yu, R. Carter, J. Zhang, Measurements of pore size distribution, porosity, effective oxygen diffusivity, and tortuosity of pem fuel cell electrodes, Fuel Cells 12 (4) (2012) 557–565. doi:10.1002/fuce.201200017.

[10] G. Inoue, K. Yokoyama, J. Ooyama, T. Terao, T. Tokunaga, N. Kubo, M. Kawase, Theoretical examination of effective oxygen diffusion coefficient and electrical conductivity of polymer electrolyte fuel cell porous components, Journal of Power Sources 327 (2016) 610–621. doi:10.1016/j.jpowsour.2016.07.107.

[11] S. Shukla, D. Stanier, M. Saha, J. Stumper, M. Secanell, Analysis of inkjet printed pefc electrodes with varying platinum loading, Journal of The Electrochemical Society 163 (7) (2016) F677–F687. doi:10.1149/2.1111607jes.

[12] D. K. Paul, R. McCreery, K. Karan, Proton transport property in supported nafion nanothin films by electrochemical impedance spectroscopy, Journal of The Electrochemical Society 161 (14) (2014) F1395–F1402.

[13] H. Iden, K. Sato, A. Ohma, K. Shinohara, Relationship among microstructure, ionomer property and proton transport in pseudo catalyst layers, Journal of The Electrochemical Society 158 (8) (2011) B987–B994.

[14] Energy Markets Fact Book 2014-2015, National Resources Canada, 2016.

[15] Climate action tracker, https://climateactiontracker.org/countries/canada/, Accessed: 2018-10-08.

[16] Hydrogen fuel cell technology- toyota canada, https://www.toyota.ca/toyota/en/safety-innovation/hydrogen-fuel-cell-mirai, Accessed: 2019-03-05.

[17] List of fuel cell vehicles, https://en.wikipedia.org/wiki/List_of_fuel_cell_vehicles, Accessed: 2019-03-05.

[18] World premiere: Alstoms hydrogen trains enter passenger service in lower saxony, https://www.alstom.com/press-releases-news/2018/9/world-premiere-alstoms-hydrogen-trains-enter-passenger-service-lower, Accessed: 2019-03-05.

[19] Nikola motor corp., https://nikolamotor.com/one#motor-features, Accessed: 2019-03-05.

[20] M. W. Ellis, M. R. Von Spakovsky, D. J. Nelson, Fuel cell systems: efficient, flexible energy conversion for the 21st century, Proceedings of the IEEE 89 (12) (2001) 1808–1818.

[21] M. Eikerling, A. Kornyshev, A. Kulikovsky, Can theory help to improve fuel cells, Fuel Cell Rev 1 (2005) 15–25.

[22] A. Kongkanand, M. Mathias, The priority and challenge of high-power performance of low-platinum proton-exchange membrane fuel cells, Journal of Physical Chemistry Letters 7 (7) (2016) 1127–1137. doi:10.1021/acs.jpclett.6b00216.

[23] R. Borup, J. Meyers, B. Pivovar, Y. Kim, R. Mukundan, N. Garland, D. Myers, M. Wilson, F. Garzon, D. Wood, P. Zelenay, K. More, K. Stroh, T. Zawodzinski, J. Boncella, J. McGrath, M. Inaba, K. Miyatake, M. Hori, K. Ota, Z. Ogumi, S. Miyata, A. Nishikata, Z. Siroma, Y. Uchimoto, K. Yasuda, K.-I. Kimijima, N. Iwashita, Scientific aspects of polymer electrolyte fuel cell durability and degradation, Chemical Reviews 107 (10) (2007) 3904–3951. doi:10.1021/cr0501821.

[24] C. Hartnig, L. Jörissen, J. Kerres, W. Lehnert, J. Scholta, Polymer electrolyte membrane fuel cells, Materials for fuel cells. 1st ed. Boca Raton, Boston, New York, Washington DC: CRC Press & Cambridge: Woodhead Publishing Ltd (2008) 101–84.

[25] A. Cecen, E. Wargo, A. Hanna, D. Turner, S. Kalidindi, E. Kumbur, 3-d microstructure analysis of fuel cell materials: spatial distributions of tortuosity, void size and diffusivity, Journal of The Electrochemical Society 159 (3) (2012) B299–B307.

[26] I. V. Zenyuk, D. Y. Parkinson, L. G. Connolly, A. Z. Weber, Gas-diffusion-layer structural properties under compression via x-ray tomography, Journal of Power Sources 328 (2016) 364–376.

[27] H. K. Atiyeh, K. Karan, B. Peppley, A. Phoenix, E. Halliop, J. Pharoah, Experimental investigation of the role of a microporous layer on the water transport and performance of a pem fuel cell, Journal of Power Sources 170 (1) (2007) 111–121.

[28] J. P. Owejan, J. E. Owejan, W. Gu, T. A. Trabold, T. W. Tighe, M. F. Mathias, Water transport mechanisms in pemfc gas diffusion layers, Journal of The Electrochemical Society 157 (10) (2010) B1456–B1464.

[29] K. Karan, H. Atiyeh, A. Phoenix, E. Halliop, J. Pharoah, B. Peppley, An experimental investigation of water transport in pemfcs the role of microporous layers, Electrochemical and solid-state letters 10 (2) (2007) B34–B38.

[30] A. Thomas, G. Maranzana, S. Didierjean, J. Dillet, O. Lottin, Thermal and water transfer in pemfcs: Investigating the role of the microporous layer, International Journal of Hydrogen Energy 39 (6) (2014) 2649–2658.

[31] J. Zhou, S. Shukla, A. Putz, M. Secanell, Analysis of the role of the microporous layer in improving polymer electrolyte fuel cell performance, Electrochimica Acta 268 (2018) 366–382. doi:10.1016/j.electacta.2018.02.100.

[32] A. Weber, M. Hickner, Modeling and high-resolution-imaging studies of water-content profiles in a polymer-electrolyte-fuel-cell membrane-electrode assembly, Electrochimica Acta 53 (26) (2008) 7668–7674.

[33] P. Mangal, M. Dumontier, N. Carrigy, M. Secanell, Measurements of permeability and effective in-plane gas diffusivity of gas diffusion media under compression, ECS Transactions 64 (3) (2014) 487–499.

[34] P. Mangal, L. M. Pant, N. Carrigy, M. Dumontier, V. Zingan, S. Mitra, M. Secanell, Experimental study of mass transport in pemfcs: through plane permeability and molecular diffusivity in gdls, Electrochimica Acta 167 (2015) 160–171.

[35] J. P. Owejan, J. E. Owejan, W. Gu, Impact of platinum loading and catalyst layer structure on pemfc performance, Journal of The Electrochemical Society 160 (8) (2013) F824–F833.

[36] S. Shukla, D. Stanier, M. Saha, J. Stumper, M. Secanell, Analysis of inkjet printed pefc electrodes with varying platinum loading, Journal of The Electrochemical Society 163 (7) (2016) F677–F687.

[37] C. Lim, C. Wang, Effects of hydrophobic polymer content in gdl on power performance of a pem fuel cell, Electrochimica Acta 49 (24) (2004) 4149–4156.

[38] S. Shukla, K. Domican, K. Karan, S. Bhattacharjee, M. Secanell, Analysis of low platinum loading thin polymer electrolyte fuel cell electrodes prepared by inkjet printing, Electrochimica Acta 156 (2015) 289–300. doi:10.1016/j.electacta.2015.01.028.

[39] Z. Qi, A. Kaufman, Low pt loading high performance cathodes for pem fuel cells, Journal of Power Sources 113 (1) (2003) 37–43.

[40] M. Secanell, K. Karan, A. Suleman, N. Djilali, Multi-variable optimization of pemfc cathodes using an agglomerate model, Electrochimica Acta 52 (22) (2007) 6318–6337.

[41] M. Secanell, B. Carnes, A. Suleman, N. Djilali, Numerical optimization of proton exchange membrane fuel cell cathodes, Electrochimica Acta 52 (7) (2007) 2668–2682.

[42] D. Song, Q. Wang, Z. Liu, T. Navessin, M. Eikerling, S. Holdcroft, Numerical optimization study of the catalyst layer of pem fuel cell cathode, Journal of Power Sources 126 (1) (2004) 104–111. doi:10.1016/j.jpowsour.2003.08.043.

[43] D. Froning, J. Brinkmann, U. Reimer, V. Schmidt, W. Lehnert, D. Stolten, 3d analysis, modeling and simulation of transport processes in compressed fibrous microstructures, using the lattice boltzmann method, Electrochimica Acta 110 (2013) 325–334.

[44] M. S. Saha, M. Tam, V. Berejnov, D. Susac, S. McDermid, A. P. Hitchcock, J. Stumper, Characterization and performance of catalyst layers prepared by inkjet printing technology, ECS Transactions 58 (1) (2013) 797–806.

[45] M. S. Saha, R. Li, X. Sun, S. Ye, 3-d composite electrodes for high performance pem fuel cells composed of pt supported on nitrogen-doped carbon nanotubes grown on carbon paper, Electrochemistry Communications 11 (2) (2009) 438–441.

[46] E. Wargo, A. Hanna, A. Cecen, S. Kalidindi, E. Kumbur, Selection of representative volume elements for pore-scale analysis of transport in fuel cell materials, Journal of Power Sources 197 (2012) 168–179.

[47] E. Wargo, T. Kotaka, Y. Tabuchi, E. Kumbur, Comparison of focused ion beam versus nano-scale x-ray computed tomography for resolving 3-d microstructures of porous fuel cell materials, Journal of Power Sources 241 (2013) 608–618.

[48] S. Thiele, R. Zengerle, C. Ziegler, Nano-morphology of a polymer electrolyte fuel cell catalyst layer—imaging, reconstruction and analysis, Nano Research 4 (9) (2011) 849–860.

[49] C. Ziegler, S. Thiele, R. Zengerle, Direct three-dimensional reconstruction of a nanoporous catalyst layer for a polymer electrolyte fuel cell, Journal of Power Sources 196 (4) (2011) 2094–2097.

[50] X. Zhang, Y. Gao, H. Ostadi, K. Jiang, R. Chen, Modelling water intrusion and oxygen diffusion in a reconstructed microporous layer of PEM fuel cells, Int. J. Hydrogen Energy 39 (30) (2014) 17222–17230. doi:10.1016/j.ijhydene.2014.08.027.

[51] M. Sabharwal, L. Pant, A. Putz, D. Susac, J. Jankovic, M. Secanell, Analysis of catalyst layer microstructures: From imaging to performance, Fuel Cells 16 (6) (2016) 734–753. doi:10.1002/fuce.201600008.

[52] W. K. Epting, J. Gelb, S. Litster, Resolving the three-dimensional microstructure of polymer electrolyte fuel cell electrodes using nanometer-scale x-ray computed tomography, Advanced Functional Materials 22 (3) (2012) 555–560.

[53] S. Litster, W. K. Epting, E. A.Wargo, S. R. Kalidindi, E. C. Kumbur, Morphological analyses of polymer electrolyte fuel cell electrodeswith nano-scale computed tomography imaging, Fuel Cells 13 (5) (2013) 935–945.

[54] H. Ostadi, P. Rama, Y. Liu, R. Chen, X. Zhang, K. Jiang, 3d reconstruction of a gas diffusion layer and a microporous layer, Journal of Membrane Science 351 (1) (2010) 69–74.

[55] P. A. García-Salaberri, J. T. Gostick, G. Hwang, A. Z. Weber, M. Vera, Effective diffusivity in partially-saturated carbon-fiber gas diffusion layers: Effect of local saturation and application to macroscopic continuum models, Journal of Power Sources 296 (2015) 440–453. doi:10.1016/j.jpowsour.2015.07.034.

[56] P. A. García-Salaberri, G. Hwang, M. Vera, A. Z. Weber, J. T. Gostick, Effective diffusivity in partially-saturated carbon-fiber gas diffusion layers: Effect of through-plane saturation distribution, International Journal of Heat and Mass Transfer 86 (2015) 319–333. doi:10.1016/j.ijheatmasstransfer.2015.02.073.

[57] M. Fazeli, J. Hinebaugh, A. Bazylak, Incorporating embedded microporous layers into topologically equivalent pore network models for oxygen diffusivity calculations in polymer electrolyte membrane fuel cell gas diffusion layers, Electrochimica Acta 216 (2016) 364–375. doi:10.1016/j.electacta.2016.08.126.

[58] J. Hinebaugh, Z. Fishman, A. Bazylak, Unstructured pore network modeling with heterogeneous pemfc gdl porosity distributions, Journal of The Electrochemical Society 157 (11) (2010) B1651–B1657. doi:10.1149/1.3486095.

[59] I. V. Zenyuk, A. Z. Weber, Understanding liquid-water management in pefcs using x-ray computed tomography and modeling, ECS Transactions 69 (17) (2015) 1253–1265.

[60] I. V. Zenyuk, D. Y. Parkinson, G. Hwang, A. Z. Weber, Probing water distribution in compressed fuel-cell gas-diffusion layers using x-ray computed tomography, Electrochemistry Communications 53 (2015) 24–28.

[61] T. Kotaka, Y. Tabuchi, P. P. Mukherjee, Microstructural analysis of mass transport phenomena in gas diffusion media for high current density operation in pem fuel cells, Journal of Power Sources 280 (2015) 231–239.

[62] K. J. Lange, P.-C. Sui, N. Djilali, Pore scale modeling of a proton exchange membrane fuel cell catalyst layer: Effects of water vapor and temperature, Journal of Power Sources 196 (6) (2011) 3195–3203.

[63] K. J. Lange, P.-C. Sui, N. Djilali, Determination of effective transport properties in a pemfc catalyst layer using different reconstruction algorithms, Journal of Power Sources 208 (2012) 354–365.

[64] J. Pharoah, H.-W. Choi, C.-C. Chueh, D. B. Harvey, Effective transport properties accounting for electrochemical reactions of proton-exchange membrane fuel cell catalyst layers, ECS Transactions 41 (1) (2011) 221–227.

[65] M. El Hannach, E. Kjeang, Stochastic microstructural modeling of pefc gas diffusion media, Journal of The Electrochemical Society 161 (9) (2014) F951–F960.

[66] R. R. Rashapov, J. T. Gostick, In-plane effective diffusivity in pemfc gas diffusion layers, Transport in Porous Media 115 (3) (2016) 411–433.

[67] G. Wang, P. P. Mukherjee, C.-Y. Wang, Direct numerical simulation (dns) modeling of pefc electrodes: Part i. regular microstructure, Electrochimica Acta 51 (15) (2006) 3139–3150.

[68] L. M. Pant, Stochastic characterization and reconstruction of porous media, Ph.D. thesis, University of Alberta (2016).
URL `http://hdl.handle.net/10402/era.42583`

[69] M. El Hannach, R. Singh, N. Djilali, E. Kjeang, Micro-porous layer stochastic reconstruction and transport parameter determination, Journal of Power Sources 282 (2015) 58–64.

[70] P. Satjaritanun, J. Weidner, S. Hirano, Z. Lu, Y. Khunatorn, S. Ogawa, S. Litster, A. Shum, I. Zenyuk, S. Shimpalee, Micro-scale analysis of liquid water breakthrough inside gas diffusion layer for pemfc using x-ray computed tomography and lattice boltzmann method, Journal of The Electrochemical Society 164 (11) (2017) E3359–E3371.

[71] V. Berejnov, D. Susac, J. Stumper, A. P. Hitchcock, Nano to micro scale characterization of water uptake in the catalyst coated membrane measured by soft x-ray scanning transmission x-ray microscopy, ECS Transactions 41 (1) (2011) 395–402.

[72] D. Susac, V. Berejnov, A. P. Hitchcock, J. Stumper, Stxm characterization of pem fuel cell catalyst layers, ECS Transactions 50 (2) (2013) 405–413.

[73] M. Andisheh-Tadbir, F. P. Orfino, E. Kjeang, Three-dimensional phase segregation of micro-porous layers for fuel cells by nano-scale x-ray computed tomography, Journal of Power Sources 310 (2016) 61–69.

[74] H. Ostadi, P. Rama, Y. Liu, R. Chen, X. Zhang, K. Jiang, Influence of threshold variation on determining the properties of a polymer electrolyte fuel cell gas diffusion layer in x-ray nano-tomography, Chemical Engineering Science 65 (6) (2010) 2213–2217.

[75] S. Komini Babu, H. T. Chung, P. Zelenay, S. Litster, Resolving electrode morphologys impact on platinum group metal-free cathode performance using nano-ct of 3d hierarchical pore and ionomer distribution, ACS applied materials & interfaces 8 (48) (2016) 32764–32777.

[76] R. Flückiger, F. Marone, M. Stampanoni, A. Wokaun, F. N. Büchi, Investigation of liquid water in gas diffusion layers of polymer electrolyte fuel cells using x-ray tomographic microscopy, Electrochimica Acta 56 (5) (2011) 2254–2262.

[77] A. D. Shum, D. Y. Parkinson, X. Xiao, A. Z. Weber, O. S. Burheim, I. V. Zenyuk, Investigating phase-change-induced flow in gas diffusion layers in fuel cells with x-ray computed tomography, Electrochimica Acta.

[78] I. V. Zenyuk, A. Lamibrac, J. Eller, D. Y. Parkinson, F. Marone, F. N. Buchi, A. Z. Weber, Investigating evaporation in gas diffusion layers for fuel cells with x-ray computed tomography, The Journal of Physical Chemistry C 120 (50) (2016) 28701–28711.

[79] S. M. Moosavi, M. Niffeler, J. Gostick, S. Haussener, Transport characteristics of saturated gas diffusion layers treated with hydrophobic coatings, Chemical Engineering Science 176 (2018) 503–514.

[80] S. Lal, A. Lamibrac, J. Eller, F. N. Büchi, Determination of water evaporation rates in gas diffusion layers of fuel cells, Journal of The Electrochemical Society 165 (9) (2018) F652–F661.

[81] I. Koprinarov, A. P. Hitchcock, X-ray spectromicroscopy of polymers: An introduction for the non-specialist (2000).

[82] J. Wu, L. G. Melo, X. Zhu, M. M. West, V. Berejnov, D. Susac, J. Stumper, A. P. Hitchcock, 4d imaging of polymer electrolyte membrane fuel cell catalyst layers by soft x-ray spectro-tomography, Journal of Power Sources 381 (2018) 72–83.

[83] M. G. George, J. Wang, R. Banerjee, A. Bazylak, Composition analysis of a polymer electrolyte membrane fuel cell microporous layer using scanning transmission x-ray microscopy and near edge x-ray absorption fine structure analysis, Journal of Power Sources 309 (2016) 254–259.

[84] S. Vierrath, F. Güder, A. Menzel, M. Hagner, R. Zengerle, M. Zacharias, S. Thiele, Enhancing the quality of the tomography of nanoporous materials for better understanding of polymer electrolyte fuel cell materials, Journal of Power Sources 285 (2015) 413–417.

[85] X. Zhang, H. Ostadi, K. Jiang, R. Chen, Reliability of the spherical agglomerate models for catalyst layer in polymer electrolyte membrane fuel cells, Electrochimica Acta 133 (2014) 475–483.

[86] X. Zhang, Y. Gao, H. Ostadi, K. Jiang, R. Chen, Method to improve catalyst layer model for modelling proton exchange membrane fuel cell, Journal of Power Sources 289 (2015) 114–128.

[87] S.-J. Lee, J. H. Yoo, K. B. Shim, S.-C. Yi, Microstructural analysis of mass transport phenomena in a pem fuel cell cathode, Journal of Ceramic Processing Research 17 (7) (2016) 773–777.

[88] T. Terao, G. Inoue, M. Kawase, N. Kubo, M. Yamaguchi, K. Yokoyama, T. Tokunaga, K. Shinohara, Y. Hara, T. Hara, Development of novel three-dimensional reconstruction method for porous media for polymer electrolyte fuel cells using focused ion beam-scanning electron microscope tomography, Journal of Power Sources 347 (2017) 108–113.

[89] Microtomography, Skyscan, Ct-analyser users guide, Version 1 (1) (2007) 16–29.

[90] M. Salzer, A. Spettl, O. Stenzel, J.-H. Smått, M. Lindén, I. Manke, V. Schmidt, A two-stage approach to the segmentation of fib-sem images of highly porous materials, Materials Characterization 69 (2012) 115–126.

[91] M. Salzer, S. Thiele, R. Zengerle, V. Schmidt, On the importance of fib-sem specific segmentation algorithms for porous media, Materials Characterization 95 (2014) 36–43.

[92] H. Schulenburg, B. Schwanitz, N. Linse, G. G. Scherer, A. Wokaun, J. Krbanjevic, R. Grothausmann, I. Manke, 3d imaging of catalyst support corrosion in polymer electrolyte fuel cells, The Journal of Physical Chemistry C 115 (29) (2011) 14236–14243.

[93] S. Zils, M. Timpel, T. Arlt, A. Wolz, I. Manke, C. Roth, 3d visualization of pemfc electrode structures using fib tomography, Fuel Cells 10 (6) (2010) 966.

[94] J. Sauvola, M. Pietikäinen, Adaptive document image binarization, Pattern recognition 33 (2) (2000) 225–236.

[95] R. Barbosa, J. Andaverde, B. Escobar, U. Cano, Stochastic reconstruction and a scaling method to determine effective transport coefficients of a proton exchange membrane fuel cell catalyst layer, Journal of Power Sources 196 (3) (2011) 1248–1257.

[96] L. Chen, G. Wu, E. F. Holby, P. Zelenay, W.-Q. Tao, Q. Kang, Lattice boltzmann pore-scale investigation of coupled physical-electrochemical processes in c/pt and non-precious metal cathode catalyst layers in proton exchange membrane fuel cells, Electrochimica Acta 158 (2015) 175–186.

[97] J. T. Gostick, Random pore network modeling of fibrous pemfc gas diffusion media using voronoi and delaunay tessellations, Journal of The Electrochemical Society 160 (8) (2013) F731–F743. doi:10.1149/2.009308jes.

[98] S. H. Kim, H. Pitsch, Reconstruction and effective transport properties of the catalyst layer in pem fuel cells, Journal of The Electrochemical Society 156 (6) (2009) B673–B681.

[99] R. Thiedmann, F. Fleischer, C. Hartnig, W. Lehnert, V. Schmidt, Stochastic 3d modeling of the gdl structure in pemfcs based on thin section detection, Journal of The Electrochemical Society 155 (4) (2008) B391–B399.

[100] X. Huang, Y. He, W. Zhou, D. Deng, Y. Zhao, Pore network modeling of fibrous porous media of uniform and gradient porosity, Powder Technology.

[101] W. Wu, F. Jiang, Microstructure reconstruction and characterization of pemfc electrodes, International Journal of Hydrogen Energy 39 (28) (2014) 15894–15906.

[102] V. P. Schulz, J. Becker, A. Wiegmann, P. P. Mukherjee, C.-Y. Wang, Modeling of two-phase behavior in the gas diffusion medium of pefcs via full morphology approach, Journal of The Electrochemical Society 154 (4) (2007) B419–B426.

[103] G. Inoue, T. Yoshimoto, Y. Matsukuma, M. Minemoto, Development of simulated gas diffusion layer of polymer electrolyte fuel cells and evaluation of its structure, Journal of Power Sources 175 (1) (2008) 145–158.

[104] P. Mukherjee, C.-Y. Wang, Stochastic microstructure reconstruction and direct numerical simulation of the PEFC catalyst layer, Journal of The Electrochemical Society 153 (5) (2006) A840–A849.

[105] P. P. Mukherjee, C.-Y. Wang, Direct numerical simulation modeling of bilayer cathode catalyst layers in polymer electrolyte fuel cells, Journal of The Electrochemical Society 154 (11) (2007) B1121–B1131.

[106] G. Wang, P. P. Mukherjee, C.-Y. Wang, Direct numerical simulation (dns) modeling of pefc electrodes part ii. random microstructure, Electrochimica Acta 51 (2006) 3151–3160.

[107] J. T. Gostick, M. A. Ioannidis, M. W. Fowler, M. D. Pritzker, Pore network modeling of fibrous gas diffusion layers for polymer electrolyte membrane fuel cells, Journal of Power Sources 173 (1) (2007) 277–290. doi:10.1016/j.jpowsour.2007.04.059.

[108] M. El Hannach, T. Soboleva, K. Malek, A. A. Franco, M. Prat, J. Pauchet, S. Holdcroft, Characterization of pore network structure in catalyst layers of polymer electrolyte fuel cells, Journal of Power Sources 247 (2014) 322–326.

[109] L. M. Pant, M. Sabharwal, S. Mitra, M. Secanell, Stochastic reconstruction and transport simulation of pefc catalyst layers, ECS Transactions 69 (17) (2015) 105–120.

[110] L. M. Pant, S. K. Mitra, M. Secanell, Stochastic reconstruction using multiple correlation functions with different-phase-neighbor-based pixel selection, Physical Review E 90 (2014) 023306. doi:10.1103/PhysRevE.90.023306.

[111] S. Torquato, Random Heterogeneous Materials:Microstructure and Macroscopic Properties, Springer, NewYork, USA, 2000.

[112] N. Parikh, J. Allen, R. Yassar, Microstructure of gas diffusion layers for pem fuel cells, Fuel Cells 12 (3) (2012) 382–390.

[113] J. Becker, V. Schulz, A. Wiegmann, Numerical determination of two-phase material parameters of a gas diffusion layer using tomography images, Journal of fuel cell science and technology 5 (2) (2008) 021006.

[114] A. Çeçen, T. Fast, E. Kumbur, S. Kalidindi, A data-driven approach to establishing microstructure–property relationships in porous transport layers of polymer electrolyte fuel cells, Journal of Power Sources 245 (2014) 144–153.

[115] R. Singh, A. Akhgar, P. Sui, K. Lange, N. Djilali, Dual-beam fib/sem characterization, statistical reconstruction, and pore scale modeling of a pemfc catalyst layer, Journal of The Electrochemical Society 161 (4) (2014) F415–F424.

[116] L. M. Pant, S. K. Mitra, M. Secanell, Multigrid hierarchical simulated annealing method for reconstructing heterogeneous media, Phys Rev E 92 (2015) 063303.

[117] A. Berson, H.-W. Choi, J. G. Pharoah, Determination of the effective gas diffusivity of a porous composite medium from the three-dimensional reconstruction of its microstructure, Phys Rev E 83 (2011) 026310.

[118] B. Lu, S. Torquato, Lineal-path function for random heterogeneous materials, Phys. Rev. A 45 (2) (1992) 922–929.

[119] B. Derjaguin, Measurement of the specific surface of porous and disperse bodies by their resistance to the flow of rarafied gases, Progress in Surface Science 45 (1-4) (1994) 337–340.

[120] G. Sasikumar, J. Ihm, H. Ryu, Dependence of optimum nafion content in catalyst layer on platinum loading, Journal of Power Sources 132 (1-2) (2004) 11–17.

[121] S. Lee, S. Mukerjee, J. McBreen, Y. Rho, Y. Kho, T. Lee, Effects of nafion impregnation on performances of pemfc electrodes, Electrochimica Acta 43 (24) (1998) 3693–3701.

[122] G. Sasikumar, J. Ihm, H. Ryu, Optimum nafion content in pem fuel cell electrodes, Electrochimica Acta 50 (2-3) (2004) 601–605.

[123] H. Iden, A. Ohma, K. Shinohara, Analysis of proton transport in pseudo catalyst layers, Journal of The Electrochemical Society 156 (9) (2009) B1078–B1084.

[124] D. Wilkinson, H. Voss, K. Prater, Water management and stack design for solid polymer fuel cells, Journal of Power Sources 49 (1) (1994) 117–127. doi:10.1016/0378-7753(93)01803-P.

[125] A. Mughal, X. Li, Experimental diagnostics of pem fuel cells, International Journal of Environmental Studies 63 (4) (2006) 377–389. doi:10.1080/00207230600800670.

[126] A. Z. Weber, R. L. Borup, R. M. Darling, P. K. Das, T. J. Dursch, W. Gu, D. Harvey, A. Kusoglu, S. Litster, M. M. Mench, et al., A critical review of modeling transport phenomena in polymer-electrolyte fuel cells, Journal of The Electrochemical Society 161 (12) (2014) F1254–F1299. doi:10.1149/2.0751412jes.

[127] H. Li, Y. Tang, Z. Wang, Z. Shi, S. Wu, D. Song, J. Zhang, K. Fatih, J. Zhang, H. Wang, et al., A review of water flooding issues in the proton exchange membrane fuel cell, Journal of Power Sources 178 (1) (2008) 103–117. doi:10.1016/j.jpowsour.2007.12.068.

[128] A. Kongkanand, P. K. Sinha, Load transients of nanostructured thin film electrodes in polymer electrolyte fuel cells, Journal of the Electrochemical Society 158 (6) (2011) B703–B711.

[129] J. M. LaManna, S. G. Kandlikar, Determination of effective water vapor diffusion coefficient in pemfc gas diffusion layers, international journal of hydrogen energy 36 (8) (2011) 5021–5029.

[130] N. Zamel, N. G. Astrath, X. Li, J. Shen, J. Zhou, F. B. Astrath, H. Wang, Z.-S. Liu, Experimental measurements of effective diffusion coefficient of oxygen–nitrogen mixture in pem fuel cell diffusion media, Chemical Engineering Science 65 (2) (2010) 931–937.

[131] D. Kramer, S. A. Freunberger, R. Flückiger, I. A. Schneider, A. Wokaun, F. N. Büchi, G. G. Scherer, Electrochemical diffusimetry of fuel cell gas diffusion layers, Journal of Electroanalytical Chemistry 612 (1) (2008) 63–77.

[132] C. Chan, N. Zamel, X. Li, J. Shen, Experimental measurement of effective diffusion coefficient of gas diffusion layer/microporous layer in pem fuel cells, Electrochimica Acta 65 (2012) 13–21.

[133] J. T. Gostick, M. W. Fowler, M. D. Pritzker, M. A. Ioannidis, L. M. Behra, In-plane and through-plane gas permeability of carbon fiber electrode backing layers, Journal of Power Sources 162 (1) (2006) 228–238.

[134] J. Shen, J. Zhou, N. G. Astrath, T. Navessin, Z.-S. S. Liu, C. Lei, J. H. Rohling, D. Bessarabov, S. Knights, S. Ye, Measurement of effective gas diffusion coefficients of catalyst layers of pem fuel cells with a loschmidt diffusion cell, Journal of Power Sources 196 (2) (2011) 674–678. doi:10.1016/j.jpowsour.2010.07.086.

[135] S. Salari, C. McCague, M. Tam, M. S. Saha, J. Stumper, M. Bahrami, Accurate ex-situ measurements of pem fuel cells catalyst layer dry diffusivity, ECS Transactions 69 (17) (2015) 419–429.

[136] J. Zhao, S. Shahgaldi, I. Alaefour, S. Yang, X. Li, Pore structure and effective diffusion coefficient of catalyzed electrodes in polymer electrolyte membrane fuel cells, International Journal of Hydrogen Energy 43 (7) (2018) 3776–3785.

[137] R. Jiang, C. K. Mittelsteadt, C. S. Gittleman, Through-plane proton transport resistance of membrane and ohmic resistance distribution in fuel cells, Journal of The Electrochemical Society 156 (12) (2009) B1440–B1446.

[138] M. Mathias, J. Roth, J. Fleming, W. Lehnert, Diffusion media materials and characterization, Handbook of fuel cellsfundamentals, technology and applications 3 (2003) 517–537.

[139] O. S. Burheim, J. G. Pharoah, H. Lampert, P. J. Vie, S. Kjelstrup, Through-plane thermal conductivity of pemfc porous transport layers, Journal of Fuel Cell Science and Technology 8 (2) (2011) 021013.

[140] O. S. Burheim, H. Su, S. Pasupathi, J. G. Pharoah, B. G. Pollet, Thermal conductivity and temperature profiles of the micro porous layers used for the polymer electrolyte membrane fuel cell, International Journal of Hydrogen Energy 38 (20) (2013) 8437–8447.

[141] N. Zamel, E. Litovsky, S. Shakhshir, X. Li, J. Kleiman, Measurement of in-plane thermal conductivity of carbon paper diffusion media in the temperature range of- 20 c to+ 120 c, Applied energy 88 (9) (2011) 3042–3050.

[142] H. Sadeghifar, N. Djilali, M. Bahrami, Effect of polytetrafluoroethylene (ptfe) and micro porous layer (mpl) on thermal conductivity of fuel cell gas diffusion layers: Modeling and experiments, Journal of Power Sources 248 (2014) 632–641.

[143] M. Khandelwal, M. Mench, Direct measurement of through-plane thermal conductivity and contact resistance in fuel cell materials, Journal of Power Sources 161 (2) (2006) 1106–1115.

[144] E. Sadeghi, N. Djilali, M. Bahrami, Effective thermal conductivity and thermal contact resistance of gas diffusion layers in proton exchange membrane fuel cells. part 1: Effect of compressive load, Journal of Power Sources 196 (1) (2011) 246–254.

[145] M. Ahadi, M. Tam, M. S. Saha, J. Stumper, M. Bahrami, Thermal conductivity of catalyst layer of polymer electrolyte membrane fuel cells: Part 1–experimental study, Journal of Power Sources 354 (2017) 207–214.

[146] R. Koresawa, Y. Utaka, Precise measurement of effective oxygen diffusivity for microporous media containing moisture by review of galvanic cell oxygen absorber configuration, International Journal of Heat and Mass Transfer 76 (2014) 549–558.

[147] T. Soboleva, K. Malek, Z. Xie, T. Navessin, S. Holdcroft, Pemfc catalyst layers: the role of micropores and mesopores on water sorption and fuel cell activity, ACS applied materials & interfaces 3 (6) (2011) 1827–1837.

[148] T. Soboleva, X. Zhao, K. Malek, Z. Xie, T. Navessin, S. Holdcroft, On the micro-, meso-, and macroporous structures of polymer electrolyte membrane fuel cell catalyst layers, ACS applied materials & interfaces 2 (2) (2010) 375–384. doi:10.1021/am900600y.

[149] K. J. Lange, C. Misra, P.-C. Sui, N. Djilali, A numerical study on preconditioning and partitioning schemes for reactive transport in a pemfc catalyst layer, Computer Methods in Applied Mechanics and Engineering 200 (9) (2011) 905–916.

[150] J. Becker, R. Flückiger, M. Reum, F. N. Büchi, F. Marone, M. Stampanoni, Determination of material properties of gas diffusion layers: experiments and simulations using phase contrast tomographic microscopy, Journal of The Electrochemical Society 156 (10) (2009) B1175–B1181.

[151] L. M. Pant, S. K. Mitra, M. Secanell, Absolute permeability and knudsen diffusivity measurements in pemfc gas diffusion layers and micro porous layers, Journal of Power Sources 206 (2012) 153–160.

[152] P. Rama, Y. Liu, R. Chen, H. Ostadi, K. Jiang, X. Zhang, R. Fisher, M. Jeschke, An x-ray tomography based lattice boltzmann simulation study on gas diffusion layers of polymer electrolyte fuel cells, Journal of Fuel Cell Science and Technology 7 (3) (2010) 031015.

[153] L. Hao, P. Cheng, Lattice boltzmann simulations of anisotropic permeabilities in carbon paper gas diffusion layers, Journal of Power Sources 186 (1) (2009) 104–114.

[154] M. Sabharwal, J. T. Gostick, M. Secanell, Virtual liquid water intrusion in fuel cell gas diffusion media, Journal of The Electrochemical Society 165 (7) (2018) F553–F563. doi:10.1149/2.0921807jes.

[155] P. A. García-Salaberri, I. V. Zenyuk, A. D. Shum, G. Hwang, M. Vera, A. Z. Weber, J. T. Gostick, Analysis of representative elementary volume and through-plane regional characteristics of carbon-fiber papers: diffusivity, permeability and electrical/thermal conductivity, International Journal of Heat and Mass Transfer 127 (2018) 687–703.

[156] W.-Z. Fang, Y.-Q. Tang, L. Chen, Q.-J. Kang, W.-Q. Tao, Influences of the perforation on effective transport properties of gas diffusion layers, International Journal of Heat and Mass Transfer 126 (2018) 243–255.

[157] J. M. Zalc, S. C. Reyes, E. Iglesia, The effects of diffusion mechanism and void structure on transport rates and tortuosity factors in complex porous structures, Chemical Engineering Science 59 (14) (2004) 2947–2960. doi:10.1016/j.ces.2004.04.028.

[158] T. Hutzenlaub, J. Becker, R. Zengerle, S. Thiele, Modelling the water distribution within a hydrophilic and hydrophobic 3d reconstructed cathode catalyst layer of a proton exchange membrane fuel cell, Journal of Power Sources 227 (2013) 260–266. doi:10.1016/j.jpowsour.2012.11.065.

[159] L. Zielke, S. Vierrath, R. Moroni, A. Mondon, R. Zengerle, S. Thiele, Three-dimensional morphology of the interface between micro porous layer and catalyst layer in a polymer electrolyte membrane fuel cell, RSC Advances 6 (84) (2016) 80700–80705.

[160] P. K. Sinha, C.-Y. Wang, Pore-network modeling of liquid water transport in gas diffusion layer of a polymer electrolyte fuel cell, Electrochimica Acta 52 (28) (2007) 7936–7945.

[161] P. P. Mukherjee, C.-Y. Wang, Q. Kang, Mesoscopic modeling of two-phase behavior and flooding phenomena in polymer electrolyte fuel cells, Electrochimica Acta 54 (27) (2009) 6861–6875. doi:10.1016/j.electacta.2009.06.066.

[162] R. Lenormand, Liquids in porous media, Journal of Physics: Condensed Matter 2 (S) (1990) SA79.

[163] R. Lenormand, E. Touboul, C. Zarcone, Numerical models and experiments on immiscible displacements in porous media, Journal of fluid mechanics 189 (1988) 165–187.

[164] N. Siegel, M. Ellis, D. Nelson, M. Von Spakovsky, A two-dimensional computational model of a pemfc with liquid water transport, Journal of Power Sources 128 (2) (2004) 173–184. doi:10.1016/j.jpowsour.2003.09.072.

[165] Z. Wang, C. Wang, K. Chen, Two-phase flow and transport in the air cathode of proton exchange membrane fuel cells, Journal of Power Sources 94 (1) (2001) 40–50. doi:10.1016/S0378-7753(00)00662-5.

[166] A. Z. Weber, R. M. Darling, J. Newman, Modeling two-phase behavior in pefcs, Journal of The Electrochemical Society 151 (10) (2004) A1715–A1727.

[167] J. Zhou, A. Putz, M. Secanell, A mixed wettability pore size distribution based mathematical model for analyzing two-phase flow in porous electrodes i. mathematical model, Journal of The Electrochemical Society 164 (6) (2017) F530–F539. doi:10.1149/2.0381706jes.

[168] J. Zhou, D. Stanier, A. Putz, M. Secanell, A mixed wettability pore size distribution based mathematical model for analyzing two-phase flow in porous electrodes ii. model validation and analysis of micro-structural parameters, Journal of The Electrochemical Society 164 (6) (2017) F540–F556. doi:10.1149/2.0391706jes.

[169] M. Eikerling, Water management in cathode catalyst layers of pem fuel cells a structure-based model, Journal of The Electrochemical Society 153 (3) (2006) E58–E70. doi:10.1149/1.2160435.

[170] M. El Hannach, J. Pauchet, M. Prat, Pore network modeling: Application to multiphase transport inside the cathode catalyst layer of proton exchange membrane fuel

cell, Electrochimica Acta 56 (28) (2011) 10796–10808. doi:10.1016/j.electacta.2011.05.060.

[171] M. El Hannach, M. Prat, J. Pauchet, Pore network model of the cathode catalyst layer of proton exchange membrane fuel cells: Analysis of water management and electrical performance, International Journal of Hydrogen Energy 37 (24) (2012) 18996–19006. doi:10.1016/j.ijhydene.2012.09.139.

[172] P. K. Sinha, P. P. Mukherjee, C.-Y. Wang, Impact of gdl structure and wettability on water management in polymer electrolyte fuel cells, Journal of Materials Chemistry 17 (30) (2007) 3089–3103. doi:10.1039/B703485G.

[173] R. Wu, X. Zhu, Q. Liao, H. Wang, Y.-d. Ding, J. Li, D.-d. Ye, A pore network study on water distribution in bi-layer gas diffusion media: effects of inlet boundary condition and micro-porous layer properties, International Journal of Hydrogen Energy 35 (17) (2010) 9134–9143. doi:10.1016/j.ijhydene.2010.06.051.

[174] R. Wu, X. Zhu, Q. Liao, H. Wang, Y.-d. Ding, J. Li, D.-d. Ye, A pore network study on the role of micro-porous layer in control of liquid water distribution in gas diffusion layer, International Journal of Hydrogen Energy 35 (14) (2010) 7588–7593. doi:10.1016/j.ijhydene.2010.04.126.

[175] Y. Ji, G. Luo, C.-Y. Wang, Pore-level liquid water transport through composite diffusion media of pemfc, Journal of The Electrochemical Society 157 (12) (2010) B1753–B1761.

[176] T. Agaesse, A. Lamibrac, F. N. Büchi, J. Pauchet, M. Prat, Validation of pore network simulations of ex-situ water distributions in a gas diffusion layer of proton exchange membrane fuel cells with x-ray tomographic images, Journal of Power Sources 331 (2016) 462–474.

[177] L. Hao, P. Cheng, Lattice boltzmann simulations of water transport in gas diffusion layer of a polymer electrolyte membrane fuel cell, Journal of Power Sources 195 (12) (2010) 3870–3881. doi:10.1016/j.jpowsour.2009.11.125.

[178] H.-J. Vogel, J. Tölke, V. Schulz, M. Krafczyk, K. Roth, Comparison of a lattice-boltzmann model, a full-morphology model, and a pore network model for determining capillary pressure–saturation relationships, Vadose Zone Journal 4 (2) (2005) 380–388. doi:10.2136/vzj2004.0114.

[179] K. Moriyama, T. Inamuro, Lattice boltzmann simulations of water transport from the gas diffusion layer to the gas channel in pefc, Communications in Computational Physics 9 (5) (2011) 1206–1218.

[180] K. N. Kim, J. H. Kang, S. G. Lee, J. H. Nam, C.-J. Kim, Lattice boltzmann simulation of liquid water transport in microporous and gas diffusion layers of polymer electrolyte membrane fuel cells, Journal of Power Sources 278 (2015) 703–717.

[181] T. Koido, T. Furusawa, K. Moriyama, An approach to modeling two-phase transport in the gas diffusion layer of a proton exchange membrane fuel cell, Journal of Power Sources 175 (1) (2008) 127–136.

[182] T. Bednarek, G. Tsotridis, Calculation of effective transport properties of partially saturated gas diffusion layers, Journal of Power Sources 340 (2017) 111–120.

[183] V. P. Schulz, E. A. Wargo, E. C. Kumbur, Pore-morphology-based simulation of drainage in porous media featuring a locally variable contact angle, Transport in Porous Media 107 (1) (2015) 13–25. doi:10.1007/s11242-014-0422-4.

[184] N. Zamel, X. Li, J. Becker, A. Wiegmann, Effect of liquid water on transport properties of the gas diffusion layer of polymer electrolyte membrane fuel cells, International Journal of Hydrogen Energy 36 (9) (2011) 5466–5478.

[185] M. Fazeli, J. Hinebaugh, A. Bazylak, Investigating inlet condition effects on pemfc gdl liquid water transport through pore network modeling, Journal of The Electrochemical Society 162 (7) (2015) F661–F668. doi:10.1149/2.0191507jes.

[186] T. Tranter, J. Gostick, A. Burns, W. Gale, Capillary hysteresis in neutrally wettable fibrous media: A pore network study of a fuel cell electrode, Transport in Porous Media 121 (3) (2018) 597–620.

[187] T. Tranter, J. Gostick, A. Burns, W. Gale, Pore network modeling of compressed fuel cell components with openpnm, Fuel Cells 16 (4) (2016) 504–515.

[188] I. V. Zenyuk, E. Medici, J. Allen, A. Z. Weber, Coupling continuum and pore-network models for polymer-electrolyte fuel cells, International Journal of Hydrogen Energy 40 (46) (2015) 16831–16845.

[189] E. Medici, I. Zenyuk, D. Parkinson, A. Weber, J. Allen, Understanding water transport in polymer electrolyte fuel cells using coupled continuum and pore-network models, Fuel Cells 16 (6) (2016) 725–733.

[190] P. B. Ryzhakov, A. Jarauta, An embedded approach for immiscible multi-fluid problems, International Journal for Numerical Methods in Fluids 81 (6) (2016) 357–376.

[191] A. Jarauta, P. Ryzhakov, Challenges in computational modeling of two-phase transport in polymer electrolyte fuel cells flow channels: A review, Archives of Computational Methods in Engineering (2017) 1–31.

[192] J. Marti, P. Ryzhakov, S. Idelsohn, E. Oñate, Combined eulerian–pfem approach for analysis of polymers in fire situations, International Journal for Numerical Methods in Engineering 92 (9) (2012) 782–801.

[193] A. Bazylak, D. Sinton, N. Djilali, Dynamic water transport and droplet emergence in pemfc gas diffusion layers, Journal of Power Sources 176 (1) (2008) 240–246.

[194] P. Suresh, S. Jayanti, Effect of air flow on liquid water transport through a hydrophobic gas diffusion layer of a polymer electrolyte membrane fuel cell, International journal of hydrogen energy 35 (13) (2010) 6872–6886.

[195] A. Theodorakakos, T. Ous, M. Gavaises, J. Nouri, N. Nikolopoulos, H. Yanagihara, Dynamics of water droplets detached from porous surfaces of relevance to pem fuel cells, Journal of Colloid and Interface Science 300 (2) (2006) 673–687.

[196] F. H. Kim, D. Penumadu, V. P. Schulz, R. Schmirler, P. Krauβ, Lattice boltzmann simulation of two phase flow through porous media and verification using high resolution x-ray and neutron tomography data, in: Poromechanics V: Proceedings of the Fifth Biot Conference on Poromechanics, 2013, pp. 2334–2343.

[197] O. Chapuis, M. Prat, M. Quintard, E. Chane-Kane, O. Guillot, N. Mayer, Two-phase flow and evaporation in model fibrous media: Application to the gas diffusion layer of pem fuel cells, Journal of Power Sources 178 (1) (2008) 258–268.

[198] M. Aghighi, J. Gostick, Pore network modeling of phase change in pem fuel cell fibrous cathode, Journal of Applied Electrochemistry 47 (12) (2017) 1323–1338.

[199] N. Belgacem, M. Prat, J. Pauchet, Coupled continuum and condensation–evaporation pore network model of the cathode in polymer-electrolyte fuel cell, International Journal of Hydrogen Energy 42 (12) (2017) 8150–8165.

[200] G. Wang, P. P. Mukherjee, C.-Y. Wang, Optimization of polymer electrolyte fuel cell cathode catalyst layers via direct numerical simulation modeling, Electrochimica Acta 52 (22) (2007) 6367–6377.

[201] J. X. Wang, J. Zhang, R. R. Adzic, Double-trap kinetic equation for the oxygen reduction reaction on pt (111) in acidic media, The Journal of Physical Chemistry A 111 (49) (2007) 12702–12710.

[202] M. Moore, A. Putz, M. Secanell, Investigation of the orr using the double-trap intrinsic kinetic model, Journal of The Electrochemical Society 160 (6) (2013) F670–F681.

[203] B. Jayasankar, K. Karan, O2 electrochemistry on pt: A unified multi-step model for oxygen reduction and oxide growth, Electrochimica Acta 273 (2018) 367–378.

[204] M. Markiewicz, C. Zalitis, A. Kucernak, Performance measurements and modelling of the orr on fuel cell electrocatalysts - the modified double trap model, Electrochimica Acta 179 (2015) 126–136.

[205] A. Parthasarathy, S. Srinivasan, A. J. Appleby, C. R. Martin, Temperature dependence of the electrode kinetics of oxygen reduction at the platinum/nafion® interfacea microelectrode investigation, Journal of The Electrochemical Society 139 (9) (1992) 2530–2537.

[206] T. A. Greszler, D. Caulk, P. Sinha, The impact of platinum loading on oxygen transport resistance, Journal of The Electrochemical Society 159 (12) (2012) F831–F840.

[207] D. R. Baker, D. A. Caulk, K. C. Neyerlin, M. W. Murphy, Measurement of oxygen transport resistance in pem fuel cells by limiting current methods, Journal of The Electrochemical Society 156 (9) (2009) B991–B1003.

[208] K. Shinozaki, Y. Morimoto, B. S. Pivovar, S. S. Kocha, Suppression of oxygen reduction reaction activity on pt-based electrocatalysts from ionomer incorporation, Journal of Power Sources 325 (2016) 745–751.

[209] R. Jinnouchi, K. Kudo, N. Kitano, Y. Morimoto, Molecular dynamics simulations on o 2 permeation through nafion ionomer on platinum surface, Electrochimica Acta 188 (2016) 767–776.

[210] K. Karan, Pefc catalyst layer: Recent advances in materials, microstructural characterization, and modeling, Current Opinion in Electrochemistry.

[211] M. Secanell, A. Putz, S. Shukla, P. Wardlaw, M. Bhaiya, L. M. Pant, M. Sabharwal, Mathematical modelling and experimental analysis of thin, low-loading fuel cell electrodes, ECS Transactions 69 (17) (2015) 157–187.

[212] P. Wardlaw, Modelling of pemfc catalyst layer mass transport and electro-chemical reactions using multi-scale simulations, Master's thesis, University of Alberta (2014).

[213] M. Moore, P. Wardlaw, P. Dobson, J. Boisvert, A. Putz, R. Spiteri, M. Secanell, Understanding the effect of kinetic and mass transport processes in cathode agglomerates, Journal of The Electrochemical Society 161 (8) (2014) E3125–E3137.

[214] K. Kudo, T. Suzuki, Y. Morimoto, Analysis of oxygen dissolution rate from gas phase into nafion surface and development of an agglomerate model, ECS Transactions 33 (1) (2010) 1495–1502.

[215] K. Kudo, Y. Morimoto, Analysis of oxygen transport resistance of nafion thin film on pt electrode, ECS Transactions 50 (2) (2013) 1487–1494.

[216] T. Suzuki, K. Kudo, Y. Morimoto, Model for investigation of oxygen transport limitation in a polymer electrolyte fuel cell, Journal of Power Sources 222 (2013) 379–389.

[217] G. Inoue, M. Kawase, Effect of porous structure of catalyst layer on effective oxygen diffusion coefficient in polymer electrolyte fuel cell, Journal of Power Sources 327 (2016) 1–10.

[218] H. Ishikawa, Y. Sugawara, G. Inoue, M. Kawase, Effects of pt and ionomer ratios on the structure of catalyst layer: A theoretical model for polymer electrolyte fuel cells, Journal of Power Sources 374 (2018) 196–204.

[219] Y. Garsany, R. W. Atkinson, M. B. Sassin, R. M. Hjelm, B. D. Gould, K. E. Swider-Lyons, Improving pemfc performance using short-side-chain low-equivalent-weight pfsa ionomer in the cathode catalyst layer, Journal of The Electrochemical Society 165 (5) (2018) F381–F391.

[220] S.-J. Shin, J.-K. Lee, H.-Y. Ha, S.-A. Hong, H.-S. Chun, I.-H. Oh, Effect of the catalytic ink preparation method on the performance of polymer electrolyte membrane fuel cells, Journal of Power Sources 106 (1-2) (2002) 146–152.

[221] J. Jankovic, D. Susac, T. Soboleva, J. Stumper, Electron tomography based 3d reconstruction of fuel cell catalysts, ECS Transactions 50 (2) (2013) 353–359.

[222] D. Banham, F. Feng, T. Fürstenhaupt, K. Pei, S. Ye, V. Birss, Effect of pt-loaded carbon support nanostructure on oxygen reduction catalysis, Journal of Power Sources 196 (13) (2011) 5438–5445.

[223] M. Aghighi, M. A. Hoeh, W. Lehnert, G. Merle, J. Gostick, Simulation of a full fuel cell membrane electrode assembly using pore network modeling, Journal of The Electrochemical Society 163 (5) (2016) F384–F392.

[224] J. Becker, C. Wieser, S. Fell, K. Steiner, A multi-scale approach to material modeling of fuel cell diffusion media, International Journal of Heat and Mass Transfer 54 (2011) 1360–1368.

[225] M. Sabharwal, A. M. V. Putz, D. Susac, J. Jankovic, M. Secanell, Improving fib-sem reconstructions by using epoxy resin embedding, ECS Transactions.

[226] Math2Market®GmbH, Geodict® (2017).
URL `http://www.geodict.com/Solutions/aboutGD.php`

[227] D. G. Lowe, Distinctive image features from scale-invariant keypoints, International journal of computer vision 60 (2) (2004) 91–110.

[228] G. Bradski, The OpenCV Library, Dr. Dobb's Journal of Software Tools.

[229] M. Secanell, A. Putz, P. Wardlaw, V. Zingan, M. Bhaiya, M. Moore, J. Zhou, C. Balen, K. Domican, Openfcst: An open-source mathematical modelling software for polymer electrolyte fuel cells, ECS Transactions 64 (3) (2014) 655–680.

[230] S. M. Pizer, E. P. Amburn, J. D. Austin, R. Cromartie, A. Geselowitz, T. Greer, B. ter Haar Romeny, J. B. Zimmerman, K. Zuiderveld, Adaptive histogram equalization and its variations, Computer vision, graphics, and image processing 39 (3) (1987) 355–368.

[231] M. Nixon, Feature extraction & image processing, Academic Press, 2008.

[232] E. Jones, T. Oliphant, P. Peterson, et al., SciPy: Open source scientific tools for Python, [Online; accessed ¡today¿] (2001–).
URL `http://www.scipy.org/`

[233] L. P. Coelho, Mahotas: Open source software for scriptable computer vision, arXiv preprint arXiv:1211.4907.

[234] S. Van der Walt, J. L. Schönberger, J. Nunez-Iglesias, F. Boulogne, J. D. Warner, N. Yager, E. Gouillart, T. Yu, scikit-image: image processing in python, PeerJ 2 (2014) e453.

[235] N. Otsu, A threshold selection method from gray-level histograms, Automatica 11 (285-296) (1975) 23–27.

[236] M. H. Wilkinson, Automated and manual segmentation techniques in image analysis of microbes, Digital Image analysis of microbes (1998) 135–171.

[237] D. Coker, S. Torquato, Extraction of morphological quantities from a digitized medium, J. Appl. Phys. 77 (12) (1995) 6087–6099. doi:10.1063/1.359134.

[238] C. L. Y. Yeong, S. Torquato, Reconstructing random media, Phys Rev E 57 (1) (1998) 495–506. doi:10.1103/PhysRevE.57.495.

[239] S. Torquato, B. Lu, Chord-length distribution function for two-phase random media, Phys Rev E 47 (4) (1993) 2950–2953.

[240] L. Pant, S. Mitra, M. Secanell, A generalized mathematical model to study gas transport in PEMFC porous media, Int. J. Heat Mass Transfer 58 (1-2) (2013) 70–79. doi:10.1016/j.ijheatmasstransfer.2012.11.023.

[241] S. Torquato, J. Beasley, Y. Chiew, Two-point cluster function for continuum percolation, The Journal of Chemical Physics 88 (10) (1988) 6540–6547.

[242] L. He, Y. Chao, K. Suzuki, A run-based two-scan labeling algorithm, IEEE Trans. Image Processing 17 (5) (2008) 749–756.

[243] J. Hoshen, R. Kopelman, Percolation and cluster distribution. I. Cluster multiple labeling technique and critical concentration algorithm, Physical Review B 14 (8) (1976) 3438–3445.

[244] A. Meijster, J. B. Roerdink, W. H. Hesselink, A general algorithm for computing distance transforms in linear time, in: Mathematical Morphology and its applications to image and signal processing, Springer, 2000, pp. 331–340.

[245] J. Zhou, Analyzing multiphase flow in membrane electrode assembly using a mixed wettability mathematical model.

[246] P. J. Kerkhof, M. A. Geboers, Analysis and extension of the theory of multicomponent fluid diffusion, Chemical Engineering Science 60 (12) (2005) 3129–3167. doi:10.1016/j.ces.2004.12.042.

[247] C. Wilke, P. Chang, Correlation of diffusion coefficients in dilute solutions, AIChE Journal 1 (2) (1955) 264–270.

[248] R. Reid, The Properties of Gases and Liquids Third Edition, McGraw-Hill, New York, 1977.

[249] D. Pantea, H. Darmstadt, S. Kaliaguine, C. Roy, Electrical conductivity of conductive carbon blacks: influence of surface chemistry and topology, Applied Surface Science 217 (1-4) (2003) 181–193.

[250] A. Espinola, P. M. Miguel, M. R. Salles, A. R. Pinto, Electrical properties of carbons-resistance of powder materials, Carbon 24 (3) (1986) 337–341.

[251] D. K. Paul, A. Fraser, K. Karan, Towards the understanding of proton conduction mechanism in pemfc catalyst layer: Conductivity of adsorbed nafion films, Electrochemistry Communications 13 (8) (2011) 774–777.

[252] D. K. Paul, K. Karan, Conductivity and wettability changes of ultrathin nafion films subjected to thermal annealing and liquid water exposure, The Journal of Physical Chemistry C 118 (4) (2014) 1828–1835.

[253] H. K. Shim, D. K. Paul, K. Karan, Resolving the contradiction between anomalously high water uptake and low conductivity of nanothin nafion films on sio2 substrate, Macromolecules 48 (22) (2015) 8394–8397.

[254] Y. Ono, Y. Nagao, Interfacial structure and proton conductivity of nafion at the pt-deposited surface, Langmuir 32 (1) (2015) 352–358.

[255] Z. Siroma, T. Ioroi, N. Fujiwara, K. Yasuda, Proton conductivity along interface in thin cast film of nafion®, Electrochemistry communications 4 (2) (2002) 143–145.

[256] Z. Siroma, R. Kakitsubo, N. Fujiwara, T. Ioroi, S.-i. Yamazaki, K. Yasuda, Depression of proton conductivity in recast nafion® film measured on flat substrate, Journal of Power Sources 189 (2) (2009) 994–998.

[257] T. Durbin, D. Delemos, Adaptive underrelaxation of picard iterations in ground water models, Groundwater 45 (5) (2007) 648–651.

[258] P. Ramachandran, G. Varoquaux, Mayavi: 3D Visualization of Scientific Data, Computing in Science & Engineering 13 (2) (2011) 40–51.

[259] A. Kusoglu, A. Kwong, K. T. Clark, H. P. Gunterman, A. Z. Weber, Water uptake of fuel-cell catalyst layers, Journal of The Electrochemical Society 159 (9) (2012) F530–F535.

[260] J. T. Gostick, Versatile and efficient pore network extraction method using marker-based watershed segmentation, Physical Review E 96 (2) (2017) 023307.

[261] G. Mason, N. R. Morrow, Effect of contact angle on capillary displacement curvatures in pore throats formed by spheres, Journal of colloid and interface science 168 (1) (1994) 130–141.

[262] J. Eller, T. Rosén, F. Marone, M. Stampanoni, A. Wokaun, F. N. Büchi, Progress in in situ x-ray tomographic microscopy of liquid water in gas diffusion layers of pefc, Journal of The Electrochemical Society 158 (8) (2011) B963–B970.

[263] A. Forner-Cuenca, J. Biesdorf, L. Gubler, P. M. Kristiansen, T. J. Schmidt, P. Boillat, Engineered water highways in fuel cells: Radiation grafting of gas diffusion layers, Advanced Materials 27 (41) (2015) 6317–6322.

[264] M. Uchida, Y. Fukuoka, Y. Sugawara, N. Eda, A. Ohta, Effects of microstructure of carbon support in the catalyst layer on the performance of polymer-electrolyte fuel cells, Journal of The Electrochemical Society 143 (7) (1996) 2245–2252. doi:10.1149/1.1836988.

[265] M. Eikerling, A. Kornyshev, Modelling the performance of the cathode catalyst layer of polymer electrolyte fuel cells, Journal of Electroanalytical Chemistry 453 (1-2) (1998) 89–106. doi:10.1016/S0022-0728(98)00214-9.

[266] P. Dobson, C. Lei, T. Navessin, M. Secanell, Characterization of the pem fuel cell catalyst layer microstructure by nonlinear least-squares parameter estimation, Journal of The Electrochemical Society 159 (5) (2012) B514–B523. doi:10.1149/2.041205jes.

[267] M. Secanell, K. Karan, A. Suleman, N. Djilali, Optimal design of ultralow-platinum pemfc anode electrodes, Journal of The Electrochemical Society 155 (2) (2008) B125–B134. doi:10.1149/1.2806171.

[268] H. Yu, C. Ziegler, M. Oszcipok, M. Zobel, C. Hebling, Hydrophilicity and hydrophobicity study of catalyst layers in proton exchange membrane fuel cells, Electrochimica Acta 51 (7) (2006) 1199–1207. doi:10.1016/j.electacta.2005.06.036.

[269] A. Fischer, J. Jindra, H. Wendt, Porosity and catalyst utilization of thin layer cathodes in air operated pem-fuel cells, Journal of Applied Electrochemistry 28 (3) (1998) 277–282.

[270] S. Gamburzev, A. J. Appleby, Recent progress in performance improvement of the proton exchange membrane fuel cell (pemfc), Journal of power sources 107 (1) (2002) 5–12.

[271] Y.-G. Yoon, G.-G. Park, T.-H. Yang, J.-N. Han, W.-Y. Lee, C.-S. Kim, Effect of pore structure of catalyst layer in a pemfc on its performance, International Journal of Hydrogen Energy 28 (6) (2003) 657–662.

[272] M. Sabharwal, M. Secanell, Microstructural analysis of electrode performance in fuel cells at varying water contents, ECS Transactions 86 (13) (2018) 51–67.

[273] J. Peron, A. Mani, X. Zhao, D. Edwards, M. Adachi, T. Soboleva, Z. Shi, Z. Xie, T. Navessin, S. Holdcroft, Properties of nafion® nr-211 membranes for pemfcs, Journal of Membrane Science 356 (1-2) (2010) 44–51.

[274] M. Mortazavi, K. Tajiri, Liquid water breakthrough pressure through gas diffusion layer of proton exchange membrane fuel cell, international journal of hydrogen energy 39 (17) (2014) 9409–9419.

[275] T.-L. Liu, C. Pan, Visualization and back pressure analysis of water transport through gas diffusion layers of proton exchange membrane fuel cell, Journal of Power Sources 207 (2012) 60–69.

[276] Z. Lu, M. M. Daino, C. Rath, S. G. Kandlikar, Water management studies in pem fuel cells, part iii: Dynamic breakthrough and intermittent drainage characteristics from gdls with and without mpls, International Journal of Hydrogen Energy 35 (9) (2010) 4222–4233.

[277] P. Satjaritanun, J. Weidner, S. Hirano, Z. Lu, Y. Khunatorn, S. Ogawa, S. Litster, A. Shum, I. Zenyuk, S. Shimpalee, Micro-scale analysis of liquid water breakthrough inside gas diffusion layer for pemfc using x-ray computed tomography and lattice boltzmann method, Journal of The Electrochemical Society 164 (11) (2017) E3359–E3371.

[278] J. Xie, F. Xu, D. L. Wood III, K. r. L. More, T. A. Zawodzinski, W. H. Smith, Influence of ionomer content on the structure and performance of pefc membrane electrode assemblies, Electrochimica Acta 55 (24) (2010) 7404–7412.

[279] S. Martin, P. Garcia-Ybarra, J. Castillo, High platinum utilization in ultra-low pt loaded pem fuel cell cathodes prepared by electrospraying, International Journal of Hydrogen Energy 35 (19) (2010) 10446–10451.

[280] K.-H. Kim, K.-Y. Lee, H.-J. Kim, E. Cho, S.-Y. Lee, T.-H. Lim, S. P. Yoon, I. C. Hwang, J. H. Jang, The effects of nafion® ionomer content in pemfc meas prepared by a catalyst-coated membrane (ccm) spraying method, International Journal of Hydrogen Energy 35 (5) (2010) 2119–2126.

[281] M. Uchida, Y. Aoyama, N. Eda, A. Ohta, New preparation method for polymer-electrolyte fuel cells, Journal of The Electrochemical Society 142 (2) (1995) 463–468.

[282] M. Uchida, Y. Aoyama, N. Eda, A. Ohta, Investigation of the microstructure in the catalyst layer and effects of both perfluorosulfonate ionomer and ptfe-loaded carbon on the catalyst layer of polymer electrolyte fuel cells, Journal of the Electrochemical Society 142 (12) (1995) 4143–4149.

[283] M. Lopez-Haro, L. Guétaz, T. Printemps, A. Morin, S. Escribano, P.-H. Jouneau, P. Bayle-Guillemaud, F. Chandezon, G. Gebel, Three-dimensional analysis of nafion layers in fuel cell electrodes, Nature communications 5 (2014) 5229.

[284] M. Sabharwal, L. M. Pant, N. Patel, M. Secanell, Computational analysis of gas transport in fuel cell catalyst layer under dry and partially saturated conditions, Journal of The Electrochemical Society 166 (7) (2019) F3065–F3080. doi:10.1149/2.0081907jes.

[285] S. Shukla, S. Bhattacharjee, A. Weber, M. Secanell, Experimental and theoretical analysis of ink dispersion stability for polymer electrolyte fuel cell applications, Journal of The Electrochemical Society 164 (6) (2017) F600–F609.

[286] W. Hu, Y. Jiang, D. Chen, Y. Lin, Q. Han, Y. Cui, Impact of pore geometry and water saturation on gas effective diffusion coefficient in soil, Applied Sciences 8 (11) (2018) 2097.

[287] F. H. Kim, D. Penumadu, V. P. Schulz, A. Wiegmann, Pore size distribution and soil water suction curve from micro-tomography measurements and real 3-d digital microstructure of a compacted granular media by using direct numerical simulation technique, in: Multiphysical testing of soils and shales, Springer, 2013, pp. 171–176.

[288] M. Starnoni, D. Pokrajac, J. E. Neilson, Computation of fluid flow and pore-space properties estimation on micro-ct images of rock samples, Computers & Geosciences 106 (2017) 118–129.

[289] B. L. Trembacki, A. N. Mistry, D. R. Noble, M. E. Ferraro, P. P. Mukherjee, S. A. Roberts, Editors' choicemesoscale analysis of conductive binder domain morphology in lithium-ion battery electrodes, Journal of The Electrochemical Society 165 (13) (2018) E725–E736.

[290] M. Ender, J. Joos, T. Carraro, E. Ivers-Tiffée, Three-dimensional reconstruction of a composite cathode for lithium-ion cells, Electrochemistry Communications 13 (2) (2011) 166–168.

[291] L. Zielke, T. Hutzenlaub, D. R. Wheeler, C.-W. Chao, I. Manke, A. Hilger, N. Paust, R. Zengerle, S. Thiele, Three-phase multiscale modeling of a licoo2 cathode: Combining the advantages of fib–sem imaging and x-ray tomography, Advanced Energy Materials 5 (5) (2015) 1401612.

[292] S. K. Babu, A. I. Mohamed, J. F. Whitacre, S. Litster, Multiple imaging mode x-ray computed tomography for distinguishing active and inactive phases in lithium-ion battery cathodes, Journal of Power Sources 283 (2015) 314–319.

[293] H. Iwai, N. Shikazono, T. Matsui, H. Teshima, M. Kishimoto, R. Kishida, D. Hayashi, K. Matsuzaki, D. Kanno, M. Saito, H. Muroyama, Quantification of sofc anode microstructure based on dual beam fib-sem technique, Journal of Power Sources 195 (4) (2010) 955–961.

[294] F. Hegge, R. Moroni, P. Trinke, B. Bensmann, R. Hanke-Rauschenbach, S. Thiele, S. Vierrath, Three-dimensional microstructure analysis of a polymer electrolyte membrane water electrolyzer anode, Journal of Power Sources 393 (2018) 62–66.

[295] A. Ashari, H. V. Tafreshi, A two-scale modeling of motion-induced fluid release from thin fibrous porous media, Chemical Engineering Science 64 (9) (2009) 2067–2075.

[296] A. Kneer, J. Jankovic, D. Susac, A. Putz, N. Wagner, M. Sabharwal, M. Secanell, Correlation of changes in electrochemical and structural parameters due to voltage cycling induced degradation in pem fuel cells, Journal of The Electrochemical Society 165 (6) (2018) F3241–F3250.